UNIVERSITAT
POLITÈCNICA
DE VALÈNCIA

DOCTORAL THESIS

CHARACTERISATION OF THE TENSILE BEHAVIOUR OF UHPFRC BY MEANS OF FOUR-POINT BENDING TESTS

Author:

Juan Ángel López Martínez

Director:

Pedro Serna Ros

Co-director:

Juan Navarro-Gregori

Acknowledgements

I am very pleased to be able to thank those people, institutions and companies that have contributed with hard work, counselling, funding, desire of innovation and patience.

First I would like to thank Professor Dr. Pedro Serna and Associated Professor Dr. Juan Navarro-Gregori, my Thesis Director and co-Director, respectively, members of the Science and Technology Institute of Concrete (ICITECH) where the research presented herein was conducted. I greatly appreciate the freedom they gave me to choose the topic I was eager to undertake and their endless help to guide it in the right way.

I wish to express my gratitude to the members of the jury and reviewers who generously spent their time to check and improve my work with their insightful and valuable comments: Prof. Dr. Gonzalo Ruiz, Prof. Dr. María Belén González, Prof. Dr. Emmanuel Denarié, Prof. Dr. Marco di Prisco and Prof. Dr. José Luis Bonet.

I am especially grateful to all the flatmates I have had over the last 4 years whom I have spent the most entertaining times. We will always remember those 'benitos' freak night conversations just to simply save the world, or to simply save ourselves after finishing PhD studies.

I am sincerely thankful to all my colleagues from ICITECH, especially those with whom I shared a table and worked side by side.

I would like to express my sincere thanks to Esteban Camacho and Hugo Coll who took care of me and taught me more than they can even imagine. I found in them everything one can possibly expect of a brother. I also wish to thank Fernando Galán, an extremely experienced civil engineer from whom I am continuously learning. It is

Abstract

Combining the most recent technologies in concrete, Ultra-High-Performance Fibre-Reinforced Concrete (UHPFRC) arises as a promising material for the near future. UHPFRC have shown how flexible concrete can be to adapt to the ever-changing social and environmental demands. With its high flexibility composition and its mechanical properties, UHPFRC is full of both unexplored and unexploited possibilities. Engineers should take responsibility for this task. However, it is fair to acknowledge that this is not an easy task and it requires the development of reliable and widely accepted design standards provided by the scientific community.

It is a fact that the widespread use of new materials in civil engineering requires the development of specific guidelines. That became clear in the case of fibre-reinforced concrete at the beginning of the 21st century. Although this technology and the advantages of its application were already known since the early 70s, its extensive use in structural applications was restricted primarily due to the lack of a reliable and widely accepted design and characterisation standard. That should have been what researchers identified as a major drawback to be overcome at the end of the 20th century.

In 1995, the task of developing both a standard test methodology to determine the post-cracking behaviour of fibre-reinforced concrete and design guidelines in accordance with it, was assigned to the RILEM technical committee TC 162-TDF. Members of that committee were aware that both assignments were interrelated and had to be pursued together, otherwise, that work would have been doomed to fail. Thanks partly to that work, the use of fibre-reinforced concrete in civil engineering applications is now feasible and it is covered by international standards. Nevertheless, there is still a long way to go when dealing with new types of concrete.

A major concern about durability, long-lasting structures and reduction of maintenance cost, as well as the development of new concrete technologies, improved knowledge of

fibre effect and a huge growth in the fibre industry accompanied by fibre price reduction have led, among other factors, to the development of new types of concrete whose mechanical behaviour substantially differs from conventional fibre-reinforced concrete. This is why current characterisation methodologies and design standards must be reviewed and adjusted to these newer materials. However, design standard revision cannot disregard former milestones achieved thanks to decades of hard work. It must offer an integrated view in which new types of concrete comprise existing ones in a broader group, because at the end of the day and despite having newer and improved properties, new types of concrete are still concrete. That is how it should be understood and how it must be reflected in newer codes and standards.

The work presented herein is focused on one of these recently developed materials that embraces major advanced technologies in concrete: Ultra-High-Performance Fibre-Reinforced Concrete (UHPFRC). This work is specifically focused on those crucial requirements for the development and widespread use of it, such as constitutive tensile characterisation and classification. This work includes a deep revision of the uniaxial tensile behaviour of concrete and its development as fibre technology has evolved. In addition, traditional characterisation standard methods as well as those recently developed for its specific use on UHPFRC are reviewed and called into question.

Throughout the document, the development of different methodologies to determine the uniaxial constitutive tensile behaviour of UHPFRC from bending tests are shown, together with a simplified characterisation proposal specially developed for being included in a standard. All developed methodologies presented herein are checked and validated. These methods are specifically designed for their application on experimental results obtained from a special type of four-point bending test, whose standardisation proposal for UHPFRC is also shown.

Finally, a classification proposal is presented as a function of more relevant UHPFRC tensile parameters necessary for design that can be directly obtained from the standard characterisation test method suggested. Proposed classification encompasses the existing classification for conventional reinforced and fibre-reinforced concrete. In it, both plain concrete and fibre-reinforced concrete are presented as a particular case of a more general tensile constitutive response for concrete. Standard methodology and classification proposed are in accordance with the evolution of concrete and unify historic milestones achieved by the international research community.

Resumen

El Hormigón de Muy Alto Rendimiento (HMAR) combina los últimos avances tecnológicos en hormigón y se erige como un material prometedor para el futuro. El HMAR ha demostrado su gran capacidad para adaptarse a las cada vez más exigentes demandas sociales y medioambientales. Con un gran abanico de posibilidades en su dosificación para conseguir las propiedades mecánicas deseadas, el HMAR es un material lleno de posibilidades aún sin explorar y sin explotar. Los ingenieros tienen la responsabilidad de esta tarea. Sin embargo, es justo reconocer que no se trata de una tarea fácil y que requiere de un desarrollo previo de códigos de diseño adecuados y ampliamente aceptados por parte de la comunidad científica.

El uso extensivo de nuevos materiales en el ámbito de la ingeniería civil requiere el desarrollo de una normativa específica. Esto quedó claro en el caso del hormigón reforzado con fibras en los primeros años del sigo XXI. Aunque la tecnología para el empleo de hormigón con fibras y las ventajas de su uso eran ya conocidos desde los años 70, su extensión a aplicaciones estructurales quedó limitada debido, principalmente, a la falta de códigos de diseño y metodologías de caracterización ampliamente aceptados.

Así lo debieron reconocer los investigadores de finales de siglo cuando en 1995 la tarea de estandarizar un nuevo ensayo para la determinación del comportamiento post-fisura del hormigón con fibras y el desarrollo de metodologías de cálculo de acuerdo a este fue encargada al comité técnico TC 162-TDF del Rilem. Los miembros de aquel comité sabían que ambas tareas estaban interrelacionadas y debían desarrollarse de manera paralela. De haberse realizado de otra manera, aquel trabajo hubiese estado condenado al fracaso. Gracias en gran parte a este trabajo, el empleo del hormigón con fibras en aplicaciones ingenieriles es posible y está contemplado por los actuales códigos de diseño. Sin embargo, queda todavía un largo camino por recorrer.

La aparición de nuevas tecnologías, el mayor conocimiento sobre la aportación de las fibras así como su industrialización y bajada de precios, las mayores preocupaciones

sobre la durabilidad estructural, incremento de la vida útil o la reducción de los costes de mantenimiento, entre otros factores, han derivado en el desarrollo de nuevas tipologías de hormigones cuyo comportamiento mecánico difiere de manera sustancial de los tradicionales hormigones con fibras. Es por ello que tanto la readaptación de las metodologías de caracterización como las metodologías de diseño deben ser reformuladas. Y esto debe hacerse de manera no disruptiva, es decir, manteniendo la línea de los hitos alcanzados en los hormigones con fibras convencionales de manera que queden integrados en metodologías de caracterización y de diseño que los engloben, porque al fin y al cabo, y aunque con nuevas y mejores propiedades mecánicas, los nuevos hormigones siguen siendo hormigones. Así debe ser entendido y así debe quedar reflejado en las nuevas normativas.

El presente trabajo se centra en uno de esos nuevos materiales desarrollados con el avance de las nuevas tecnologías como es el HMAR. En especial, este documento se centra en ese aspecto tan fundamental para el desarrollo de nuevos hormigones como es la caracterización mecánica y la tipificación. Este trabajo incluye una revisión del comportamiento mecánico uniaxial a tracción del hormigón y de su evolución con la aparición de las diferentes tecnologías. Además, se revisan y se ponen en cuestión los sistemas tradicionales de caracterización, así como los nuevos sistemas desarrollados en los últimos años para su empleo específico en el HMAR.

A lo largo del documento se desarrollan diferentes metodologías para la obtención del comportamiento constitutivo a tracción del HMAR, así como la propuesta de una metdología simplificada de caracterización especialmente diseñada para ser incluida en una norma, todas ellas debidamente validadas. Estas metodologías son de aplicación específica a los resultados experimentales obtenidos mediante un ensayo a cuatro puntos sin entalla, cuya propuesta de estandarización para el HMAR ha sido también desarrollada.

Finalmente, se presenta una propuesta de tipificación de acuerdo a los parámetros más relevantes del comportamiento a tracción del HMAR que son necesarios para el diseño y que pueden ser directamente obtenidos del ensayo de caracterización propuesto. Esta clasificación engloba a la clasificación existente para el hormigón armado convencional y los actuales hormigones con fibras, de manera que se presenta la actual definición de hormigón con fibras como un caso particular de estos nuevos hormigones, respetando al máximo la evolución de este material y aunando los logros conseguidos por la comunidad científica.

Palabras clave: ultra-high performance fibre-reinforced concrete (UHPFRC), hormigón de muy alto rendimiento (HMAR), análisis inverso, análisis inverso simplificado, ensayo estándar, ensayo de flexotracción a cuatro puntos, ensayo sin entalla, tipificación, model de rotula plástica, comportamiento uniaxial constitutive a tracción, caracterización, endurecimiento, comportamiento post-fisura.

Resum

Dins de les combinacions de les tecnologies més recents en el formigó, el formigó de molt alt rendiment reforçat amb fibres (UHPFRC) sorgeix com un material prometedor per al futur pròxim. L'UHPFRC ha demostrat poder ser un formigó flexible per adaptar-se a les sempre canviants demandes socials i mediambientals. Amb una gran flexibilitat en la seua composició i les seues propietats mecàniques, l'UHPFRC està ple de possibilitats de ser explorades i explotades. Els enginyers han de prendre la responsabilitat d'aquesta tasca. No obstant això, és just reconèixer que això no serà fàcil i requerirà el desenvolupament de normes de disseny fiables i àmpliament acceptades per la comunitat científica.

És un fet que l'ús generalitzat de nous materials en l'enginyeria civil requereix l'elaboració de directrius específiques. Això va quedar clar en el cas del formigó reforçat amb fibres a principis de segle XXI. Encara que aquesta tecnologia i els avantatges de la seva aplicació ja eren coneguts des de principis dels 70, el seu ampli ús en aplicacions estructurals es va restringir en els seus inicis a causa de la falta d'una normativa de disseny i caracterització que fora fiable i àmpliament acceptada. Aquest hauria d'haver estat l'inconvenient més important identificat pels investigadors i que calia ser superat a finals del segle XX.

El 1995, la tasca de desenvolupar tant una metodologia experimental estàndard per a determinar el comportament post-fissuració i de normatives de disseny del formigó reforçats amb fibres, va ser assignada a la comissió tècnica RILEM TC 162-TDF. Els membres d'aquest comitè eren conscients que les dues tasques estaven relacionades entre si i van haver de ser abordades conjuntament, en cas contrari, el treball haguera estat condemnat al fracàs. Gràcies en part a aquell treball l'ús del formigó reforçat amb fibres en aplicacions d'enginyeria civil és ara factible i està cobert per les normes internacionals. No obstant això, encara hi ha un llarg camí per recórrer quan es tracta de nous tipus de formigons.

Hi ha una gran preocupació al voltant de la durabilitat, la vida útil de les estructures i la reducció del cost de manteniment, juntament amb el desenvolupament de noves tecnologies de formigó, un millor coneixement de l'efecte de la fibra i un enorme creixement en la indústria de la fibra acompanyat per la reducció del preu de la fibra, han conduït, entre altres factors, al desenvolupament de nous tipus de formigons, el comportament mecànic dels quals es diferencia substancialment dels formigons reforçats amb fibres convencionals. És per això que les metodologies de caracterització actuals i les normes de disseny han de ser revisades i ajustades a aquests nous materials. No obstant això, la revisió del codis de disseny no pot prescindir de les antigues fites aconseguides gràcies a dècades de treball dur. S'ha d'oferir una visió integrada en la qual els nous tipus de formigons integren els ja existents en un grup més ampli, ja que, al cap i la fi i malgrat tenir propietats noves i millorades, els nous tipus de formigons són encara un tipus de formigó. Així es com s'hauria d'entendre i reflectir-se en els nous codis i normes.

El treball presentat en aquest document es centra en un d'aquests materials que s'han desenvolupat recentment i que abasta les principals tecnologies avançades en el formigó: el Formigó de Molt Alt Rendiment Reforçat amb Fibres (UHPFRC). Aquest treball se centra específicament en els requisits fonamentals per al desenvolupament i l'ús generalitzat d'aquest, com ara la caracterització i classificació del comportament constitutiu a tracció. Aquest treball inclou una revisió profunda del comportament a tracció uniaxial del formigó i els seus canvis al temps que la tecnologia de les fibres ha evolucionat. A més, els mètodes tradicionals estàndard de caracterització, així com els recentment desenvolupats per al seu ús específic en l'UHPFRC són revisats i qüestionats.

Al llarg del document, es mostra el desenvolupament de diferents metodologies per a determinar el comportament constitutiu a tracció uniaxial de l'UHPFRC, juntament amb una proposta de caracterització simplificada especialment desenvolupada per poder ser inclosa en normativa. Totes les metodologies desenvolupades presentades en aquest document han estat comprovades i validades. Aquests mètodes estan dissenyats específicament per a la seva aplicació en els resultats experimentals obtinguts a partir d'un tipus especial d'assaig de flexió a quatre punts, a més també s'inclou una proposta d'estandardització per a l'UHPFRC.

Finalment, es presenta una proposta de classificació en funció dels paràmetres més rellevants del comportament a tracció de l'UHPFRC que són necessaris per al disseny i que es poden obtindre directament del mètode d'assaig estàndard suggerit per a la caracterització de l'UHPFRC.

La classificació proposada té amb compte la classificació existent per al formigó armat convencional i el reforçat amb fibres. En ella, tant el formigó en massa com el formigó reforçat amb fibres es presenten com un cas particular d'una resposta constitutiva a tracció més general per al formigó. La metodologia estàndard i la classificació

proposada estan d'acord amb l'evolució de formigó i unifica les fites històriques assolides per la comunitat científica internacional.

Paraules clau: formigó de molt alt rendiment (FMAR), anàlisi inversa, anàlisi inversa simplificada, assaig estàndard, assaig a flexió a terços, assaig a flexió a quatre punts, assaig a flexió sense entalla, classificació, model de ròtula, comportament constitutiu uniaxial a tracció, caracterització, enduriment per deformació, debilitament per deformació.

Table of contents

List of figures

Chapter 1

Chapter 2

Chapter 3

Chapter 4

Chapter 5

Chapter 6

Chapter 7

Appendix I

Appendix II

List of tables

Chapter 1

Chapter 2

Chapter 3

Chapter 4

Chapter 5

Chapter 6

Chapter 7

Appendix I

Appendix II

List of abbreviations and notation

List of abbreviations

Materials:

DSC   Densified Small Particle Concrete
ECC   Engineered Cement Composite
FRC   Fibre Reinforced Concrete
HPC   High-Performance Concrete
HPFRCC   Hige-Performance Fibre-Reinforced Cement Composite
HSC   High-Strength Concrete
RPC   Reactive Powder Concrete
SCC   Self-Compacting Concrete
SIFCON   Slurry Infiltrated Concrete
UHPC   Ultra-High Performance Concrete
UHPFRC   Ultra-High Performance Fibre-Reinforced Concrete
VHPFRC   Very-High Perfomance Fibre-Reinforced Concrete

Mechanics:

5P-IA	Simplified Five-Point Inverse Analysis
CMOD	Crack Mouth Opening Displacement
COD	Crack Opening Displacement
FCM	Fictitious Crack Model
FEM	Finite Element Analysis
FPBT	Unnotched Four-Point Bending Test
I-IA	Iterative inverse analysis
TBTP	Unnotched Third-Point Bending Test
PBP-IA	Point-by-Point inverse analysis
UTT	Uniaxial Tensile Test
SLS	Serviceability Limit State
ULS	Ultimate Limit State

Institutions:

ACHE	Asociación Científico-Técnica del Hormigón Estructural / Spanish Scientific and Technical Association for Structural Concrete
AFGC	Association Française de Génie Civil
DAfStB	Deutscher Ausschuss für Stahlbeton / German Association for Reinforced Concrete
JSCE	Japan Society of Civil Engineers
RILEM	Réunion Internationale des Laboratoires et Experts des Matériaux, systèmes de construction et ouvrages (The International Union of Laboratories and Experts in Constructioni Materials, Systems and Structures)
SETRA	Service d'Etudes Technique des Routes et Autoroutes
SIA	Swiss Society of Engineers and Architects

List of notations

Capital Greek letters:

Δ	variation
ΔL	length increase
$\Delta \delta_b$	flexural displacement increase
$\Delta \delta_c$	displacement increase due to hinge length assumption
$\Delta \delta_{cp}$	displacement increase due to crack postion
$\Delta \delta_s$	shear displacement increase
$\Delta \sigma$	stress increase
Δx	x coordinate increase

Small Greek Letters:

α	$\varepsilon_{t,u}/\varepsilon_{t,el}$
β	$\varepsilon_{t,d}/\varepsilon_{t,el}$
γ	$f_{t,u}/f_{t,el}$ (hardening ratio); toughness index and shear rotation angle
γ_k	characteristic value of γ
δ	displacement at mid span
δ_b	displacement due to bending
δ_{el}	displacement at cracking strength in a UTT; displacement at cracking strength in a TPBPT
δ_{cr}	displacement at tensile strength in a UTT
δ_n	normalised displacement
δ_s	displacement due to shear
δ^*	displacement at mid span with crack location correction
δ^{**}	displacement at mid span with crack location and hinge length correction

δ_{DT}	distance from displacement transducer to the bottom face of the specimen
δ_{max}	displacement at maximum load
δ_{40}	displacement at a 40% loss of stiffness
δ_{75}	displacement at a 75% loss of stiffness
δ_{loc}	displacement at crack localisation point
δ_{80u}	displacement at 80% of bending strength in the unloading branch
δ_{30u}	displacement at 30% of bending strength in the unloading branch
ε	strain
ε_I	first stage of the strain – curvature relationship
ε_{II}	second stage of the strain – curvature relationship
ε_{III}	third stage of the strain – curvature relationship
ε_{IV}	fourth stage of the strain – curvature relationship
ε_V	fifth stage of the strain – curvature relationship
ε_m	average strain
ε_t	strain at most tensioned fibre in the hinge
$\varepsilon_{t,el}$	strain at cracking strength
$\varepsilon_{t,u}$	strain at tensile strength
$\varepsilon_{t,u,k}$	characteristic value of $\varepsilon_{t,u}$
$\varepsilon_{t,u,s}$	strain at SLS
$\varepsilon_{t,u,d}$	strain at ULS
$\varepsilon_{t,d}$	strain at change of slope
$\varepsilon_{t,c}$	characteristic strain (strain at zero stress)
κ	ratio between hinge length and specimen depth
λ	slenderness ratio
μ	$\varepsilon_{t,c}/\varepsilon_{t,el}$
σ	stress
σ_{fl}	equivalent stress in bending

σ_{max}	flexural strength
σ_{40}	equivalent stress in bending at a 40% loss of stiffness
σ_{75}	equivalent stress in bending at a 75% loss of stiffness
σ_{loc}	equivalent stress in bending at crack localisation point
σ_{80u}	equivalent stress in bending at 80% of flexural strength in the unloading branch
σ_{30u}	equivalent stress in bending at 30% of flexural strength in the unloading branch
σ_N	nominal strength
σ_w	stress – crack opening relationship
τ	shear stress
τ_{max}	maximum shear stress
υ	coefficient of Poisson
φ	hinge rotation
ϕ	hinge curvature
ϕ_c	hinge curvature when ε_t is equal to $\varepsilon_{t,c}$
ϕ_{ch}	curvature inside the characteristic length
ϕ_{cr}	curvature of the crack part in the Casanova and Rossi hinge model
ϕ_d	hinge curvature when ε_t is equal to $\varepsilon_{t,u}$
ϕ_{el}	hinge curvature when ε_t is equal to $\varepsilon_{t,el}$
ϕ_{max}	hinge curvature at flexural strength
ϕ_n	normalised curvature
ϕ_m	average hinge curvature
ϕ_u	hinge curvature when ε_t is equal to $\varepsilon_{t,u}$
ϕ_{ul}	unloading curvature

Capital Roman Letters:

A	area
A_Q	shear area
B	empirical constant parameter
D	characteristic size of structure
D_0	reference size
E	elastic modulus
E^*	unloading modulus
$F_{R,i}$	load at a specific crack opening according to EN-14651
G	shear modulus
G_F	fracture energy
G_f	area under the line defined by the first line of σ_w and its intersection with the w axis
I	Modulus of inertia
K	fibre orientation coefficient
L	length or span
M	bending moment
M_I	first stage of the bending moment – curvature relationship
M_{II}	second stage of the bending moment – curvature relationship
M_{III}	third stage of the bending moment – curvature relationship
M_{IV}	fourth stage of the bending moment – curvature relationship
M_V	fifth stage of the bending moment – curvature relationship
$M_{c,i}$	bending moment at the compressed area at the stage i
$M_{t,i}$	bending moment at the tensile area at the stage i
$N_{c,i}$	axial force at the compressed area at the stage i
$N_{t,i}$	axial force at the tensile area at the stage i
P	load

P_1	key point 1
P_2	key point 2
P_3	key point 3
P_4	key point 4
P_5	key point 5
P_{max}	maximum load
P_w	load at a specific crack opening
Q	shear force
S_o	initial stifness
S_{75}	75% of initial stifness
S_{40}	40% of initial stifness

Small Roman Letters:

a	specimen depth
a_0	notched depth
a_i	constant parameter that defines the bilinear σ_w relationsihp
b	width
b_i	constant parameter that defines the bilinear σ_w relationsihp
d	distance between crack surface and mid-span measure at most compressed face
e	specimen depth
f_c	compressive strength
f_{Fts}	serviceability residual strength
f_{Ftu}	ultimate residual strength
$f_{R,i}$	equivalent stress in bending at a specific crack opening according to EN-14651
f_t	cracking strength
$f_{t,k}$	characteristic cracking strength

$f_{t,u}$	tensile strength
$f_{t,u,k}$	characteristic tensile strength
g_f	dissipated energy per unit of volume
h	depth
l	length
l_{ch}	characteristic fracture mechanics length
l_c	characteristic length in TPBT
l_{cs}	characteristic structural length
l_m	gage length
n	number of cracks
s	hinge length
s_{av}	average crack spacing
u	longitudinal elongation of the hinge springs
w	crack opening
w_d	crack opening at change of slope
w_c	characteristic crack opening (crack opening at zero stress)
w_o	intersection of the first line of the bilinear σ_w to the w axis
w_i	average crack spacing at crack localisation
x	position of the neutral axis
x_n	neutral axis depth
x_{el}	crack depth at cracking strength
x_u	crack depth at the end of the hardening phase
y	vertical coordinate in the hinge

Chapter 1

Introduction

1.1. Motivation

Ultra-High Performance Fibre-Reinforced Concrete (UHPFRC) has proven to be a promising material for its use in civil engineering applications thanks to the research work conducted and applications developed in the last decade worldwide. However, its widespread use still depends on several factors, such as: (i) its high raw material cost; (ii) lack of engineers' skills to find out specific designs and construction systems for UHPFRC; (iii) lack of suitable and reliable codes; (iv) no tools available to evaluate the long-term benefits of UHPFRC structures.

One of the main issues that has delayed the widespread use of UHPFRC in structural applications has been its high cost. The raw material cost of UHPRC is about 10 times higher than ordinary concrete, which makes both contractors and owners wary of using it. Experience has proved that an economical UHPFRC design is not achieved only by reducing the weight of a conventional design in ordinary concrete as much as possible. What is really important to develop a competitive solution is to find out the applications, designs, structural systems or manufacturing processes in which UHPFRC shows its great potential. Innovative materials require innovative and bold engineers capable of seeing beyond traditional construction procedures and designs, and of reinventing traditional engineering notions. However, it is fair to acknowledge that this is no easy task, but one that requires engineers possessing a certain degree of expertise and material behaviour knowledge.

To overcome this, the scientific community must provide proper tools, i.e. design guidelines and recommendations, to facilitate engineers' work. Here lies another limitation factor that has delayed the use of UHPFRC: lack of widely accepted and reliable UHPFRC design guidelines, which have started to appear in the last few years.

It is true that UHPFRC improves the durability and service life of structures thanks to its low porosity and excellent crack control. However, difficulties encountered when considering long-term benefits in a project have also contributed to the delay. The most important issue while conceiving a structure is not the construction cost, but the overall cost throughout its service life by considering both social (i.e. economical) and environmental costs. However, no suitable tools are currently available to evaluate that. Worse still, what really matters to most owners and contractors is the initial investment, rather than either maintenance or environmental costs.

Even though all the above-mentioned limiting factors of UHPFRC should be treated, this research document focuses on the improved knowledge of the mechanical behaviour in tension of UHPFRC and its classification. The reason and motivation behind both are found in the applications recently developed in Spain using UHPFRC; e.g., the pedestrian bridge over the Ovejas ravine in Alicante built in 2013 (Figure 1.1) (López et al., 2014b); the pedestrian bridge over the V-21 in Puzol (Valencia) built in 2014 (López et al., 2016); the pedestrian bridge in Guadassuar (Valencia) built in 2015.

The development of all these applications has shown all the limiting factors needed to be overcome when using UHPFRC. In particular, there is the utmost importance of acquiring profound knowledge of UHPFRC tensile behaviour to make the most of it, to reduce the material volume as much as possible, and to achieve a competitive design compared to conventional materials, such as ordinary concrete or steel. This is why UHFPRC tensile behaviour characterisation was the starting point of all these designs.

Figure 1.1 General view of the 43.5-metre span pedestrian bridge over the Ovejas ravine in Alicante (Spain).

Despite UHPFRC technology having been available for almost two decades, it is surprising that the characterisation of UHPFRC tensile behaviour remains a challenge for researchers. When the design process of the pedestrian bridge over the Ovejas ravine started, one question first arose. How can we manage to obtain the tensile properties of UHPFRC for both hardening and softening behaviour from bending tests? One might think that it would have been simpler to derive it from direct tensile tests. However as with most common research and industry facilities, we lacked the suitable equipment to do this. It is fair to acknowledge that the methods to derive UHPFRC tensile properties from bending tests already exist, but it is not easy for most engineers to apply them.

Lack of a simple, accurate, objective and standardised methodology to determine the tensile properties of UHPFRC was identified then as the main limiting factor to the widespread use of UHPFRC. So a decision was made to focus on developing a new method. The developed method had to be easy enough for anyone with basic maths and geometry knowledge to be able to apply it. This method also had to be objective so that no matter who applied it, the results would be the same. It had to be accurate and have barely any variability so that the results could be safely applied. The method also had to offer the mechanical properties strictly required for design purposes; characterisation and design had to go hand in hand. Having identified the problem and what needs were to be performed, the question was how to do it.

In a first approach, one might wonder whether conventional characterisation and design methods for either ordinary concrete or fibre-reinforced concrete can be applied. However, it is known that the mechanical behaviour of UHPFRC substantially differs from that of conventional concrete and fibre-reinforced concrete. This is why current characterisation methodologies and design guidelines should be reviewed and, if necessary, adjusted to UHPFRC. If this were the case, newer characterisation standards and design guidelines could not disregard the former milestones reached in both conventional concrete and fibre-reinforced concrete thanks to decades of hard work. They must offer an integrated view in which new concrete types comprise existing ones in a broader group because, at the end of the day, and despite having newer and improved properties, new concrete types are still concrete. This is how it should be understood and how it must be reflected in newer codes and standards.

Finding a solution to all this is what the present work pursues. The task of putting everything together to foster the development of suitable and widely accepted UHPFRC design guidelines for engineers confers this work sense. This is no easy task, but one that requires, from a researcher viewpoint, profound knowledge on the: (i) evolution of the tensile properties of all concrete types; (ii) characterisation tests and methodologies to derive tensile properties; (iii) the analytical structural behaviour of simple structures. Moreover from an engineering angle, thorough knowledge is required of: (i) current design guidelines; (ii) the constitutive laws proposed to check different limit states and the parameters that define them and, what may be the most

important issue, (iii) the ability to simplify complex notions and analytical models to offer a simple and accurate enough approach for design purposes. This is what can be found in this work.

1.2. Objectives

This work focuses on one single main purpose, which consists in improved knowledge on ***the determination of the material properties of UHPFRC in tension*** to foster the development of suitable UHPFRC design guidelines for engineers who are willing to reinvent and revolutionise the civil engineering field. More specifically, this work aims to ***develop a suitable characterisation test setup and methodology to be proposed as a standard, which enables the determination of those tensile parameters required for both UHPFRC classification and the design of UHPFRC structures***. This main objective has been divided into secondary goals to guarantee success. The secondary objectives are listed below:

1. Justification of the need to improve the characterisation test setups and methodologies for UHPFRC.
2. Justification of the most suitable test setup to determine the tensile properties of UHPFRC using a single test.
3. Development and validation of a suitable closed-form analytical model to describe UHPFRC behaviour in a characterisation test.
4. Development and validation of simple inverse analysis tools to derive constitutive UHPFRC behaviour from bending tests.
5. Proposal and its justification of a standard UHPFRC classification according to the required parameters in tension for design purposes.
6. Proposal and its justification of a standard test setup and a simplified methodology to derive the tensile properties of UHPFRC required for it to be classified.

1.3. Document structure

The document is arranged in seven chapters. To better understand the work, reading the document chapter by chapter is recommended as any chapter cannot be fully understood without having read the previous ones. However, if the sole intention is to read the classification proposed for UHPFRC and the proposed characterisation test setup and methology only from an application viewpoint without having to know the scientific basis, Chapter 6 contains everything required for this purpose.

Chapter 1 is entitled *Introduction*. In this chapter, the starting point of the work is defined, along with the objectives pursued and the way the whole work is arranged.

Chapter 2 is entitled *State of the Art: review and analysis*. In this chapter, Objectives 1 and 2 are tackled. An extensive review of evolution throughout history towards

UHPFRC is made in this chapter, together with a review of its constitutive behaviour, standard test setup and methodologies for its determination, and existing fracture mechanics non-linear hinge models to model its behaviour.

Chapter 3 is entitled *Closed-form non-linear hinge model*. In this chapter, Objective 3 is accomplished. In it, a non-linear hinge model is specifically developed to determine the load-deflection behaviour of UHPFRC in a third-point bending test (TPBT). It is a closed-form analytical model that takes into account the non-linear behaviour in tension of UHPFRC, the shear effect and the position of the crack. It allows the selection of a specific characteristic length and justifies using linear elastic behaviour in compression.

Chapter 4 is entitled *Iterative Inverse Analysis Methods.* In this chapter a load-curvature inverse analysis method (I-IA) is proposed, based on the previously developed non-linear hinge model, to derive the tensile properties of UHPFRC from the experimental load-deflection curves obtained from unnotched third-point bending tests. This method is also experimentally validated by its comparison to the existing point-by-point inverse analysis (PBP-IA).

Chapter 5 is entitled *Simplified Five-Point Inverse Analysis Method*. In this chapter, and in the previous one, Objective 4 is accomplished. A parametric study that varies the tensile constitutive parameters of UHPFRC in the non-linear hinge model is carried out, and simplified equations that relate the constitutive behaviour to the load-deflection response are derived. The simplified five-point inverse analysis method (5P-IA) is proposed and validated.

Chapter 6 is entitled *Characterisation test and methodology proposal*. In this chapter, Objectives 5 and 6 are accomplished. Current classifications of UHPFRC, according to its tensile parameters, are analysed and a classification proposal is made. A third-point bending test is proposed as a standard test to determine all the tensile properties required to classify UHPFRC.

Chapter 7 is entitled *Conclusions*. In this chapter, the major conclusions of this work that derive from fulfilling the objectives are described, along with a proposal of further works for the near future.

The document concludes with the bibliographic references used and two Appendixes. Appendix I describes the experimental programme carried out to validate the non-linear hinge model and the inverse analyses presented (I-IA and PBP-IA). Appendix II describes the experimental programme conducted to validate the developed 5P-IA by its comparison to the PBP-IA results.

Chapter 2

State of the Art: review and analysis

2.1. The path to UHPFRC

2.1.1. Brief review of the birth of reinforced concrete

The modern story of concrete may date back to John Smeaton, who pioneered the use of 'hydraulic lime' to construct the third Eddystone Lighthouse from 1756 to 1759. He probably developed the first hydraulic lime product by calcining limestone that contained clay, and by adding Italian pozzolanic earth to provide additional strength (McKee, 1973). Following the path initiated by Smeaton, Joseph Aspdin patented a material called Portland cement in 1824. It consisted of a blend of limestone, clay and other minerals in a specific proportion, which were calcined and ground into fine particles. As Portland cement alone had poor workability, it was combined with a small proportion of gypsum to slow down the hydration rate and to keep concrete workability longer. The basis of current cements had been established.

Cement was mixed with water and pebbles, brick powder, sand, gravel or other aggregates to produce what we currently call concrete. Major problems with its use in early engineering applications were related to the low tensile strength and lack of ductility of the material itself. In the mid-19th century it was noticed that these problems could be partially solved by adding a metallic reinforcement to the concrete mixture. Once that was known, it is not surprising that engineers started using this metallic reinforcement in many different ways to improve the performance of this material.

Generally speaking, the reinforcement used in concrete can be currently classified depending on whether the reinforcement is continuous or discontinuous. With continuous reinforcement, one can distinguish between ferrocement, and what we nowadays commonly call reinforced concrete; fibre-reinforced concrete is the best example of a discontinuous reinforcement.

The history of ferrocement dates back to 1848 and many considered it the earliest use of reinforced concrete in a generic sense. On that date, Joseph Louis Lambot constructed several rowing boats, plant pots, seats and other items using a material that he called 'Ferciment' in his 1852 patent (Paul et al., 1978). Nowadays, ferrocement consists of multiple closely spaced layers of mesh or fine rods completely embedded in cement mortar. The mesh can be made of metallic or another suitable material (ACI 549R-97). This material is mainly thought to be used in thin-walled structures or elements of less than 25 mm. In others applications, ferrocement is non-competitive due to the high price of steel wire meshes and the labour required to place them (Nedwell et al., 1994).

According to Naaman (Naaman, 2007), the idea of using a discontinuous reinforcement of fibres in concrete was born in Oakland, California, thanks to Ahoille Berard. In 1874 he applied a patent under the name of 'Improvement in artificial stone for paving' (Berard, 1874). In it he described the process to obtain an artificial grey granite stone block by filling a mould with a composition formed by mixing two parts of gravel, two parts of sand, two parts of hydraulic lime, one part of granular waste iron (a sort of fibre) and water. However, use of fibres in concrete was not immediately successful and found its larger application field in thin elements made with asbestos fibre-reinforced mortar in the early years of the 20th century. However, its use decayed once it was discovered that the prolonged inhalation of asbestos fibers can cause serious and fatal illnesses. It was necessary to wait until the 1990s to find an increasingly widespread use of fibre concrete in engineering applications.

What is currently known as 'reinforced concrete' started with Joseph Monier, a French gardener, who incorporated a mesh of iron rods into large planting pots in 1849. The first reinforced concrete structural application is probably due to Françoise Coignet, who built an iron-reinforced concrete structure in 1853, his own house, which still stands (Coignet, 1855). In that case, iron was not used for adding strength to concrete, but for keeping different walls in monolithic construction. Shortly afterwards, the main advantages of using reinforcing concrete with steel rods were shown mainly by Monier and Hennebique with the development of several patented construction methods for beams, pipes, piles and floor slabs (Calavera, 2003).

Contrarily to ferrocement and fibre-reinforced technologies, the use of steel or iron rods for concrete reinforcement quickly spread, and standards for its application appeared in different countries at the beginning of the 20th century. Reinforced concrete rapidly became the construction material *par excellence* in civil engineering (Fernández-Cánvoas, 1981), and the evolution of reinforced concrete knowledge and

technology has been vast ever since. Great improvement in design codes and construction technology, and also in concrete matrix performance, has taken place throughout the past century.

2.1.1.1 Evolution of reinforced concrete in codes and construction technology

From the first standard code for concrete that appeared in 1903 in Switzerland (Switzerland, 1903) to current codes, major advances in knowledge of the structural behaviour of concrete and its technology have been clearly seen. The following list, far from being an exhaustive list of all the improvements in the design codes along history, attempts to show the major key milestones accomplished that have outlined current codes:

- Incorporation of the probabilistic theory for strength and loads characterisation, first proposed in 1906 by German engineer Max Mayer (Mayer, 1926)
- Improvement of reinforced steel to confer greater bond strength to the matrix, high strength and ductility. Different types of steel have been developed until current existing rebars, such as Austrian Isteg steel rebars (Steinman, 1935), or Austrian Tor steel rebars (Hajnal-Kónyi, 1956). Yielding strength of rebars soon reached 400 MPa, and the main purpose was to allow the development of a visible cracking net before structural failure.
- Prestressing technology was patented in 1928 by Eugène Freysinet (Freyssinet, 1928) and was extensively used in civil engineering after World War II. Prestressing technology improved over the years with the development of high yielding strength steel and knowledge of long-term concrete behaviour (Branson, 1977).
- The Plastic Theory for sectional analyses using either a rectangular or a parabolic-rectangular diagram (Nielsen, 1984), which allowed a better use of compressive concrete strength, increased the reinforcement ratio and reduced the span/depth ratio in several engineering applications (Calavera, 2003).
- Improving shear concrete behaviour to avoid unexpected brittle failure in existing structures: consideration of the bending-shear interaction (Paez et al., 1952); fracture mechanics of concrete and scale-effect equations; shear behaviour models (Kupfer, 1964; Collins et al., 1980).
- Limiting and estimating crack width and minimum cover to secure long-term reinforcement behaviour and to guarantee the structure's target service life.
- Non-linear analysis of concrete (CEB-FIP, 1979) and the strut-and-tie model for D-regions (Schlaich et al., 1987).

All these improvements have been incorporated into codes over the years to satisfy two basic principles in design: serviceability and structural safety. These principles are accomplished by meeting the requirements specified in the serviceability and ultimate limit states. A third principle has been currently added to the new MC2010, based on

building or infrastructure sustainability from an environmental, social and economic perspective (Sakai, 2013). However, its full implementation and correct evaluation may still have a long way to go.

2.1.1.2 Evolution of concrete matrix performance

As concrete technology and design codes improved and evolved, so did the matrix properties of concrete, whose continuous evolution has focused on solving major concrete problems: (i) heaviness; (ii) low tensile to compressive strength ratio; (iii) high weight to strength ratio; (iv) poor volumetric stability; (v) poor toughness; (vi) durability-sensitive to project design, environmental exposure, construction and the porous nature of concrete (Fernández-Cánvoas, 1981).

A race to increase concrete compressive strength began in the mid-20th century (Naaman et al., 2012). There may be several reasons for this: (i) according to design codes, most concrete properties, such as tensile strength, shear strength or bond strength, are related to one single property, compressive strength, which can be determined with a low coefficient of variation, and can be considered reasonably representative of concrete mechanical behaviour; (ii) a better understanding of the concrete mix design was reached with new aggregate packing theories and formulations to increase packing density; (iii) cement became increasingly better in the last 50 years; (iv) advances in concrete treatments and curing conditions were made; (v) water reducers were developed. In the 1980s, the way to produce high strength concrete that exceeded 200 MPa became known (Bache, 1981). It was accomplished by using low water to binder ratios, special aggregate particles to achieve higher dense particle packing, water-reducer additives and curing. However, using such high compressive strength concrete was restricted to either laboratory tests or specific applications, and it was not until the 21st century that its use extended to structural applications.

Even though ductility was ensured at the structural level when using steel reinforcement, mass concrete was still brittle in both compression and tension terms. To solve this problem and to increase concrete tensile strength, the former concept of reinforcing concrete with discontinuous fibres dispersed homogeneously inside the concrete matrix was rescued in the investigations conducted at the same time by Romualdi (Romualdi et al., 1964) and Krenchel (Krenchel, 1964), who demonstrated the effectiveness of short steel fibres to reduce concrete brittleness. Investigations on fibre-reinforced concrete have never stopped since to deal with different types of fibres (shape, aspect ratio, type of material) and amounts, and to show that using fibres increases tensile resistance, ductility, stiffness, crack control, durability, and both fatigue and impact performance. However, its extensive use has been delayed over the years until the present-day due to: (i) lack of reliability in the fibre concrete response since its behaviour depends so much on the type and dose of fibres, the interaction of the fibres with the matrix, and the orientation and dispersion of fibres in the elements;

(ii) lack of a suitable method to determine post-cracking tensile strength, and its incorporation into existing design procedures (Massicotte et al., 2000).

Improvement in the packing density of concrete and the use of finer materials, together with the development of newer chemical additives such as superplasticisers, viscosity agents, etc., led to a flowable concrete in the early 1990s which was able to maintain stability and to allow self-compaction (Tanigawaet al.1990). This type of concrete started to be used in those applications in which a high reinforcement ratio discouraged following vibrations techniques, and also in precasting factories to reduce the noise produced while vibrating concrete and, therefore, to reduce occupational hazards.

The major advances made in concrete matrix performance can be summarised as three general features: (i) high compressive strength; (ii) ductility and cracking control due to use of fibres; (iii) special selection of fine and ultrafine particles, which leads to low porosity, high durability and self-compactability. If all these three technologies are combined together with the use of conventional passive or active reinforcement, a solution to the aforementioned major problems of concrete may, at least, be partially solved in certain applications with improvement in its long-term behaviour.

Even though the combination of these three known and existing technologies may seem to be easy, it took several decades of development thanks to research and innovative companies. Several different types of concretes were developed until the definition of a fairly standardised type of concrete that combined these technologies was internationally agreed on and used in civil engineering and architecture.

2.1.1.3 Special concretes

The idea of incorporating new technologies into concrete was born probably due to necessity of solving specific engineering problems that conventional materials were unable to overcome. Once technologies had been developed, engineers likely found a business opportunity in certain specific market niches. This may be the reason to explain the fact that most of the newer concretes developed from the 1980s appeared under a commercial trademark, such as Densit[®], CRC[®], BPR[®], Ductal[®], CEMTECmultiscale[®], BSI[®,] etc. In parallel to that development, researchers started giving scientific names to both newer concretes and technologies which aimed to provide their better understanding and standardisation. A very good summary of the evolution of concrete typologies, in which both trademarks and scientific names are included, from the 1970s to date can be found in (Naaman et al., 2012). An overview of that is shown below.

It is difficult to establish when the term FRC was first used to refer to Fibre-Reinforced Concrete. It can be stated that this term appeared around the 1970s (Naaman, 2007). This term refers to any type of fibre reinforcement, no matter what the fibre shape, aspect ratio, amount or material is. Nowadays, the term FRC can refer to those concretes with a low-mid range compressive strength (up to 80 MPa) that exhibit

softening tensile behaviour. The use of this concrete type is currently covered by codes, and its tensile response can be determined by EN-14651 thanks to the thorough work conducted by RILEM TC162-TDF.

In 1972 the cement plant Aalborg Portland launched the "new concrete" development project based on the assumptions that it is possible to develop cement-based materials with ultra-high strength and durability (www.densit.com). This project led to DSP technology (Densified Systems that contain homogeneously arranged ultrafine Particles), which consisted in improving the packing density of the concrete paste fraction by special fine aggregate selection (silica fume), using superplasticisers and low water to binder ratios, and attaining compressive strength above 200 MPa, thanks also to the use of extremely hard aggregates like bauxite or granite. DSP technology was patented in 1978 under the Densit$^{®}$ trademark. Hans Henrik Bache presented his very impressive discoveries during the second international conference on superplasticisers in concrete in 1981 (Bache, 1981) and shocked the concrete community, which was still having trouble producing a concrete of 25 to 30 MPa in the field. In 1983, Densit was established as an independent company and started selling its products all over the world to become probably the first company that did business with special high strength and high durability concrete.

The terms HSC and HPC were coined in the 1980s by many researchers worldwide to mean High Strength Concrete and High Performance Concrete, respectively. The term High Strength Concrete referred to a concrete with characteristic compressive strength between 50 and 120 MPa. The term High Performance Concrete included those HSC with improved durability properties. However, this performance durability improvement seemed more qualitative than quantitative.

The evolution of DSP technology, in combination with fibre technology, led H. H. Bache to develop in 1987 Compact Reinforced Composite (CRC$^{®}$), which was patented the same year by Aalborg Portland A/S (Bache, 1987). CRC$^{®}$ technology incorporated the addition of a large volume (5%-10%) of short (6-mm long) steel fibres to the concrete matrix, which provided high ductility and allowed a large amount of reinforcement to be used. This product has been commercially available on the market since 1995. Nowadays, the company Hi-Con A/S has the exclusive rights to its use and commercialisation.

Also in the 1980s the so-called SIFCON (Slurry Infiltrated Fibre Concrete) technology was developed. SIFCON can be considered a special type of FRC with a large amount of fibres, up to 20% in volume, which exhibits a strain-hardening tensile response, and involves a different production process. While fibres in FRC are added to the wet or dry concrete mix, SIFCON is prepared by infiltrating cement slurry into a bed of fibers, which are preplaced and packed tightly in moulds (Lankard, 1984).

In an attempt to differentiate strain-hardening from strain-softening FRCs material behaviour, Naaman suggested using the term HPFRCC in the first international

workshop on High Performance Fibre-Reinforced Cement Composites, which was held in Mainz in 1991. Generally speaking, HPFRCC can be considered any concrete that exhibits a strain hardening tensile stress-strain response, accompanied by multiple cracking (and a relatively large energy absorption capacity), as well as good workability, high strength (HSC) and good durability (HPC).

The term Ultra-High Performance Concrete (UHPC) was first used (de Larrard et al., 1994) in 1994 to refer to an optimised particle-packing material. In 1995, P. Richard and M. Cheyrezy established the basis of RPC (Reactive Powder Concrete) technology (Richard et al., 1995), which was first used in the early 1990s by researchers at Bouygues' laboratory in France. RPC is composed of very fine powders (cement, sand, quartz powder and silica fume, with no coarse aggregates), steel fibres, superplasticiser and extremely low water to binder ratios. A very dense matrix was achieved by optimising the granular packing of dry fine powders with a maximum grain particle size of 0.6 mm. The amount of fibres used was between 1.5% and 3% of 13-mm long steel fibres. The achieved compactness and ductitlity conferred RPC ultra-high strength and durability.

RPC technology (or BPR in French) led to the development of Ductal through the coordinated work of three French companies: Lafarge, Bouygues and Rhodia. In 1997, first field applications using RPC such as Ductal were completed with the construction of the pedestrian bridge in the city of Sherbrooke, Quebec, Canada (Blais et al., 1999).

As of the 21st century, the term RPC has been gradually replaced worldwide with UHPFRC (Ultra-High Performance Fibre-Reinforced Concrete) (Rossi, 2000), although it is sometimes referred to as UHPC for simplicity. Lot of types of UHPFRC have been developed worldwide since then, and an increasingly growing number of structural and architectural applications have been developed worldwide over the years in France (Resplendino et al., 2013), Australia (Cavill et al., 2003), Japan (Tanaka, 2013), the USA (Graybeal B. , 2013), Switzerland (Denarié et al., 2015), Spain (Sernaet al., 2014), Canada (Adelineet al., 1998), Germany (Fehling et al., 2004), Austria (Reichel et al., 2009), The Netherlands (Tirimanna et al., 2013) and The Czech Republic (Viteket al., 2015).

2.1.2. *Ultra-High Performance Fibre-Reinforced Concrete (UHPFRC)*

Lots of types of UHPFRC have already been developed worldwide with different mix compositions, types and amounts of fibres, flowability, compressive strength, tensile behaviour, thermal curing, etc. However, according to the most recent standards in UHPFRC (AFGC, 2013) (NF P18-470, 2016) (SIA 2052: 2014-12), a general definition of UHPFRC can be proposed:

"Ultra-High Performance Fibre-Reinforced Concrete (UHPFRC) is defined as a hydraulic cement-based composite material, which combines three technologies in concrete: (i) high characteristic compressive strength of more than 130 MPa; (ii) ductile behaviour under tension due to the presence of fibres, which can provide or not

a pseudo strain-hardening stress-strain response accompanied by multiple cracking depending on fibre volumetric fraction, fibre aspect ratio, and also fibre distribution inside the structural element; (iii) a special selection of fine and ultrafine aggregates that provides dense particle packing, high durability and certain degree of flowability."

Traditionally, the minimum compressive strength used to be considered UHPFRC has been 150 MPa (SETRA-AFGC, 2002). However, the development of new UHPFRC and applications have revealed that the optimum solution to guarantee competitiveness for several applications falls within the 130 MPa range (Walraven, 2012). This was probably the reason why the new French standard proposed a minimum of 130 MPa for the characteristic compressive strength obtained from cylindrical ϕ150/300-mm specimens, or 145 MPa from 100-mm cubes.

Fibres can be used in a wide volumetric fraction range, commonly between 1% and 3%, to ensure ductile behaviour in both compression and tension, and with narrow variability. Most of the typical fibres used are smooth-straight steel fibres with a length range of 6 mm to 20 mm, and with a slenderness ratio above 65 (to improve the matrix-fibre bond) and below 80 (to improve workability). Although their use is less frequent, twisted and hooked-end fibres can also be employed. When specific requirements are involved, a combination of different fibre types can be used. The use of different types and amounts of fibres leads to distinct tensile behaviours. Nowadays, the way to classify and evaluate the tensile performance of UHPFRC in either hardening or softening behaviour remains unclear.

The typically used raw materials are Portland cement, quartz powder, silica fume, quartz sand (with a grain size no higher than 2 mm), superplasticiser and water, and with a water to cement ratio that is commonly lower than 0.25. Other materials can also be utilised, such as ground blast furnace slag, fly ash, glass powder, hard ground aggregates, etc. UHPFRC uses a large amount of cement, normally higher than 700 kg/m^3, and binder, above 1,000 kg/m^3. Since the technology that produces and develops UHPFRC is currently well-known, the UHPFRC mix design depends mainly on locally available materials rather than commercial products, which helps reduce UHPFRC production costs.

Low water to binder ratios and a required compressive strength of at least 130 MPa ensure UHPFRC high durability. However, the term 'high durability' should be defined. As a first proposal, the French standard (NF P18-470, 2016) proposed a set of minimum values of chloride penetration, gas diffusion and porosity that any concrete which aims to be considered UHPFRC should accomplish in a specific test.

By combining the most recent technologies in concrete, UHPFRC, either combined with reinforcement or not, arises as a promising material for the near future. UHPFRC has shown how flexible concrete can adapt to society's recent demands. With high flexibility in its composition, concrete, and more specifically UHPFRC, is full of

unexplored possibilities, or even unexploited possibilities (Aïtcin, 2000). However, caution and patience are needed since further research is required to gain a better understanding of newer materials to be able to benefit more from them.

2.2. UHPFRC limitations and future perspectives

As a matter of fact, UHPFRC enhances the material properties of conventional concrete in terms of toughness, ductility, strength in both tension and compression, durability, cracking control, impact, fatigue, bond, etc. These performance properties lead to a reduced dead load of structures, which results in slenderer designs; smaller amount of raw materials; fewer steel rebars are used; reduced labour; prolonged service life of structures; reduced maintenance costs; etc. However, to quote what Pietro Gambarova wrote about FRC (Gambarova, 2007), it can be stated that UHPFRC is still 'a character looking for a playwright able to write a proper comedy'. Engineers know about UHFPRC performance, but need to know how and where they have to focus its potential. This is only possible through a profound understanding of UHFPRC's mechanical behaviour, which must be supported on widely accepted design codes.

Despite UHPFRC having already been used in different structural and architectural applications all over the world, it is fair to recognise that its use is still limited. The reason for this may lie in the construction industry's lack of enthusiasm, which is always reluctant to use *more expensive* materials as both public and private purchasers are mainly worried about initial construction costs. Moreover, they are unprepared for acknowledging and quantifying the long-term benefits of more durable materials (Gambarova, 2007), even when they know that economic benefits in the construction industry come in the long term. One consequence of this situation is the slowness to update and develop *design codes*, which results in reduced UHPFRC use (Walraven, 2009). Therefore, two main aspects are identified as the limiting factors for UHPFRC's widespread use: (i) high UHPFRC costs; (ii) lack of design codes.

2.2.1. Raw material costs of UHPFRC

According to Aïtcin (Aïtcin, 2000), the price of 1 m^3 of the UHPFRC used to build the Sherbrooke footbridge was around 1,000 €/m^3. This price may frighten most engineers, who still compare this price to the price that 1 m^3 of conventional concrete costs. However, the price of UHPFRC should not be given in €/m^3, but in €/ton as UHPFRC structures are much lighter than ordinary concrete ones and are, hence, closer to steel designs. According to recent economic studies on different pedestrian bridges alternatives devised in distinct materials conducted by López (López et al., 2016a), UHPFRC is competitive compared to steel if the UHPFRC design keeps the weight of a steel one; UHPFRC is also competitive compared to concrete if UHPFRC designs maintain the weight between 3 and 4 times lower than the equivalent design in conventional concrete. If long-term benefits are taken into account, these restrictions can become more flexible.

An analysis of the raw materials required to produce UHPFRC shows that approximately 50% of the total price is due to fibres if common UHPFRC with 2% in the volume of steel fibres is considered. Over the last 20 years, there has been a huge increase in fibre production and fibre suppliers all over the world. This has lowered the price of fibres, which now cost around 2.5 €/kg, and make UHPFRC costs less expensive. In 2000, Aïtcin predicted a raw material cost for UHPFRC of around 600 €/m^3 to 650 €/m^3 (Aïtcin, 2000) for that near future, and probably his prediction comes close to the current UHFPRC raw material cost for 150 MPa UHPFRC.

2.2.2. Design recommendations for UHPFRC

The use of a new material for structural or architectural applications requires the development of design guidelines and standards. From the standpoint of engineers and constructors, they need a reliable guide that makes a good quality design and manufacturing process possible to allow them to follow easy rules that ensure structural safety, durability and economic viability. Form the standpoint of public or private purchasers, they need a design project whose safety and service life have been evaluated and guaranteed according to standard design guidelines. They need to feel that the new structure does not imply additional risks.

If no design codes are available, risks have to be assumed by both engineers and structure ownerships. These projects require the collaboration of either research institutes or the academy. As design codes are lacking, designs tend to be too safe and, therefore, not well optimised, which results in non-economical applications. However, this is probably the best, or the only, way to start in such a slow evolving industry like the construction one is.

The first constructions made in UHPFRC, far for being cost-efficient, actually contributed to UHPFRC knowledge. Following the state of the art in the literature and after constructing the first full-scale prototypes and structures, the first recommendations for the design of prestressed UHPFRC beams appeared in Australia, which were focused on Ductal® properties (Gowripalan et al., 2000). In 2002, Interim Recommendations were published, developed by AFGC-Sétra in France (AFGC-Sétra, 2002). As UHPFRC became more popular, new guidelines appeared worldwide. In 2006, the Japanise Society of Civil Engineers published other recommendations (JSCE, 2006) to design UHPFRC (they called it UFC), which established the basis for the outstanding structures that they have built so far.

In the USA, one of the pioneers to use and develop UHFPRC was the FHWA (Federal Highway Administration). According to its website, UHPFRC has been used in some way in more than 50 bridges and pedestrian bridges in the last 11 years. Its experience is shared by reports that can be directly obtained from its website (FHWA, 2013) (FHWA, 2014).

In 2013, the new French recommendations were published (AFGC, 2013) as a revision of the Interim recommendations of 2002, which included knowledge acquired in the meantime between both documents. Even though it comprises major items of the background of applications in France, these are the most popular recommendations to date, at least in Europe. These recommendations became a standard in France (NF P18-470, 2016; NF P18-710, 2016) in 2016. In Switzerland, another draft standard is currently being developing, which collects all the UHPFRC experience acquired in the last few years (SIA 2052: 2014-12).

In Germany, an ambitious R&D programme was conducted from 2005 to 2012 under the guidance of the University of Kassel, which will lead shortly to the German standard for UHPFRC. Another UHPFRC guideline is expected to appear in Spain by 2017.

There are founded reasons to believe that a huge development in UHPFRC applications is yet to come. Administrations and private purchasers are becoming increasingly aware of the material and its possibilities. Experience obtained from existing applications, together with new design codes, will foster the use of UHPFRC for years to come.

2.3. Tensile behaviour evolution

Knowledge of UHPFRC tensile behaviour is the result of several decades of attempts made to understand and characterise the tensile behaviour of plain concrete and, afterwards, the tensile behaviour of fibre-reinforced concrete. It is considered that a better comprehension of UHPFRC tensile behaviour can be gained if a brief review of the knowledge acquired over the years on tensile behaviour of both plain fibre-reinforced concretes is firstly presented. In order to gain a better understanding of the following sections, the way that current codes have dealt with the tensile behaviour of these concretes is also presented. Finally, a brief summary of current knowledge on UHPFRC tensile behaviour is presented.

2.3.1. Tensile behaviour of conventional concrete

By using a very stiff tensile machine and a small concrete specimen, Hughes and Chapman (Hughes et al., 1966) were probably among the first to obtain a complete stress-strain behaviour of mass concrete in 1966. An example of what can be obtained is shown in Figure 2.1. Accordingly, behaviour in stage 1 can be considered almost linear elastic. At the end of stage 1, the curve becomes non-linear due to the microcracks that distribute all over the specimen. These microcracks are not visible to the naked eye and their width is too small. Immediately before the end of stage 2, microcracks and deformation start to concentrate on a small material volume around one of the cracks. As deformation increases, a point is reached at which that cross-section is unable to carry more load, and a still indiscernible macrocrack appears just

after the maximum load is reached. From this point onwards, additional deformation on the failure section, which is called fracture zone, takes place while the material outside this fracture zone is elastically unloaded. As load decreases after the first fracture zone has developed, only a single fracture zone appears (Petersson, 1981).
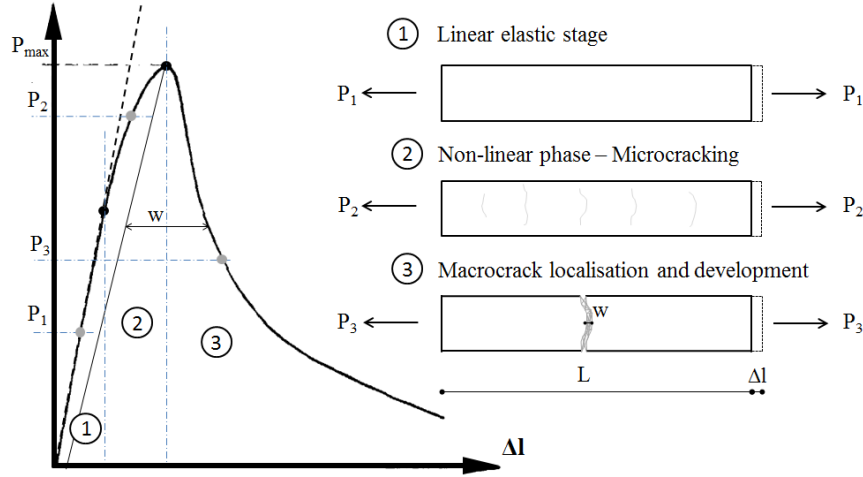
Figure 2.1. An example of the complete tensile stress-strain curve for concrete

According to the results presented in 1969 by Heilman et al. (Heilmannet al., 1969), the fracture zone width is narrow, i.e. in a cross-section next to the fracture process zone deformations are not affected by the crack and remain in an elastic regime. Therefore, it is possible to describe discrete fracture zone behaviour as an opening that is able to transfer stress (σ_w). The stress that the opening can transfer is according to its width ($\sigma_w(w)$). This concept is the basis of the so-called fictitious crack model (FCM), originally suggested by Hillerborg (Hillerborget al., 1976). In this approach it is assumed that when a crack appears, it is not a 'real' crack, i.e. it is not a stress-free crack, but is a 'fictitious' crack that is able to transfer stress between the crack planes according to its opening up to a certain value from which the crack becomes a stress-free crack (w_c). Using this model, total specimen (ΔL) deformation, measured on the gauge length (L), can be described using Eq. 2.1.

$$\Delta L = \varepsilon\, L + w$$

Eq. 2.1

where ε is the strain in the material outside the fracture zone, and w is zero before tensile strength is reached.

From Eq. 2.1, it is possible to derive the mean strain of the specimen in Figure 2.1 by dividing it by gauge length. The mean strain is shown in Eq. 2.2

$$\varepsilon_m = \varepsilon + \frac{w}{L}$$

Eq. 2.2

According to the results presented by Heilmann et al., the strain outside the fracture zone may be considered independent of gauge length throughout the test as it remains constant along specimen length and equals ε. After maximum strength has been reached, the crack opening measurement remains constant regardless of the gauge length used. Therefore, the mean strain depends on gauge length: the longer gauge length is, the lower the mean strain, and conversely. This means that it is unsuitable to consider that the stress-strain curve is a material property after maximum stress as it depends on gauge length. From another angle, it can be stated that it is absolutely necessary to indicate gauge length if an unloading stress-strain relationship is shown.

A better way to describe the tensile response of concrete is to use two relationships: (i) a stress-strain relationship for the material prior to maximum strength being reached and for the material outside the fracture zone after macrocrack localisation; (ii) a stress-crack opening relationship inside the fracture zone.

It should be remarked that even though the ascending non-linear branch in Figure 2.1 involves microcracking in concrete, it has been traditionally attributed to volumetric energy absorption, independently of gauge length. This is why the slight hardening phase in concrete has been described using a stress-strain relationship despite being already cracked (see MC2010).

Conceptually speaking, the defined stress-crack opening response does not have to be a material property itself. When studying the fracture mechanics of steel, the fracture process is characterised by a necking zone dominated by shear forces and strongly affected by the state of the stress; i.e., either plane stress or plane strain (Petersson, 1981). This means that the fracture behaviour of a material like steel strongly depends on its thickness. However in concrete, differences between plane stress and plane strain are minimum since a material fracture is due to crack development and no shear deformation takes place. Therefore, the stress-crack opening relationship is independent of specimen thickness and, if considering deterministic concrete behaviour, in which no statistical effects like fibre distribution and orientation are considered, the stress-crack opening relationship can be assumed to be a material property.

According to uniaxial tensile tests on plain concrete, the stress-crack opening function first very drastically descends, and then the slope slows down from a strength range of about 15-33% of tensile strength. The initial work by Hillerborg et al. (Hillerborg et al., 1976) described the softening curve as a decaying exponential with a horizontal asymptote. In 1981, Petersson (Petersson, 1981) proposed a bilinear form for simplicity reasons. In his work, Petersson proposed to locate the change of slope at 30% of tensile

strength. According to the work by Wittmann et al. (Wittmann et al., 1988), the Model Code (MC1990, 1990) established the change of slope at 15% of tensile strength. In 1989, Rokugo et al. (Rokugo et al., 1989) proposed a 25% tensile strength, and finally the new Model Code (MC2010, 2010) adopted a 20% tensile strength as the the slope strength change.

In MC2010, the tensile response of concrete has been simplified by using a bilinear relationship for both the stress-strain and the stress-crack opening relationship. The proposed tensile behaviour is shown in Figure 2.2. According to it, the change of slope of the stress-strain response is defined at 90% of tensile strength, and assumes a strain hardening capacity at a peak of 0.15‰. Tensile strength is obtained according to compressive strength, and the elastic modulus is considered the same as in compression. The change of slope in the stress-crack opening relationship is established at 20% of tensile strength. Its corresponding crack opening and the crack opening at the end of the fracture process zone are defined according to fracture energy (G_F) and tensile strength. For a common C30, the parameters that defined the tensile behaviour of concrete are in accordance with MC2010, and are shown in Figure 2.2:

- $f_{t,u}$= 2.9 MPa; G_F = 0.14 KJ/m^2; w_d= 0.048 mm; w_c= 0.241 mm
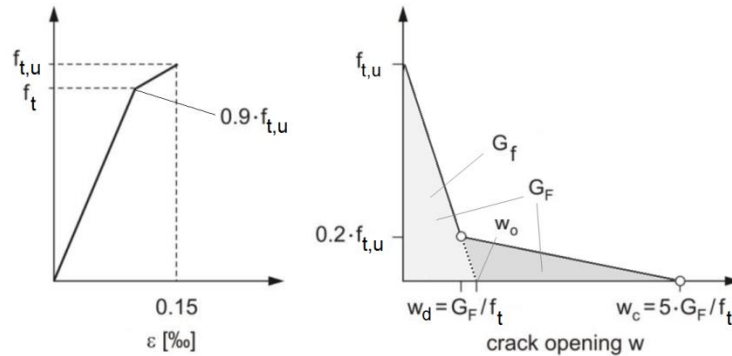
Figure 2.2. Concrete tensile behaviour according to (MC2010, 2010)

Fracture energy (G_F) is defined as the area under the stress-crack opening relationship and represents the total energy dissipated by the fracture per unit area of the crack plane (Bazant, 2002). As stated in (Hillerborg et al., 1976), and corroborated by Planas et al. (Planas et al., 1992), within a realistic size range, the maximum load of plain concrete structures and their size effect are controlled by the initial slope of the stress-crack opening relationship. This means that the ultimate load of structures is always governed by a macrocrack, whose opening in the maximum load state, is smaller than that which corresponds to change of slope.

This fact, together with the several problems encountered when determining fracture energy (G_F) due to the large tail of the descending stress-crack opening curve (Bazant,

2002), led to the definition of parameter G_f, which represents the area under the line defined by the initial slope of the stress-crack opening law and its intersection with the w axis (see Figure 2.2).

The most important phenomenon of the fracture mechanics in concrete is probably scaling and size effect. Existing test data reveal that the strength and post-peak load-carrying capacity of concrete structures decrease with an increase in size. From the scaling and size effect point of view, another important material parameter defined according to tensile strength and fracture energy is the fracture's characteristic length. According to (Hillerborg et al., 1976), characteristic length (l_{ch}) is a material parameter that relates to the size of the zone in which energy is dissipated during crack propagation, and can be obtained following Eq. 2.3.

$$l_{ch} = \frac{EG_F}{f_t^{\,2}}$$

<div align="right">Eq. 2.3</div>

In a more general sense, the fracture's characteristic length can be defined as the maximum length that ensures stable crack growth in a concrete specimen subjected to a pure axial load (Spasojevic, 2008). This length is found at the equilibrium of the total elastic energy stored per unit of area immediately before macrocrack formation (G) with fracture energy (G_F).

For a uniaxial load-displacement tensile response of concrete, the total energy available per unit of area that can be released by the specimen up to crack localisation point is obtained following Eq. 2.4 (Spasojevic, 2008), and by assuming perfectly linear behaviour up to the maximum load:

$$G = \frac{1}{2}\frac{P_{max}\delta}{A} = \frac{P_{max}^{\,2}L}{2EA^2} = \frac{f_t^{\,2}}{2E}L$$

<div align="right">Eq. 2.4</div>

Crack growth stability is guaranteed if the available strain energy is lower than the fracture energy, according to Griffith's balance energy criterion (Griffith, 1921). For the limit case, when these two energies are balanced, the fracture's characteristic length (l_{ch}) can be obtained according to Eq. 2.5.

$$l_{ch} = \frac{2EG_F}{f_t^{\,2}}$$

<div align="right">Eq. 2.5</div>

By comparing Eq. 2.3 and Eq. 2.5, we note that the Hillerborg characteristic length is half the length of a specimen subjected to an axial tension load, in which just enough elastic strain energy is stored to create a complete fracture surface.

This parameter has been used as a brittleness index of concrete. The shorter the characteristic length, the more brittle the material becomes, and conversely. Moreover, brittleness of structural failure can be quantified by using a parameter such as D/l_{ch}, where D is the characteristic structure size (e.g., beam depth). Existing test data reveal that the strength and post-peak load-carrying capacity of concrete structures decrease with an increasing size (D). A simple example of this is the scale-effect law proposed in (Hillerborg, 1983) for a specific test setup, which is shown in Figure 2.3. In it, the specimen depth (h) to characteristic length (l_{ch}) ratio is represented against the flexural strength (f_{fl}) to tensile strength (f_t) ratio on a logarithm scale. We can see that flexural strength decreases as depth increases.
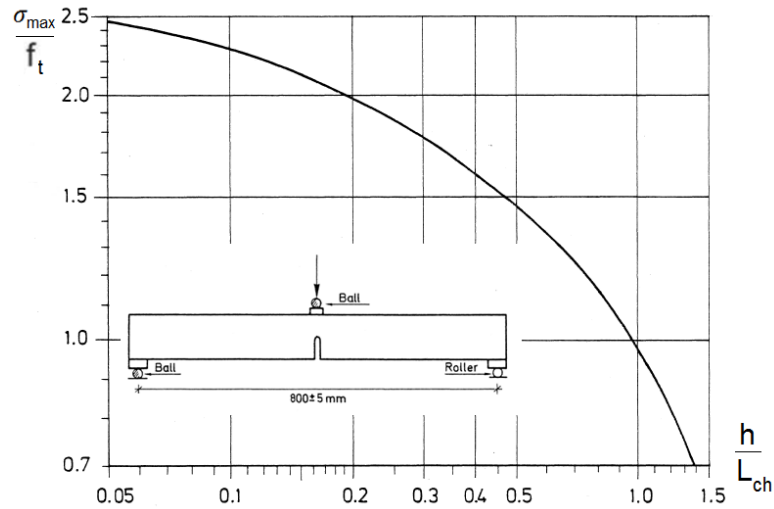
Figure 2.3 The scale effect law for notched prisms in bending (Hillerborg, 1983)

The curve in Figure 2.3 shows the shape of the size effect law proposed by Bazant (Bazant, 1984), which follows Eq. 2.6. In that equation, σ_N is nominal strength, B is an empirical constant parameter, and D_0 is the reference size, which is another empirical constant and may differ from l_{ch}. According to (Bazant, 1989), a basic criterion for the acceptability of a non-linear fracture mechanics model for concrete is that they must describe the size effect law.

$$\sigma_N = Bf_t \left(1 + \frac{D}{D_0}\right)$$

Eq. 2.6

Determination of fracture parameters of concrete was an important issue to deal with in the 1980s, especially for concrete fracture community members. Three standard methods were proposed to RILEM to determine the different parameters related to the fracture mechanics of concrete, such as fracture energy, resistance against cracking, or fracture process zone size. A brief summary of these methods can be found in (Bazant, 1989). Due to the difficulties encountered while performing direct tensile tests, mainly regarding the stress field distribution and the gripping system, all the proposed tests were flexural tests done on notched beams. Of them all, the only not based on linear elastic fracture mechanics, and probably the method that mostly influenced the subsequent development of fibre-reinforced concrete, was the Work-of-Fracture Method (Hillerborg, 1985), proposed as a RILEM standard test method (RILEM TC50, 1985).

This method proposed a beam specimen loaded in three-point bending with a central notch in which the load versus displacement at mid-span is recorded. Specific details of the test can be found in (RILEM TC50, 1985). Based on the fictitious crack model (Hillerborg et al., 1976), this method uses the area under the load-displacement curve, i.e. toughness, to derive the fracture energy of concrete.

Despite this method being size-dependent, it offered a simple test to use in the laboratories at that time as it does not require any sophisticated equipment and allows the determination of useful results. Using such a widely accepted model like the fictitious crack model, and the easy-to-understand fracture energy concept as an alternative to linear elastic fracture mechanic models, was widely accepted by those who worked with fibre-reinforced materials. Extending this fracture-based method to fibre-reinforced concrete was a quick process, and several standards for the experimental characterisation of fibre-reinforced toughness began to appear all over the world.

2.3.1.1 Considering the tensile behaviour of conventional concrete in codes

The tensile behaviour of concrete has been a secondary issue in concrete development from the early 20th century to the 1960s. Compressive strength was sufficiently representative of concrete quality. In addition, the test methods to determine it offered greater repeatability than the methods followed to determine other properties, in which tensile forces dominated. Furthermore, it was soon noticed that all the parameters needed to design could be derived from concrete compressive strength using simple formulations. Thus concrete properties, such as the shear strength, bond strength, tensile strength or flexural strength, could be easily obtained from compressive strength. These were the reasons that justify why the material properties of concrete have been traditionally characterised only by its compressive strength.

Unlike compressive strength, tensile strength plays a minor role in codes, and is used only to obtain the necessary cracking bending moment to estimate crack opening and deformations in cracked situations.

Although the concrete response in tension is low compared to compressive strength, the fracture in tension can be responsible for failures at different loads than those predicted by the classic beam theory in structures with a relatively large or small size. In fact flexural strength is used instead of tensile strength when estimating the cracking bending moment according to current codes (MC2010). The difference between flexural strength and tensile strength is called either a size or scale effect, and is associated with the release of energy into the front of a large crack due to the existence of strain-softening in a large microcracking zone ahead of the tip of a continuous crack (Bazant, 1989). This scale effect is mainly of the fracture mechanics type (deterministic) rather than of a statistical one, and would exist even if the material response were completely deterministic.

Fracture mechanics in concrete may be important with unreinforced structural elements in which tensile strength is conferred only to concrete. Yet when steel bars reinforcement is used, the size effect due to the energy release in the crack tip is very low. In fact current codes do not consider size effect in bending as they do not even consider tensile contribution which, however, is quite an accurate assumption. In this case, size effect is avoided by imposing a minimum of reinforcement on the structure to avoid brittle failures. In shear designs, size effect is considered in two different ways: (i) concrete contribution to shear is reduced by a scale effect parameter according to effective depth; (ii) limitation of the distance between stirrups according to effective depth.

Even though tensile behaviour in concrete is of little importance in design, the new Model Code (MC2010) offers an approach for the expected concrete tensile behaviour, which has been divided into two separate responses: (i) a stress-strain response up to the tensile strength peak; (ii) a stress-crack opening relationship to describe the behaviour of the microcrack concrete inside the fracture process zone (defined as the zone in which the material undergoes softening damage) according to fracture energy, as previously described.

2.3.2. Tensile behaviour of fibre-reinforced concrete

In parallel to increased knowledge on the fracture mechanics of plain concrete, knowledge on fibre-reinforced concrete has continuously evolved over the years. The discontinuous nature of fibres has led structural engineers in the 1980s to conceive fibres as diffuse reinforcement, similarly to the way that ferrocement works. This assumption involves researchers having to find a quantitative method to relate the major parameters that influence fibre performance to predict tensile response by starting with knowledge of the mechanical properties of matrix and fibres alone. These major parameters are the matrix mix-design, aggregate size, material, geometry and

surface treatment of fibres, the pouring system and member geometry (di Prisco et al., 2007). However, subsequent research has shown that it was extremely difficult to predict tensile behaviour from these parameters, and a decision was made to consider fibre-reinforced concrete to be a single material characterised by its toughness, which had to be characterised by suitable tests.

It is surprising to find that the first standard to determine the toughness properties of fibre-reinforced concrete (RILEM 49TFR, 1984) appeared 1 year before the Work-of-Fracture Method proposed by Hillerborg and designed to determine the fracture of plain concrete (RILEM TC50, 1985). The delay in introducing a standard test method to evaluate the fracture characteristics of concrete reflects engineers' lack of interest in this topic (Gopalaratnam et al., 1995).

This was not the case of fibre-reinforced concrete. Standards were of huge interest for the FRC community. Between 1984 and 1994, 13 standards were developed by the FRC community in Europe, North America and Japan. They all consisted in an unnotched beam tested in an unnotched third-point bending test (a special type of four-point bending test in which the distance between the load and support rollers is one third of the span), in which the commonest span to depth ratio equalled 3. Different parameters were proposed to characterise the toughness of this concrete type: (i) energy dimensionless indices; (ii) energy absorption; (iii) residual strength indices. A complete collection of these tests is described in (Gopalaratnam et al., 1995).

Although those tests were size-dependent, their main purpose was to compare the performance of different types of fibres, determine the influence of fibre volume, length, and its surface treatment, etc. In the 1990s, the fibre-reinforced concrete topic was in fashion. More than 1,000 publications dealt with fibre action and FRC properties, characterised by any of the standards which mainly offered results from a qualitative point of view. However, these publications rarely dealt with the structural design of FRC (Chanvillard, 2000). Actually it was not needed because major applications of fibre-reinforced concrete were tunnels and floors, which did not require a strong tool for design purposes.

At the end of the 1990s, existing standard methods did not provide any of the relevant material properties required for analysis and design, which led, in some cases, to empirical design methods (Massicotte et al., 2000). This situation meant that fibre-reinforced concrete was sometimes poorly perceived by engineers given the lack of reliability of the fibre concrete mix, and false expectations for certain types of applications, which masked all the benefits of fibres. The time had come to think again (Barret al., 1996).

A step forward from laboratories results to the structural application was needed, and it was only possible by developing new characterisation methods that provided reliable data to design. It was noted that notched three-point bending tests, as proposed in the Work-of-Fracture recommendation for plain concrete (RILEM TC50, 1985), reduced

the variability of test results, and were more suitable to characterise the post-cracking behaviour of concrete needed for design (Barret al., 1996) by measuring either the load-crack mouth opening displacement (CMOD) or the load-deflection response. According to this configuration, the complete deformation is always localised at the notch plane, while the rest of the beam does not undergo significant inelastic deformations (Gopalaratnam et al., 1995), which is a considerable advantage. It minimises the energy dissipated over specimen volume and, therefore, all the absorbed energy can be directly attributed to the fracture along the notch plane (fracture energy) and can directly correlate to the material response. This fact is essential to characterise the stress-crack opening behaviour by toughness criteria, as formerly noticed by Hillerborg when the Work-of-Fracture method for plain concrete was proposed (Hillerborg, 1983). Other notched tests, such as notched direct tension tests, should also be considered as possible test specimens. However, the existing difficulties to carry out these tests meant having to focus research on flexural tests.

The task of developing a new test to determine the post-cracking behaviour of fibre-reinforced concrete and its suitable implementation for structural designs was commissioned to the Rilem Technical Committee, TC 162-TDF, set up in 1995. As previous experience had shown, both test and design methods had to go hand in hand, and had to be treated simultaneously because they are interrelated. Otherwise work was doomed to failure.

The technical committee was divided into two groups. One group described the post-cracking behaviour of fibre-reinforced concrete by a stress-strain diagram ($\sigma - \varepsilon$). The other group used a stress-crack opening relationship ($\sigma - w$) by following the fictitious crack model. It is noteworthy that the RILEM TC 162 work was focused on steel fibre-reinforced concretes (SFRC) that exhibited tension softening behaviour in tension. A round robin test programme was carried out in which both notched uniaxial tensile tests and notched three-point bending tests were conducted.

2.3.2.1 Stress-crack opening relationship (RILEM TC 162-TDF)

This work was due to the joint effort of both the FRC and fracture concrete community, and summarised the most relevant knowledge acquired until that time. The design principles developed by the $\sigma - w$ group of the RILEM TC 162-TDF were based on the fictitious crack model (FCM) and are fully described in (RILEM TC 162-TDF, 2002). Even though FCM was originally intended to be used in combination with the Finite Element Model (FEM), it was demonstrated in the 1990s that it was possible to readapt the model to other numerical and analytical applications (RILEM TC 162-TDF, 2002).

Figure 2.4 shows FCM in a crack for plain concrete and also for fibre-reinforced concrete. As we can deduce from Figure 2.4, a fictitious crack appears once cracking tensile strength is reached (f_t). This model considers that crack bridging forces are normal to the fracture plane.

With plain concrete, the fictitious crack (softening tensile branch) can be divided into two different stages according to crack opening: (i) the process zone in which microcracking takes places; and (ii) the aggregate interlock. Between a zero crack opening, that corresponds to a tensile stress of f_t, and the characteristic crack opening (w_c), defined as the crack opening in which the transferred stress is zero, the transferred stress is characterised by the stress-crack opening relationship σ_w , which is in accordance with crack opening (w).

With fibre-reinforced concrete, and assuming that fibres and the matrix can be considered a single composite material, the fictitious crack model is analogous to that proposed for plain concrete. In this case, not only are the microcracking process zone and the aggregate interlock the only stress transfer mechanisms, but also fibre bridging. Use of fibres has two main consequences on FCM: (i) increased fracture energy (G_f); and (ii) a higher value for characteristic crack opening (w_c), which can be roughly considered half the fibre length. This means that in fibre-reinforced concrete structures, under service and ultimate loads, only fictitious cracks appear as a real crack, i.e. a stress-free crack,, which appears only at very large crack openings. Despite this fact, FCM can be used regardless of either plain concrete or fibre-reinforced concrete being modelled because the only important input is the stress-crack opening relationship.
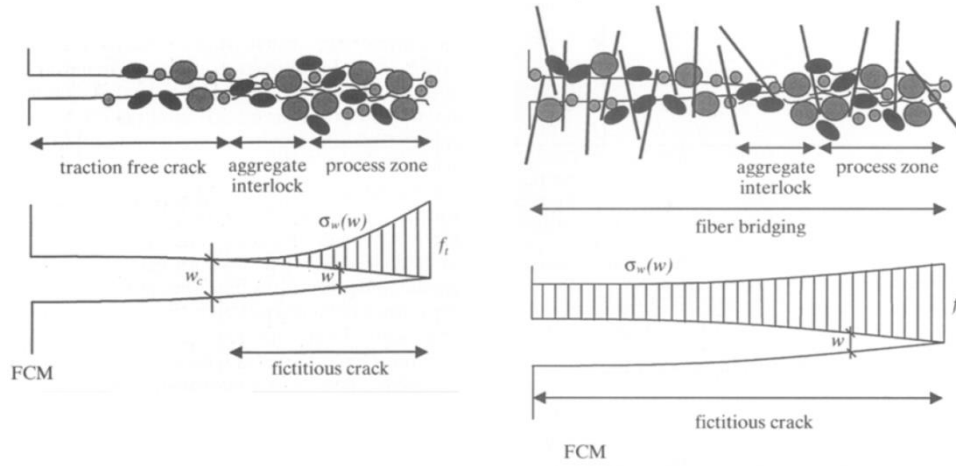
Figure 2.4 Fictitious crack model for plain concrete (left) and fibre-reinforced concrete (right)

Figure 2.5 depicts a typical stress-crack opening relationship for both plain and fibre-reinforced concrete obtained from the experimental results. The results are shown for a normal-strength and a high-strength concrete. With fibre-reinforced concrete, the number between brackets in Figure 2.5, right, represents the amount of fibres in kg/m^3 used. The used fibres were hooked-end 60-mm long. These results formed part of the

round robin tests carried out by the RILEM TC 162-TDF (RILEM TC 162-TDF, 2003a) on notched cylinder specimens, tested in a uniaxial tensile test. From the results shown in Figure 2.5, the increase in both fracture energy (G_f) and characteristic crack opening (w_c) provided by fibre-reinforced concrete comes over quite clearly.

The most widespread stress-crack opening law used for modelling plain concrete was the bilinear relationship, in which the stress at the change of slope was fixed to a stress value within the 15-33% range of tensile strength (see 2.3.1). In fibre-reinforced concrete, a similar model can be fitted to the results in Figure 2.5, right, up to a zero stress at a crack opening of around half the fibre length.

The $\sigma - w$ task group proposed the uniaxial tensile test to derive the stress-crack opening relationship of fibre-reinforced concrete (RILEM TC 162-TDF, 2001). As flexural methods are easy to perform and former recommendations to determine concrete toughness also proposed this test, several methods appeared in order to derive stress-crack opening behaviour from bending tests. This procedure is the so-called inverse analysis. A more detailed explanation of these procedures is provided in 2.6.
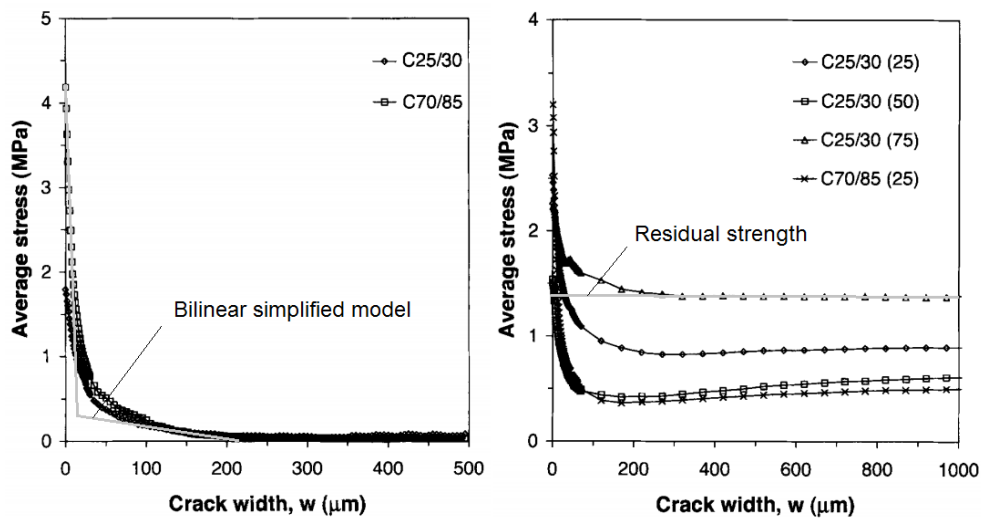
Figure 2.5 The typical stress-crack opening relaionship for plain concrete (left) and fibre-reinforced concrete (right) (RILEM TC 162-TDF, 2003a).

The $\sigma - w$ design method was not highly relevant for the development of the subsequent design methods for fibre-reinforced concrete. The reason may lie in the results shown in Figure 2.5, right. As we can see, the conventional bilinear stress-crack opening model can be easily substituted for a drop-constant stress-crack opening relationship. This constant stress corresponds to the so-called *residual strength*. What is really important is that this residual strength can be considered constant within the most common crack width ranges of the structural design (up to approx. 2 mm) for

both ULS and SLS. This model makes the design of a simpler fibre-reinforced structure without significantly underestimating the composite mechanical capacity.

Having noticed that, Henrik Stang (Stang, 2000) proposed a characterisation method based on what he called *verification charts*. These charts were a set of numerical model results in which load versus CMOD in notched three-point bending tests, the RILEM-beam test, were plotted for four different toughness indices (γ) and for a specific cracking strength value. The toughness index was defined as the ratio between uniaxial tensile residual strength and cracking strength. The toughness indices used to determine each verification chart were 1, 0.75, 0.5 and 0.25. For each cracking strength value, four different drop-constant stress-crack opening laws in uniaxial tension were determined according to each toughness index. A numerical model was then used to determine the load-CMOD curve for each drop-constant tensile law to define the verification chart. The curves in the verification chart were compared to the experimental load-CMOD results. The material can be classified according to its toughness class for a certain crack opening. This method requires having prior knowledge of cracking strength.

To better comprehend this method, Figure 2.6 was plotted. In Figure 2.6, left, a bilinear stress-crack opening was assumed for fibre-reinforced concrete with a cracking tensile strength of 3 MPa. Four different toughness classes were considered, 1, 0.75, 0.5 and 0.25, which led to a four different drop-constant stress-crack opening relationships. A numerical model (Stang, 2000) was used to determine the load-CMOD curve in the RILEM notched three-point bending test (depth = 150 mm; width = 150mm; span = 500 mm; notched depth = 25 mm) according to EN 14651.
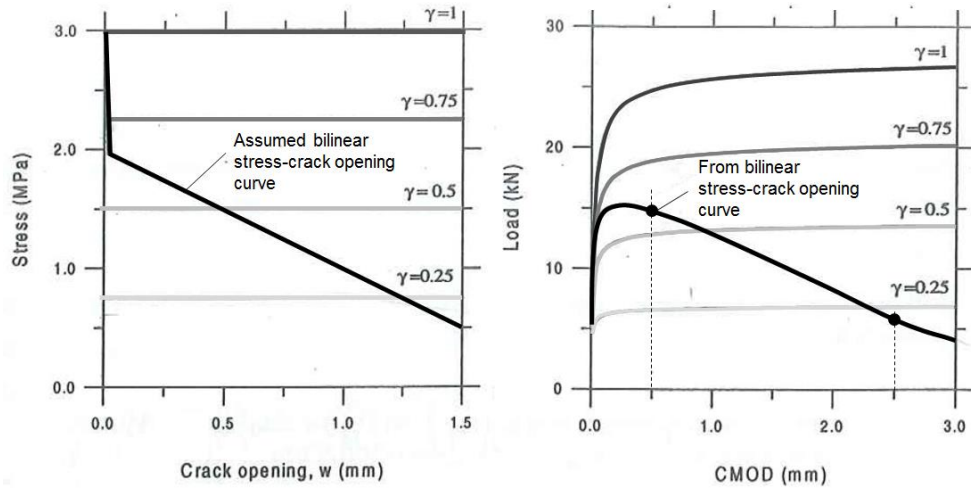
Figure 2.6 The assumed bilinear stress-crack opening relationship and drop-constant hypothesis according to each toughness index (left); verification charts and load-CMOD from the assumed bilinear relationship (right) (Stang, 2000).

According to Figure 2.6, right, for a maximum crack width design criterion of 0.5 mm, it is safe to assume a drop-constant stress-crack opening relationship according to the toughness class of 0.5; i.e. a uniaxial residual strength of 1.5 MPa in this particular case. In the same way, it is safe to assume a drop-constant stress-crack opening relationship according to the toughness class of 0.25; i.e. a uniaxial residual strength of 0.75 MPa for a maximum crack width design criterion of 2.5 mm for this particular case.

One of the main problems of verification charts is that they depend on cracking tensile strength. However, there is a way to do away with that. According to Figure 2.6, right, assuming both perfectly plastic behaviour in tension and linear elastic in compression leads to a maximum bearing equivalent stress capacity in bending of 3 times the uniaxial equivalent residual stress, no matter what the cracking tensile strength value, according to the plastic theory. Then a verification chart is no longer needed to determine a uniaxial residual strength up to a certain crack opening. If considering both flexural test geometry and the plasticity theory, it is safe to consider, up to a certain crack opening, a residual strength obtained according to Eq. 2.7, in which P_w is the load at a certain crack opening, h is specimen depth; b is specimen width, a_o is the notched depth, and σ_{fl} is the equivalent strength in bending.

$$\sigma_{res}(MPa) = \frac{\sigma_{fl}}{3} = \frac{3P_wL}{2b(h-a_o)^2} \cdot \frac{1}{3} \sim 0.11P_w(kN)$$

Eq. 2.7

If the load-CMOD curve in Figure 2.6, right, for the bilinear stress-crack opening response assumed in Figure 2.6, left, is used, a load of approximately 15 kN and 6 kN is obtained for CMOD on 0.5 mm and 2.5 mm, respectively. According to Eq. 2.7, the uniaxial residual tensile strengths that correspond to these values are 1.65 MPa and 0.66 MPa, which correspond to a toughness class of 0.55 and 0.22, respectively. In this way, a drop-constant stress-crack opening relationship can be derived from the load-CMOD curves obtained from a three-point bending test up to a certain CMOD without the need for a verification chart, and also without having to know the cracking strength of fibre-reinforced concrete.

2.3.2.2 Stress-strain relationship (RILEM TC 162-TDF)

Early on in the 21st century, design methods based on the stress-crack opening relationship were unable to achieve enough simplicity to be used in design. Conventional design methods were based on sectional analyses in which a stress-strain relationship is needed. Unlike conventional reinforced concrete in which the tensile contribution of concrete is neglected, the stress-strain RILEM task group proposed using a stress-strain relationship in tension to consider fibre contribution.

The parameters that defined the stress-strain relationship were obtained not only from the notched three-point bending test using the specimen and test setup geometry described in EN 14651, but also from the values shown in Figure 2.7. The method to obtain the stress-strain relationship was described in (RILEM TC 162-TDF, 2003c) and is shown in Figure 2.8. This method was developed for a concrete compressive strength C25/30 and a maximum amount of 60-mm long hooked-end fibres of 75 kg/m^3.

A round robin test was conducted by RILEM TC 162 members following the notched three-point bending test described in EN 14651 (RILEM TC 162-TDF, 2003b). A summary of the obtained test results, on which the stress-strain method is based, is shown in Figure 2.7. The load-CMOD of these concretes did not exhibit hardening.
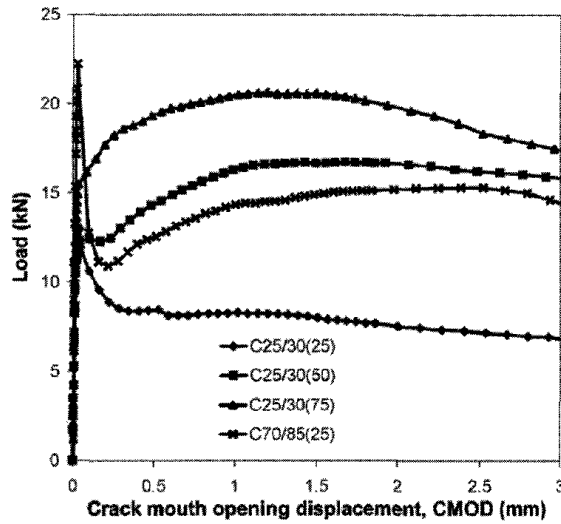
Figure 2.7 The load-CMOD curves obtained from the round robin test (up) (RILEM TC 162-TDF, 2003); the finally chosen parameters to describe the tensile properties of fibre-reinforced concrete (down).

In a first step, and following the current trend of the time, the equivalent strength values based on toughness indices (area under the load-deflection curve) were proposed. However, following fracture community members' advice, the load-deflection curve was substituted for the load-CMOD one. Instead of using the area under the curve, the strength that corresponded to a certain CMOD value was proposed. The committee defined four strength parameters ($F_{R,i}$) (see Figure 2.7, right) that corresponded to a CMOD of 0.5, 1.5, 2.5 and 3.5 mm. These load parameters were transformed into the equivalent flexural strength ($f_{R,i}$) using the formulation in Eq. 2.8, in which a_o is the notched depth. These values were used to determine the stress-strain relationship. Note the similitude with the stress-crack opening proposal in Eq. 2.7.

$$f_{R,i} = \frac{3F_{R,i}}{2b(h - a_o)^2}$$

Eq. 2.8

The proposed stress-strain model is shown in Figure 2.8. Cracking tensile strength is obtained from the flexural strength of the matrix without fibres. A scale effect coefficient is used to transform flexural strength into uniaxial cracking strength. Parameters σ_1 and σ_2 in Figure 2.8 are derived from the equivalent strength at a CMOD of 0.5 mm ($f_{R,1}$) and 3.5 mm ($f_{R,4}$), respectively. It is assumed that the stress profile for these CMOD is linear in compression and perfectly plastic in tension, with a crack depth of 66% and 90% the depth from the notch, as shown in Figure 2.9. It is also noteworthy that the stress-strain softening line was obtained using CMODs of 0.5 mm and 3.5 mm. According to Figure 2.5, within this range the stress-crack opening relationship is linear and the hypothesis is valid.

This method provided a simple tool to evaluate the sectional bearing capacity of fibre-reinforced concrete. It proposed a bilinear softening relationship in which the first line had barely any impact on the sectional behaviour of the fibre composite. It agreed with the uniaxial tensile behaviour of the concretes tested and shown in Figure 2.5.

Note that the strain does not vary according to specimen depth. This assumption may be valid if a drop-constant stress-strain law is used. However, using a bilinear relationship requires dependence on specimen depth as the slope of the softening line is steeper the larger beam depth becomes. A mix between the stress-strain and stress-crack opening RILEM proposals is proposed in MC2010.
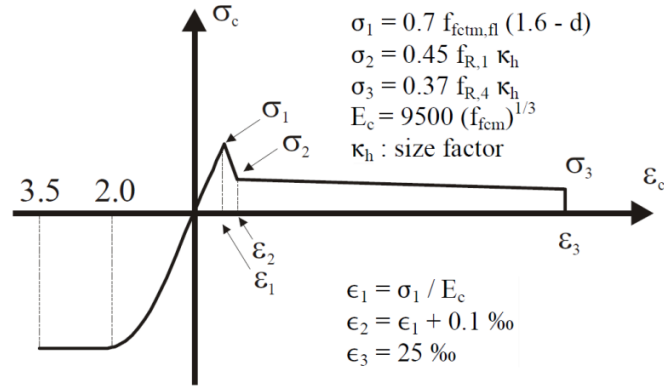
Figure 2.8 The stress-strain relationship acccording to RILEM TC 162-TDF obtained from the notched three-point bending test.
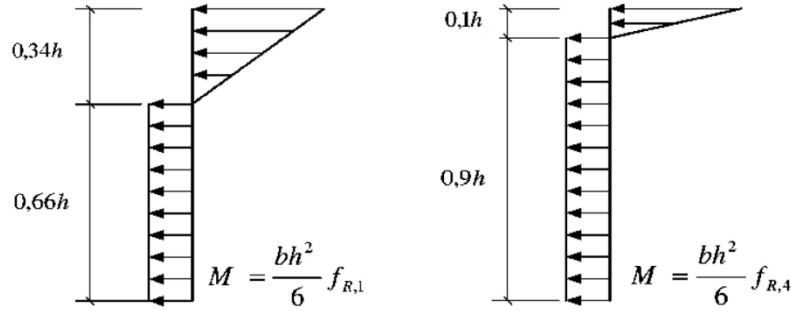
Figure 2.9 Stress distribution assumption in the notched three-point bending test for a CMOD of 0.5 mm and 3.5 mm according to (RILEM TC 162-TDF, 2003c).

2.3.2.3 MC2010 proposal for fibre-reinforced concrete

The MC2010 proposal is based on RILEM studies. In it, two different simplified types of constitutive tensile models for fibre-reinforced concrete are proposed: (i) a rigid plastic model; and (ii) a linear model.

The rigid plastic model well matches the idea of using the constant-drop stress-crack opening relationship presented in 2.3.2.1. In this case, uniaxial residual strength is unique and corresponds to a CMOD of 2.5 mm ($F_{R,3}$), which can be associated with a ULS situation. Even though the uniaxial residual strength in SLS can differ from this value, the MC2010 does not distinguish between ULS and SLS for this model. The rigid plastic model is shown in Figure 2.10, left. The constant stress of rectangular block (f_{Ftu}) can be determined by Eq. 2.7, using load $F_{R,3}$ that corresponds to a CMOD of 2.5 mm. The constant stress drops to zero at a certain maximum crack opening accepted for design, which is usually 2.5 mm.
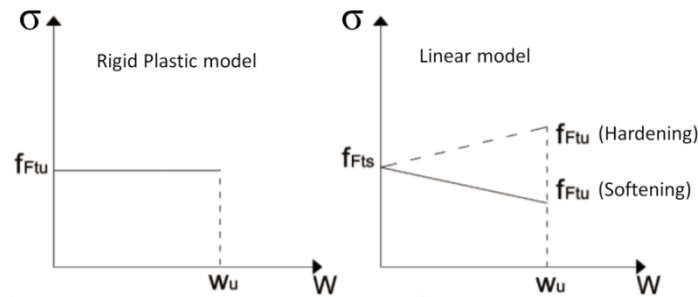
Figure 2.10 The stress-crack opening simplified models according to MC2010

The linear model can be derived from the three-point bending test (EN-14651) using the load that corresponds to a CMOD of 0.5 mm and 2.5 mm. Parameters f_{Fts} and f_{Ftu}, represent serviceability and ultimate residual strength, respectively. Serviceability

residual strength (f_{Fts}) has the same physical meaning as the residual strength (σ_2) proposed by RILEM (see Figure 2.9, left), and is obtained from parameter $f_{R,1}$. However in this case, no size factor is applied.

$$f_{Fts} = 0.45\, f_{R,1}$$

Eq. 2.9

Ultimate residual strength is obtained from parameter $f_{R,3}$ instead of $f_{R,4}$ as proposed in the RILEM method. This parameter is obtained following Eq. 2.10 if a maximum crack opening accepted for design of 2.5 mm is considered. In this case, if $f_{R,3} > 1.3$ $f_{R,1}$ ultimate residual strength is higher than serviceability residual strength, and the fibre-reinforced concrete is stated to exhibit post-cracking hardening. Otherwise, it is stated to exhibit post-cracking softening. The classification of fibre-reinforced concrete is not only made by its residual strength values, but also by its ratio. The condition that $f_{R,3}$ is at least 0.5 times $f_{R,1}$ must be accomplished to consider fibres in design.

The formulation in Eq. 2.10 is obtained by considering that crack depth coincides with specimen depth; i.e. the whole cross-section is under tension. The model assumes a linear variation of stresses along specimen depth with a maximum tensile stress of f_{Fts} at the top. The equilibrium of this stress distribution to achieve a bending moment which corresponds to that at a CMOD of 2.5 mm leads to Eq. 2.10.

$$f_{Ftu} = 0.5\, f_{R,3} - 0.2\, f_{R,1}$$

Eq. 2.10

As mentioned earlier, a sectional analysis requires a stress-strain relationship. However, the MC2010 simplified method gives a stress-crack opening relationship. In order to make the design procedure simpler, crack opening is converted into strain by dividing crack opening by structural characteristic length (l_{cs}). Note that the referred length has nothing to do with the Hillerborg characteristic length. In this case, characteristic length may be considered the minimum distance to a crack in which the strain profile in the average cross-section can be considered linear, therefore the Navier-Bernoulli hypothesis can be applied. The MC2010 considers that structural characteristic length is the minimum value between the average crack spacing and crack depth; i.e. the distance between the neutral axis and the tensile side of the cross-section.

One important step forward given by the simplified linear model proposed in the MC2010 is that strain is not fixed, but depends on the cross-section size. In this way, the previously introduced deterministic size effect is in some way taken into account. In addition, a maximum strain design value of 2% and 1% is considered for bending and tension, respectively.

The statistical size effect in fibre-reinforced concrete is represented mostly by fibre orientation. In order to take this size effect type into account, the MC2010 proposed a fibre orientation factor (K), which should be according to fibre length, beam geometry and the pouring system. However, no detailed information has yet been provided about the specific values of K.

The inverse analysis method to determine stress-crack opening behaviour from a bending test provided by MC2010 is an evolution process of the RILEM method, which was developed for fibre-reinforced concrete that exhibit deflection-softening behaviour. However, the method has been extended to fibre-reinforced concretes that exhibit deflection-hardening without modifying the initial hypotheses. According to the results provided by some authors (Amin et al., 2015; de Montaignac et al., 2012), the MC2010 method overestimates the post-cracking strength of fibre-reinforced concrete, and suggests this method should be reviewed.

An example of the MC2010 method overestimation can be found in (de Montaignacet al., 2012). Figure 2.11 shows their load-deflection bending results, performed according to EN 14651, on three different fibre-reinforced concrete types. Concrete compressive strength was around 50 MPa. Two different fibre types were used: (i) RC 80/60 (F60); and (ii) RC 65/35 (F35). Two fibre doses of 1% and 1.25% in volume are represented.
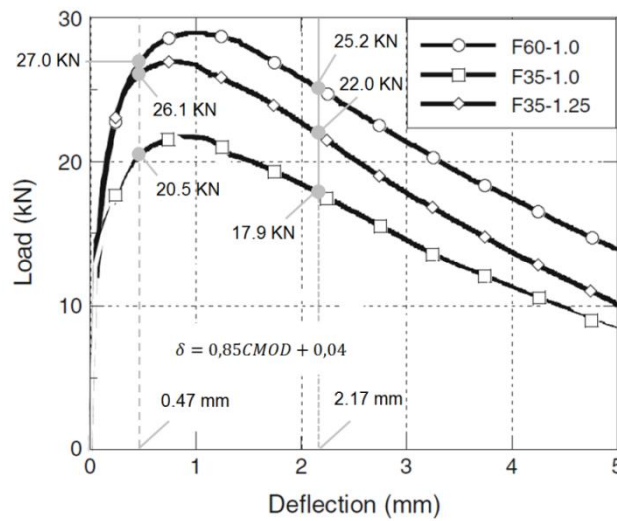
Figure 2.11 Load-deflection results from a three-point bending test according to EN 14651 for different types and amounts of fibres

According to EN 14651, CMOD can be derived from the deflection at mid-span. Then the method suggested by MC2010 can be applied to these experimental curves. In Figure 2.11, the residual flexural strengths for a CMOD of 0.5 mm and 2.5 mm are

depicted. Unlike the bending test on deflection softening in fibre-reinforced concrete (see Figure 2.7), these concrete types do not exhibit softening after the first cracking of the matrix. This fact leads to a less sloped initial slope of their stress-crack opening relationship.
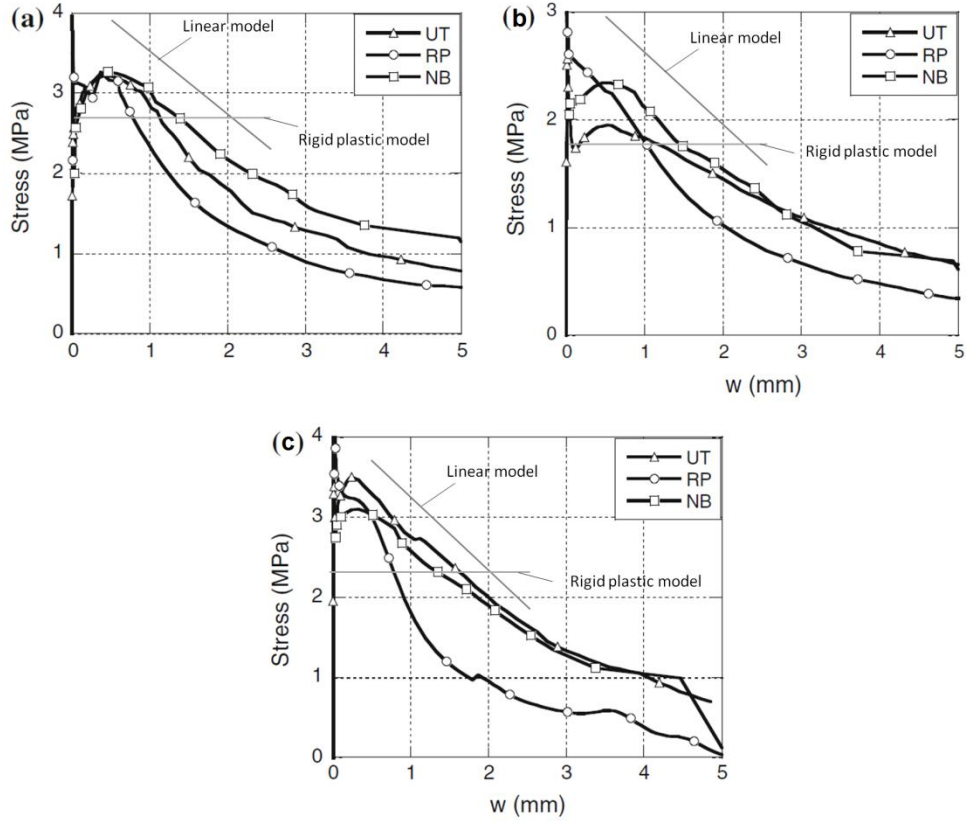
Figure 2.12 Inverse analysis results from the experimental test data obtained from uniaxial tensile tests (UT), notched three-point bending tests (NB), and round panel tests (RP), and their comparison to the MC2010 proposal.

Parameters f_{Fts} and f_{Ftu} have been determined for both the rigid plastic and the linear models proposed by MC2010. The results are depicted in Figure 2.12, together with the results obtained from the uniaxial tensile tests (UT) and the numeric inverse analysis results obtained, in turn, from notched bending tests (NB) and round panel tests (RP) (de Montaignac et al., 2012). As depicted from Figure 2.12, the results offered by MC2010 are systematically higher than those obtained from an inverse analysis methodology applied to the same experimental results and other test methods. These results were also confirmed in (Amin et al., 2015).

2.3.2.4 Summary

Fibre-reinforced concrete works as a single material and is characterised by its post-cracking stress-crack opening behaviour, which can be considered an intrinsic material property if statistical effects, such as fibre orientation, are not taken into account. As for plain concrete, the stress-crack opening relationship can be modelled accurately by a bilinear relationship (see Figure 2.5). However, as the stress-crack opening can be considered linear within the crack opening design range (from 0 to 2.5 mm), a linear relationship and a stress-constant relationship were proposed. The parameters that defined these relationships are the so-called residual tensile strength values, which are obtained according to a certain stress distribution hypothesis for a given crack mouth opening displacement using the residual flexural strength values obtained from notched three-point bending tests.

Notched three-point bending tests have imposed over upon both uniaxial tensile and other bending tests. Compared to uniaxial tensile tests, bending tests are easier to conduct and require less specific equipment. Compared to unnotched four-point bending tests, even though notched tests offer a higher average post-cracking value than unnotched tests, the obtained variability is lower since the position of the crack in notched tests more strongly influences load-deflection behaviour (Chanvillard, 2000)

Simplified methods to derive the stress-crack opening relationship from the notched three-point bending tests proposed in MC2010, which are based on the RILEM TC-162 work, were developed to be used in deflection-softening materials characterised by a stress-crack opening relationship, as shown in Figure 2.5; i.e. an initial steeper slope with a sudden stress drop, followed by a soft line. Their extension to other concretes, in which the initial slope is not so steep, should be reviewed as they may overestimate post-cracking strength.

2.3.3. UHPFRC tensile behaviour

From a mechanical point of view, UHPFRC is not very different from conventional fibre-reinforced concrete, or even plain concrete. Conceptually, if a uniaxial tensile test is carried out on an UHPFRC specimen, and force versus displacement is recorded, the shape of this curve is similar to that for plain concrete (see Figure 2.1), but with a large energy absorption in the three main stages in which its tensile behaviour can be divided. Figure 2.13 shows a typical uniaxial UHPFRC response. Compared to the uniaxial plain concrete response in either Figure 2.1 or Figure 2.2, we note that the only difference is found in the scale.

This difference is due to the high-performance mechanical properties of UHPFRC compared to either plain or conventional fibre-reinforced concrete. UHPFRC has a smaller particle size and higher compacity, which lead to greater compressive strength and a stronger bond between the matrix and fibres. In addition, fibre dose is commonly higher. Due to bond improvement, short fibres can be used efficiently, which makes the microcracking phase longer. A typical volume fraction for UHPFRC is 2% (AFGC-

Sétra, 2002). As fibres are expensive, researchers have attempted to reduce fibre content to a minimum, but maintain strain-hardening properties. This was what Wille et al. did (Wille et al., 2011), who were able to ensure this behaviour with a 1.5% content in a volume of smooth 13/0.20 fibres in a 50 mm-thick dog-bone specimen. In (Kim et al., 2008), strain-hardening behaviour was also obtained using a 1.2% fibre content from bending tests. UHPFRC is not commonly manufactured with less than 1% to ensure a certain degree of ductility in both compression and tension. The commonest fibres used for UHPFRC are steel fibres, characterised by a high yielding strength and a high elastic modulus. All these facts lead to a uniaxial tensile response characterised by:

- Higher cracking strength
- A longer microcracking phase and larger volumetric energy dissipation prior to macrocrack localisation. In UHPFRC, the microcracking phase is visible to the naked eye, but only if the surface gets wet or special paintings are used.
- Larger fracture energy

At this point it is important to remark that even though the non-linear loading branch shown in Figure 2.13 involves microcracking in concrete, it has been traditionally attributed to volumetric energy absorption and is, therefore, independent of specimen size. This assumption was also taken for the work developed herein.
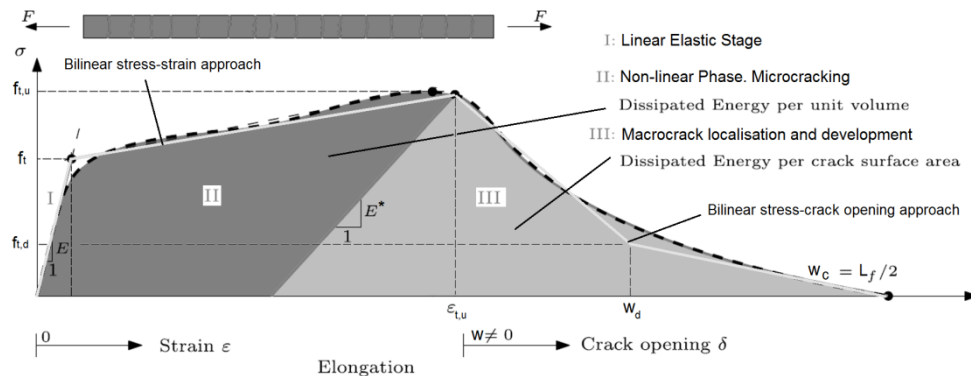
Figure 2.13 Typical uniaxial UHPFRC response (Wille et al., 2014)

That is why everything previously stated for modelling either plain concrete or fibre-reinforced concrete in tension is valid for UHPFRC. As MC2010 suggested for plain concrete, UHPFRC tensile behaviour has to be divided into two different relationships. For simplicity, and with no significant accuracy loss, a bilinear stress-strain relationship can be considered (Figure 2.13). As macrocrack propagation is a discrete phenomenon, it has to be modelled by a stress-crack opening relationship by assuming the fictitious crack model of Hillerborg. For UHPFRC, it is also simpler to assume a bilinear relationship for either design or characterisation purposes.

If the quadrilinear behaviour is assumed in tension, eight parameters are needed to obtain a complete description of UHPFRC tensile behaviour. These parameters are: (i) elastic modulus (E), which can be considered the same in both tension and compression; (ii) cracking strength (f_t) which, according to (Wille et al., 2014), can be defined as the fictitious point of the transition from ideal linear elastic to best fitted linear strain-hardening behaviour; (iii) ultimate strength ($f_{t,u}$), defined as the maximum bearing capacity in tension; (iv) its associated strain capacity ($\varepsilon_{t,u}$); (v) unloading modulus (E^*), which is to be considered the same regardless of the level of stress attained; (vi) strength at the change of slope ($f_{t,d}$) which, according to the bilinear models developed for concrete, can be defined as a percentage of ultimate strength; (vii) its associate crack opening (w_d); (viii) the crack opening at zero stress, also known as characteristic crack opening (w_c), which is usually defined as half the maximum fibre length (l_f). Using these parameters, it is possible to determine parameters such as dissipated energy per unit of volume (g_f), fracture energy (G_F), and also crack opening parameter (w_o), defined in 2.3.1, which may play an important role in design.

It is important to know the order of magnitude of the values that characterise UHPFRC tensile behaviour. For this purpose, the uniaxial test results according to different authors (Frettlöhr et al., 2011; Markovic, 2006) are shown in Figure 2.14 and in Figure 2.15.

Figure 2.14 shows the uniaxial tensile results for two UHPFRCs with different compressive strengths. UHPFRC with an average compressive strength of 169 MPa was reinforced with 2% in volume of straight 13/0.16 steel fibres. UHPFRC with an average compressive strength of 211 MPa was reinforced with 2% in volume of straight 13/0.2 steel fibres. Despite the higher slenderness value of the fibres used in the 169 MPa concrete, which means a larger number and larger surface of fibres, it seems that bond strength, which is greater the higher compressive strength goes, is predominant. From these results, typical values for the uniaxial tensile parameters of UHPFRC can be derived.

Figure 2.15 illustrates the uniaxial tensile results for two UHFPRCs with an average compressive strength of around 120 MPa, and with different fibre type. Monofibre UHPFRC has 2% in volume of 13/0.2 steel fibres; hybrid UHPFRC has 1% in volume of 13/0.2 steel fibres and 1% in volume of 80/40 hooked-end fibres (l/d = 40/0.5). Compared to the results in Figure 2.14, cracking strength, ultimate strength, strain capacity and crack opening at the change of slope are quite different. However, the characteristic crack opening seems relatively constant with a value of half the length of the larger fibre, as pointed out in (Wille et al., 2014).

As also discovered for plain concrete (see 2.3.1.1), the strength at the change of slope can be considered a percentage of ultimate strength. According to these results and those found in (Wille et al., 2014; Nguyen et al., 2014; Graybeal et al., 2013; Mahmud

et al., 2013; Tailhan et al., 2013; Wille et al., 2011; Kim et al., 2008; Kanakubo, 2006), a $f_{t,d}/f_{t,u}$ ratio of 1/3 seems to be a good assumption for UHPFRC.
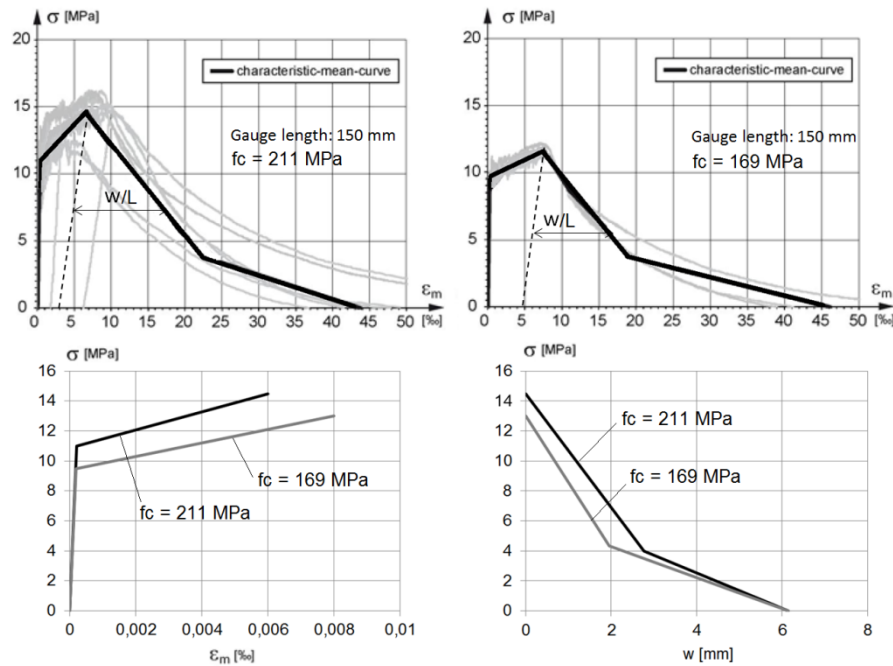
Figure 2.14 Uniaxial tensile tests for different compressive strength UHPFRCs with 2% 13-mm long steel fibres (Frettlöhr et al., 2011) and their corresponding stress-strain and stress-crack opening behaviour.

As seen in Figure 2.14 and Figure 2.15, the change of slope may take place within the crack opening design range, from 0.1 to 2.5 mm. For conventional fibre-reinforced concrete (see Figure 2.5, right), the change of slope takes place at such a low crack opening that it can be neglected. In fibre-reinforced concrete in which a relatively large amount of long fibres are used (see Figure 2.12), the change of slope may take place at a higher crack opening than 2.5 mm, and a linear assumption is still valid for design. If we are confident that the change of slope of concrete is beyond the design crack opening range, a linear model may be accurate enough. However for UHPFRC, and probably also for certain fibre-reinforced concrete types, it is quite likely that this change of slope falls within the design range. This is why the stress-crack opening relationship should be offered as a bilinear law. By knowing this law, designers are able to simplify it depending on the maximum crack opening assumed for different design conditions.
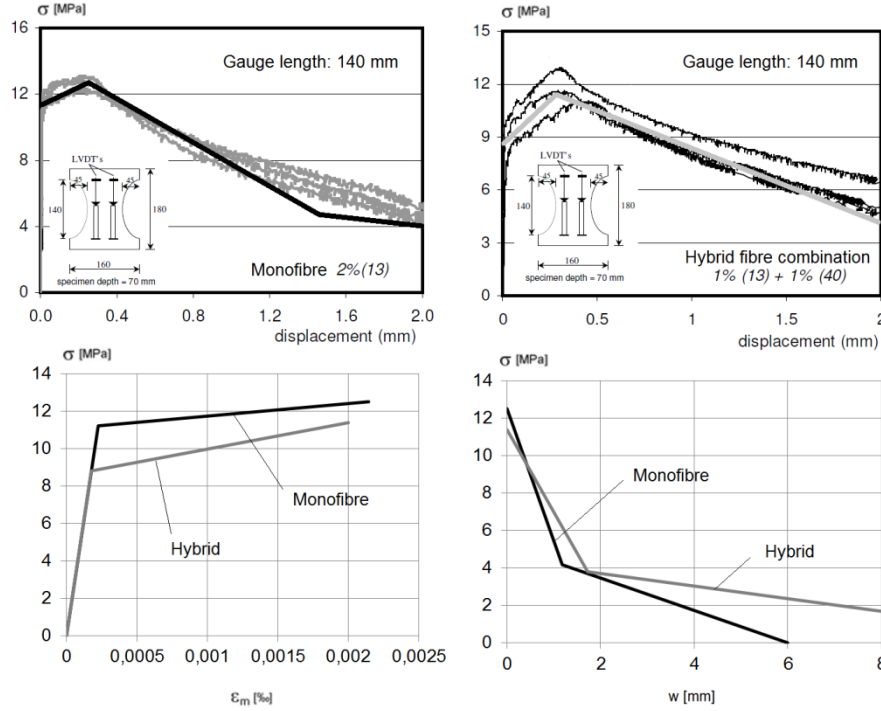
Figure 2.15 Uniaxial tensile tests for different types of fibre reinforced UHFPRC (monofibre and hybrid) (Markovic, 2006) and their corresponding stress-strain and stress-crack opening behaviour.

One of the main characteristics of UHFPRC is that it can exhibit a hardening phase, accompanied by multiple microcracking, under certain favourable fibre orientation conditions (Tailhan et al., 2004; Mahmud et al., 2013). Even though UHFPRC can exhibit strain-softening behaviour under certain conditions in structural elements, the specimens used to characterise its tensile properties normally offer strain-hardening behaviour in tension if approximately a minimum 2% content in the volume of steel fibres is used (Kim et al., 2008). Figure 2.16 shows this behaviour in three different test setups.

Even though the unloading modulus has been roughly estimated to derive the stress-crack opening relationship in both Figure 2.14 and Figure 2.15, according to (Wille et al., 2014), it is safe to use an unloading modulus within the range of 10-20% the elastic modulus regardless of fibre type and amount. In addition, as it can be assumed that the elastic modulus is the same in both compression and tension, this parameter can be obtained according to current standard tests.

Finally, after the discussion developed in this section, it can be concluded that the initial eight parameters needed to define UHPFRC tensile behaviour can be reduced to only four: (i) cracking strength (f_t); (ii) ultimate tensile strength ($f_{t,u}$); its associate strain ($\varepsilon_{t,u}$); and crack opening at the change of slope (w_d).
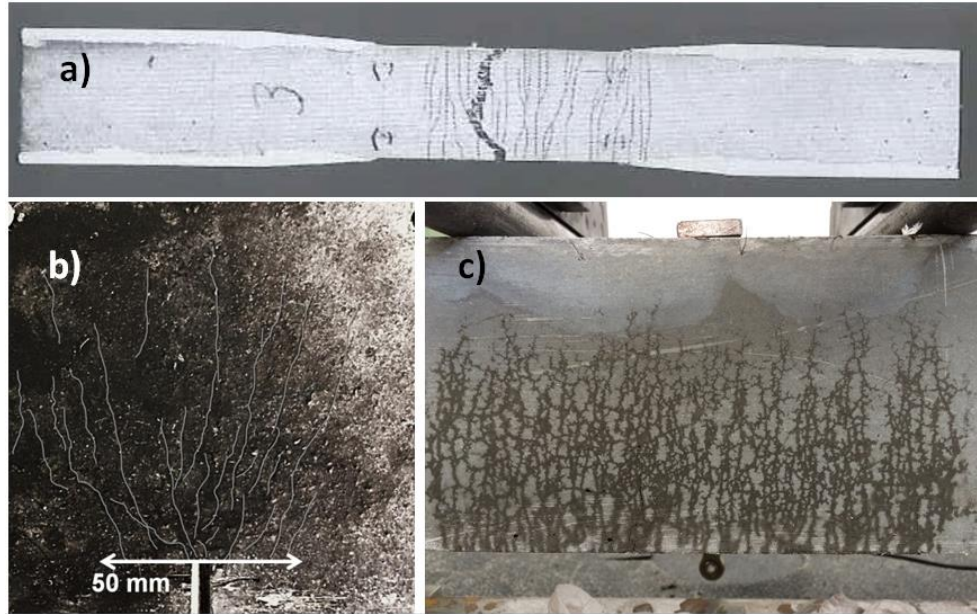
Figure 2.16 The strain-hardening phase accompanied by multiple microcracking for different test setups: a) uniaxial tensile test (Graybeal et al., 2012); b) notched three-point bending test; and c) unnotched four-point bending test

At this point, several questions arise that have no easy answer. If UHPFRC tensile behaviour is similar (in shape) to that of fibre-reinforced concrete, can standard test setups and methods be used to characterise UHPFRC tensile behaviour? Are the post-cracking linear or stress-constant models proposed by MC2010 suitable for UHPFRC modelling? Since a pronounced hardening-phase accompanied by multiple microcracking is a differential property of UHPFRC, could the standard notched three-point bending test (EN-14651) be used to characterise this stage? Should stress-strain and stress-crack opening behaviour be characterised from different tests? Is it possible to obtain whole UHPFRC behaviour in tension previously defined from a single test? If we have stated that all concrete types, even plain concrete, exhibit a non-linear phase accompanied by a certain degree of microcracking prior to crack localisation, what is the strain limit or the minimum number of microcracks to be distinguished between softening and hardening immediately after reaching cracking strength? Is the strain-hardening behaviour exhibited by UHFPRC a material property or a structural one? What are the differential properties that should be used to classify UHPFRC?

These questions about UHPFRC (i) tensile classification, (ii) characterisation and (iii) design must be dealt with from an integrated view as they are interconnected. Once the uniaxial tensile behaviour of UHPFRC has been analysed, differential parameters can be selected to propose a UHPFRC classification. To determine these parameters, suitable characterisation methods must be developed. These parameters must coincide with the required parameters for design. Only an overall picture of these three features can ensure success in the process.

2.4. UHPFRC classification

Following the definition for UHPFRC proposed in 2.1.2, UHPFRC can be considered a special type of high-performance fibre-reinforced cement composite (HPFRCC) if the definition in the Preface of the 6th and 7th Symposium on HPFRCC (Reinhardt et al., 2015; Parra-Montesinos et al., 2011) and JSCE recommendations (JSCE, 2008) is used. It states that HPFRCC can be considered all those concretes that exhibit a strain-hardening tensile stress-strain response, accompanied by multiple cracking and a relatively large energy absorption capacity. However, reaching strain-hardening behaviour in a UHPC matrix not only depends on fibre type and amount, the matrix strength or bond between the matrix and fibres, but also on specimen size and geometry, the pouring system, support conditions, structural redundancy, etc. Even though strain-hardening behaviour cannot be ensured in structural elements, a minimum of 2% content in volume of steel fibres guarantees strain-hardening behaviour in the most frequently used material characterisation test setups.

A general fibre-reinforced concrete classification, according to its tensile stress-strain response, is shown in Figure 2.17. As stated earlier, one key in the tensile behaviour of fibre-reinforced concrete is whether it exhibits strain-hardening or strain-softening behaviour in tension. Among the concretes that exhibit strain-softening in tension, deflection-hardening or deflection-softening in bending can be distinguished. It is important to remark that all strain-hardening materials exhibit deflection-hardening behaviour in bending.

The standard EN-14651 test has been traditionally used to characterise and classify conventional strain-softening fibre-reinforced concrete according to MC2010. However, it is still necessary to define a standard classification for strain-hardening materials, as well as a standard test to characterise their behaviour. A brief review of the current proposed classifications for these concrete types has been made.
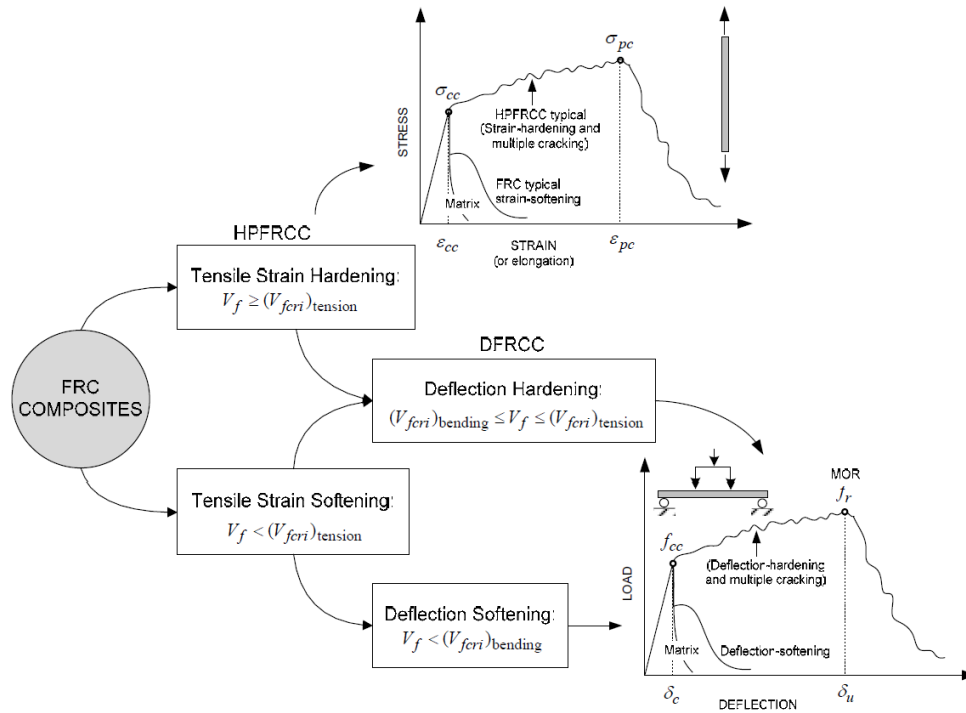
Figure 2.17 General classification of fibre-reinforced concretes according to their tensile stress-strain response (Naaman et al., 2006)

2.4.1. Classification proposed by Naaman et al.

According to Naaman (Naaman et al., 2006), strain-hardening fibre reinforced composites can be sorted according to three main parameters: (i) ultimate tensile strength ($f_{t,u}$); (ii) its corresponding strain ($\varepsilon_{t,u}$); and the elastic modulus (E). Not considering cracking strength (f_t) to classify this type of composites is due to simplicity and its low influence on design. According to him, cracking strength is no easy parameter to be determined, and knowing exactly the initial cracking strength value is not that important. Its classification proposal is summarised in Figure 2.18. Naaman proposed five different classes of strain-hardening fibre reinforced concretes: T-2.5; T-5; T-10; T-15; T-20. While the first letter indicates "tension", the number represents a lower bound for characteristic ultimate tensile strength.

Thus if Class T-10 is specified, it means that a minimum characteristic ultimate tensile strength of 10 MPa is required. In addition, Naaman imposed two more conditions that a strain-hardening material must satisfy: (i) the elastic modulus must be higher than 10500 Mpa; and (ii) the characteristic strain at the peak must equal or be higher than 5‰. Most existing concretes satisfy the first clause, but it may be more difficult to

fulfil the second one. According to that clause, the tensile behaviour of those concretes shown in Figure 2.14 and Figure 2.15 does not reach the performance needed to be considered strain-hardening materials. However, they exhibit a strain-hardening behaviour accompanied by multi-microcracking. The reason for this larger strain bond lies in the fact that Naaman wanted to ensure that strain-hardening behaviour remained even after the rebars reached their yielding strain to guarantee ductility.

Some concerns arises from this attempt to classify strain-hardening materials. As the strain at the peak has been demonstrated to be size-dependent, what would the specimen geometry and the test setup be to determine the strain at the peak? Is the strain value proposed enough to ensure microcracking up to the reinforcement yield strain? Does it make sense? When using strain-hardening materials, what is intended is to reduce cracking in SLS to a minimum instead of avoid cracking in ULS. This is why the proposed strain limit of 5‰ may be too high.
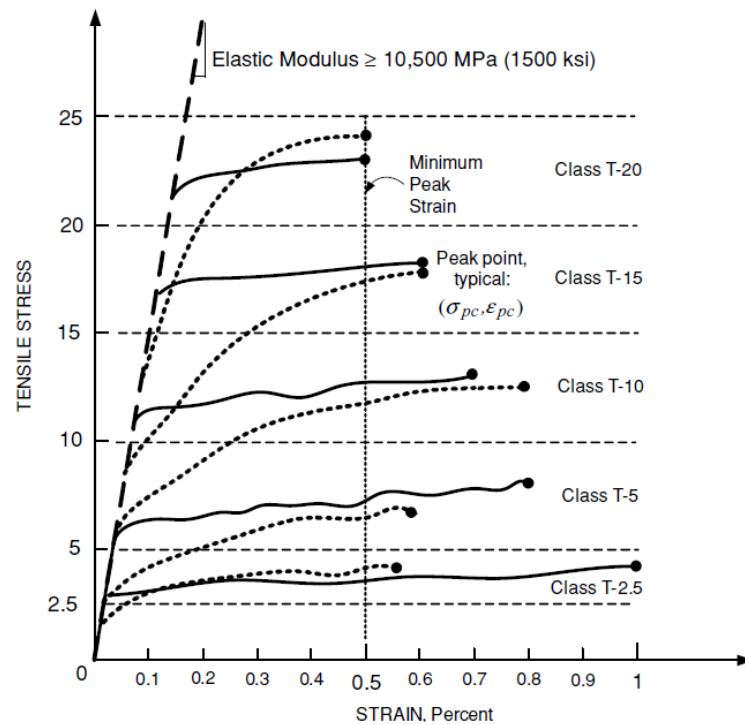
Figure 2.18 Proposed classification of strain-hardening fibre-reinforced concretes according to Naaman (Naaman et al., 2006)

2.4.2. Classification proposed by Wille et al.

The above classification defined the strain-hardening behaviour in terms of strength and ductility criteria. Another criterion could be the volumetric energy absorption capacity prior to tension softening (g) (see Figure 2.13). The classification proposed in (Wille et al., 2014) divides the stress-strain behaviour of cement-based composites into four levels. Levels 3 and 4 correspond to strain-hardening materials, and distinguishing between them according to energy properties is suggested. Levels 1 and 2 correspond to "tensile strain-softening" and "deflection-hardening". Level 3 is named "tensile strain-hardening", while level 4 is called "high-energy absorbing". In order to better distinguish between them, Wille et al. (Wille et al., 2014) proposed an energy limit bound between these two levels, according to which a "g" value of 50 kJ/m^3 is suggested (see Figure 2.19).
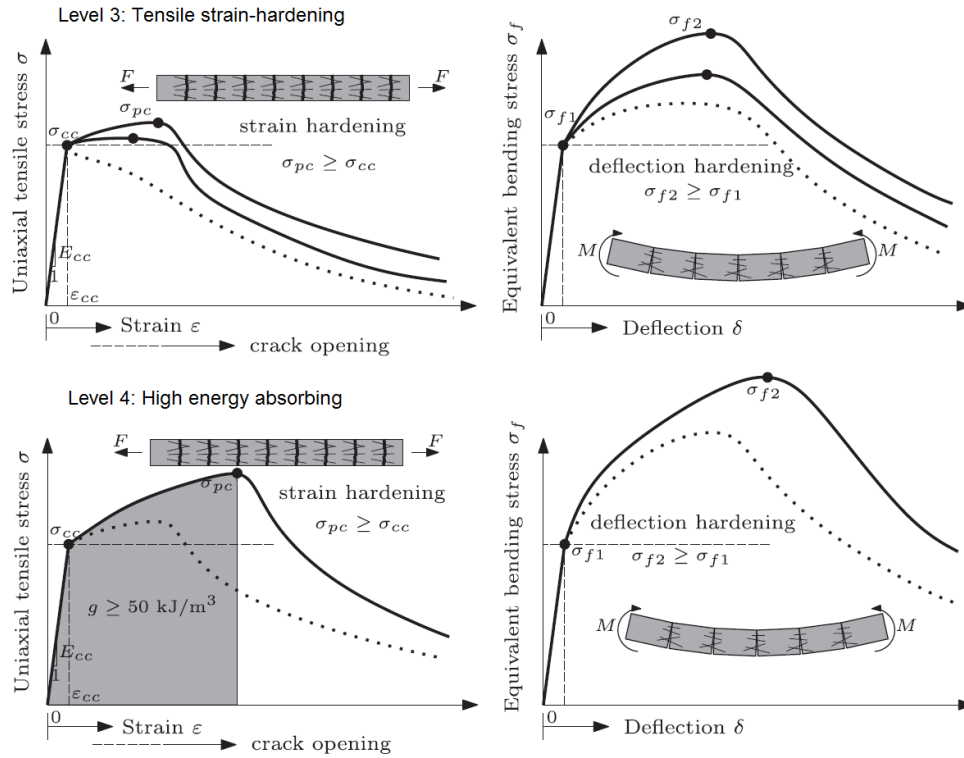
Figure 2.19 The strain-hardening classification according to the absorbed volumetric energy (Wille et al., 2014)

Volumetric energy absorption prior to tension-softening (g) is calculated for the UHPFRCs shown in Figure 2.14 and Figure 2.15. For the UHPFRCs in Figure 2.14, volumetric strain energies of 75 kJ/m^3 and 88 kJ/m^3 are obtained for the 169 MPa and

211 MPa concretes, respectively. For the UHPFRCs in Figure 2.15, volumetric strain energies of 24 kJ/m^3 and 19 kJ/m^3 are obtained for the monofibre and hybrid concrete, respectively. According to this classification, these UHPFRCs correspond to Levels 4 and 3.

Adopting these criteria requires the description of the type of specimen used, the test, and the methodology used to determine the volumetric strain energy as the strain prior to strain-softening may be a size-dependent parameter. In (Wille et al., 2014), the volumetric energy values within the range of 55-94 kJ/m^3 were obtained for a UHPFRC that had a compressive strength higher than 200 MPa and a fibre content within the 1.5-3% range in volume. These values were obtained in unnotched dog-bone tensile tests using a gauge length of 76 mm and a square cross-section of 25 mm. A value of 25 kJ/m^3 was reported by Jungwirth and Muttoni for Ceracem$^{®}$ with a 2.5% volume fraction of fibres (Jungwirth et al., 2004).

Even though this classification helps distinguish the level of performance of strain-hardening materials in tension, it is probably not the best way to classify them from a design point of view. All the attempts made to date in plain and fibre-reinforced concretes for their classification based on energy criteria, i.e. toughness, have failed in their subsequent step to design. This is why a classification criterion based on strength and/or ductility values seems more suitable.

2.4.3. Classification proposed by the French standard

The French standard (NF P18-470, 2016) and the guidelines published by the AFGC (AFGC, 2013) have proposed an alternative method to classify UHFPRC. According to this classification, a design method is proposed. The French standard considers that there are three different UHPFRC types: (i) strain-softening; (ii) low strain-hardening; and (iii) high strain-hardening.

The strain-softening type corresponds to those UHPFRCs whose average constitutive behaviour in tension is strain-softening. The low-hardening type corresponds to those UHPFRCs that are strain-hardening on average, but their constitutive law is strain-softening in terms of the characteristic law, and by taking into account the fibre orientation factor. From the material characterisation and design point of view, they are treated as type 1. Only the stress-crack opening relationship is taken into account, which has to be obtained from the notched three-point bending test.

The third concrete type corresponds to those concretes whose average and characteristic behaviours in tension is strain-hardening, even when the fibre orientation factor has been taken into account. In this case, the constitutive tensile relationship is a stress-strain one up to the peak. No consideration of the softening branch for these concretes has been made as the maximum strain value allowed is the end of the hardening branch.

Defined in this way, the French standard proposes a UHPFRC classification in terms of strength in which only two parameters are required: (i) cracking strength (f_t); (ii) the ratio between cracking strength (f_t) and ultimate tensile strength ($f_{t,u}$); i.e., the hardening ratio (γ). According to these values, the UHPFRC is classified.

Most of the UHPFRCs produced to date belong to type 2: i.e., low hardening concrete. Even though characteristic relationship in tension indicates softening, this does not mean that the structure cannot exhibit strain-hardening behaviour. In fact when UHPFRC is combined with reinforcement, multi-microcracking is frequent upon service loads with small crack openings. Neglecting this behaviour may be too conservative and does not help obtain the better benefits of UHPFRC. It would probably be more suitable to consider the stress-strain behaviour, not as an intrinsic or material property but varying according to element size and the expected fibre orientation. In this way, a minimum strain value at the end of the hardening phase obtained from a standard test should be proposed, similarly to Naaman's proposal. Then this value should be modified according to structural member size, reinforcement, or boundary conditions. If forces redistribution is not possible for localised deformations, neglecting the strain-hardening capacity of UHFPRC may be adequate, but not in the other cases.

2.4.4. Classification proposed by the Swiss standard

The Swiss standard (SIA 2052: 2014-12) classifies UHPFRC performance into three classes: UO, UA and UB. This classification is made according to three main parameters: (i) cracking strength (f_t); (ii) hardening ratio (γ); (iii) the strain at the end of the hardening phase ($\varepsilon_{t,u}$).

Class UO corresponds to a strain-softening material. A minimum cracking strength of 7 MPa is required. This class does not consider hardening behaviour. Class UA refers to low-hardening UHPFRC. A minimum cracking strength of also 7 MPa is required for this class. The hardening ratio must be higher than 1.1 and the strain at the end of the hardening must be higher than 1.5‰. Class UB refers to strain-hardening UHPFRC with improved strength and ductility. The minimum cracking strength required is 8.5 MPa, the minimum hardening ratio is 1.2, while the minimum strain at the end of the hardening phase is 2.5‰. All these parameters correspond to the characteristic values obtained from the proposed specific test.

This recommendation makes no reference to softening behaviour as it does not consider it in calculations. This may be accurate for very thin elements in which strain-hardening is very strong and crack width values are low even in ULS. However for the design of most reinforced structural elements in UHPFRC, a stress-crack opening relationship should be provided as crack opening design in ULS may reach around 2.5 mm if considering that reinforcement is far away from its yielding. In these circumstances, no UHPFRC is able to hold a microcracking regime yet and, thus, a stress-crack opening relationship is needed for design.

2.4.5. Summary

The previous review of the current classification proposal for UHPFRC suggests using strength and deformability criteria to classify UHPFRC strain-hardening behaviour. We have already mentioned the difficulties of defining what sort of material can be considered strain-hardening material. Two main criteria arise for this: (i) the strain at the end of the hardening phase and (ii) the hardening ratio.

It is commonly considered that a minimum characteristic value for a hardening value (γ) of 1 is required to be considered UHPFRC. However, it is important to note that even if in all the characterisation tests performed a strong microcracking process is obtained; i.e. a hardening ratio higher than 1 when obtaining characteristics values, the characteristic ultimate strength may be below the characteristic cracking strength. In this case, should a UHPFRC which always shows strain-hardening be considered a strain-softening one? Should the hardening ratio be processed by its average or by its characteristic value? Note that in order to answer these questions, it is necessary to know the characterisation test and the method used to determine these values.

Naaman et al. proposed a minimum strain value at the end of the hardening phase of 5‰ in order to ensure microcracking, even when rebars yield. Due to the fact that this strain value in SLS is never reached and a common strain value for rebars in ULS is 10‰, it may be better to limit the strain value to a value that guarantees a microcracking process in SLS with negligible crack opening. This is probably the idea carried out in the Swiss standard, which chose a minimum strain value of 1.5‰ and 2‰ at the end of the hardening phase. In addition, according to several tensile tests performed on standard UHPFRC with a common 2% of steel fibres, a minimum strain value of 2‰ is often reached, which exhibits hardening and allows the formation of multiple microcracks. (Baby et al., 2013; Kanakubo, 2006; Kim et al, 2010; Nguyen et al, 2012; Park et al., 2012; Tailhan et al., 2012; Wille et al., 2011).

It is worth mentioning that all the classification proposals for UHPFRC focus on defining its strain-hardening behaviour. However, we cannot forgot that UHFPRC is a special fibre-reinforced concrete type and its post-cracking behaviour should also be characterised. As in fibre-reinforced concrete, this relationship is immensely important in design. As stated in 2.3.3, in UHPFRC it is important to know the complete bilinear stress-crack opening relationship as the change of slope likely occurs within the crack opening design interval. It is known that characteristic crack opening (w_c) is related to fibre length. In addition, as there is no stress-drop at the beginning of the softening stage, the stress at the zero crack opening is the same as that at the end of the hardening phase. This is why the complete stress-crack opening behaviour can be defined by simply finding the point at the change of slope. This point should probably be incorporated into the UHPFRC classification as it provides us a notion about the post-cracking ductility of UHPFRC.

As mentioned in 2.3.3, the stress at the change of slope may be considered constant function of the tensile strength regardless of fibre type and amount. This fact can also be appreciated in Figure 2.14 and Figure 2.15. This is why the strength at the change of slope could be defined according to ultimate tensile strength. Then the only necessary parameter left to classify the post-cracking behaviour of UHPFRC is the crack opening at the change of slope. This parameter varies according to fibre amount, length and bond. Therefore, once the stress-strain behaviour is known (f_t, γ and $\varepsilon_{t,u}$), the stress-crack opening one can be characterised by adding two parameters: (i) fibre length and (ii) crack opening at the change of slope.

A UHPFRC post-cracking behaviour classification according to these two parameters would be possible and would determine other important parameters for the fracture mechanics of UHPFRC, such as fracture energy (G_F or G_f) (see 2.3.1).

2.5. Selecting the suitable test setup

Test setup must be chosen according to the parameters that have been decided to be used for the UHPFRC classification as test setup characterisation must provide these parameters. According to 2.4.5, it seems that stress-strain parameters, as well as stress-crack opening parameters, are needed for designing using UHPFRC.

Following the trend in conventional fibre-reinforced concrete, it is not unusual to find that notched three-point bending has been proposed to characterise the stress-crack opening behaviour of UHPFRC (AFGC, 2013). Recognising the difficulties to derive the stress-crack opening relationship from this type of test, AFGC members proposed a more complex methodology based on mechanical models, which were originally developed for conventional fibre-reinforced concrete, such the non-linear hinge model developed by Casanova and Rossi (Casanova et al., 1996). As this model does not take into account the strain-hardening nature of UHPFRC, this method should be reviewed.

The notched three-point bending test was specifically developed to determine the stress-crack opening relationship in strain-softening materials. As no significant inelastic deformations are localised on the notch-plane in these materials, all the absorbed energy can be attributed to the fracture along the notch-plane, and toughness can be a suitable parameter to define softening behaviour. However in UHPFRC, and using the notch depth proposed in EN-14651, a large region may undergo plastic deformations after the first crack takes place (Spasojevic, 2008). The toughness measurement from this test can no longer be used. In this case we wonder whether the notched three-point bending test is suitable for the UHPFRC post-cracking behaviour characterisation. What new problems would arise?

In certain considerations, UHPFRC post-cracking behaviour could probably be obtained from this test. However, it is quite difficult to obtain a suitable hardening behaviour from it since deformations are localised at the notch, which forces an

unnatural crack pattern distribution. This is why unnotched tests have arisen in recent years as an alternative to notched tests to characterise UHPFRC strain-hardening behaviour (AFGC, 2013; Baby et al., 2012; Wille et al., 2012).

Nowadays, UHPFRC tensile behaviour characterisation is still a challenge, and no agreement on the standard test set up, advisability of notch, or even specimen shape and size, has yet been reached. We wonder, in fact, whether we need different test setups for stress-strain and post-cracking behaviour characterisations. At this point one could think about the convenience of having a single test to determine both stress-strain behaviour and stress-crack opening behaviour. Would it be possible?

In order to answer these questions, a brief review of the commonest tests that allow the determination of fibre-reinforced concrete tensile behaviour is made hereafter, together with a brief analysis of the characterisation methods proposed in current UHPFRC standards.

2.5.1. Uniaxial tensile test

The uniaxial tensile test may be the most appropriate method to determine UHPFRC tensile behaviour (Naaman et al., 2006) since it directly provides tensile behaviour without having to resort to inverse analysis methodologies. However, these tests are challenging to perform and are very sensitive to several factors: specimen imperfections, loading machine stiffness, shrinkage, boundary conditions, stress concentrations at fixation points or the non-uniformity of the material itself (Kanakubo, 2006; Ostergaard et al., 2005; Qian et al., 2007). Recent works have been carried out to develop suitable easy-to-conduct tests (Graybeal et al., 2013; Reineck et al., 2010; Denarié et al, 2015), and to clarify how specimen shape and the gripping system influence the test results on UHPFRC specimens (Wille et al., 2014).

With a direct tensile test, a force-elongation curve is usually obtained. Elongation is always referred to a certain gauge length used to obtain the average strain that refers to that length. Once the microcracking stage finishes, a single crack starts developing, while the rest of the specimen undergoes inelastic unloading. By knowing both the unloading modulus and elongation, it is possible to obtain the stress-crack opening behaviour by assuming a fictitious crack model (see 2.3.1). This is the procedure used to derive the relationships in Figure 2.14 and Figure 2.15. Note that the stress-strain curve is a pre-peak non-linearity zone that can be attributed to volumetric energy absorption, as it happens with plain concrete. This means that the stress-strain hardening behaviour in this region is gauge length-independent. Even though this assertion can lead to discussion, it is assumed in the present document.

A very good recap of different direct tensile test setups performed on UHPFRC and fibre-reinforced concrete can be found in (Wille et al., 2014). These tests were classified into three main groups: (i) dog-bone tests; (ii) unnotched tests; (iii) notched tests. It is important to remark that dog-bone tests are unnotched tests, while unnotched tests refer to those with no dog-bone shape. Twenty-four different test setups were

collected. They differed in geometry, attachment to machine (glued, anchored or clamped; fixed or pinned) and presence or absence of a notch. A wide range in variations was noted while performing direct tension tests. No standard method is available. Regarding the test setup, subsequent findings are highlighted:

- Long constant areas allow the investigation of multiple cracking and average crack spacing (strain-hardening behaviour)
- Notched specimens facilitate investigations of material softening (stress-crack opening behaviour)
- Unlike unnotched tests, the failure plane in notched tests is predefined by the location of the notch, which does not have to be the weakest plane. Thus variability is larger and the material mechanical performance obtained is better (Amin et al., 2015).
- Pinned end conditions ensure an even stress distribution prior to cracking, but do not support an even crack opening throughout the cross-section in comparison to a fixed boundary condition
- Larger cross-sectional areas at the supports and a smooth geometry transition are recommended to avoid support failures and to reduce stress concentrations.

All the difficulties encountered when performing direct tensile tests lead to the use of relatively small specimens, in which the small dimension is smaller than 100 mm and is usually smaller than 50 mm. It fosters fibre orientation effects, which may be the cause of a considerable overestimation of UHPFRC's tensile mechanical properties. Using large fibres and difficulties to readapt this test to larger sizes both make the effect of fibre orientation even more relevant.

This fact, together with greater preparation efforts and the need for specific and expensive machines, have led researchers to focus on bending tests. This does not mean that a direct tensile test is not a suitable test, but is only intended to justify the more extended use of bending tests in both the design and research fields.

2.5.2. Bending tests

Bending tests are the most popular type to determine tensile properties in concrete because they more realistically simulate the conditions of many practical situations, and are also a simpler alternative to direct tensile tests (Gopalaratnam et al., 1995). However, they imply more difficult interpretations of the results, and also require sophisticated inverse analysis methods to accurately obtain the specimen's tensile behaviour.

These are the most widely used tests to characterise the tensile properties of fibre-reinforced concrete (Casanova et al., 1996; Chanvillard, 2000). Two types of bending tests have been commonly used to determine the tensile properties of fibre-reinforced concrete: (i) notched three-point bending tests, used to determine the post-cracking tensile law; (ii) unnotched four-point bending tests, used to establish elastic properties,

to determine toughness parameters and, with strain-hardening materials, to characterise strain hardening behaviour.

As previously stated, it would be convenient to have a single test to determine all the tensile parameters required for design and quality control purposes. The advantages and disadvantages of notched and unnotched bending tests are summarised below.

2.5.2.1 Notched three-point bending test

Since the thorough work carried out by RILEM TC 162-TDF task group, tensile properties of FRCs have been obtained from notched three-point bending tests. Although this is a suitable test for FRCs to determine their post-cracking behaviour, it is hard to obtain a reliable strain-hardening response of UHPFRCs with them.

As previously mentioned, in a strain-softening material tested according to EN-14651, one single crack propagates along specimen depth once the cracking strength at the crack tip is reached. The rest of the specimen can be considered elastically unloaded and the absorbed energy can be entirely attributed to the fracture along the notch. In this way, a toughness measurement can be used to characterise its softening behaviour. In addition, load-CMOD can also be used to characterise this behaviour.

However, this is not the case of UHPFRC. For the test setup proposed in EN-14651, the crack notch is not enough to avoid a significant part of the beam that comes close to the notch undergoing plastic deformations. In this area, several cracks may appear in the region close to the notch (Figure 2.20) and a multi-microcracking stage may take place during the test. Conventional inverse analyses methods in RILEM and MC2010 do not take this phenomenon into account and assume that crack mouth opening displacement is due to the opening of a single crack instead of being smeared in several cracks (Figure 2.20). This assumption leads to the overestimation of the tensile properties in strain-hardening materials. In Figure 2.20, right, we can see that the maximum load is reached at a CMOD of around 1.5-2 mm; i.e. at a COD of around 1-1.5 mm. However upon maximum load, the crack opening of the softening crack was measured in 0.3 mm using a crack width ruler. This means that all the recorded elongation measurements did not correspond to one single crack, but to a group of them as the material was able to develop a microcracking phase despite having notched the specimen. This is why the notched three-point bending test is unsuitable for analysing UHPFRC strain-hardening behaviour.
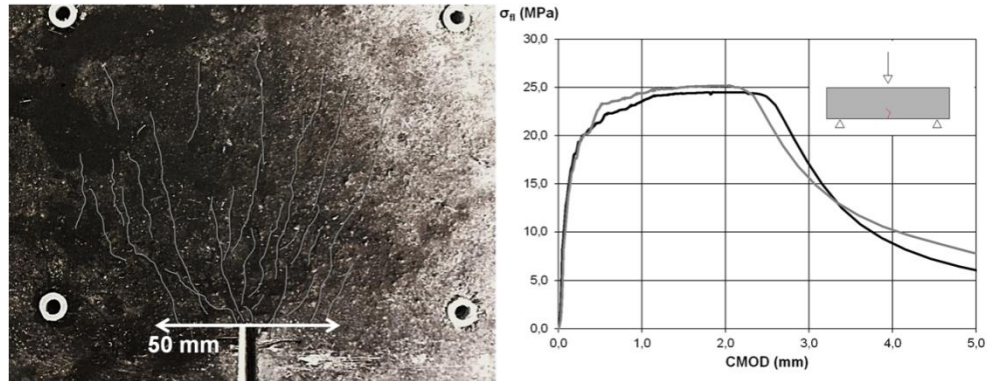
Figure 2.20 Multi-microcracking in a UHPFRC specimen notched three-point bending test according to EN-14651 (left) and its corresponding load-CMOD curve (right).

In fact when inverse analysis procedures are applied to the load-COD curves obtained from strain-hardening materials in the standard EN-14651 test, similar constitutive stress-crack opening relationships to that shown in Figure 2.21 are derived from them. Figure 2.21 shows two stress-crack opening curves. The grey line corresponds to the inverse analysis results according to the French standard obtained from a 166 MPa UHPFRC that contained 2% of 15/0.2 mm steel fibres (Randl et al., 2016). The black line is merely a freehand drawing that represents what it is expected for UHPFRC, which agrees with the results in Figure 2.14 and Figure 2.15. The proposed inverse analysis overstimates the fracture energy of UHPFRC due to a bad assumption of the crack opening measurement given multiple microcracking and, worse still, strain-hardening behaviour determination is not possible.
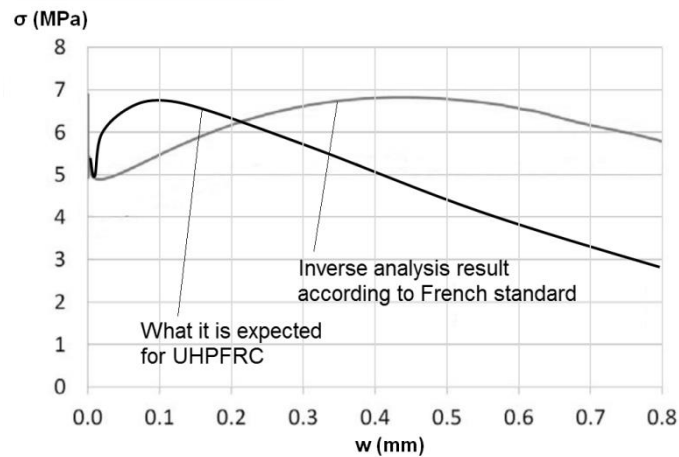
Figure 2.21 The stress-crack opening relationship obtained from notched three-point bending tests according to EN-14651 (Randl et al., 2016).

Since multi-microcracking will take place even if a notch is made on the specimen, it is better to dispense with the notch and test a larger area, which is subjected only to a constant bending force, in which the micro-cracking process is free to develop. In this way, the unnotched four-point bending test seems more appropriate.

2.5.2.2 Unnotched four-point bending test

The unnotched four-point bending test provides a large area with a relatively constant bending moment. Point loads create a disruption in the stress field close to the points where they are applied, whose influence is weaker the higher the slenderness ratio goes (L/h). In spite of this, the average properties in the area between loads are assumed and a smeared crack approach is considered to study the strain-hardening behaviour of UHPFRC. From these tests, the experimental load (P) – displacement at mid-span (δ) relationship is commonly recorded. The commonest unnotched four-point bending test is the third-point bending test in which the distance between load rollers is one third the beam span. This test setup is shown in Figure 2.22.
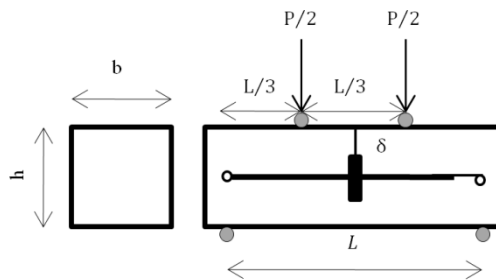
Figure 2.22 The third-point bending test setup

As notched three-point bending tests cannot be used to determine the strain-hardening behaviour of UHFPRC, unnotched four-point bending tests could prove suitable tests to obtain the tensile properties of materials such as UHPFRC. However, stress-crack opening relationship characterisation might be complex, and a suitable methodology to determine it has not yet been developed.

It is now worth remembering that in the late 1990s, the notched three-point bending test was proposed instead of the four-point bending test to characterise fibre-reinforced concrete tensile behaviour. As already mentioned, this was due mainly to the fact that a notch was better for post-cracking characterisation. However, another advantage was found: the notched three-point bending test reduced the variability of the results (Gopalaratnam et al., 1995) compared to an unnotched four-point bending test.

This claim is somewhat tricky as two different effects may be distinguished and evaluated. It is fair to acknowledge that notched four point bending tests may have wide variability, but only if the position of the macrocrack in the constant bending moment area is not taken into account. That was pointed out by Chanvillard

(Chanvillard, 2000), who gave a simple demonstration to show that after crack localisation, and for a same rotation angle of the crack, the measured displacement could vary up to 50% depending on crack position. However, when taking into account crack position, variability can reduce to the extent of becoming even lower than in a three-point bending test. The reason for this is found in the nature of the notch. As pointed out by Amin et al. (Amin et al., 2015), in an unnotched test with a relatively large area subjected to the same forces, failure takes place in the weakest section; i.e., where the fibre dose is always less than the average. However in notched tests, one random section is chosen as the failure one; i.e. the notched section. In this section the fibre dose can vary much more, mainly according to randomness. The notched section can be the weakest, the strongest, or anything in between (see Figure 2.23). So the expected scatter must be higher.

Figure 2.23 represents the previous discussion. In it, a hypothetic probability distribution of the fibre dose along the beam is shown. In an unnotched test, failure takes place in the weakest zone inside the shaded area, which is expected to have a smaller percentage of fibres than the average. The scatter will be lower the larger the central area is. In a notched test, failure takes places in the notch section, which has a random fibre dose.
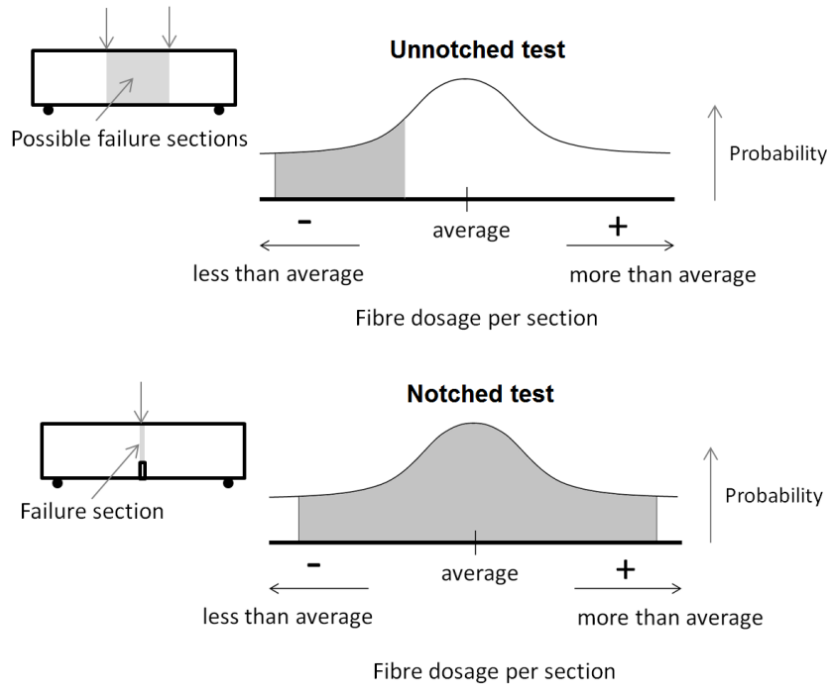
Figure 2.23 Origin of the variablity in notched and unnotched tests

The previous discussion leads to one conclusion: a notched four-point bending test leads to less scatter than the three-point bending test, but only if the crack position in the failure zone is taken into account. This may be the reason for the wide variability in determining the toughness indices in the 1990s, and also the high variation coefficients that appear in the fibre-reinforced German recommendations (DAfStB, 2015), which maintain the unnotched four-point bending test for fibre-reinforced characterisation without considering crack position.

If variability can be reduced, then it is possible to derive the strain hardening behaviour of UHPFRC from these tests (Baby et al., 2013). The only remained question is if it is also possible to obtain post-cracking behaviour from them.

One possibility to achieve this is to make an analogy with unnotched direct tension tests results. Figure 2.24 shows typical stress *versus* an elongation response from a UPHFRC unnotched direct tensile test specimen. In this test, the increase in deformation after the peak is due to both the increase in crack opening and the decreased deformation of the material outside the crack area, as mentioned in 2.3.3. This behaviour in strain-hardening materials is determined by the unloading modulus (E^*). According to Figure 2.24, the stress (σ)-crack opening (w) relationship after the peak is described by Eq. 2.11 and Eq. 2.12, according to the elongation at the end of the linear elastic stage (δ_{el}) and the peak (δ_{cr}), stress variation ($\Delta\sigma < 0$), the unloading modulus (E^*), gauge length (l_m), the average crack opening at peak (w_i), and average crack spacing (s_{av}).
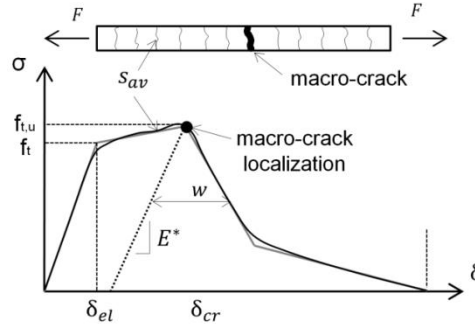
Figure 2.24 A typical strain-hardening tensile response of UHPFRC

$$w = w_i + (\delta - \delta_{cr}) - \frac{\Delta\sigma}{E^*} l_m \quad ; \quad \Delta\sigma < 0$$

Eq. 2.11

$$w_i = \frac{(\delta_{cr} - \delta_{el})}{l_m} \cdot s_{av}$$

Eq. 2.12

Let's imagine that this behaviour is used to describe the behaviour of each cross-section fibre in a four-point bending test after crack localisation takes place inside the constant bending area. Inside this area, the bending moment is constant and shear forces can be neglected. Thus each section fibre is subjected only to an axial force, so it is possible to apply the model used to describe uniaxial tensile behaviour. Applying this model will lead to a similar non-linear hinge model to that proposed in (Stang et al., 1998) and (Ostergaardet al., 2005) (see 2.7.3.3 and 2.7.3.4). This means that it is possible to derive the stress-crack opening relationship from a four-point bending test using a non-linear hinge model. It requires developing a new model that takes into account the strain-hardening response of UHPFRC. A full description of these models and how they work is found in 2.7.3.

2.5.3. Standard tests in UHPFRC recommendations

The existing standard for UHPFRC design includes three different types of characterisation tests: (i) uniaxial tensile test (Swiss standard); (ii) notched three-point bending test (French standard); and (iii) unnotched four-point bending test (both French and Swiss standards). As previously mentioned, bending tests require an inverse analysis procedure. The next sections describe the characterisation test setups proposed by both the French and Swiss standards, together with the inverse analysis procedure proposed in the French standard for the three-point bending test. The inverse analysis methods proposed for unnotched four-point bending tests by both standards are described in 2.6.2.

2.5.3.1 Standard tests in the French standard

The French standard proposes a different test setup to derive UHPFRC tensile properties according to its classification. As described in 2.4.3, the French standard considers three UHPFRC types: (i) strain-softening; (ii) low strain-hardening; (iii) high strain-hardening. The methodology proposed in the French standard assumes that the concrete type is previously known, which may be sometimes difficult to establish.

For classes (i) and (ii), two different tests are required (see Figure 2.25). Firstly, a third-point bending test has to be performed to determine cracking strength. This value is determined based on the loss of linearity notion, which assumes that the first crack can be determined in a bending test at the point where significant loss of linearity is detected. A more detailed explanation of this method and its disadvantages are explained in 2.6.2.2. Once cracking strength has been determined, a notched-three point bending test must be carried out in which the CMOD must be recorded. The CMOD has to be corrected using the CMOD at cracking strength. Then in order to derive UHPFRC post-cracking behaviour, a point-by-point inverse analysis is proposed according to the criteria developed in (Chanvillard, 2000) using the kinematic assumption proposed by Casanova and Rossi (Casanova et al., 1996) for strain-softening materials. More details about the point-by-point method and kinematic assumption can be found in 2.6.1.4 and 2.7.3.2, respectively.

It is important to note that the French standard does not follow MC2010 to determine the post-cracking behaviour of fibre-reinforced concrete, even when assuming either strain-softening (i) or low strain-hardening behaviour (ii). This is probably due to lack of confidence in the MC2010 method when it extends beyond strain-softening materials, characterised by a stress drop immediately after cracking. Another possibility is that point-by-point inverse analysis methods have been headed by French researchers, who wish to promote these methods as they consider them better than existing ones.
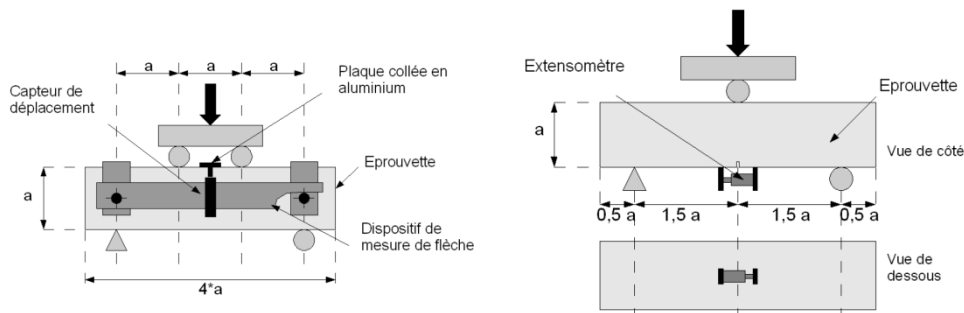
Figure 2.25 The proposed characterisation tests for class (i) and (ii) proposed by the French standard. Third-point bending test (left) and three-point bending test (right)

Even though the assumptions and methods proposed in the French standard are fully detailed in further sections, the main drawbacks of this characterisation methodology are indicated below:

- First cracking strength determination is subjected to a subjective criterion as loss of linearity point is not objectiveley defined.
- The kinematic assumption of Casanova and Rossi assumed that the curvature out of the crack plane remains in a linear stage throughout the loading and unloading process. Even though this is true for strain-softening materials, it is not the case for strain-hardening materials according to that explained in 2.5.2.1.
- A point-by-point inverse analysis requires using a computer, which needs to be written in any existing programming language. This is not in line with the simplicity criteria of design standards, and may scare engineers and laboratories.

For class (iii), the French standard considered that only stress-strain hardening behaviour matters for design. For its determination, a third-point bending test on a thin specimen is proposed (see Figure 2.26). Two different methods to derive the bilinear stress-strain UHPFRC hardening behaviour are proposed: (i) a point-by-point method; (ii) a simplified method. Each method is described in 2.6.1.4 and 2.6.2.2, respectively.

While method (i) has all the disadvantages of the point-by-point inverse analysis derived from lack of simplicity, method (ii) is so simple that it may be not as accurate as required. Such lack of precision is due to using the loss of linearity point and the assumption of a linear curvature distribution along the beam instead of a non-linear one.
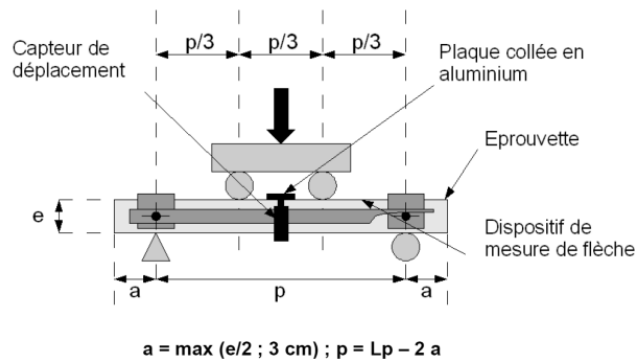
Figure 2.26 Third-point bending test for UHPFRC class (iii) characterisation according to the French standard.

It is worth noting that the specimen depth limitation depends on the UHPFRC class type. In the test setups that correspond to class type (i) and (ii) (see Figure 2.25), specimen depth should be 5 and 7 times the length of the larger fibre used, while specimen depth is only limited to 3 times that length in the characterisation test for class type (iii) (see Figure 2.26). The latter limitation is proposed also by Naaman and Reinhardt (Naaman et al., 2006). It is clearly an attempt to favour the development of strong hardening behaviour that may not be found in a larger specimen. More information about the specimen geometry proposed for these tests can be found in (NF P18-470, 2016).

2.5.3.2 Standard tests in the Swiss standard

Unlike the French standard, the Swiss standard proposes the same characterisation tests for the three different concrete types considered. Two different test setups are proposed: (i) a direct tensile test and (ii) a third-point bending test. It is mandatory to do both for initial tests. However, for quality control only the third-point bending test is proposed.

The aim of these tests is to obtain the stress-strain hardening behaviour of UHPFRC. It does not include any methodology to derive post-cracking behaviour from these tests because all the tensile parameters required for design in the Swiss standard are strain-hardening parameters. This means that they do not consider any situation beyond the micro-cracking stage of UHPFRC. An overview of this standard leads to the

conclusion that it is to be applied to structures made of thin UHPFRC layers that exhibit strong strain-hardening behaviour and ensure micro-cracking, even in the ULS situation. This also explains the small specimen size proposed (Figure 2.27) and the fact that its size does not depend on fibre length.

The proposed direct tensile test has to be carried out on a dog-bone specimen with a fixed end boundary condition. The specimen geometry is fixed and is not in accordance with fibre length. Its size is shown in Figure 2.27, left. The results of this test can be directly used to determine the UHPFRC class type.
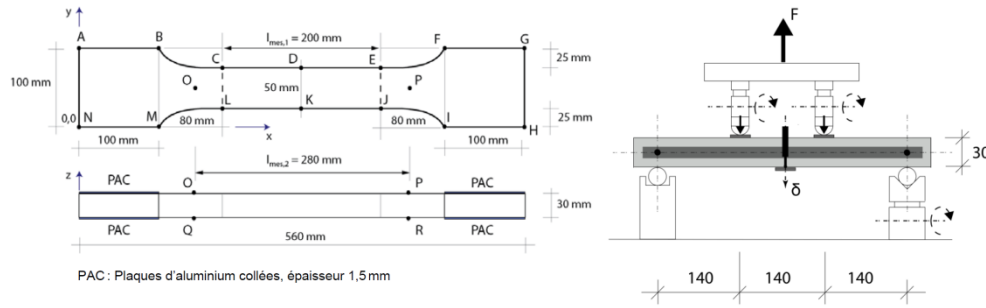
Figure 2.27 The characterisation test setup proposed in the Swiss standard. Uniaxial tensile test specimen (left) and test setup and specimen size for the third-point bending test (right)

The proposed third-point bending test has to be carried out following the configuration and specimen size shown in Figure 2.27. Specimen width is 100 mm. The load-deflection at mid-span is recorded and a simplified inverse analysis methodology is used to determine UHPFRC bilinear strain-hardening behaviour. The inverse analysis method proposed in the Swiss standard is described in 2.6.2.3.

2.5.4. Advisability of a single test

It is obvious that having a single test from which complete UHPFRC tensile behaviour can be derived is quite advantageous. However, what it is discussed in this section is whether specimen size should be established or if, on the contrary, the specimen used to characterise UHPFRC behaviour should vary according to the structural element size that the test represents.

It is important to remember that the notched three-point bending method proposed by both RILEM TC 162-TDF and MC2010, and normalised in EN-14651, proposes a single test with a fixed geometry, which is considered suitable for fibre-reinforced concrete with a maximum aggregate size of 32 mm and a maximum fibre length of 60 mm. This means that the tensile relationship obtained from this test is not the "intrinsic" constitutive relationship (it probably does not exist), but the tensile relationship in that specific test, and with that specific geometry and that specific pouring system. Later these material characterisation parameters, the so-called residual

tensile strength values, are modified by using a different variety of coefficients to take into account fibre orientation and variability (DAfStB, 2015)). However, these coefficients are independent of the material characterisation and are applied to the design stage.

This is the same characterisation system used for compressive strength in conventional concrete. The compressive strength obtained from the standard cylinder is not the "intrinsic" compressive strength value, but a representative value for it. Everybody knows that compressive strength depends on size and geometry. However, design methods have been evolved using that standardise compressive strength value as a reference.

So this is why it is thought that having a single test set up and geometry can facilitate the further development of suitable codes. However, not everyone thinks the same way. It is also evident that if we test a specimen with a similar size to the structural element member by a similar pouring procedure, characterisation directly gives the tensile response which has to be used in design, because specimen is representative of the structure's fibre distribution (Chanvillard, 2000). This is what it is proposed in the French standard, which establishes the test geometry according to fibre length or structure depth. It also proposes a methodology to correct edge effects due to placement, sawing or notching in an attempt to obtain an "intrinsic" tensile response of UHPFRC. In addition, this "intrinsic" response has to be affected once again by a fibre orientation coefficient, in which edge effects once again play an important role. At this point, an important question arises: is it worth correcting edge effects to obtain an intrinsic tensile response if another orientation coefficient must be applied afterwards?

It is probably not worth it as it implies more work and the possibility of misunderstanding in the UHPFRC application with so many coefficients. For both UHPFRC and conventional fibre-reinforced concrete, it seems more convenient to have a single test to obtain some representative values of the tensile response of UHPFRC, values that can be used for design by applying fibre orientaion correction factors. In this way, the characterisation method finishes when the parameters that define tensile behaviour in the selected standard specimen are obtained.

2.5.5. Summary

The direct tensile test is probably the most suitable test as it directly determines both stress-strain hardening and post-cracking behaviour by one single test. It is simpler to analyse and does not require any complicated methodology to determine all the parameters that define UHPFRC tensile behaviour. Even though the fracture energy in UHPFRC is larger than in other fibre-reinforced concrete types, which helps to stabilise the direct tension test, this test type is still difficult to perform well in most quality control laboratories.

At this point it is important to define the aim of this work. If this work was devised to develop a test that characterises UHPFRC tensile behaviour in full detail and

accurately, i.e. from a pure research point of view, the direct tensile test should probably be chosen. However, if a standard test to determine those parameters needed for design aims to look for, e.g., a standard test on which a standard design code is based, a bending test is probably more suitable. For this purpose, an easy-to-perform test setup with few testing equipment requirements is more desirable. As simpler tests require more complicated analyses of the result methods, research efforts may focus on simplifying these methods by reducing them to a simple formulation, like RILEM TC 162-TDF did for strain-softening fibre-reinforced concrete. It is important to note that both the French and Swiss worked along this line.

With this purpose in mind, and if the intention is to obtain both stress-strain and post-cracking behaviours from a single test, the unnotched four-point bending test arises as the most promising test setup to achieve just this. The notched three-point bending test should be ruled out given the difficulties to characterise stress-strain behaviour due to the localised deformation at the notch. Besides, the multi micro-cracking stage that appears even with the presence of a notch makes the post-cracking behaviour analysis more difficult with this test type, and the scatter may be higher due to the notch.

The unnotched four-point bending test and, more specifically the third-point bending test, which is the most widespread unnotched four-point bending test used, allows stress-strain behaviour to be determined as it offers a large area subjected to a constant bending force in which shear forces can be neglected. However, further hypotheses are required to determine the post-cracking behaviour from the load-displacement at mid-span results.

This is why a profound review of existing methods used to derive the tensile properties of UHPFRC from the results obtained from unnotched four-point bending tests is required. With this review, the possibility of obtaining a complete description of UHPFRC tensile behaviour must be analysed, and if that is possible, existing methods must be the starting point on which subsequent simplified methods should be based.

2.6. The four-point bending test: inverse analysis methods

An inverse analysis consists in deriving the tensile response of any concrete type from the results obtained in a bending test. Thus an inverse analysis procedure does not give the tensile behaviour of concrete that has to be used in design, rather the tensile behaviour that concrete exhibited in a specific bending test setup with a specific geometry. It is worth mentioning that the inverse analysis does not involve the determination of fibre orientation coefficients (statistical size effects). However, the inverse analysis must take into account deterministic size effects.

Several methods have been proposed to carry out the inverse analysis. The different proposed methods have a point in common: they attempt to reproduce the experimental measurements by means of more or less complex models, which depend directly on the uniaxial tensile and compressive parameters. These methods can be sorted into two

main groups: (i) methods based on the experimental key points taken from tests, called simplified methods; (ii) methods based on a complete experimental law. The latter can be also classified according to how the parameters adjustment is made in iterative methods and point-by-point methods. Iterative methods assume a constitutive law in both compression and tension. During the iterative process, these parameters are modified to minimise the error between the proposed model and the experimental results. Point-by-point methods build the constitutive law progressively in each loading step. This process leads to a rough constitutive law, which requires a post-process for its easy implementation and use.

The methods based on a complete experimental law use load-deflection, load-strain at the tension face or the load-average curvature between load points curves to reproduce the test and to derive uniaxial tensile and compressive parameters. These methods can be sorted according to the above-mentioned experimental laws used for adjustments. The proposed classification is summarised in Figure 2.28.
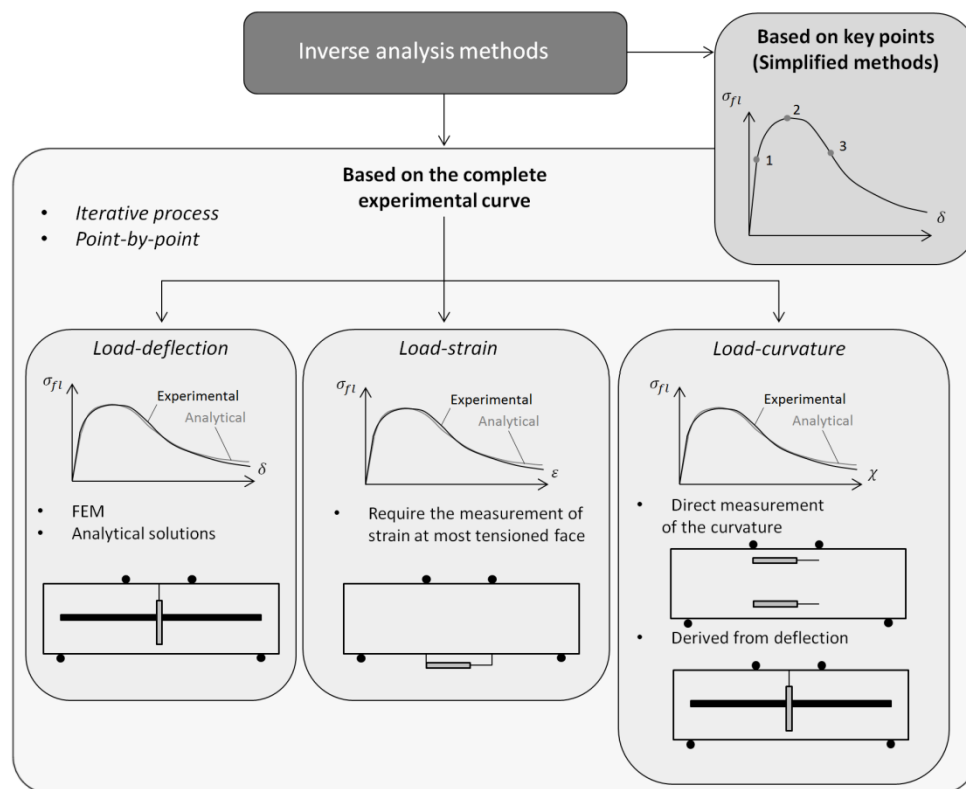
Figure 2.28 Classification of inverse analysis methodologies

The inverse analysis procedures included in group (ii) require a computer analysis and being skilled in structural analyses. As they tend to be more accurate, they are the methods used for research purposes. However, from either a structural design or a quality control point of view, science should offer an accurate, objective and easy-to-conduct procedure (simplified method). It is also a must that the constitutive relationships derived from simplified methods accurately reproduce the behaviour obtained during the test. Therefore, simplicity, objectivity and accuracy are the main goals pursued when developing simplified inverse analyses.

This is the case of the well-known simplified inverse analysis methods proposed by RILEM TC 162-TDF and MC2010 (see 2.3.2.2 and 2.3.2.3), applied to bending test results performed on notched specimens following EN-14651. In this case the key points are residual flexural strength parameters $f_{R,1}$ and $f_{R,4}$ in the RILEM method, and $f_{R,1}$ and $f_{R,3}$ in the MC2010 method. The formulation proposed to obtain residual tensile parameters σ_2 and σ_3, in the RILEM method, or f_{Fts} and f_{Ftu}, in the MC2010, corresponds to the inverse analysis method.

2.6.1. Method based on the complete experimental law

2.6.1.1 Load-deflection method

Load-deflection methods are commoner and more intuitive, and determine the tensile parameters by comparing the load-deflection experimental curve and the analytical curve proposed. The theoretical load-deflection curve is obtained by more or less complex FEM models. The main problem of these methods lies in the long time taken to solve each iteration step until the numerical simulation fits the experimental results, and also in the hypothesis required to obtain deflection during unloading. These are also the most ancient methods. The first inverse analysis method found was that proposed by Serna (Serna, 1984). In it, a displacement-based finite element method was used to fit the numerical model to the load-displacement experimental curve. This model used a trilinear stress-strain relationship in tension, with a drop after first cracking. This model also considered shear deflection. It is not a fracture mechanics model, and no information about whether the scale effect could be reproduced is included.

Non-linear 2D FEM, using fracture mechanics models such the crack band model and its subsequent evolutions, is able to reproduce post-cracking behaviour. Their main problem is the time it takes to find a solution as the load-deflection curve must be obtained several times by varying the constitutive parameters until the numerical solution properly fits the experimental results. Many authors are satisfied by working only with the loading branch, which cannot be right as post-cracking behaviour influences the peak load. Thailand et al. (Tailhan et al., 2004) proposed a 2D FEM model with a displacement formulation, but it did not consider any hypothesis for the unloading branch.

Both Ostergaard et al. (Ostergaard et al., 2005) and Soranakom et al. (Soranakom et al., 2007) proposed a model which took it into account and enabled the determination of softening parameters. The former proposed a hinge model, which considered the crack position, a specific hinge length and a numerical analysis to obtain the stress-strain curve that best fitted the experimental results. The latter suggested a method based on a closed-form formulation for moment-curvature relationships based on a trilinear assumption of the tensile σ-ε law (Soranakom et al., 2008). After maximum load, this model assumed a damage area length to reproduce the unloading branch.

2.6.1.2 Load-strain method

The load-strain method was recently developed in (Baby et al., 2012). This method requires measuring the average strain on the tension face between the applied loads using two staggered LVDTs on the tensile face, as shown in Figure 2.29. According to them, this configuration also allows the determination of the crack localisation point, i.e. the end of the hardening phase. For each load-strain experimental measure, a mechanical equilibrium in the central section is achieved to determine the tensile stress-strain law by a point-by-point process. A linear elastic behaviour in compression is used given the high compressive strength of UHPFRC. This process leads to a rough constitutive law in tension, which has to be transformed.

Scheme of the lower face
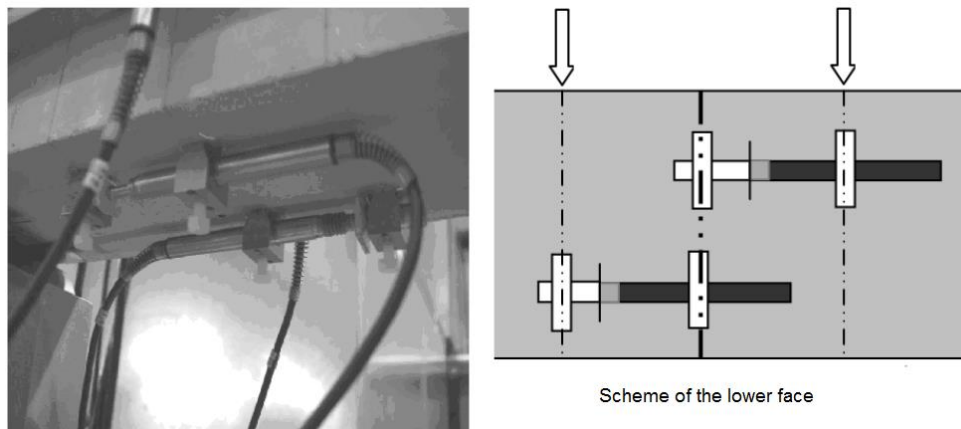
Figure 2.29 Strain measurement on the bottom tensile face at the central one third using two staggered LVDTs according to (Baby et al., 2012)

Although it has not yet been proposed, the load-strain method can also be used with an iterative method instead of a point-by-point method. In this case, by assuming a constitutive relationship in tension, it is possible to determine a closed form formulation for the moment-strain in the most tensioned face relationship following a similar process to that proposed in (Soranakom et al., 2007). As it is a closed form

formulation, the determination of the load-strain response for each assumed constitutive tensile law is fast, and the iterative process takes less time than in an FEM.

2.6.1.3 Load-curvature method

The load-curvature method requires the determination of the average curvature in the central one third. It can be a direct measurement by using a minimum of two LVDTs, as stated in (Kanakubo, 2006), or an indirect measurement (see Figure 2.28). In the latter case, deflection is converted into an average curvature between load points by an equation that relates these two variables. This relationship is what it is called the displacement to curvature transformation throughout this document.

In (Rigaud et al., 2011), displacement to curvature transformation is used which is based on the assumption of a linear curvature distribution between supports and the applied load points. This relationship is shown in Eq. 2.13. According to (Rigaud et al., 2011), it can be used only until crack localisation. It is worth remarking that this equation does not take into account shear deformations and can be applied only to thin specimens. Once the experimental load-curvature is obtained, a similar point-by-point process to (Baby, et al., 2012) is followed after transformation to establish the tensile parameters.

$$\phi = \frac{216}{23L^2}\delta$$

<div align="right">Eq. 2.13</div>

In (Qian et al., 2007), another equation is suggested, based on structural elastics mechanics that states taking into account the influence of shear, but is less successful. In this case, curvature correlates with displacement not at mid-span, but under the load roller (δ_u).

$$\delta_u = \left(\frac{15L^2}{162} + \frac{h^2}{4}\right)\phi$$

<div align="right">Eq. 2.14</div>

In both cases, these hypotheses underestimate the curvature (Baby et al., 2012) for two main reasons: (i) not considering shear deflection; and (ii) considering a linear displacement to curvature transformation, even when UHPFRC is in a non-linear stage. In (Baby et al., 2013), an iterative displacement to curvature transformation based on the double integration of the curvature over the prism specimen length is proposed. In a second step, a similar point-by-point process to (Baby et al., 2012) and (Rigaud et al., 2011) is used.

2.6.1.4 Point-by-point method

The point-by-point method has been used by several authors and it is proposed in the French standard as the method that derives UHPFRC tensile properties from either a

load-strain or load-curvature experimental law. As far as it is known, the first point-by-point inverse analysis was proposed by Chanvillard in (Chanvillard, 2000) as a method to determine the stress-crack opening relationship from an unnotched four-point bending test.

Inspired by this method, (Baby et al., 2012) proposed a point-by-point inverse analysis method to derive the stress-strain response. The stress-strain curve is based on the equilibrium of moment and forces in a sectional analysis for each value of either average strain at the most tension face or the average curvature at mid-span and the corresponding bending moment. The major advantage of the point-by-point method is that the tensile stress-strain relationship does not need to be defined. This model assumes two major hypotheses: (i) strain-plane remains plane throughout the loading process within gauge length; and (ii) linear elastic behaviour exists in compression. This model was developed for a rectangular cross-section of width b and depth h. In that model, ε_t is the strain at the most tensioned fibre and σ_t is its associated stress. Compressive stress and strain were considered negative, and tensile stress and strain positive.

Two different loading steps are considered: loading step i and loading step $i + 1$. Between these two loading steps, the strain at the extreme tension fibre increases from $\varepsilon_{t,i}$ to $\varepsilon_{t,i+1}$, and the corresponding stress changes from $\sigma_{t,i}$ to $\sigma_{t,i+1}$. There are two different curvatures ϕ_i and ϕ_{i+1} for these two loading steps. The following formulation corresponds to the load-curvature method. However, its adaptation to the load-strain method is simple. More detailed information can be found in (Baby et al., 2012).

This method requires a starting point. The parameters to define a starting point can be determined from the linear elastic branch of the experimental load-curvature (or strain) curve. By applying the linear elastic theory to the strain at the most tension face, its corresponding stress and curvature can be easily determined. After defining a first step, step i is always defined and only step $i + 1$ remains undetermined. This step can be determined following Eq. 2.15 to Eq. 2.20, in which N_c and N_t are the axial force in the zone under compression and tension, respectively, and M_c and M_t are the bending force in the zone under compression and tension, respectively.

$$N_{c,i+1} = -bE\phi_{i+1}\left(\frac{\varepsilon_{t,i+1}}{\phi_{i+1}h} - 1\right)^2 \frac{h^2}{2}$$

Eq. 2.15

$$M_{c,i+1} = -bE\phi_{i+1}\left(2 + \left(\frac{\varepsilon_{t,i+1}}{\phi_{i+1}h}\right)^3 - 3\frac{\varepsilon_{t,i+1}}{\phi_{i+1}h}\right)\frac{h^3}{6}$$

Eq. 2.16

$$N_{t,i+1} = \frac{\phi_i}{\phi_{i+1}} N_{t,i} + b \frac{1}{\phi_{i+1}} \frac{\sigma_{t,i+1} + \sigma_{t,i}}{2} \left(\varepsilon_{t,i+1} - \varepsilon_{t,i} \right)$$

<div align="right">Eq. 2.17</div>

$$M_{t,i+1} = \frac{\varepsilon_{t,i+1}}{\phi_{i+1}} N_{t,i+1} + \frac{\phi_i^2}{\phi_{i+1}^2} \left(M_{t,i} - \frac{\varepsilon_{t,i}}{\phi_i} N_{t,i} \right) - b \frac{\sigma_{t,i+1}\varepsilon_{t,i+1} + \sigma_{t,i}\varepsilon_{t,i}}{2\phi_{i+1}^2} \left(\varepsilon_{t,i+1} - \varepsilon_{t,i} \right)$$

<div align="right">Eq. 2.18</div>

$$N_{t,i+1} + N_{c,i+1} = 0$$

<div align="right">Eq. 2.19</div>

$$M_{t,i+1} + M_{c,i+1} = M_{i+1,experimental}$$

<div align="right">Eq. 2.20</div>

Figure 2.30 shows a typical curve obtained after a point-by-point inverse analysis applied to the experimental results from a third-point bending test on UHPFRC with an average compressive strength of 160 MPa and 2% of 13/0.2 mm steel fibres (López et al., 2015). It should be noted that this curve is very difficult to work with. According to the tensile behaviour proposed for UHPFRC in 2.3.3, a quadrilinear assumption in tension could accurately reproduce UHPFRC tensile behaviour. This is why a quadrilinear tensile law was fitted to the inverse analysis results by keeping the same area under the curve (see Figure 2.30) and minimising the error between the two curves.
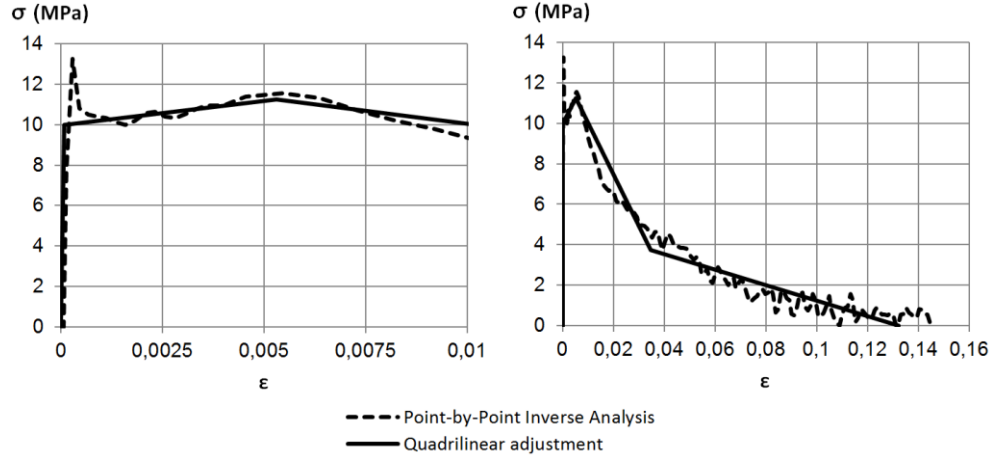
Figure 2.30 The point-by-point inverse analysis obtained from an unnotched four-point bending test and its qudrilinear fitting for a 50-mm gauge length (López et al., 2015)

It is worth noting that certain instability may be found while following this method, especially when the experimental load-curvature has ups and downs. In this case, suitable filters to obtain a smooth load-curvature curve are needed before applying the point-by-point inverse analysis method.

2.6.2. Methods based on key points: simplified methods

Simplified methods take only a few specific points from the results obtained during the FPBT. These points are usually: (i) flexural strength and (ii) loss of linearity point. These are the methods proposed in the French and the Swiss standards, and the method proposed by Kanakubo (Kanakubo, 2006). Despite these methods being easy to implement, they offer some uncertainty as to their accuracy and objectivity. Their most relevant advantages and disadvantages are reviewed below. It is important to remark that existing simplified methods aim to only determine the hardening stress-strain behaviour of UHPFRC, and they mention nothing about the post-cracking behaviour of UHPFRC.

2.6.2.1 Simplified method by Kanakubo

In order to derive the tensile hardening properties of UHPFRC from unnotched four-point bending tests, Kanakubo (Kanakubo, 2006) proposed a simplified method, probably inspired by either the RILEM or MC2010 method for fibre-reinforced concrete, to be applied to unnothced four-point bending tests. The test setup is shown in Figure 2.31.
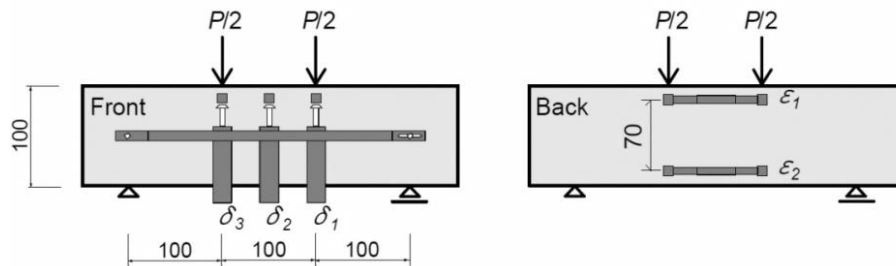
Figure 2.31 The unnotched four-point bending test setup proposed by Kanakubo (Kanakubo, 2006)

As in those methods, Kanakubo proposed a certain stress distribution along the specimen depth at two stages. Unlike those methods, these two stages were not defined for a certain crack opening or displacement at mid-span. The two proposed stages were (i) first crack and (ii) flexural strength. Using these two key points, Kanakubo proposed two different models (see Figure 2.32).

In case 1, first cracking strength and maximum tensile strength are determined from the bending moment at the first crack and at the maximum bearing capacity, respectively.

In this case, the stress and strain at cracking, as well as the maximum tensile stress and its corresponding tensile strength, can be derived following Eq. 2.21 to Eq. 2.24. All the parameters in these equations are referred to in Figure 2.32. Both crack depth and ultimate tensile strength are derived after solving Eq. 2.23 and Eq. 2.24.
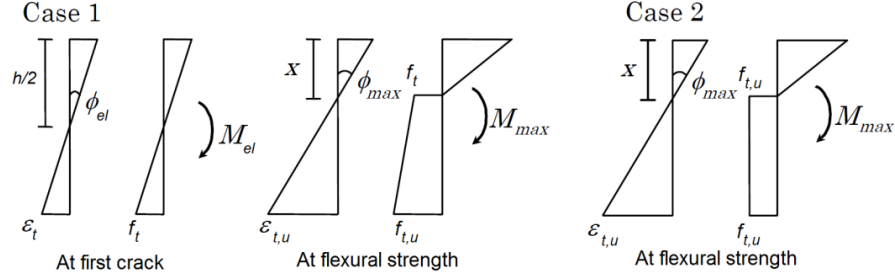
Figure 2.32 The stress distributions for the two inverse analysis models proposed by Kanakubo (Kanakubo, 2006)

$$\varepsilon_t = \frac{h\phi_{el}}{2}$$

Eq. 2.21

$$f_t = \frac{6M_{el}}{bh^2}$$

Eq. 2.22

$$\sum N = 0 \ \Rightarrow \frac{Eb\phi_{max}}{2}x^2 = \frac{b}{2}(f_t + f_{t,u})(h - x)$$

Eq. 2.23

$$M_{max} = \frac{Eb\phi_{max}}{3}x^3 + \frac{b}{6}(f_t + 2f_{t,u})(h - x)^2$$

Eq. 2.24

$$\varepsilon_{t,u} = \phi_{max}(h - x)$$

Eq. 2.25

In case 2, stress distribution is supposed to be uniform on the tensile side, and only tensile strength is calculated from the moment at flexural strength. In this case, the ultimate tensile strength can be determined by solving Eq. 2.26 and Eq. 2.27. Its corresponding strain can be derived from Eq. 2.25.

$$\sum N = 0 \quad \Rightarrow \frac{Eb\phi_{max}}{2} x^2 = b\, f_{t,u}(h - x)$$

<div align="right">Eq. 2.26</div>

$$M_{max} = \frac{Eb\phi_{max}}{3} x^3 + \frac{f_{t,u}b}{2} (h - x)^2$$

<div align="right">Eq. 2.27</div>

Kanakubo assumes a linear elastic distribution in compression. As the equation system he proposed is undetermined, one value has to be previously known or established. This is why Kanakubo proposed measuring the average curvature by two LVDTs, as pointed out in Figure 2.31.

This simple inverse analysis method requires a more complex test setup. Both displacement at mid-span and also the LVDTs that allow the average curvature to be determined must be recorded. Two major problems arise when applying this method: (i) the cracking point is very difficult to determine objectively if no further definition of it is provided; (ii) as it is well-known, the hardening phase ends before flexural strength is achieved. Therefore, this method overestimates both the maximum tensile strength and its corresponding strain.

2.6.2.2 Simplified method in the French standard

The French standard proposes two different setups to characterise UHPFRC tensile behaviour, which are described in its Appendices D and E: (i) a flexural test on prismatic specimens if the characteristic value of $f_{t,u}$ is lower than the characteristic value of f_t (Appendix D); (ii) a flexural unnotched four-point bending test done on thin slabs if the characteristic value of $f_{t,u}$ is higher than the characteristic value of f_t (Appendix E) (see Figure 2.33).

The test setup (i) requires two tests: (1) an unnotched third-point bending test to determine elastic tensile strength; and (2) a notched three-point bending test to determine the stress-crack opening relationship. No mention is made of how to determine the strain-hardening behaviour as it is considered that this UHPFRC type has to be modelled as conventional fibre-reinforced concrete. Furthermore, the methodology pointed out in the French standard to characterise the stress-crack opening relationship in test setup (i) is the point-by-point inverse analysis, which requires using a computer and an iterative process. It may not be the best choice for a standard procedure.

The test setup (ii) requires only one test in which the measurement taken may be either displacement at mid-span or the strain at the most tensioned face. From these results, three different types of inverse analysis are proposed: (1) a simplified inverse analysis; (2) a point-by-point load-curvature inverse analysis with linear elastic deflection to curvature transformation; (3) a point-by-point load-strain inverse analysis. Only stress-

strain hardening behaviour is derived from these methods. No mention is made of how the stress-crack opening relationship is obtained from these tests. A subsequent analysis focuses on the way cracking strength (f_t), the elastic modulus (E), the maximum tensile strength ($f_{t,u}$) and its corresponding strain ($\varepsilon_{t,u}$) are obtained in the simplified analysis.
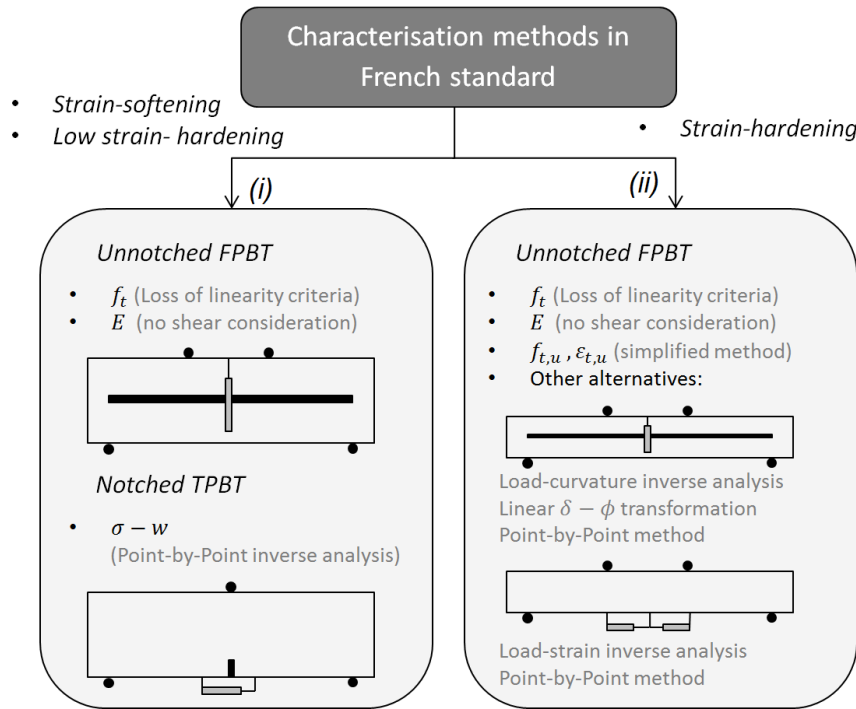
Figure 2.33 The characterisation test and inverse analysis method proposed in the French standard

Both Appendices D and E provide a simplified method to determine tensile strength (f_t). Although some little differences may be found between these methods, both are based on the visual determination loss of linearity point. However, the determination of this point is not as clear as it may seem in a deflection-hardening material like UHPFRC. The strain-hardening behaviour of UHPFRC makes that the loss of stiffness in the load-deflection curve is too small to be easily identified. Figure 2.34 shows a typical UHPFRC response in an unnotched four-point bending test. As we can see, no sudden drops are detected in the experimental measurements.

If someone were asked to select the loss of linearity point in Figure 2.34, one could hesitate and select different points depending on the scale and weight of the lines chosen to plot the curve. Figure 2.34 shows the same experimental curve on two

different scales. A circular hollow point (see Figure 2.34, left) and a square hollow point (see Figure 2.34, right) were used to point out the stress level, where the authors considered loss of the linearity point localised on each curve. This point was different for each curve, therefore this method seems inappropriate if a more clear and objective definition is not provided.
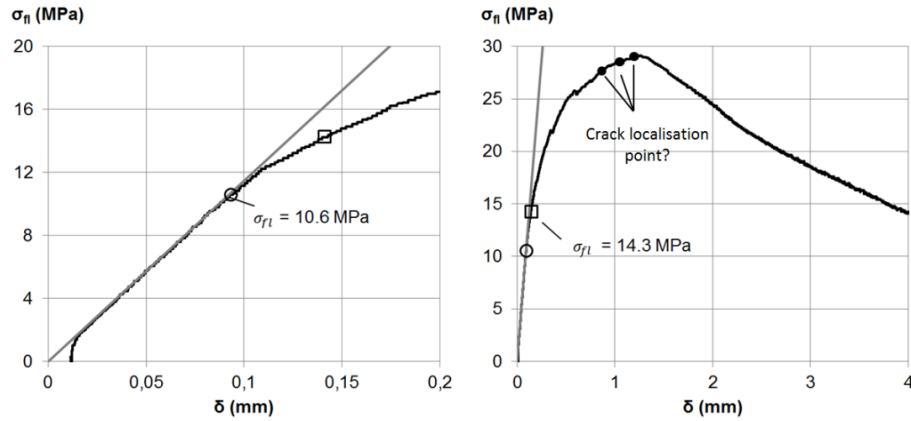
Figure 2.34 Determination of tensile strength according to the scale and crack localisation point estimation

Having selected loss of linearity point, a scale-effect coefficient is proposed in Appendix D, which is not mentioned in Appendix E. This coefficient takes the same shape as the scale-effect coefficient proposed in MC1990 and kept in MC2010 for plain concrete (see Eq. 2.28). This coefficient originally linked flexural strength ($f_{ct,fl}$) with tensile strength (f_t). However, the French standard establishes a relationship between loss of linearity point and elastic tensile strength. While MC1990 and MC2010 proposed an α coefficient of 0.06, the research in (Chanvillard et al., 2003) proposed a value of 0.08 for UHPFRC. In that research, a higher value for this parameter was justified by assuming the more brittle nature of UHPFRC compared to standard concretes. Of course, this assertion can be questioned and may be considered barely precise. Based on previous work, the French standard assumed a value of 0.08 for UHPFRC. Whether this coefficient fitted the results obtained in (Chanvillard et al., 2003) is not questioned, but even if this coefficient could be accurate, it could not be strictly called a scale-effect coefficient in any case as the difference between the apparent loss of linearity point and tensile strength is not due to a macrocrack localisation, but to the plastic branch. This is why the whole procedure should be reviewed.

$$f_t = f_{ct,fl} \frac{\alpha \, h^{0.7}}{1 + \alpha \, h^{0.7}}$$

Eq. 2.28

A simplified method to determine the elastic modulus is also described, but the formulation proposed does not take into account shear influence, which is noticeable if the L/h ratio is low (Graybeal, 2006).

A simplified method to obtain stress and strain at the end of the hardening phase can be found in Appendix E by assuming an elasto-plastic tensile law. This procedure is similar to that proposed by Kanakubo in *Case 2* (see 2.6.2.1) as the tensile properties are derived from one single point, flexural strength. Unlike the method proposed by Kanakubo, the simplified method proposed in the French standard obtains the curvature at the maximum load using an equation that derives from the linear elastic theory (see Eq. 2.13). Once this curvature value has been obtained, parameter x can be solved from Eq. 2.29. Then it is easy to obtain $f_{t,u}$ and $\varepsilon_{t,u}$ by applying Eq. 2.30 and Eq. 2.31.

$$M_{max} = (2x^3 - 3x^2 + 1)\frac{bh^3\phi E}{12}$$

<div align="right">Eq. 2.29</div>

$$f_{t,u} = \frac{1}{2}(1-x)^2 h\phi E$$

<div align="right">Eq. 2.30</div>

$$\varepsilon_{t,u} = \frac{f_{t,u}}{E} + \phi xh$$

<div align="right">Eq. 2.31</div>

This method has three main problems: (i) the key point used is flexural strength, whose deflection and load are higher than the point that correspond to the crack localisation point (Figure 2.34, right). Even though the difference is in load terms small, it can be high in deflection terms, which can lead to overestimate strain at the end of the hardening phase. A linear relationship is also proposed to obtain the average curvature in the constant bending moment area at the maximum load. This assumption is inaccurate and the method should be reviewed.

2.6.2.3 Simplified method in the Swiss standard

The Swiss standard proposes two methods to determine UHPFRC tensile properties: (i) an uniaxial tensile test; and (ii) a four-point bending test performed on thin slabs with a 420-mm span, 30-mm thick and 100-mm width. A simplified inverse analysis procedure is proposed in the method (ii). It is based on selecting two key points (A and B). Point A indicates the end of the elastic phase, while point B corresponds to flexural strength.

Unlike in the French Standard, determination of the end of the elastic phase is not based on a visual criterion. The following definition is found: the end of the elastic phase takes place when a loss of stiffness of 1% is produced with respect to the initial one. The main problem of this criterion is due to the fact that a little deviation in the estimation of the elastic modulus can induce an important error in the estimation of the first cracking strength. That is why this standard suggests making three loading-unloading cycles to achieve a better definition of this part of the curve. This fact complicates a little bit the test procedure. Another property that can be determined in this part of the curve is the elastic modulus. The equation used to determine it is based on the linear elastic theory and does not take into account the shear forces. However, as the L/h ratio is 14, this hypothesis appears to be reasonable.

Like in the French standard, the point at maximum load is used to determine the end of the hardening phase. Following a similar procedure to that used in Model Code 2010, a simplified stress distribution is assumed at the maximum load. Unlike Kanakubo and the French standard method, this hypothesis includes the assumption that the neutral axis is located at a distance of 0.82 times the specimen height from the most tensioned fibre (see Figure 2.35, left). This assumption leads to a coefficient of 0.383, which is applied to the equivalent flexural strength (σ_{max}) to obtain parameter $f_{t,u}$.
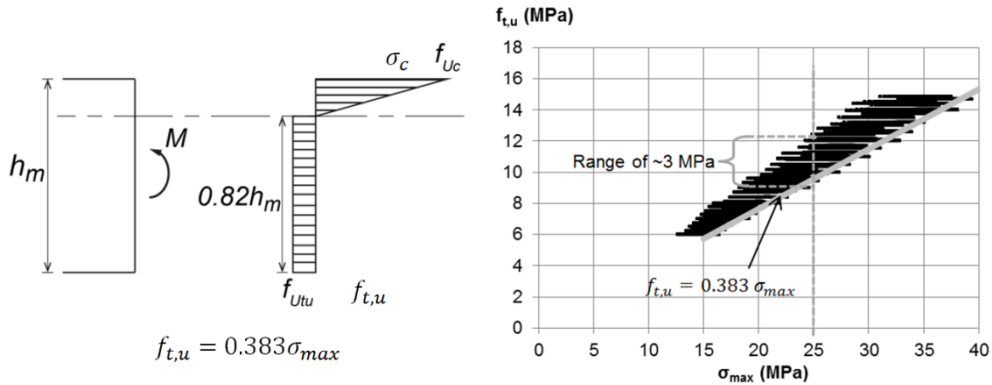
Figure 2.35 Stress distribution assumption at the maximum load in the fprSIA 2052:2014-12 (left); analytical relationship between $f_{t,u}$ and flexural strength (σ_{max}) for different UHPFRC tensile constitutive laws (right)

In order to check that hypothesis, an analytical simulation of more one million different UHPFRCs obtained by varying its sectional stress-strain response was made in (López et al., 2016b). This simulation follows the non-linear hinge model developed in Chapter 3. Figure 2.35 (right) shows the obtained results in which the relationship between the maximum flexural strength (σ_{max}) and the maximum tensile strength ($f_{t,u}$) is depicted. The black points represent the results of all the simulated concretes, while the grey line represents the Swiss standard proposal.

Some conclusions can be drawn from these results. The method proposed in the Swiss standard is safe and represents a lower maximum tensile strength value.This equation is valid for today's commonest UHPFRCs (behaviour comes close to elasto-plastic behaviour in tension) tested in thin specimens. However, if a more precise general method capable of being extended to other strain-hardening materials is required, this method should be improved. If this method were extended to other concretes or specimen sizes, variability would become a problem. A common flexural strength value for a UHPFRC that contains 2% in volume of steel fibres is around 25 MPa. As seen in Figure 2.35, right, the ultimate tensile strength of the UHFPRCs with a flexural strength of 25 MPa can vary between 9 MPa and 12 MPa, depending on specimen size, hardening ratio and fracture energy. This may be considered wide variability if parameter $f_{t,u}$ is to be used for material characterisation purposes.

Figure 2.35 also proves that there is no simple linear equation that relates the maximum tensile strength with flexural strength; i.e., the neutral axis is not constant and depends on specimen depth, the fibre distribution along the failure section, and the type and amount of fibres. It is important to note the similarity with the drop constant model proposed by MC2010 for fibre-reinforced concrete. In this case, the neutral axis is assumed to be the whole depth and the resulting coefficient is 1/3. In other words, MC2010 assumes elastic perfectly plastic behaviour in tension. However, the Swiss standard realises that the strain at the maximum tensile strength must be limited to gain accuracy, proposing a coefficient of 0.383.

If parameter $f_{t,u}$ happens to be higher than f_t, a simple procedure based on the French standard is proposed to determine $\varepsilon_{t,u}$. The Swiss standard proposes a kind of an iterative process that is not difficult to conduct until ultimate tensile strength is exceeded. The methodology to obtain the maximum tensile strength and its corresponding strain corresponds to different key points. While $f_{t,u}$ is determined using the maximum strength, the determination of $\varepsilon_{t,u}$ is not prefixed and has to be obtained in an iterative process. Using this method implies determining the average curvature from displacement at mid-span. As in the French standard, a linear transformation is used, which offers an inaccurate average curvature value when load is higher than 70% of the maximum load (López et al., 2014) approximately. As in the other simplified methods, no information is provided about how to obtain post-cracking UHPFRC behaviour.

2.6.3. Summary

The most standard and easiest to perform unnotched four-point bending tests are those in which only load-displacement at mid-span is recorded as either the direct measurement of the curvature or even the measurement of the strain at the most tension fibre makes the test method more sophisticated. Then if the simplicity of the test setup is an initial condition, the unnotched four-point bending test that includes the measurement of displacement at mid-span seems the best choice.

From all the inverse analyses presented, simplified methodologies seem the best choice for their implementation by engineers and laboratories. However, the hypotheses on which current existing methods are based are not accurate and lack an objective selection of key points.

What would be desirable is to have a methodology that allows the accurate determination of all the parameters which define both the bilinear stress-strain and stress-crack opening relationships that characterise UHPFRC tensile behaviour from a single test (the unnotched four-point bending test) using a simple back-of-the-envelope calculation applied to certain values of the load-deflection curve, which must be objectively selected. Its development becomes an important issue for the international research community. As this method does not currently exist, its development could foster the use of UHPFRC, a better understanding of its mechanical performance and could enhance design methodologies.

How can a methodology like that be developed? One of the possible ways of achieving this is to use a load-curvature inverse analysis method that indirectly determines the experimental curvature. As existing displacement to curvature transformations are not accurate enough and cannot be used on the unloading branch, the first step is to improve this transformation. It is also important to remark that a closed-form bending moment versus curvature solution ($M - \phi$) is available for a trilinear stress-strain relationship in tension (see 2.6.1.1). Therefore, a closed form by assuming quadrilinear behaviour can be obtained. This closed form solution allows a parametric study of all the parameters that define the sectional stress-strain response of UHPFRC. From this parametric study, it would not be foolish to think that a relationship between certain key points of the load-curvature curve and tensile parameters can be found out.

The inverse methods developed to date for unnotched four-point bending tests are not able to obtain the stress-crack opening behaviour of UHPFRC. This is why it is absolutely necessary to take a look at existing analytical fracture models in bending. The most suitable one for this task is probably the non-linear hinge model because it has already been successfully used for inverse analyses (see 2.6.1.1). A brief review of these models is offered in 2.7.

2.7. Analytical fracture models in Bending: the non-linear hinge model

Traditionally, modelling the bending behaviour of concrete has been a very important issue, especially for the fracture mechanics community, as fracture mechanics models were the first to be able to reproduce the scale effect that concrete shows in bending. The most famous fracture mechanics models are the *Fictitious Crack Model,* first proposed by Hillerborg (Hillerborg et al., 1976), and the *Crack Band Model,* first proposed by Bazant (Bazant, 1976). These two models offer a simply description of crack formation in plain concrete. They were conceived to be used together with a

FEM tool. However, these approaches can be easily adopted in other simpler analytical models. The most extended fracture mechanics model that enables the analytical description of the bending behaviour of concrete, including conventional reinforced concrete, is probably the non-linear hinge model.

The non-linear hinge model can be considered a special case of the crack band model in 1D. While finite element width is related to the maximum aggregate size in the crack band model, the so-called non-linear hinge length (s) is related to specimen depth in the non-linear hinge model. The non-linear hinge model requires the average strain plane to remain plane on the boundaries of the hinge. This allows the analysis of the crack section as a Navier-Bernoulli section, whose behaviour is characterised by a moment-rotation relationship. Additional hypotheses are needed to transform the strain beyond crack opening initiation into crack opening. More relevant non-linear hinge models are described in (RILEM TC 162-TDF, 2002)

The biggest advantage of these non-linear hinge models is that they enable an analytical solution of the load-deflection response of either plain concrete or fibre-reinforced concrete. Having obtained an analytical solution, its parameterisation is possible and the influence of the parameters that define the tensile response of fibre-reinforced concrete on the load-deflection curve can be studied.

A brief review of the existing fracture models can be found in the subsequent sections.

2.7.1. Discontinuous models: Fictitious Crack Model

As described in 2.3.1, the *Fictitious Crack Model* assumes that when a crack appears, it is not a 'real' crack; i.e. it is not a stress-free crack, but a 'fictitious' crack capable of transfering stress between crack planes according to its opening up to a certain value from which the crack becomes a stress-free crack that is unable to transmit any stress.

In this model the crack is modelled by a single crack plane. This discontinuous crack consideration can be modelled easily in FEM formulations using the so-called interface elements, where σ-w information is included. This model also assumes that a crack initiates when cracking strength (f_t) is reached at any point of the element.

When a crack develops in plain concrete, the fracture process zone, i.e. the area in which the material undergoes strain-softening, is large compared to the area under strain-hardening, while concrete undergoes linear unloading in the surroundings of the fracture process zone. The linear, non-linear and fracture process zones of plain concrete are shown in Figure 2.36. For conventional fibre-reinforced concrete, the fracture process is similar as concrete does not undergo significant non-linear hardening behaviour. However, it may be different in UHPFRC as a significant area that surrounds the crack can undergo strain-hardening and some additional hypotheses should be adopted.
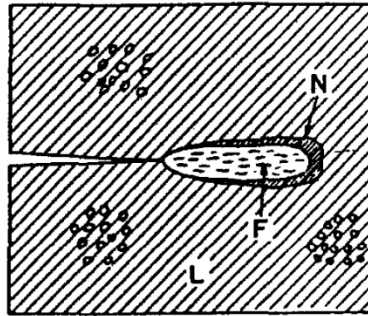
Figure 2.36 The linear zone (L), non-linear zone (N) and fracture process (S) zones in a plain concrete fracture (Bazant, 1989)

The fracture process zone that was previously defined as the area under strain-softening was called the fictitious crack. The stress distribution on the crack plane according to this opening is shown in Figure 2.37. Note that stress distribution according to the crack opening is similar to that proposed for FRC and UHPFRC.
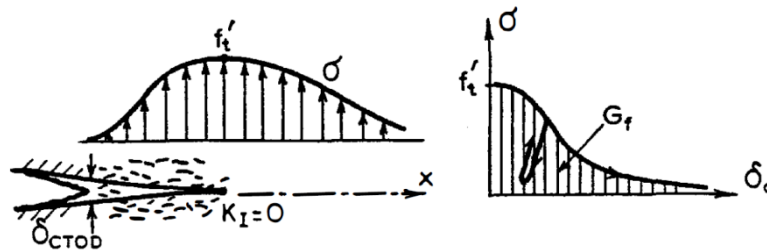
Figure 2.37 Stress distribution according to the crack opening in the crack plane proposed by Hillerborg et al (Bazant, 1989).

This model was first used in 1976 by Hillerborg et al. to obtain the moment-crack depth curve. As far as it is known, it was the first time someone noticed that the maximum bending moment was reached in a situation in which a significant area along specimen depth underwent strain-softening. Obviously this maximum bending moment was greater than the cracking bending moment. This model was repeated for different beam depths, and offered a simple easy-to-understand explanation of the size effect in bending, due to the post-cracking behaviour of plain concrete. These results can be easily extrapolated to fibre-reinforced concrete.

2.7.2. Continuous models: the Crack Band Model

As described in (Bazant, 1989), the basic idea of the crack band model proposed by Bazant (Bazant, 1976) was to offer an alternative to characterise the material behaviour in the fracture process zone in a smeared (or continuous) manner through a strain-

softening constitutive relation. Unlike the FCM, the crack band model requires an additional parameter: the crack band width on which the strain is smeared in order to assure the same energy dissipation. As pointed out by Bazant, crack band width is assumed to be approximately between once and 6 times the maximum aggregate size.

The imposition of a constant crack band width is required to avoid mesh sensitivity, and to assure that energy dissipation due to fracture per unit of length is constant and equals fracture energy. In order to achieve this, the stress-crack opening relationship has to be converted into a stress-strain relationship, with the strain smeared on crack band width. The model proposed by Bazant is shown in Figure 2.38, where the crack band width on which the strain is smeared is shown. When crack band width approaches zero, the crack band becomes identical to the fictitious crack model.
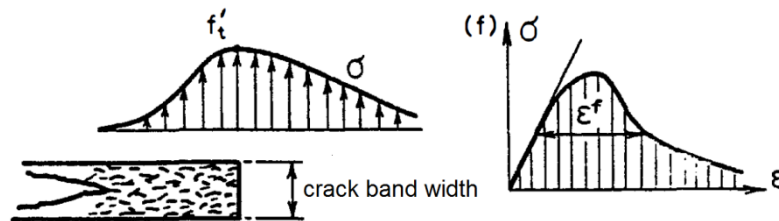
Figure 2.38 Stress-distribution according to the crack opening in the crack band proposed by Bazant (Bazant, 1989).

2.7.3. The non-linear hinge model

With the development and better understanding of mechanical of fibre-reinforced concrete behaviour, it was noted that the tensile force transfer over the crack became more relevant in the concrete response. This fact, together with the need to not only model the bending behaviour of these concrete types to explain the size effect, but to also derive easy methodologies to determine residual tensile strength, led to several analytical non-linear hinge models being developed in the 1990s.

If an analytical fracture mechanics bending model is to be developed, a non-linear hinge model is probably the best choice. As previously mentioned, a non-linear hinge model can be considered a particular 1D case of the crack band model. It consists of a 1D continuous crack model in which certain kinematic assumptions are made within a certain length surrounding the crack. These assumptions mean that within hinge length, fracture behaviour can be reduced to a single cross-section regardless of the real state of the stress that surrounds the crack plane. The original idea of the non-linear hinge model is to separately analyse the section of the structural element where the crack is formed and to assume that the rest of the structure behaves in a linear elastic stage. The non-linear hinge must connect to the rest of the structure. So the boundaries of the non-linear hinge have to remain plane and loaded with generalised stresses.

Several non-linear hinge models can be found in the literature, which are differentiated by their kinematic assumptions and their crack hinge lengths. As they were initially developed for FRCs, they all assume that deformation is localised in a single crack, while the rest of the beam behaves in a linear-elastic stage, which agrees with softening behaviour.

This is not the case with UHPFRC, which is characterised by strain-hardening behaviour. In this case deformation localisation takes place after a non-linear microcracking phase has been undertaken, which extends beyond hinge length. This was pointed out by Spasojevic (Spasojevic, 2008), who showed the real state of stress of the area that surrounds the crack in a bending test. One of her results is shown in Figure 2.39, in which the stress regime for three different stages up to maximum load are shown. Unlike what is expected for plain concrete and fibre-reinforced concrete, in which concrete remains in a linear elastic stage outside the fracture process zone, in UHPFRC a non-linear strain-hardening region appears which must be taken into account when modelling it (black shaded area).
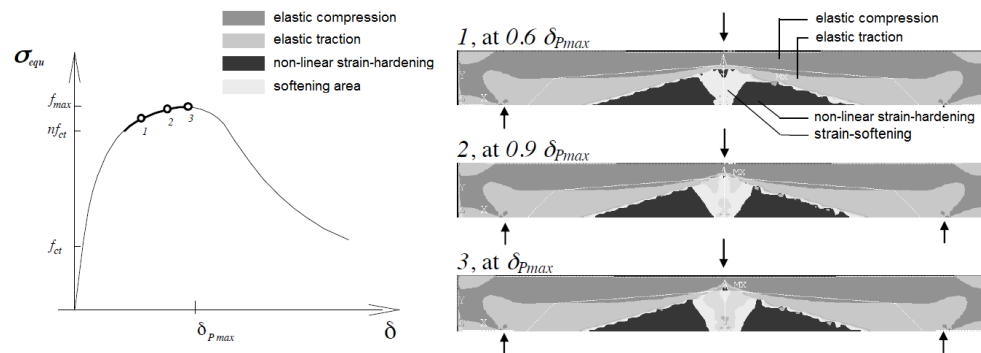
Figure 2.39 Analytical stress regimes in a beam in bending, with plastic yielding in tension up to 2‰ (Spasojevic, 2008).

According to (RILEM TC 162-TDF, 2002), there are three main non-linear hinge models that describe the bending behaviour of FRCs: (i) the simplified approach by Pedersen (Pedersen, 1996); (ii) the simplified approach by Casanova and Rossi (Casanova et al., 1996); and (iii) the explicit formulation by Stang and Olesen (Olesen, 2001)(Stang et al., 1998). The other non-linear hinge models found in the literature include those proposed by Maalej and Li (Maalej et al., 1994) and Ulfkjaer (Ulfkjaer et al., 1995). All these models were developed for the FRCs of that time: i.e., FRCs with a remaining stress after cracking in direct tension that was roughly less than half the tensile strength of the matrix (Casanova et al., 1996). The only available non-linear hinge model that considers strain-hardening behaviour is that proposed by Ostergaard et al. (Ostergaard et al., 2005), which is a generalisation of the model proposed by

Olesen et al. (Olesen, 2001). Specific details of these non-linear hinge models are presented below, and are based on the (RILEM TC 162-TDF, 2002) summary.

2.7.3.1 Pedersen

The model proposed by Pedersen (Pedersen, 1996) assumed that the fictitious crack surfaces remains plane and that the crack opening angle (φ^*) equates the overall angular deformation of the non-linear hinge (φ) (see Figure 2.40). In this approach, the crack opening at the bottom of the non-linear hinge can be directly determined from the crack opening angle (or the overall angular deformation of the non-linear hinge) and crack length (a), following Eq. 2.32.

$$w_{cmod} = \varphi a = \varphi^* a$$

Eq. 2.32
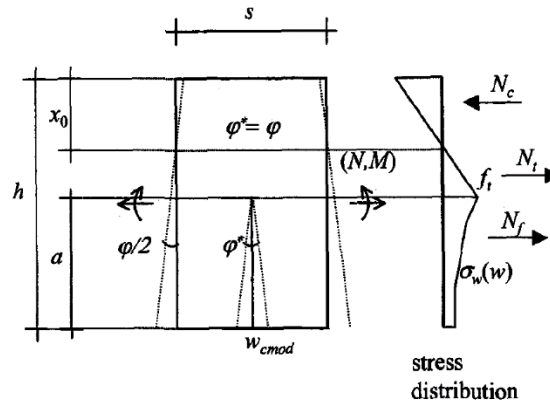
Figure 2.40 The non-linear hinge model proposed by Pedersen (RILEM TC 162-TDF, 2002)

According to that model, any stress-crack opening relationship can be used. From a certain angular overall angular deformation of the non-linear hinge (φ) (or average curvature (ϕ)) and for a given crack depth, the crack opening profile along it is defined, and the stress distribution is then determined using the stress-crack opening relationship. The relationship between the average curvature and overall angular deformation is given in Eq. 2.33 according to non-linear hinge length (s).

$$\phi = \frac{\varphi}{s}$$

Eq. 2.33

This model assumes that a single crack is formed within the non-linear hinge once cracking strength is reached at the crack tip. It also assumed a linear elastic behaviour

in compression and a rectangular cross-section. Figure 2.40 illustrates the assumed distribution of stresses.

By means of this stress distribution, Pedersen proposed an equilibrium of axial and bending forces to derive a non-linear equation that describes the non-linear bending moment-overall angular deformation of the non-linear hinge model for each axial force value. A simple numerical iteration technique was required to solve the non-linear hinge model.

2.7.3.2 Casanova & Rossi

Casanova and Rossi (Casanova et al., 1996; Casanova et al., 1997) proposed another non-linear hinge model by applying the same hypothesis used in Pedersen's model for the relationship between overall angular deformation and the crack opening angle. The overall curvature of the non-linear hinge is expressed according to the curvature of the cracked part and the curvature of the elastic part, and by assuming a parabolic variation of the curvature between the crack hinge boundaries (which remain in a linear elastic stage) and the curvature of the cracked part. The elastic curvature at the boundaries of the non-linear hinge can be derived following Eq. 2.34. The curvature of the cracked part can be obtained following Eq. 235 based on Figure 2.40, where term ε_c corresponds to the strain on the top face in compression. This model also assumes that non-linear hinge length (s) is twice crack depth (x). All these assumptions lead to Eq. 2.36, which defines the kinematic behaviour of the non-linear hinge.

$$\phi_{el} = \frac{M}{EI}$$

Eq. 2.34

$$\phi_{cr} = \frac{\varepsilon_c}{x_o}$$

Eq. 235

$$\phi = (2\phi_{el} + \phi_{cr})\frac{2x^2}{3}$$

Eq. 2.36

In this model, the non-linear equilibrium equation proposed by Pedersen can be used to derive the non-linear behaviour of the non-linear hinge. However, precautions must be taken to change the curvature in Eq. 2.33 for the average curvature value proposed in Eq. 2.36.

It is worth noting that this model was proposed in the French standard as the standard method to determine the stress-crack opening relationship from a notched three-point bending test. It is important to remember that this method was developed for strain

softening materials in which the beam remains in a linear elastic stage beyond the hinge boundaries. However, it can be established from Figure 2.39 that beyond the hinge, UHPFRC does not remain in a linear elastic stage, but in a plastic one. This phenomenon is qualitatively represented in Figure 2.41. We can see that the real curvature state in UHPFRC is greater than predicted by the linear-elastic theory since UHPFRC undergoes strain-hardening beyond the crack area. This results in underestimating the average curvature on the non-linear hinge if the Casanova and Rossi model is used. This is why the method proposed in the French standard should be reviewed and the influence of this hypothesis should be quantified.
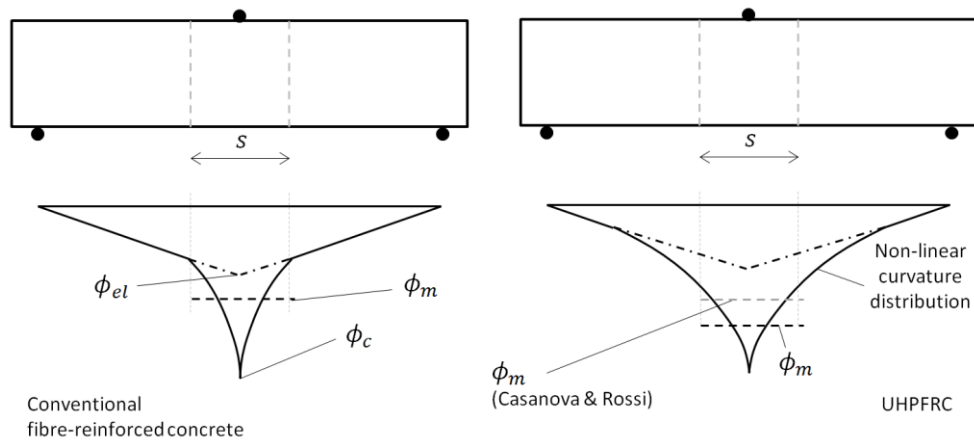
Figure 2.41 Curvature distributions in a notched three-point bending test for fibre-reinforced concrete (left) and UHPFRC (right), the and qualitative average curvature determination according to the Casanova and Rossi model

2.7.3.3 Stang & Olesen

A huge step forward in analysing the bending behaviour of fibre-reinforced concrete was taken by Stang and Olesen (Olesen, 2001). They proposed a closed-form solution for the non-linear hinge response when a multilinear stress-crack opening relationship was assumed. Unlike the Pedersen and Casanova-Rossi models, this model assumes that crack surfaces do not remain plane and that deformation is governed by the stress-crack opening, crack depth and overall angular deformation (or average curvature) (see Figure 2.42). These assumptions impose the condition that the non-linear hinge boundaries remain plane after deformation.

According to Figure 2.42, the non-linear hinge is modelled as incremental layers of springs that act without transferring shear between each other. The hinge boundaries are assumed to remain plane during the whole deformation process. In Figure 2.42, the longitudinal elongation of springs is denoted $u(x)$. where x is the vertical coordinate. The average curvature of the non-linear hinge is ϕ. In this model, the elongation u of a

layer can be expressed following Eq. 2.37, in which σ_w is the stress at a certain crack opening. Note that this equation is the same as Eq. 2.2 if the entire equation is divided by gauge length which, in this case, is the non-linear hinge length (s)

$$u = \frac{\sigma_w}{E} s + w$$

<div align="right">Eq. 2.37</div>

Figure 2.42 Stang and Olesen's non-linear hinge model

Using this hypothesis and the equilibrium of generalised forces on the non-linear hinge boundaries, Stang and Olesen proposed a closed form solution with zero axial force and a bi-linear stress-crack opening relationship (Stang et al., 1998). Note that this model allows the parameterisation of the bending behaviour of a fibre reinforced concrete according to the bilinear stress-crack opening relationship. This was the model used to derive the load-deflection curves shown in Figure 2.6, which set the basis for the σ-w design method developed by RILEM TC 162-TDF. However, also note that this method, according to Eq. 2.37, does not take into account the strain-hardening behaviour of UHPFRC.

2.7.3.4 Ostergaard et al.

The Ostergaard model (Ostergaard et al., 2005) is a generalisation of the Stang and Olesen non-linear hinge model for strain-hardening concretes. This model considers both a bilinear strain-hardening relationship and a post-cracking bilinear stress-crack opening relationship. The same hypotheses assumed by the Stang and Olesen model are contemplated. However, a different relationship for the longitudinal elongation of springs is used by taking into account the strain-hardening response of UHPFRC. According to Ostergaard et al., the longitudinal elongation of a spring after strain at

peak that is reached can be expressed following Eq. 2.38, where E^* is the unloading modulus, which differs from E as a non-linear stress-strain is reached in UHPFRC.

$$u = \varepsilon_{t,u} s + w - \frac{f_{t,u} - \sigma_w}{E^*} \, s$$

<div align="right">Eq. 2.38</div>

Note that Eq. 2.11, which defines the crack opening (w) according to the elongation (δ) measured within gauge length (l_m), the elongation at the maximum load (δ_{cr}) and the stress variation after the maximum load ($\Delta\sigma$), is the same equation that defines the elongation of each spring layer into which the non-linear hinge is divided (Eq. 2.38).

This model is probably the most suitable non-linear hinge model that has existed to date to reproduce UHPFRC behaviour. However, it lacks a closed-form solution that offers an analytical description of: (i) the average curvature on the non-linear hinge length; (ii) the average strain and crack width on any spring layer; (iii) crack depth; (iv) the load-deflection curve in un unnotched four-point bending test, which allows the determination of these curves without requiring any numerical methods and, therefore, simplifies the methodology.

2.7.3.5 Non-linear hinge length

The non-linear hinge length is a very important parameter as it determines the post-cracking load-deflection response of the beam under bending. The idea of modelling the bending failure of concrete beams by developing a fictitious crack on an elastic layer with a length proportional to beam depth was first introduced by Ulfkjaer et al. (Ulfkjaer et al., 1995).

Hinge length that equals half the specimen depth is used in the Stang and Olesen model, and a hinge length twice the crack depth is proposed in the Casanova and Rossi model. These models are proposed for a three-point bending test. The Ostergaard model was calibrated for a four-point bending test, and a hinge length of 0.9 times the specimen depth was discovered to best fit FEM models.

(Spasojevic, 2008) discovered that the non-linear hinge length in a three-point bending test was variable according to crack length, as proposed by Casanova and Rossi. However, this relationship is not linear and seems to stabilise after reaching the maximum load. It was also discovered that this value changes with specimen depth. For a common standard specimen depth, a constant value that falls within the range of 0.4 to 0.5 times the specimen depth seems appropriate.

2.7.3.6 Summary

After a brief review of the existing non-linear hinge methods, it seems that the only one that can accurately reproduce UHPFRC behaviour is the Ostergaard model. However, a closed form solution, like that proposed by Stang and Olesen, could firstly facilitate the

process of determining how UHPFRC tensile parameters influence the load-deflection response, and then the process to establish a simple relationship between them. This is why the Stang and Olesen model, together with the Ostergaard model, are the foundations for the closed form non-linear hinge developed herein.

Furthermore, it is known that hinge length selection may influence the model response, especially after crack localisation takes place. It is also well-known that this length may be in accordance with specimen depth. Special care should be takent to select this length and a special section is dedicated to it in this work.

Chapter 3

Closed-form non-linear hinge model

3.1. Introduction

The complete description of load-displacement at mid-span behaviour of UHPFRC in a four-point bending test requires a non-linear fracture mechanics model because the discrete phenomenon of macrocrack formation plays a very important role in this behaviour. The model developed herein can be applied only to a third-point bending test (TPBT) setup, which is a specific type of four-point bending test according to the geometrical conditions in Figure 3.1.
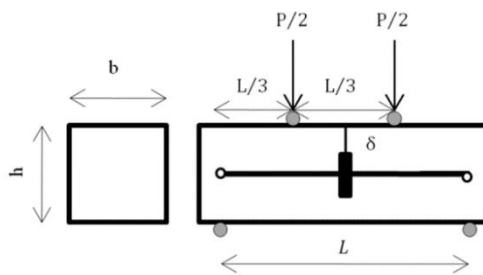
Figure 3.1 The third-point bending test (TPBT) setup

If an analytical closed-form non-linear fracture mechanics bending model is to be developed, a non-linear hinge model is probably the best choice. It consists of a continuous crack model in which certain kinematic assumptions are made along a

given length surrounding the crack (hinge length) inside which deformations are smeared.

These assumptions mean that inside hinge length, concrete behaviour can be reduced to a single cross-section regardless of the real state of the stress surrounding the crack. According to the previous review of existing non-linear hinge models, the only available model that considers strain-hardening behaviour is that proposed by Ostergaard et al. (Ostergaard et al., 2005), which is a generalisation of the model proposed by Olesen (Olesen, 2001). These two models have been used as a reference to undertake this work. The research significance of this chapter is described in **Error! Reference source not found.**. The development of the non-linear hinge model proposed herein is described in two separate sections, 3.3 and 3.4.

Section 3.3 describes the analytical non-linear hinge model that is proposed to describe the bending response of UHPFRC in a TPBT for a given constitutive relationship in tension. It has been developed for the main purpose of setting up the basis to subsequently develop the inverse analysis methodologies described in Chapters 4 and 5. A summary of the proposed non-linear hinge model is presented in Figure 3.2 and is briefly described in the lines below.

The non-linear hinge model entails having to define the *material behaviour* of UHPFRC. This model assumes linear elastic behaviour in compression, and tensile behaviour defined by two relationships: a bilinear stress-strain relationship up to the peak and a bilinear stress-crack opening one in softening. The assumed constitutive material relationship is shown in Figure 3.2 (a).

After being defined, the material behaviour must be turned into smeared stress-strain behaviour inside the non-linear hinge after crack localisation takes place, Figure 3.2 (b)(3.3.3). The complete stress-strain behaviour inside the hinge is the input that the model uses to describe the *sectional behaviour inside the hinge*. It allows the average curvature inside it to be determined (3.3.4), needed to derive the *"structural"* load-displacement law (3.3.5) obtained from that specific material's behaviour, and also for a specific hinge length. During the process, other relationships, such as average strain, the crack width on any layer, and the crack depth at any load, can be obtained.

Section 3.4 describes those issues that are not strictly needed to define the non-linear hinge model, but their study is absolutely necessary for its analytical validation and to fully comprehend the model. A short description of this section content is given below.

According to 2.7.3, the non-linear hinge model developed by Stang (Stang et al., 1998) requires the boundaries of the non-linear hinge to remain plane after deformation. Note that this model is intended to be used in TPBTs to model the central one-third area, which is indeed a D-region. A preliminary linear analysis to prove that an average strain plane can be assumed on the boundaries of this area is conducted in 3.4.1.
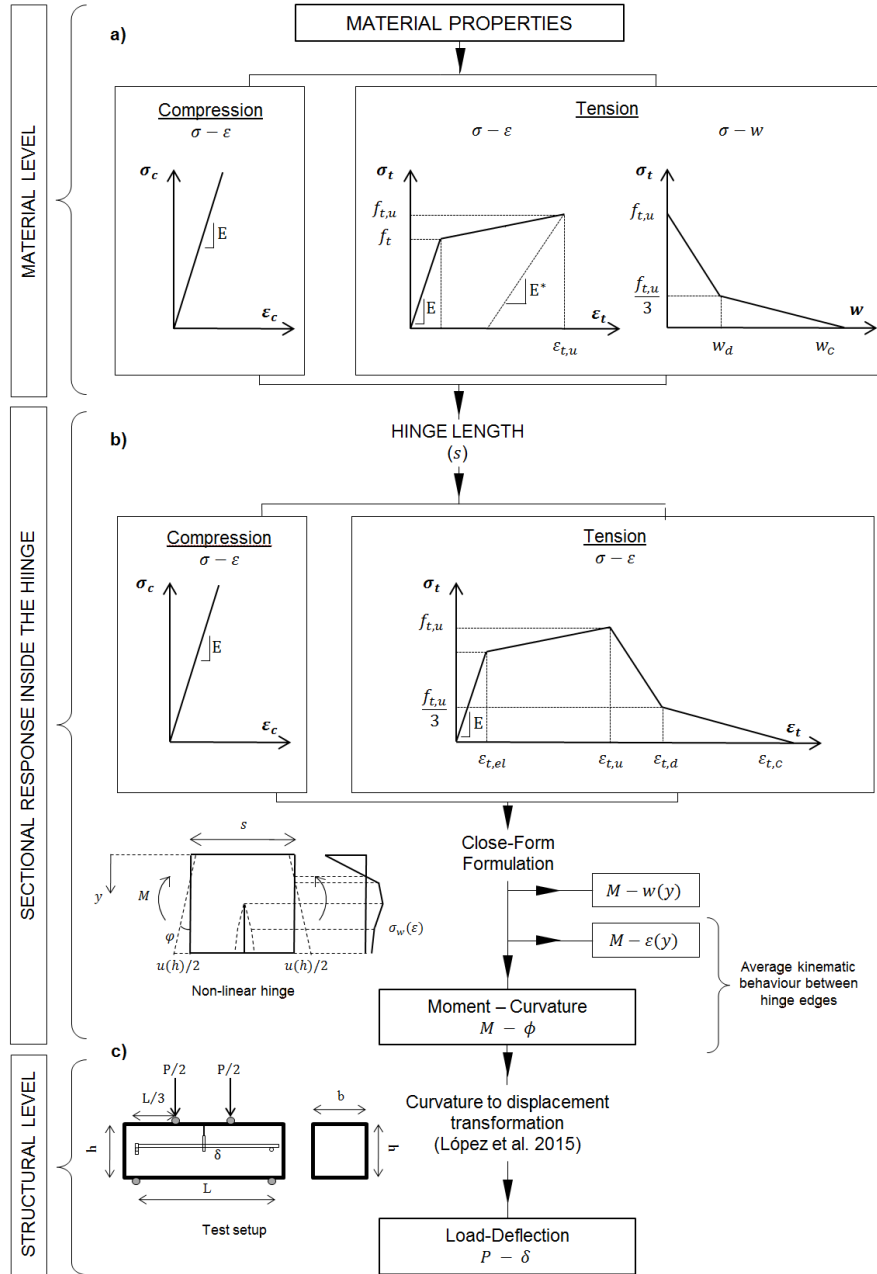
Figure 3.2 Non-linear hinge model scheme

The formulation required to consider a characteristic length according to specimen depth is described in 3.4.2. Moreover, as one of the major uncertainties in a TPBT is the crack's position, a simple formulation for its consideration is presented in 3.4.3. In addition, a preliminary study to justify the linear behaviour assumption in compression is made in 3.4.4

According to Bazant (Bazant, 1989), the validation of a fracture mechanics model requires it being able to reproduce the scale effect found in concrete. This is why an analytical study of the scale effect in conventional concrete, fibre-reinforced concrete with high fracture energy and UHPFRC is carried out (3.4.5) using the developed model.

Finally, a summary of the results, the applicability of the model, and its advantages and disadvantages, are described in the last section of this chapter (3.5).

3.2. Improvements of the non-linear hinge model developed

The non-linear hinge model developed herein takes the initial formulation for strain-hardening materials proposed in (Ostergaardet al., 2005). Unlike this model, the model developed herein proposes an analytical closed-form solution, which is also based on the work developed in (Soranakom et al., 2007), but uses a specific constitutive relationship in both tension and compression for UHPFRC.

The developed model takes a further step in the description of the non-linear hinge model by describing the analytical closed-form formulation to derive the moment-curvature, the moment-strain in any section fibre relationship inside the non-linear hinge and the load-deflection curve, which enables a comparison between the results offered by the model and the experimental results.

The new model also offers a newer and more accurate closed-form formulation to derive the deflection at mid-span according to the average curvature in the constant bending moment area.

A new and simple closed-form formulation that takes into account both the crack position and the desired characteristic length for the test are other improvements that the new model offers.

3.3. Closed-form non-linear hinge model

3.3.1. Constitutive hypothesis

The developed hinge model entails having to assume a constitutive behaviour in both tension and compression (Figure 3.3). The direct tensile tests performed on the UHFPRC specimens according to Chapter 2 have shown that a bilinear stress-strain law along the ascending branch in tension is accurate enough to describe UHPFRC

behaviour. For design purposes, a bilinear stress-crack opening curve, similar to that proposed in (Chanvillard, 2000; RILEM TC 162-TDF, 2002), is chosen to describe softening tensile behaviour. In order to simplify the subsequent formulation, a decision was made to set the stress at the change of slope at one third of ultimate tensile strength ($f_{t,u}$ in Figure 3.3), which agrees with the state-of-the-art analysis. It is worth noting that this value is the same as that proposed in (Petersson, 1981) for conventional concrete. However, it differs from the value of one fifth proposed by MC2010 also for conventional concrete.

The constitutive law in compression is also considered linear elastic at any stress. Since UHPFRC is defined as a concrete with a compressive strength greater than 130 MPa, this hypothesis seemed adequate for reproducing its behaviour in a TPBT as it can be considered linear up to a strain deformation of about 2.5‰ (Spasojevic, 2008).

The parameters that define the constitutive behaviour of UHPFRC are: cracking strength (f_t); ultimate tensile strength ($f_{t,u}$) and its corresponding strain ($\varepsilon_{t,u}$); the crack opening at the change of slope (w_d); the characteristic crack opening or the crack opening at zero stress (w_c); the elastic modulus (E); the unloading modulus (E^*). Another interesting parameter that can contribute to improved knowledge of the hardening phase is the average spacing between cracks in the microcracking phase (s_{av}). However, this parameter is not included in the model.
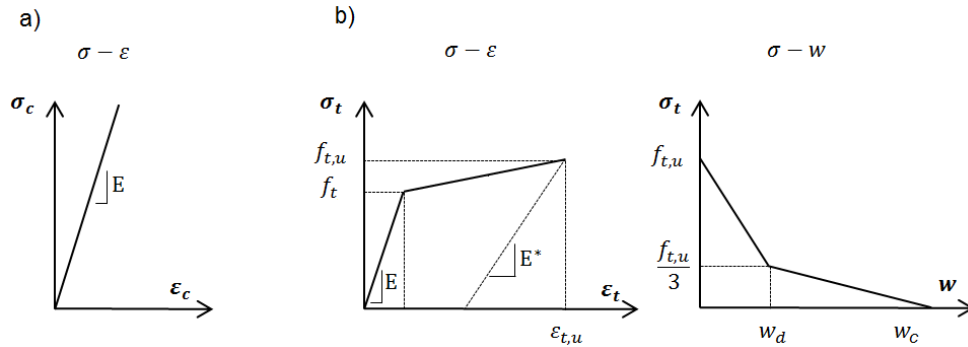
Figure 3.3 The constitutive laws assumed in both compression (a) and tension (b)

3.3.2. Definition of the non-linear hinge

The non-linear hinge model proposed herein is based on Olesen's model (Olesen, 2001), but includes different hypotheses to take into account the strain-hardening behaviour of UHPFRC according to (Ostergaard et al., 2005). The proposed non-linear hinge scheme is shown in Figure 3.4 for a TPBT. The two variables in the test setup configuration in Figure 3.4 are specimen depth (h) and span (L), which define the slenderness ratio ($\lambda = L/h$).

As we can see in Figure 3.4, the considered non-linear hinge length is $L/3$, which matches the constant bending moment area. The use of this specific hinge length is justified in 3.3.5.3, and the consequences of this assumption are described in 3.4.2. Note that, as defined in this way, hinge length depends only on specimen depth if the slenderness ratio remains constant, which agrees with traditional non-linear hinge models.

Once the stress at the most tensioned fibre reaches the peak tensile stress, a macrocrack appears with maximum tensile stress $f_{t,u}$ at the crack tip. To be able to apply the Navier-Bernoulli hypothesis, the crack is smeared along the non-linear hinge length regardless of the real state of the stress inside this area. Therefore, the non-linear hinge model represents the average UHPFRC behaviour inside hinge length. The hinge must connect to the rest of the structure, and it is necessary to check that the average strain profile on the boundaries of the non-linear hinge remains plane throughout the loading process, even after crack localisation.
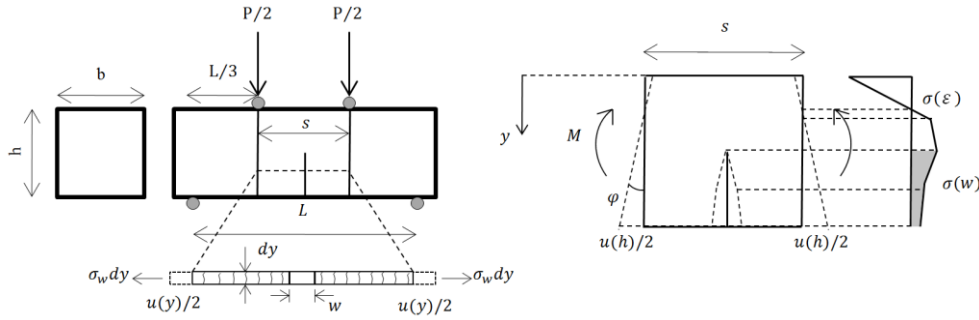
Figure 3.4 Four-point bending test with a non-linear hinge (left); hinge deformation geometry (right)(RILEM TC 162-TDF, 2002).

As in (Stang et al., 1998), the hinge is modelled as incremental layers of springs that act without transferring shear forces between each other. According to Figure 3.4, (2φ) is the angular deformation, $(u(y))$ is the associated longitudinal deformation of springs into which the beam depth can be divided, where y is a vertical coordinate, (ϕ) is the average curvature of the hinge, $(\varepsilon(y))$ is the average longitudinal strain of the springs, and ε_t is the average strain on the most tensioned fibre, i.e. the average longitudinal strain when $y = h$. The relationships between these parameters are given by Eq. 3.1.

$$\phi = 2\frac{\varphi}{s} \quad ; \quad \varepsilon(y) = \varepsilon(h) + \phi(y - h) = \frac{u(y)}{s} \quad ; \quad \varepsilon(h) = \varepsilon_t = \frac{u(h)}{s}$$

Eq. 3.1

The material properties of UHPFRC in tension are defined using a stress-strain relationship in the microcracking phase and a stress-crack opening relationship beyond the macrocrack onset, as depicted in Figure 3.3. However, it is easier to determine the

sectional response within the non-linear hinge using a smeared stress-strain relationship, and by assuming that the strain plane remains plane within the hinge. Therefore, a suitable kinematic link between the strain and crack opening should be found out.

According to (Spasojevic, 2008), a macrocrack appears once strain $\varepsilon_{t,u}$ is reached. It is important to note that UHPFRC is already cracked when the macrocrack stage starts. However, it has been traditionally assumed that the microcracking phase is attributed to volumetric energy absorption, independently of gage length and is, therefore, size-independent. This is why it is possible to consider crack initiation after $\varepsilon_{t,u}$ has been reached. Indeed before this value is reached, the crack opening is so small that it can be considered null.

Following the scheme in Figure 3.4(left) and the constitutive relationship in tension in Figure 3.3, the deformation u of a layer can be obtained following Eq. 3.2. This equation is an adaptation of that proposed in (Olesen, 2001) and it takes into account the strain-hardening stage of UHPFRC, which was first proposed in (Ostergaard et al., 2005). By combining Eq. 3.1 and Eq. 3.2, the strain of each spring can be obtained following Eq. 3.3. Note that the stress-crack opening relationship σ_w depends on crack opening w, which also depends on y. By assuming that $\sigma(w)$ can be represented as a bilinear curve, the stress-crack opening relationship is shown in Eq. 3.4, where a_i and b_i are the constant parameters to be determined for each line of the softening curve.

$$u(y) = \varepsilon_{t,u} \cdot s + \frac{(\sigma_w(y) - f_{t,u})}{E^*} \cdot s + w(y)$$

<div align="right">Eq. 3.2</div>

$$\varepsilon(y) = \varepsilon_{t,u} + \frac{(\sigma_w(y) - f_{t,u})}{E^*} + \frac{w(y)}{s}$$

<div align="right">Eq. 3.3</div>

$$\sigma_{w,i}\big(w(y)\big) = f_{t,u}(b_i - a_i w(y)) \quad i = 0,1$$

<div align="right">Eq. 3.4</div>

By solving $\varepsilon(y)$ in Eq. 3.3 and Eq. 3.4, Eq. 3.5 is derived according to the parameters defined in Eq. 3.5. It is important to remark that similarly to the non-linear hinge model developed in (Olesen, 2001), $w(y)$ and $\sigma_w(y)$ are linear functions in y in each interval of the multi-linear $\sigma_i(w)$ function. This fact allows the determination of the average strain in the hinge according to the crack opening.

$$\varepsilon(y) = \frac{1}{s}[w(y)(1 - \alpha_i) - \beta_i] + \varepsilon_{t,u}$$

<div align="right">Eq. 3.5</div>

$$\alpha_i = \frac{a_i f_{t,u} s}{E^*} \quad ; \quad \beta_i = \frac{(1 - b_i) f_{t,u} s}{E^*}$$

Eq. 3.6

According to the constitutive relationship shown in Figure 3.3, the stresses at the zero crack opening, w_d and w_c correspond to $f_{t,u}$, $f_{t,u}/3$ and 0, respectively. By imposing these conditions in Eq. 3.4, parameters a_i and b_i, can be determined for each curve. The parameters that define a_i and b_i for both stress-crack opening lines are shown in Eq. 3.7 and Eq. 3.8.

$$b_1 = 1 \quad ; \quad a_1 = -\frac{1}{3w_d}$$

Eq. 3.7

$$b_2 = \frac{w_c}{3(w_c - w_d)} \quad ; \quad a_2 = \frac{1}{3(w_c - w_d)}$$

Eq. 3.8

By introducing these parameters into Eq. 3.5, the average strain versus crack opening along the hinge depth can be obtained. These relationships are shown in Eq. 3.9 and Eq. 3.10.

$$\varepsilon\left[w(y)\right] = \varepsilon_{t,u} + \frac{w(y)}{s}\left[1 - \frac{2f_{t,u} s}{3E^* w_d}\right], \quad 0 < w < w_d$$

Eq. 3.9

$$\varepsilon\left[w(y)\right] = \varepsilon_{t,u} + \frac{w(y)}{s} - \frac{f_{t,u}}{3E^*}\left[\frac{w(y) + 2w_c - 3w_d}{w_c - w_d}\right], \quad w_d < w < w_c$$

Eq. 3.10

3.3.3. Crack-opening – strain relationship

If the hypothesis of considering plane strain deformation inside the non-linear hinge is valid, the sectional hinge response can be determined using a smeared stress-strain relationship within the hinge. Therefore, it is possible to turn the softening stress-crack opening material relationship into a stress-strain relationship inside the non-linear hinge. As derived from Eq. 3.9 and Eq. 3.10, the strain inside the hinge and the crack opening are linked by a linear relationship. So as the stress-crack opening is defined as a bilinear relationship, the softening stress-strain relationship must also be a bilinear curve. The only parameters to be determined in the stress-strain law are $\varepsilon_{t,d}$, and ε_c, which can be obtained from Eq. 3.9 and Eq. 3.10 when w equals w_d and w_{max} following Eq. 3.11 and Eq. 3.12.

$$\varepsilon_{t,d} = \frac{w_d}{s} + \varepsilon_{t,u} - \frac{2f_{t,u}}{3E^*}$$

<div align="right">Eq. 3.11</div>

$$\varepsilon_{t,max} = \frac{w_c}{s} + \varepsilon_{t,u} - \frac{f_{t,u}}{E^*}$$

<div align="right">Eq. 3.12</div>

Figure 3.5 depicts the constitutive $\sigma - \varepsilon$ law used to describe the sectional response of the non-linear hinge, which is derived from the material's properties (Figure 3.3), along with the notation of the six parameters used to model the UHPFRC sectional response within the non-linear hinge. The elastic modulus (E) is considered the same in both compression and tension. The other five parameters that define the tensile law are: (i) first cracking tensile strength f_t; (ii) ultimate tensile strength $f_{t,u}$, and (iii) its associate strain $\varepsilon_{t,u}$; (iv) the strain at the intersection of the softening lines $\varepsilon_{t,d}$; (v) the maximum strain with zero stress $\varepsilon_{t,c}$. To simplify the subsequent formulation, four normalised parameters were introduced, α, β, μ, and γ, as defined in Eq. 3.13. The normalised stress-strain law is shown in Figure 3.5, right.

$$\varepsilon_{t,el} = \frac{f_t}{E}; \quad \alpha = \frac{\varepsilon_{t,u}}{\varepsilon_{t,el}}; \quad \beta = \frac{\varepsilon_{t,d}}{\varepsilon_{t,el}}; \quad \mu = \frac{\varepsilon_{t,c}}{\varepsilon_{t,el}}; \quad \gamma = \frac{f_{t,u}}{f_t}$$

<div align="right">Eq. 3.13</div>
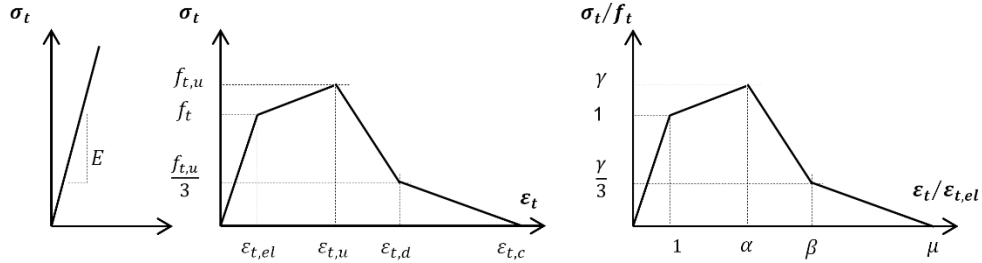
Figure 3.5 Constitutive relationship inside the non-linear hinge length (left) and normalised constitutive relationship (right)

3.3.4. Closed-form formulation

By assuming the constitutive relationship in Figure 3.6 and that the strain plane remains plane inside the hinge, the generalised forces (axial and bending forces) can be obtained by integrating the compression and tension stress blocks. Following the steps pointed out in (Soranakom et al., 2007), the axial and flexural capacity of the non-linear hinge can be expressed according to two parameters. In this case, the average curvature (ϕ) and the strain at the most tensioned fibre (ε_t) are used. Despite it being

common to use crack depth instead of strain at the most tensioned fibre, a decision was made to do that as the strain at the most tensioned face can be directly related to the crack opening (w).

As the stress-strain relationship defined in 3.3.3 is a quadrilinear curve, five different integration cases can be found, depending on the strain reached at the most tensioned fibre according to Figure 3.6: (Stage I) linear elastic up to the matrix-cracking strain, $\varepsilon_{t,el}$; (Stage II) the strain-hardening behaviour characterised by multiple microcracking up to crack localisation, $\varepsilon_{t,u}$; (Stage III and IV) softening behaviour characterised by macrocrack development up to the strain at zero stress, $\varepsilon_{t,c}$; (Stage V) fibre debonding.
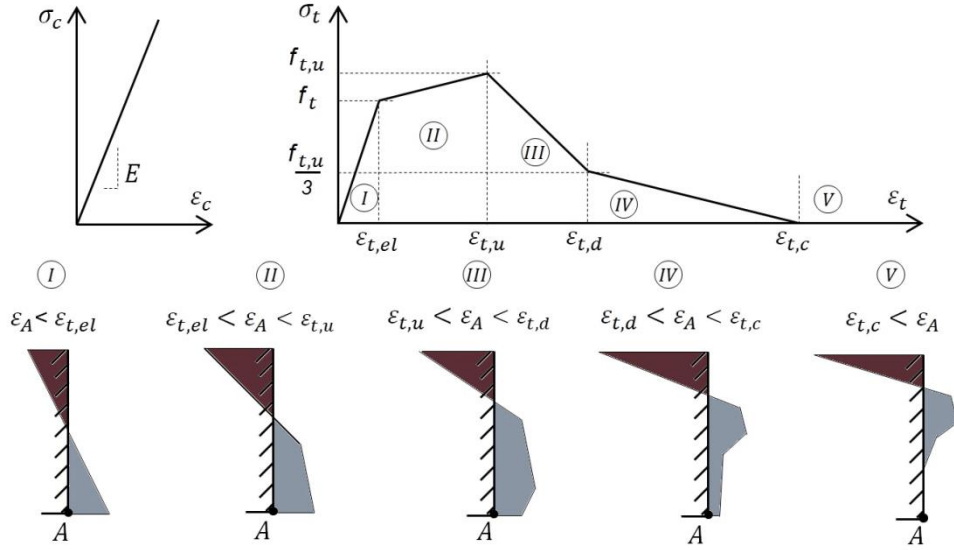
Figure 3.6 Stress-strain relationship (above) for different stages (below).

From the axial force equilibrium, ϕ-ε_t can be derived. Once this relationship has been established, the bending moment equation can be used to determine the M-ϕ relationship. The M-ε_t relationship can be easily obtained using the previous two relationships. The M-crack depth relationship can also be obtained from the latter relationship and Eq. 3.1.

3.3.4.1 $M - \phi - \varepsilon_t$ relationships

Following the steps pointed out in (Soranakom et al., 2007), the M-ϕ-ε_t relationship is obtained for the constitutive normalised parameters in Figure 3.6. By considering a non-reinforced rectangular $b \times h$ cross-section with null axial force according to the assumption that plane sections remain plane, the closed-form $M - \phi$ formulation was obtained using the $\sigma - \varepsilon$ law in Figure 3.6. For each stage, the axial force and bending

moment can be expressed according to the constitutive law parameters, the average curvature and the strain at the most tensioned face. Using the axial force equation and the null axial force condition in the section, the strain at the tension face can be expressed according to the curvature that divided each stage.

Table 3.1 defines curvature values ϕ_{el}, ϕ_u, ϕ_d, ϕ_c are also defined. These parameters correspond to the curvature at which the strains at the most tensioned fibre are $\varepsilon_{t,el}$, $\varepsilon_{t,u}$, $\varepsilon_{t,d}$, and $\varepsilon_{t,c}$, respectively. Table 3.2 shows the strain at the most tensioned fibre versus the average curvature of the hinge relationship according to the considered quadrilinear stress-strain relationship (Figure 3.6), defined by the normalised parameters in Eq. 3.13.

By substituting the equations in Table 3.2 in the bending moment equation, it is possible to obtain the $M - \phi$ relationship in accordance with the constitutive parameters. The equations that define this relationship are shown in Table 3.3.

Table 3.1 Curvature values among the different stages

ϕ Intervals	
End of Stage I	$\phi_{el} = \dfrac{2f_t}{Eh}$
End of Stage II	$\phi_u = \dfrac{f_t h\alpha + f_t h B_u}{Eh^2}$ $B_u = \sqrt{\alpha + (\alpha - 1)\gamma}$
End of Stage III	$\phi_d = \dfrac{3f_t\beta + \sqrt{3}f_t B_d}{3Eh}$ $B_d = \sqrt{3\alpha - (3 + \alpha - 4\beta)\gamma}$
End of Stage IV	$\phi_c = \dfrac{3f_t\mu + \sqrt{3}f_t B_c}{3Eh}$ $B_c = \sqrt{\alpha(3 - \gamma) + \gamma(3\beta + \mu - 3)}$

Table 3.2 The ε_t– ϕ closed-form formulation suggested for a UHPFRC rectangular cross-section with null axial force.

Stage I $\phi \leq \phi_{el}$

$$\varepsilon_{t,I}(\phi) = \phi \frac{h}{2}$$

Stage II $\phi_{el} \leq \phi \leq \phi_u$

$$\varepsilon_{t,II}(\phi) = \frac{f_t(\alpha - \gamma) + (\alpha - 1)(hE\phi - C_{\varepsilon 1h})}{E(\alpha - \gamma)}$$

$$C_{\varepsilon 1h} = \sqrt{\frac{hE\phi[2f_t(\alpha - \gamma) + hE\phi(\gamma - 1)]}{\alpha - 1}}$$

Stage III $\phi_u \leq \phi \leq \phi_d$

$$\varepsilon_{t,III}(\phi) = \frac{1}{E(3\alpha - 3\beta - 2\gamma)}[f_t(\alpha - 3\beta)\gamma + (\alpha - \beta)(3hE\phi - C_{\varepsilon 1s1})]$$

$$C_{\varepsilon 1s1} = \sqrt{\frac{A_{\varepsilon 1s1} + 6hEf_t(\alpha - 3\beta)\gamma\phi + 6h^2E^2\gamma\phi^2}{(\alpha - \beta)}}$$

$$A_{\varepsilon 1s1} = 3f_t{}^2(\gamma - \alpha)(3\beta + \alpha(\gamma - 3) + 2\gamma - 3\beta\gamma)$$

Stage IV $\phi_d \leq \phi \leq \phi_c$

$$\varepsilon_{t,IV}(\phi) = \frac{f_t\gamma\mu + (\mu - \beta)(3hE\phi - C_{\varepsilon 1s2})}{E(\gamma - 3\beta + 3\mu)}$$

$$C_{\varepsilon 1s2} = \sqrt{\frac{f_t{}^2(A_{\varepsilon 1s2} + A_{\varepsilon 2s2}) - 6hEf_t\gamma\mu\phi + 3h^2E^2\gamma\phi^2}{\beta - \eta}}$$

$$A_{\varepsilon 1s2} = 3\gamma(\beta - 1)(3\beta - \gamma) - \gamma\mu(\gamma + 6\beta - 9)$$

$$A_{\varepsilon 2s2} = \alpha(\gamma - 3)(\gamma - 3\beta + 3\mu)$$

Stage V $\phi_c \leq \phi$

$$\varepsilon_{t,V}(\phi) = \frac{-f_t A_{\varepsilon 1u} + 3hE\phi}{3E}$$

$$A_{\varepsilon\varepsilon 1u} = \sqrt{3(\alpha(3 - \gamma) + \gamma(\eta + 3\beta - 3))}$$

Table 3.3 *The $M - \phi$* closed-form formulation for a UHPFRC rectangular cross-section with null axial force

Stage I $\phi \leq \phi_{el}$

$$M_I(\phi) = \frac{bh^3}{12}E\phi$$

Stage II $\phi_{el} \leq \phi \leq \phi_u$

$$M_{II}(\phi) = \frac{bh}{6E(\alpha - \gamma)^2\phi}[A_{M1h}\phi^2 + A_{M2h}C_{M1h} + Eh\phi(A_{M3h} + A_{M4h}C_{M1h})]$$

$A_{M1h} = 2E^2h^2(\gamma - 1)(\alpha + \gamma - 2)$

$A_{M2h} = 2f_t(\alpha - 1)(\gamma - \alpha)$

$A_{M3h} = 3f_t(\alpha - \gamma)(\alpha + \gamma - 2)$

$A_{M4h} = 4(\alpha + \gamma - \alpha\gamma - 1)$

$C_{M1h} = \sqrt{\dfrac{Eh\phi[2f_t(\alpha - \gamma) + Eh(\gamma - 1)\phi]}{\alpha - 1}}$

Stage III $\phi_u \leq \phi \leq \phi_d$

$$M_{III}(\phi) = \frac{b}{6E^2(3\beta - 3\alpha + 2\gamma)^2\phi^2}[f_t^{\,3}A_{M1s1}A_{M2s1} + f_t^{\,2}A_{M3s1}C_{M1s1} + f_tC_{M2s1} + C_{M3s1}]$$

$A_{M1s1} = (\alpha - \gamma)(\alpha(3 - \gamma) - 3\beta + \gamma(3\beta - 2))$

$A_{M2s1} = 3(\alpha + 1)(\alpha - \beta) - 2\gamma(2\alpha - 3\beta + 1)$

$A_{M3s1} = 2(\alpha - \beta)(\alpha - \gamma)(\alpha(3 - \gamma) - 3\beta + \gamma(3\beta - 2))$

$C_{M1s1} = \sqrt{\dfrac{3f_t^{\,2}(\alpha - \gamma)(\alpha(3 - \gamma) - 3\beta + \gamma(3\beta - 2)) - 6Ef_th(3\beta - \alpha)\gamma\phi + 6E^2h^2\gamma\phi^2}{\alpha - \beta}}$

$C_{M2s1} = Eh(3\beta - \alpha)\gamma\phi(2(\alpha - \beta)C_{1s1} - 3Eh\phi(3\alpha - 3\beta + 2\gamma))$

$C_{M3s1} = 4E^2h^2\gamma\phi^2(Eh\phi(3\alpha - 3\beta + 2\gamma) - 2(\alpha - \beta)C_{1s1})$

Stage IV $\phi_d \leq \phi \leq \phi_c$

$$M_{IV}(\phi) = \frac{b}{18E^2(-3\beta + 3\mu + \gamma)^2\phi^2}\left[f_t{}^3(A_{M1s2} + \mu\,A_{M2s2} + \mu^2\,A_{M3s2}) + f_t{}^2A_{M4s2}C_{M1s2} + f_tC_{M2s2} + C_{M3s2}\right]$$

$$A_{1s2} = (\gamma - 3\beta)^2[3\alpha(1 + \alpha) - \gamma(3 + \alpha(3 + \alpha) - 2\alpha\beta - 3\beta^2)]$$

$$A_{2s2} = (\gamma - 3\beta)[6\alpha^2(3 - \gamma) + \gamma(15\beta^2 - 8\beta\gamma + 9\gamma - 18) + 3\alpha(6 + \gamma(4\beta + \gamma - 9))]$$

$$A_{3s2} = 27\alpha(1 + \alpha) - 9\gamma(3 + \alpha(6 + \alpha) - 2\alpha\beta - 2\beta^2) + 9\gamma^2(3 + \alpha - 2\beta) - 2\gamma^3$$

$$A_{4s2} = 2(\beta - \mu)[3\gamma(\beta - 1)(3\beta - \gamma) - \gamma\mu(6\beta + \gamma - 9) + \alpha(\gamma - 3)(3\mu - 3\beta + \gamma)]$$

$$C_{1s2} = \sqrt{\frac{f_t{}^2(3\gamma(\beta - 1)(3\beta - \gamma) - \gamma\mu(6\beta + \gamma - 9) + \alpha(\gamma - 3)(\gamma + 3\mu - 3\beta)) - 6Ehf_t\gamma\mu\phi + 3E^2h^2\gamma\phi^2}{\beta - \mu}}$$

$$C_{2s2} = 3Eh\gamma\mu\phi(3Eh\phi(3\mu - 3\beta - \gamma) - 2(\mu - \beta)C_{1s2})$$

$$C_{3s2} = 6E^2h^2\gamma\phi^2(Eh\phi(3\beta + \gamma - 3\mu) + 2(\mu - \beta)C_{1s2})$$

Stage V $\phi_c \leq \phi$

$$M_V(\phi) = \frac{b}{54E^2\phi^2}\left[f_t{}^3A_{M1u} + A_{M2u}\right]$$

$$A_{M1u} = -3[\alpha^2(\gamma - 3) + \alpha(3\gamma - 2\beta\gamma - 3) - \gamma(\mu^2 + \beta\mu + 3\beta^2 - 3)]$$

$$A_{M2u} = 2\sqrt{3}\left[f_t{}^2(\alpha(3 - \gamma) + \gamma(\mu + 3\beta - 3))\right]^{3/2}$$

Figure 3.7 (left) shows an example of the different curves of the moment versus the curvature relationship inside the non-linear hinge for the five different stages according to the constitutive relationship in Figure 3.6, and also to the equations in Table 3.3. Figure 3.7 (right) shows the strain at the most tensioned fibre versus the curvature relationship according to the equations in Table 3.2.

Using the equations in Table 3.2 and the moment-curvature relationship in Table 3.3, the bending moment versus the average strain on different layers along specimen depth can be obtained using Eq. 3.1. Figure 3.8 shows the bending moment versus the average strain in the non-linear hinge length relationship on different layers for a common UHPFRC behaviour. The employed stress-strain parameters correspond to the average stress-strain relationship obtained for UHPFRC with 2% of the 13/0.2 mm steel fibres in the 100 mm-depth specimen described in (López et al., 2015). The legend shows the normalised depth (y/h) from the top of the specimen, where the maximum strain on the most compressed layer is around 2-3‰, and the hypothesis of linearity in compression can be questioned because the yielding strength in

---

compression is around 2.5‰ (Spasojevic, 2008). This is why its influence should be quantified.
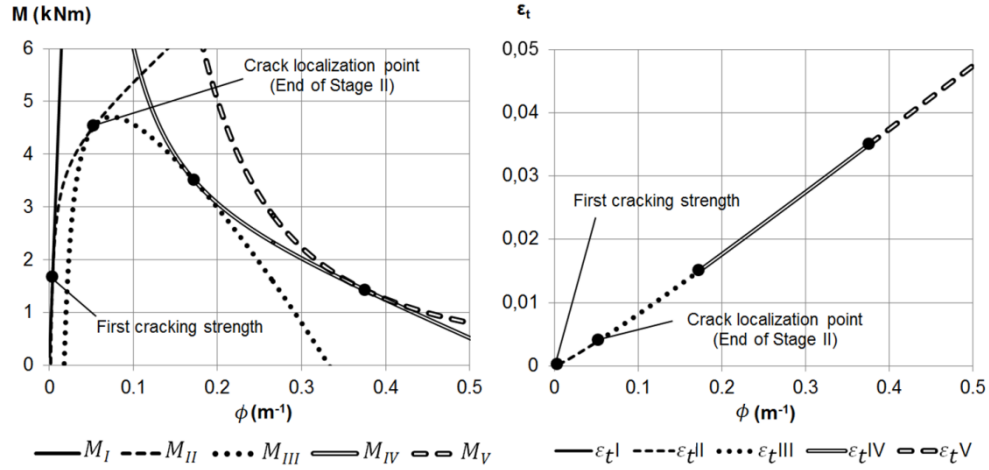
Figure 3.7 The analytical moment-curvature curves (Table 3.3) and the average strain-curvature curves (Table 3.2) for a UHPFRC rectangular cross-section specimen with $b=h=0.1$ m and $f_t=10$ MPa, $E=50$ GPa, $\gamma=1.2$; $\alpha=20$; $\beta=75$; $\mu=175$.
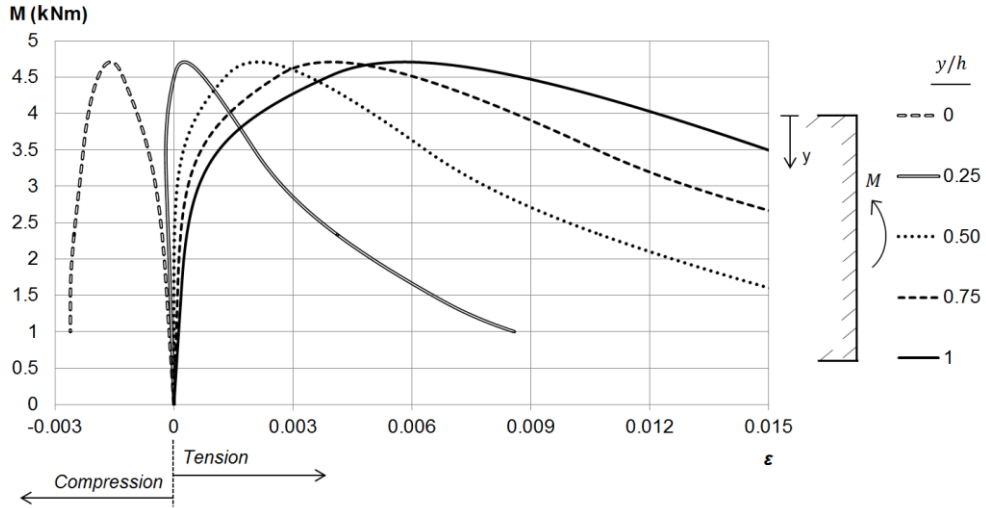
Figure 3.8 The analytical moment-strain relationship on different sectional layers for a UHPFRC rectangular cross-section specimen with $b=h=0.1$ m; $f_t=10$ MPa, $E=50$ GPa, $\gamma=1,2$; $\alpha=20$; $\beta=75$; $\mu=175$

3.3.4.2 Bending moment - crack opening relationship

Given a stress-strain relationship inside the non-linear hinge, which was previously derived from the constitutive material response following Eq. 3.11 and Eq. 3.12, the strain at the most tensioned spring of hinge ε_t can be determined using the equations in Table 3.2 for any curvature value. Afterwards, the strain at each spring $\varepsilon(y)$ can be obtained using Eq. 3.1. Then the crack opening at any spring $w(y)$ can be derived from Eq. 3.9 and Eq. 3.10 by solving $w(y)$, as indicated in Eq. 3.14 and Eq. 3.15. Note that if the strain at the most tensioned spring (ε_t) is smaller than $\varepsilon_{t,u}$, the crack opening can be considered zero.

$$w[\varepsilon(y)] = s \left(\varepsilon(y) - \varepsilon_{t,u} \right) \left[1 + \frac{2f_{t,u}}{3E^* \left(\varepsilon_{t,d} - \varepsilon_{t,u} \right)} \right], \quad \varepsilon_{t,u} < \varepsilon < \varepsilon_{t,d}$$

Eq. 3.14

$$w[\varepsilon(y)] = s \left(\varepsilon(y) - \varepsilon_{t,u} \right) + \left[\frac{s\, f_{t,u} \left(\varepsilon(y) - 3\varepsilon_{t,d} + 2\varepsilon_{t,c} \right)}{3E^* \left(\varepsilon_{t,c} - \varepsilon_{t,d} \right)} \right], \quad \varepsilon_{t,d} < \varepsilon < \varepsilon_{t,c}$$

Eq. 3.15

Figure 3.9 (left) offers an example of the crack opening distribution along specimen depth in different load stages. As seen in Figure 3.9, it depends on the average strain profile inside the hinge in each load step. If a slenderness ratio of 4.5 and a specimen depth of 100 mm is considered, the hinge length is 150 mm, which is in accordance with the hinge model developed herein.

The depicted strain profiles correspond to the load values on the unloading branch after reaching maximum flexural strength. At maximum load, the model estimates a crack opening of 0.3 mm. Although it does not come over very clearly in Figure 3.9, the stress – crack opening profile did not remain plane because the slope of the lines that defined the $\varepsilon - w$ relationship are not the same (see Eq. 3.9 and Eq. 3.10), while the strain profile remains plane. Note that the crack in Figure 3.9 starts at the end of the hardening phase; e.g., only the macrocrack is depicted. Obviously, the crack depth extends beyond the softening initiation.

In order to show this, the stress profile at the maximum load and in the different load stages in the unloading branch (80%, 60% and 40% of the maximum load) are represented in Figure 3.10 and Figure 3.11. The pictures on the left represent the whole stress profile, while those on the right expand the tensile zone to allow it to be better viewed. The stress profile is obtained from the strain profile as the stress-strain relationship is known.

138
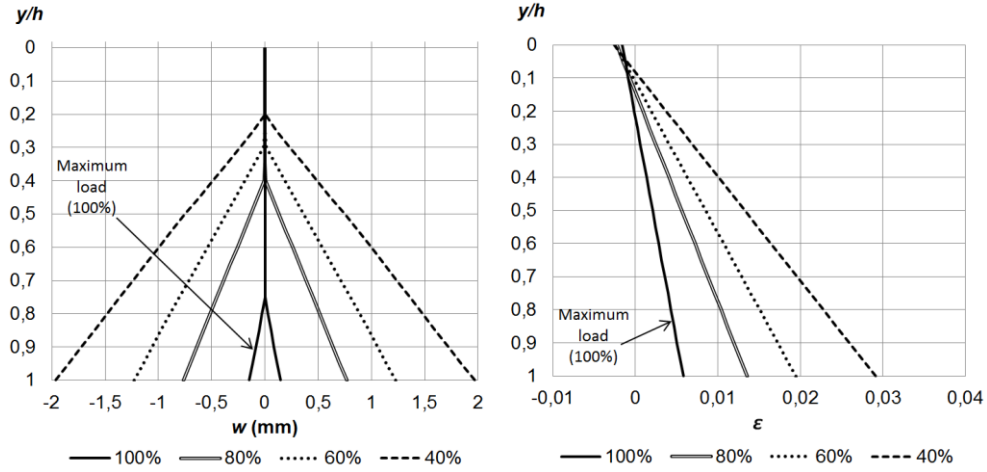
Figure 3.9 Crack opening and crack depth (left), and strain plane along specimen depth (right) for UHPFRC with $b=h=0.1$ m; $L/h=4.5$; $f_t=10$ MPa; $E=50$ GPa; $\gamma=1.2$; $\alpha=20$; $\beta=75$; $\mu=175$; $s=150$ mm; $E^*=10$ GPa, in different load stages.
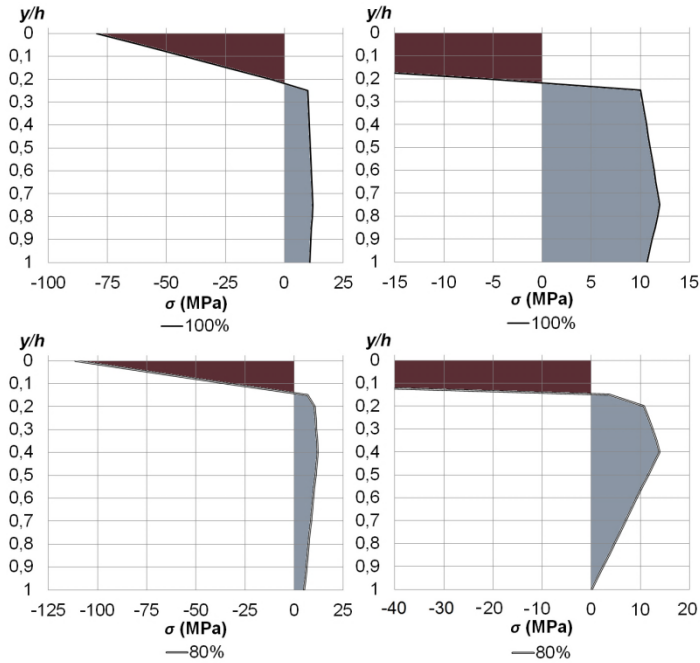
Figure 3.10 Stress distribution in different load stages for a UHPFRC rectangular cross-section with $b=h=0.1$ m; $f_t=10$ MPa; $E=50$ GPa; $\gamma=1.2$; $\alpha=20$; $\beta=75$; $\mu=175$.
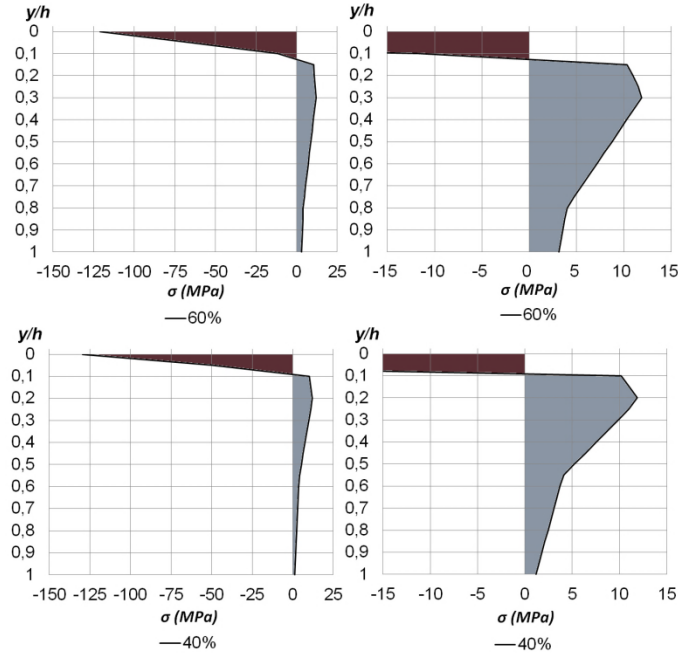
Figure 3.11 Stress distribution in different load stages for a UHPFRC rectangular cross-section with $b=h=0.1$ m; $f_t=10$ MPa; $E=50$ GPa; $\gamma=1.2$; $\alpha=20$; $\beta=75$; $\mu=175$.

Figure 3.10, top, shows the average stress profile at maximum load on the boundaries of the non-linear hinge. We can notice that maximum load is reached after crack localisation has taken place as the tensile stress profile undergoes softening. In this particular case, the neutral axis is at a distance of $0.79h$ from the bottom face. It is worth remembering that the Swiss standard developed their simplified inverse analysis formulation by assuming a rigid-perfectly plastic behaviour in tension and the position of the neutral axis at a distance of $0.82h$. However, this value depends on both the considered constitutive behaviour and specimen depth.

From the closed-form formulation and the considered parameters of the tensile properties of UHPFRC, a maximum bending moment of 4.71 kNm is obtained, which leads to an equivalent flexural strength of 28.3 MPa. According to the Swiss standard, a maximum tensile strength of 10.8 MPa is derived with that maximum equivalent strength. Formulation is not at all bad, but should improve if a more accurate determination of the tensile properties of UHPFRC is made.

In this particular case, a maximum stress value at the most compressed face of 79.6 MPa, 111.4 MPa, 121.1 MPa and 129.4 MPa are obtained at the maximum load and at 80%, 60% and 40% of the maximum load in the unloading branch, respectively. It leads to a maximum strain of 1.6‰, 2.2‰, 2.4‰, 2.6‰. Remember that UHPFRC

remains linear elastic in compression up to a strain value of around 2.5‰. According to the obtained values, UHPFRC may undergoe a non-linear stage in compression during the unloading process. Therefore, the influence of the linear elastic hypothesis should be evaluated.

3.3.4.3 Bending moment vs. crack depth

If we know the strain at the most tensioned fibre and the corresponding curvature for each load stage obtained from Table 3.1, Table 3.2 and Table 3.3, the bending moment versus the crack depth relationship can be easily derived. In this section, two different crack depths are defined: (i) the crack depth at the end of the linear stage (x_{el}); and (ii) the crack depth at the end of the hardening phase (x_u). Another parameter that can be easily determined is the neutral axis depth (x_n); i.e. the point at which the average stress is null in the section. All these parameters are normalised by specimen depth. By assuming that the x coordinate starts at the top face (see Figure 3.9, Figure 3.10 and Figure 3.11), the different above-described normalised depth positions can be obtained following Eq. 3.16. Normalised x_{el}, x_u and x_n can be derived from Eq. 3.16 when ε_i takes the values of $\varepsilon_{t,el}$, $\varepsilon_{t,u}$ and 0, respectively. All the values in Eq. 3.16 are given in absolute values. By using Eq. 3.16, $M - x_i$ was obtained for the case study in Figure 3.9, Figure 3.10 and Figure 3.11. As the relationship between ε_t and x_i is known, $\varepsilon_t - x_i$ is also easy to obtain. The results of both curves are shown in Figure 3.12 and Figure 3.13, respectively. These results agree with the stress distribution in 3.3.4.2.

$$x_i = 1 - \frac{\varepsilon_t - \varepsilon_i}{\phi h}$$

Eq. 3.16
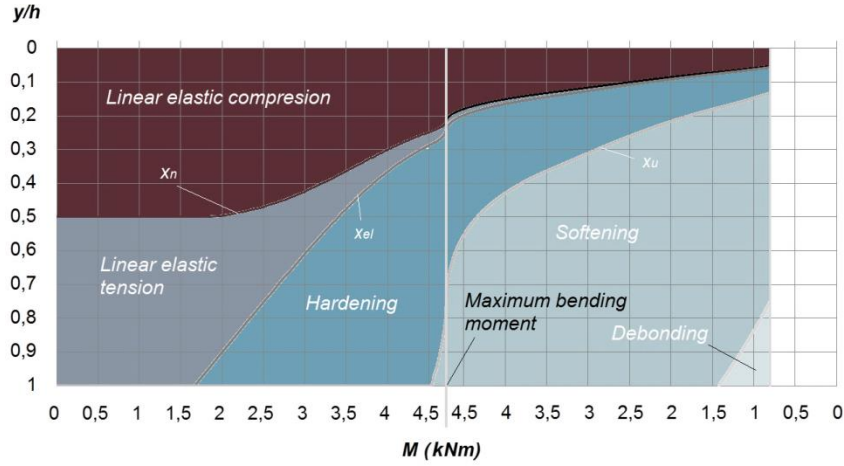
Figure 3.12 Neutral axis position and crack depth according to the bending moment for a UHPFRC rectangular cross-section with $b=h=0.1$ m; $f_t =10$ MPa; $E=50$ GPa; $\gamma=1,2$; $\alpha=20$; $\beta=75$; $\mu=175$.
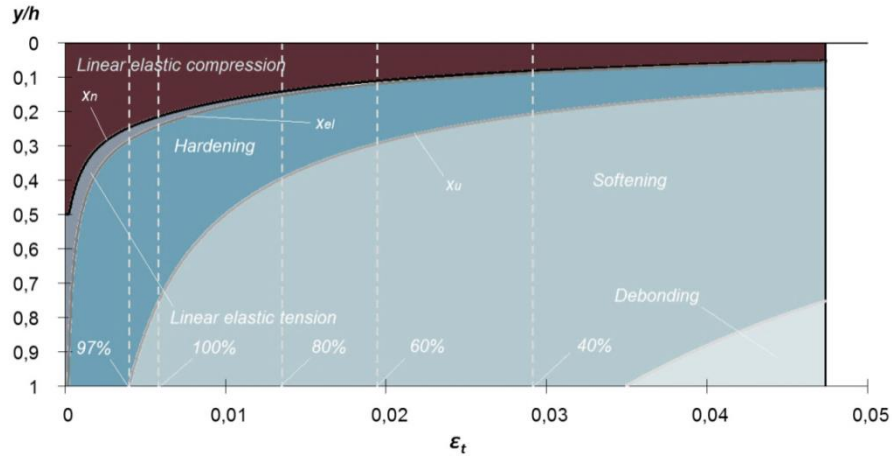
Figure 3.13 Neutral axis position and crack depth according to the strain at the most tensioned fibre for a UHPFRC rectangular cross-section with $b=h=0.1$ m; $f_t=10$ MPa; $E=50$ GPa; $\gamma=1.2$; $\alpha=20$; $\beta=75$; $\mu=175$.

3.3.5. Average curvature to displacement at mid-span in a FPBT

Non-linear hinge models are usually accompanied by a simplified formulation to determine the displacement according to any of the kinematic parameters of the hinge. The most widely used kinematic parameter for this purpose is the average curvature inside the hinge, which is the parameter used herein. This fact explains why the closed-form $M-\phi$ formulation is explicitly developed instead of $M-\varepsilon_t$ or $M-x_i$. If the development of a simple and accurate ϕ to the displacement at mid-span (δ) transformation were possible, the $M-\delta$ relationship could be straightforwardly derived according to the constitutive relationship of UHPFRC, specimen geometry and the test setup. This is the main purpose of the present section.

According to the state-of-the-art review, currently two curvature to the deflection transformations exist (see 2.6.1.3), and have been proposed to be used in inverse analysis methodologies in (Rigaudet al., 2011; Qian et al., 2007). The main problems of these transformations are described in 2.6.1.3, and are reminded herein.

In both transformations, the curvature is not accurately determined from the displacement for two main reasons: (i) the shear deflection is not considered, whose effect is important when the slenderness ratio is low; (ii) a linear displacement to curvature transformation is considered, even when the UHPFRC is in a non-linear stage. These are the two main problems to be dealt with.

The deflection to curvature transformation method developed herein is focused on a TPBT and its extension to other FPBTs should be checked. The $\delta-\phi$ relationship is established by Timoshenko equations (Eq. 3.17). By considering a non-linear curvature

distribution, the non-linearity in bending is taken into account. Shear deflection can be large enough to be neglected, and its influence depends on the slenderness ratio (Graybeal, 2006).

$$\delta = \frac{L}{2} \int_0^{L/2} \phi(x)dx - \int_0^{L/2} \phi(x) \left[\frac{L}{2} - x \right] dx + \frac{1}{GA_Q} \int_0^{L/2} Q(x)dx$$

Eq. 3.17

The last term of Eq. 3.17 can be easily solved if shear stiffness is considered constant during the test; i.e. no shear cracking appears in the TPBT. This fact can be assumed since no shear cracking has been pointed out by any of the authors in these types of tests on UHPFRC specimens for common spans and depths, and according to the shear stress values obtained in 3.4.1. So by considering a Poisson's ratio of 0.2 (AFGC, 2013) and a shear area of *5bh/6*, which is in line with the Timoshenko theory, the last term of Eq. 3.17 can be solved using Eq. 3.18, which takes into account the shear distribution in a TPBT.

$$\frac{1}{GA_Q} \int_0^{L/2} Q(x)dx = \frac{PL}{6GA_Q} = \frac{2PL(1 + v)}{6EA_Q} = \frac{12PL}{25Ebh}$$

Eq. 3.18

The integration of Eq. 3.17 requires a curvature distribution hypothesis along the beam in accordance with the applied load. Even though the theoretical $M - \phi$ relationship was obtained (Table 3.3), the inverse relation $\phi - M$ is very difficult to obtain, and analytically integrating the resulting equations to obtain the $\phi - \delta$ relationship can be a very complicated issue. For this reason, it is necessary to assume a $\phi(x)$ distribution, which has to be easily integrated and must approach the theoretical relationship.

The easiest procedure consists in assuming a linear curvature distribution in Zone 2 (see Figure 3.14) and a constant one in Zone 1 (see Figure 3.14). This hypothesis is consistent with the TPBT since this is the real curvature distribution expected in the TPBT in the linear stage. Eq. 3.19 shows this hypothesis.

Parameter ϕ represents the average curvature in Zone 1. Before crack localisation, the average curvature is the same as the curvature at each point inside Zone 1. However after crack localisation has taken place, the non-linear hinge model enables the consideration of an average curvature inside the non-linear hinge. If the considered hinge length is $L/3$, the curvature distribution in Zone 1 can be taken as constant. According to this assumption, the disturbed cracked section is considered to be smeared over Zone 1, which coincides with specimen depth in the case of a slenderness ratio (L/h) of 3.

$$\phi(x) = \begin{cases} \dfrac{3\phi}{L}x & x \leq \dfrac{L}{3} \\[2ex] \phi\dfrac{L}{3} < x \leq {}^{L}\!/_{2} \end{cases}$$

Eq. 3.19
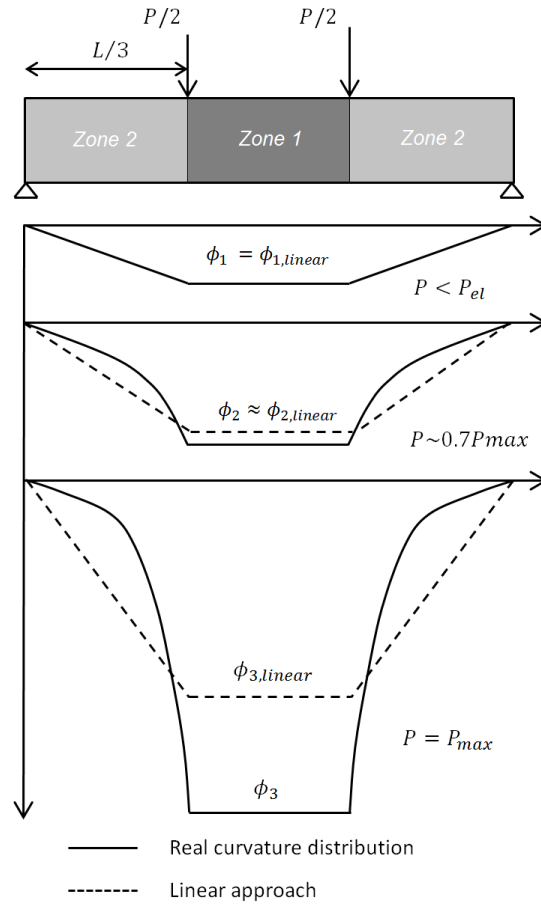
Figure 3.14 Qualitative comparison between the real curvature distribution and the linear approach for different loading steps and the same displacement at mid-span.

The linear approach provides an exact solution up to the first cracking stress. In addition, for load levels of up to approximately 70% of the maximal flexural load, curvatures deviate slightly from the elastic curvatures (Spasojevic, 2008) given the slight loss of stiffness up to this point (see Figure 3.7, left). On the contrary, this

hypothesis greatly underestimates the curvature above this value for a given displacement at mid-span (Baby et al., 2013).

Figure 3.14 illustrates how this hypothesis works. In a first step, this assumption is completely accurate when the applied load is lower than the first cracking load. In a second step with an applied load of about 70% of the maximum bearing capacity, the curvature is slightly underestimated at Zone 1 due to an overestimation in Zone 2. At this point, it is necessary to remark that both the curvature distributions shown in Figure 3.14 correspond to the same applied load and the same displacement at mid-span because we are looking for the curvature that is in correspondence to the displacement measure at mid-span for each loading step. In a third step, as load increases, the underestimation of the curvature for the same displacement also increases. In Figure 3.14, ϕ_i and $\phi_{i,linear}$, represent the average curvature distribution expected in a TPBT when considering a hinge length equal to Zone 1 length and the curvature obtained using the linear approach.

In order to improve the linear assumption, it is necessary to develop a new hypothesis. Since the curvature law quickly increases close to the maximum load, a natural logarithm curve (Eq. 3.20) is used. This curve is defined so that its initial slope corresponds to the slope of the linear-elastic beams theory for each loading step.

$$\phi(x) = \begin{Bmatrix} -\dfrac{2PL}{Ebh^3}\ln\left(1-\dfrac{3x}{L}\right) x < \dfrac{L}{3} \\ \phi\dfrac{L}{3} \le x \le {L}/{2} \end{Bmatrix}$$

Eq. 3.20

By replacing Eq. 3.19 and Eq. 3.20 in Eq. 3.17, the $\delta - \phi$ relationship can be obtained. The results are shown in Eq. 3.21and Eq. 3.22 for the linear approach and the logarithm approach, respectively.

$$\delta = \frac{23L^2}{216}\phi + \frac{12P}{25Eb}\left(\frac{L}{h}\right) \rightarrow Linear\ hypothesis$$

Eq. 3.21

$$\delta = \frac{5L^2}{72}\phi + \frac{P}{6Eb}\left(\frac{L}{h}\right)^3 + \frac{12P}{25Eb}\left(\frac{L}{h}\right) \rightarrow Logarithm\ hypothesis$$

Eq. 3.22

The equation that allows the determination of the average curvature in Zone 1 from the deflection measured at mid-span from both hypotheses is easily derived from Eq. 3.21 and Eq. 3.22. These are the equations used for the inverse analysis procedure described in Chapters 4 and 5, and are shown in Eq. 3.23 and Eq. 3.24. Note that Eq. 3.23 is the

same as that proposed in the French and Swiss standard, but with the addition of shear deformation.

$$\phi = \frac{216}{23L^2}\left[\delta - \frac{12P}{25Eb}\left(\frac{L}{h}\right)\right] \rightarrow Linear\ hypothesis$$

Eq. 3.23

$$\phi = \frac{72}{5L^2}\left[\delta - \frac{P}{6Eb}\left(\frac{L}{h}\right)^3 - \frac{12P}{25Eb}\left(\frac{L}{h}\right)\right] \rightarrow Logarithm\ hypothesis$$

Eq. 3.24

3.3.5.1 Analytical validation

The TPBT is an isostatic test, so the bending moment law is defined by the equilibrium equations for each loading step. If the beam is divided into *n* points with a gap of *Δx* between them, the bending moment at each point can be easily determined. Using the $M - \phi$ closed-form in Table 3.3, it is possible to determine the curvature law along the beam that is associated with each applied load. After establishing the curvature law, it is possible to obtain the displacement due to the bending along the beam by the double integration of the curvature. In a first integration step, rotation angle (φ) is obtained using Eq. 3.25, and by also considering that the rotation angle at mid-span is null. In a second step, the displacement due to bending (δ_b) can be determined using Eq. 3.26 and by considering the null displacement on the supports (Figure 3.15).

$$\Delta\varphi = \phi \cdot \Delta x$$

Eq. 3.25

$$\Delta\delta_b = \varphi \cdot \Delta x$$

Eq. 3.26

Since shear forces can play a significant role in total displacement, it is necessary to determine it. As with the bending moment distribution, shear distribution can be simply determined using the equilibrium equations. Shear rotation angle (γ) is obtained using Eq. 3.27, where *Q is* the shear force, *G* is the shear stiffness and A_Q is the effective shear area. By the direct integration of the rotation angle, the displacement due to shear forces (δ_s) can be determined using Eq. 3.28 (Figure 3.15).

$$\gamma = \frac{Q}{GA_Q}$$

Eq. 3.27

$$\Delta\delta_s = \gamma \cdot \Delta x$$

Eq. 3.28
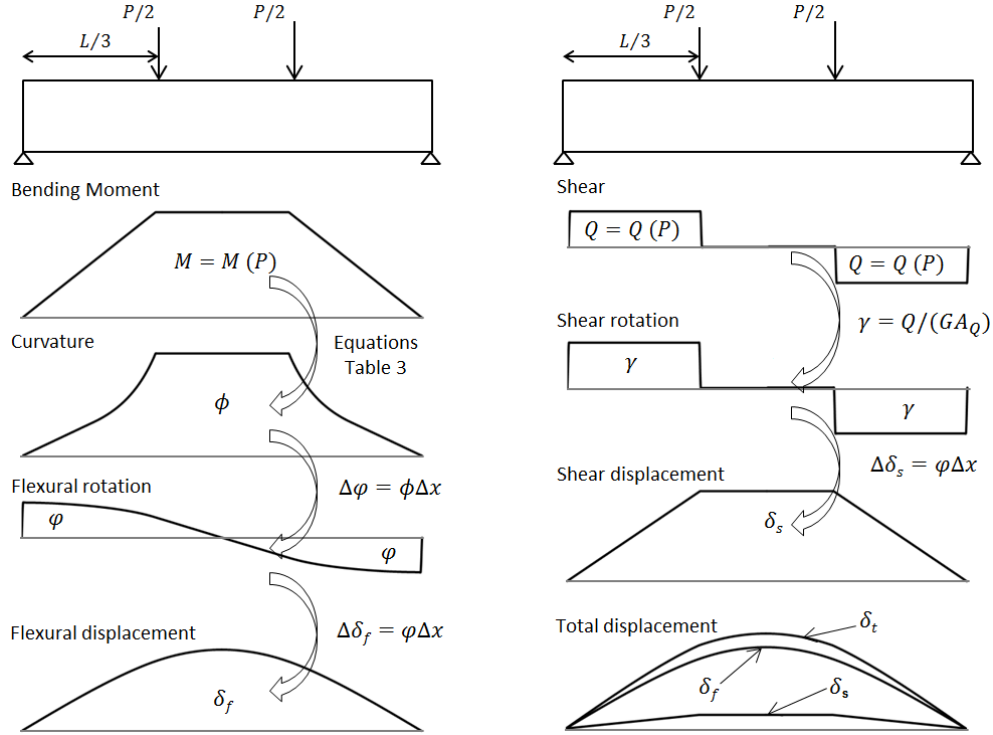
Figure 3.15 Procedure to obtain the load-displacement load up to maximum load due to the flexural and shear forces in an FPBT.

In order to analytically check the displacement to curvature transformation, a numerical load–deflection curve is simulated using the described double integration method. The results shown in Figure 3.16 are obtained for a prismatic specimen with a 100x100 mm square cross-section and a 450-mm span; i.e. a slenderness ratio of 4.5. Checks are also made to see if similar results are obtained for other common specimen sizes, such as 150x150x450, 100x100x300, 50x50x (450,300,150), 200x40x600 and 40x200x600 mm. It is also necessary to define the stress-strain parameters inside the hinge. The selected parameters are: $f_t=$ 9 MPa; $f_{t,u}=$ 10 MPa; $\varepsilon_{t,u}=2.5$‰; $\varepsilon_{t,d,}=$ 1.5%; $\varepsilon_{t,c,}=$ 3.5%; $E=50$ GPa. Similar results can be seen for other UHPFRC types. By following the above-described numerical procedure, geometry and mechanical properties, the load – deflection curve at mid-span up to the maximum load is included in Figure 3.16, left.
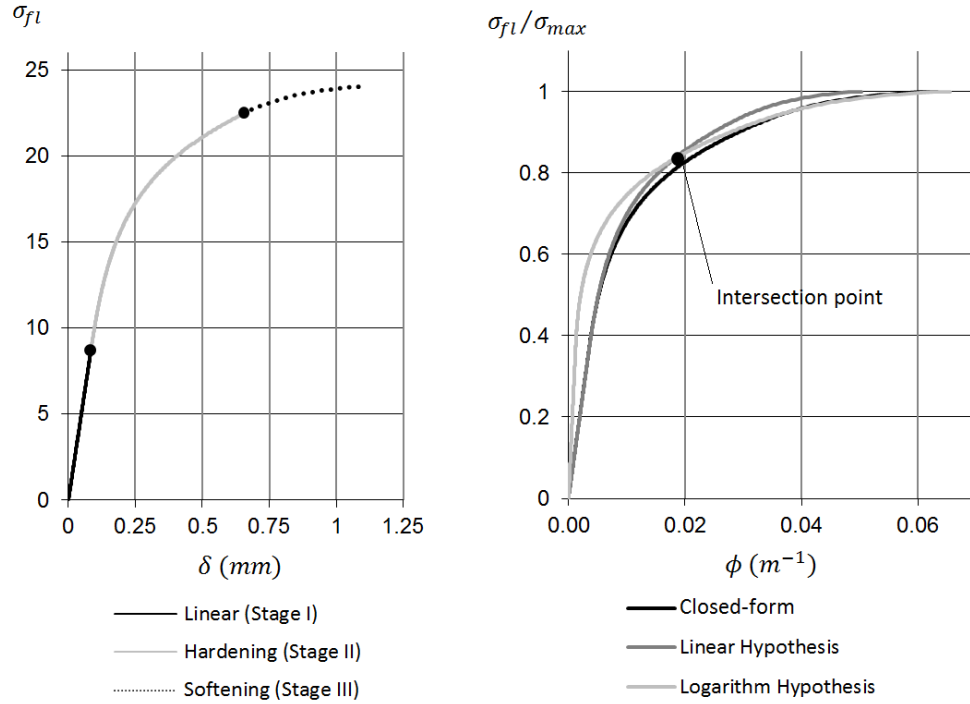
Figure 3.16 The numerical load-deflection curve at mid-span for a prismatic 100x100x450mm TPBT with: $f_t= 9$ MPa; $f_{t,u}= 10$ MPa; $\varepsilon_{t,u}=2.5‰$; $\varepsilon_{t,d}= 1.5\%$; $\varepsilon_{t,c}= 3.5\%$; $E=50$ GPa.

Using the load – deflection curve in Figure 3.16, left, and Eq. 3.23 and Eq. 3.24, the load-curvature curves for the linear and logarithm hypotheses are obtained and are represented in Figure 3.16, right. Using the closed-form $M - \phi$ formulation, the analytical load-curvature curve is also obtained and represented for that specific tensile response. Figure 3.16 (right) offers these three curves. As expected, the theoretical and linear hypotheses almost coincide by up to 70% of the bearing load. Over 70% of the maximum load, the linear hypothesis starts to separate from the theoretical one, while the logarithm hypothesis comes increasingly closer, up to 90%, of the maximum load, when they coincide.

Since the linear hypothesis offers a more accurate estimation at the beginning, and the logarithm approach does so at the end, the best choice is to split the displacement to curvature transformation into two parts by its intersection point (Figure 3.16, right). The final $\phi - \delta$ relationship proposed herein is shown in Eq. 3.29. Another way to define this equation, and perhaps an easier way to introduce it into a spreadsheet, is by taking the highest values obtained by both hypotheses. This alternative form is shown

in Eq. 3.30, and we can observe that both formulations lead to the same δ to ϕ transformation.

$$\phi(\delta) = \begin{cases} \dfrac{216}{23L^2}\left[\delta - \dfrac{12P}{25Eb}\left(\dfrac{L}{h}\right)\right] & \delta \leq \dfrac{PL}{Ebh}\left[\dfrac{12}{25} + \dfrac{9}{16}\left(\dfrac{L}{h}\right)^2 - \dfrac{1}{1200}\left(\dfrac{L}{h}\right)^2\right] \\ \dfrac{72}{5L^2}\left[\delta - \dfrac{P}{6Eb}\left(\dfrac{L}{h}\right)^3 - \dfrac{12P}{25Eb}\left(\dfrac{L}{h}\right)\right] & \delta > \dfrac{PL}{Ebh}\left[\dfrac{12}{25} + \dfrac{9}{16}\left(\dfrac{L}{h}\right)^2 - \dfrac{1}{1200}\left(\dfrac{L}{h}\right)^2\right] \end{cases}$$

Eq. 3.29

$$\phi(\delta) = max \begin{cases} \dfrac{216}{23L^2}\left[\delta - \dfrac{12P}{25Eb}\left(\dfrac{L}{h}\right)\right] \\ \dfrac{72}{5L^2}\left[\delta - \dfrac{P}{6Eb}\left(\dfrac{L}{h}\right)^3 - \dfrac{12P}{25Eb}\left(\dfrac{L}{h}\right)\right] \end{cases}$$

Eq. 3.30

Applying this transformation requires using the elastic modulus (E). Following the linear elasticity theory, and taking shear deflection into account, elastic modulus can be obtained following Eq. 3.31 from one point (δ_i, P_i) in the linear ascending loading branch of the curve.

$$E = \dfrac{P_i}{\delta_i b}\left[\dfrac{23}{108}\left(\dfrac{L}{h}\right)^3 + \dfrac{12}{25}\left(\dfrac{L}{h}\right)\right]$$

Eq. 3.31

In order to understand why a linear hypothesis tends to increasingly separate above 70% of the maximum load, and why the logarithm hypothesis acts in the opposite way, Figure 3.17 is offered. In Figure 3.17, the curvature distribution along the half-beam length for four different loading steps, 50%, 70%, 90% and 100% of the maximum bearing capacity, is drawn for both the different curvature distribution hypotheses, and also the analytical distribution given by the formulation in Table 3.3. For each loading step, the average curvature (ϕ) is taken from the curvatures values in Figure 3.16 (right). By using Eq. 3.19 and Eq. 3.20, the curvature distribution along the beam is obtained for both the linear and logarithm hypotheses.

It is important to remark that the three curvature distributions along the beam offer the same displacement at mid-span for all the load steps, and that the really important parameter is the curvature at Zone 1, which is the average curvature inside the non-linear hinge. As expected, the linear distribution requires a smaller average curvature due to an overestimation in Zone 2 once the analytical curvature distribution loses its linearity. Despite the logarithm hypothesis distribution not being defined at the point where the load is applied ($L/3$), it offers good results when the load is over 70% of the maximum load due to its fast growth.

Based on the obtained results, it can be stated that the proposed δ to ϕ transformation improves existing ones up to the maximum load. I is also simple to use and to implement in a spreadsheet. Although the method is analytically reliable, it is necessary to check it out using the experimental results.
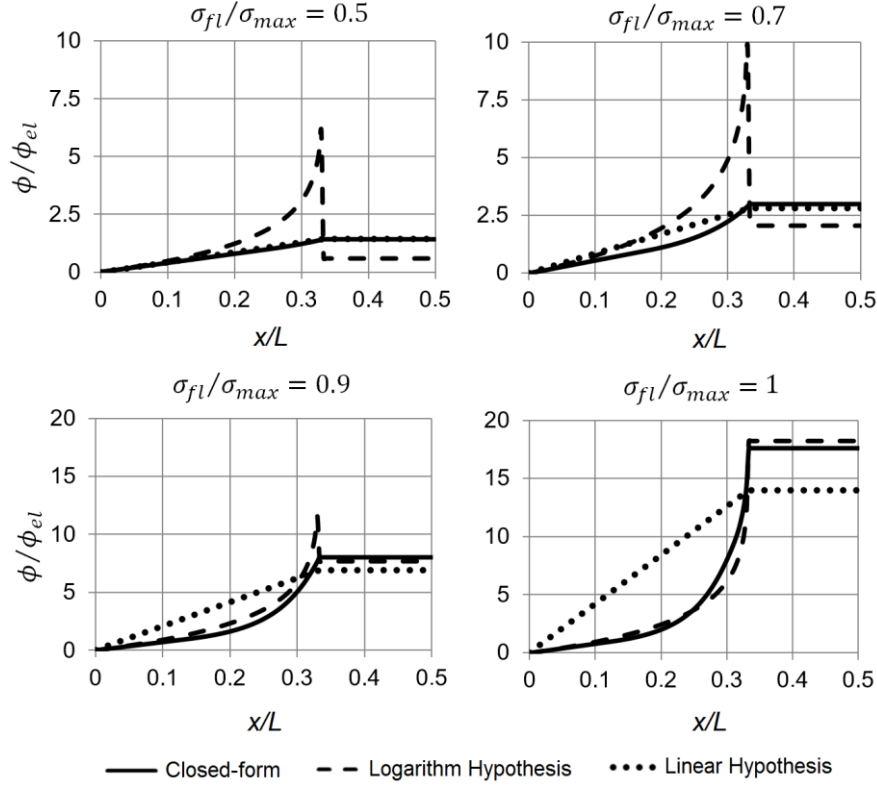
Figure 3.17 Curvature distribution along the half-length beam for several loading steps using the different suggested hypotheses. *f$_t$ = 9 MPa; f$_{t,u}$ = 10 MPa; ε$_{t,u}$ = 0.25%; ‰; ε$_{t,d}$= 1.5%;ε$_{t,c,}$= 3.5%; E=50 GPa, b=0.1m; h=0.1m; L=0.45m.*

3.3.5.2 Experimental validation

The deflection to average curvature transformation method is validated up to maximum load by a theoretical analysis. Besides, the TPBTs performed in (Kanakubo, 2006), in which both the deflection and average curvatures at mid-span were measured, are used to validate the suggested transformation, even in the unloading branch. The deflection to curvature methods proposed in (Rigaudet al., 2011; Qian et al., 2007) are also compared to the experimental data.

The results obtained from the proposed δ to ϕ transformation are checked using the results obtained by Kanakubo (Kanakubo, 2006). Among other aspects, Kanakubo dealt with the inverse analysis problem for UHPFRC. He performed several TPBTs on 100x100x300 prismatic specimens, and measured not only the displacement at mid-span, but also the average strain on both the compressed and tensile faces (Figure 3.18). From the strain measures, and knowing the distance between both LVDTs, it is possible to obtain the average curvature in the central one-third (Zone 1). A comparison between these experimental average curvature values and those obtained by the different δ to ϕ transformations is made.

Displacement at mid-span should be corrected according to the position of the macrocrack before the δ to ϕ transformation to obtain better accuracy in the average curvature estimation after crack localisation (Groegeret al., 2012; Chanvillard, 2002). However since no data are available, its influence for this work is neglected. Only those UHPFRC specimens in which the macrocrack appears inside the central one third are selected. The selected specimens are: BH-2, BH-3, BV-1 and BV-2 (Kanakubo, 2006).
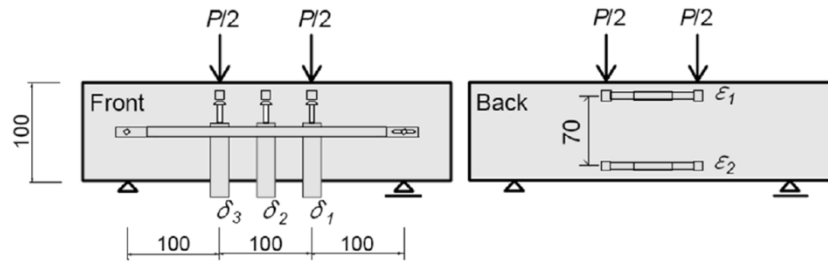
Figure 3.18 The TPBT setup carried out by Kanakubo (Kanakubo, 2006)

The δ to ϕ transformation is also carried out following the equations proposed by Rigaud (Rigaudet al., 2011) and Qian (Qian et al., 2007). The results of the four specimens are depicted in Figure 3.19. The new model very precisely reproduces the experimental results.

Most deviation is located between 70-80% of the maximum load on the ascending branch since neither linear distribution nor logarithm distribution is suitable. However, the new procedure offers a better approach than the previous ones. The new method works much better than others at above 70-80% of the maximum flexural load and on the descending loading branch. Figure 3.19 shows that while the Rigaud and Qian methods produce a significant deviation from the experimental results, the new method reproduces the test even on the unloading branch.
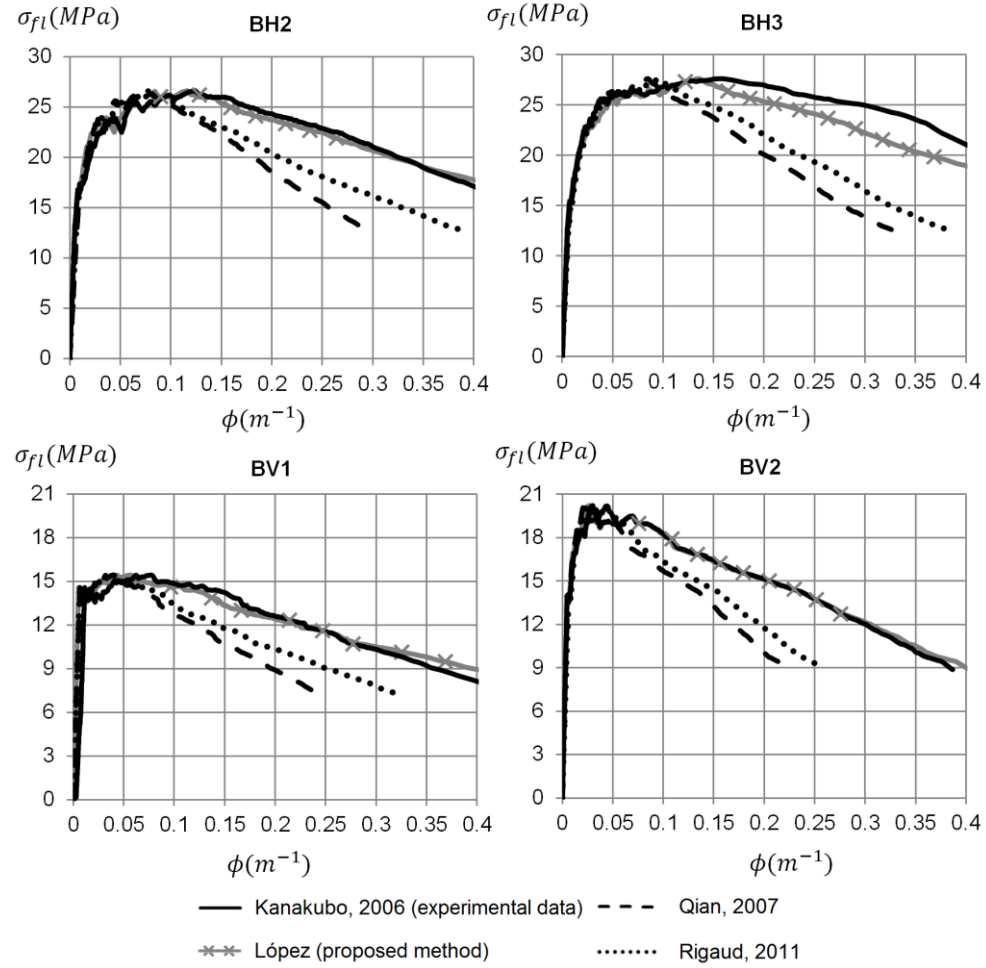
Figure 3.19 The δ to ϕ transformation using the Qian, Rigaud and Lopez methods and their comparison with the experimental results in specimens BH1, BH2, BV1 and BV2 (Kanakubo, 2006)

Figure 3.20 depicts the comparison made between the different methods shown for the BH-2 specimen. The results reveal that, as expected, the methods of Rigaud et al. (Rigaudet al., 2011) and Qian et al. (Qian et al., 2007) underestimate the curvature value at high level loads because of the linear approach that they assumed. Despite using a linear hypothesis, the curvature in the elastic stage is overestimated for a given displacement in these methods, which reults in an underestimation of the elastic modulus (Figure 3.20). The only difference between the Rigaud method (Rigaud et al., 2011) and the linear transformation developed herein is the consideration of shear

deflection. Depending on its size, it may significantly influence specimen behaviour (Graybeal, 2006).
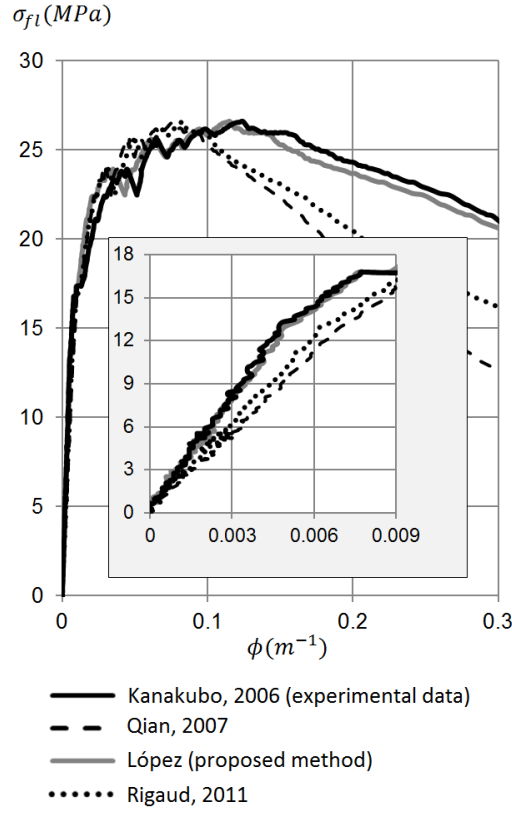
Figure 3.20 Comparison made using the methods of Qian et al., Rigaud et al. and López to the experimental results for the BH-2 specimen.

In the linear elastic phase, the elastic modulus can be easily obtained for a TPBT using Eq. 3.32. In a TPBT, the curvature in the linear elastic phase can be deduced from Eq. 3.23. Both Eq. 3.33 and Eq. 3.34 show the curvature at the mid-span in the linear elastic phase with and without considering shear deflection, respectively.

$$E = \frac{M}{I\phi} = \frac{2PL}{\phi bh^3}$$

Eq. 3.32

$$\phi_{with\_shear} = \frac{216}{23L^2} \left(\delta - \frac{12PL}{25Ebh} \right)$$

Eq. 3.33

$$\phi_{without\_shear} = \frac{216\delta}{23L^2}$$

<div align="right">Eq. 3.34</div>

By substituting Eq. 3.33 and Eq. 3.34 in Eq. 3.32, the relationship between the elastic modulus obtained with and without considering shear deflection can be obtained. This relationship is shown in Eq. 3.35. In these tests the slenderness ratio (L/h) is 3, which means an error of 25% in the elastic modulus estimation if no shear deflection is considered. The analytical results agree with the experimental results shown in Figure 3.20. Therefore by taking shear deflection into account, it is essential to ensure an accurate δ to ϕ transformation.

$$\frac{E_{with\_shear}}{E_{without\_shear}} = 1 + 2.254\left(\frac{h}{L}\right)^2$$

<div align="right">Eq. 3.35</div>

The new proposed methodology improves the existing δ to ϕ transformation methods, and also offers a very good approach to the average curvature measures taken in Zone 1. Thus by this transformation, it is not necessary to measure the average curvature every time a TPBT is conducted, which is sometimes hard to perform since the proposed methodology can reproduce it accurately from the easy deflection at mid-span measure. Note that its accuracy is checked only with deflection-hardening concretes, which are the case of UHPFRCs.

3.3.5.3 Implications for hinge length

The determination of the displacement at mid-span is based on using the average curvature (ϕ) inside the central one-third. As the δ to ϕ transformation is demonstrated to be accurate when the average curvature is measured in Zone 1, hinge length cannot be any other than the central one-third length; i.e. the distance between load rollers. As the method was developed for the TPBT, this length is always one third of the span. This hypothesis leads to a variable hinge length according to both the slenderness ratio and specimen depth. Defined in this way, hinge length is in accordance with not only specimen depth, but also with the slenderness ratio (λ), as Eq. 3.36 shows.

$$s = \frac{L}{3} = \frac{\lambda}{3}h$$

<div align="right">Eq. 3.36</div>

If the slenderness ratio is set, crack hinge length depends only on specimen depth. The research in (Ostergaard et al., 2005) concludes that for a 90% hinge length, specimen depth best fits the FEM models for an FPBT. The commonest TPBT setup uses a slenderness ratio of 3. This test setup leads to a crack hinge length that equals specimen

depth, which comes close to the crack hinge length value proposed in (Ostergaardet al., 2005) for a TPBT. However, if a slenderness ratio of 4.5 is used, hinge length will be one and a half the specimen depth, which does not agree with the commonly assumed characteristic length value.

Therefore, a simple method to work the desired characteristic length must be implemented into the closed-form non-linear hinge model developed so far, which is developed in 3.4.2.

3.4. Checks and supplements to the non-linear hinge model

This section describes issues that are not strictly necessary for the non-linear hinge model definition, but their study is completely necessary for its analytical validation and to fully comprehend the model. A short description of this section content is provided below.

According to 2.7.3, the non-linear hinge model developed by Stang (Stang et al., 1998) requires the boundaries of the non-linear hinge to remain plane after deformation. Note that this model is intended to be used in TPBTs to model the central one-third area, which is indeed a D-region. A preliminary linear analysis run to prove that an average strain plane can be assumed on the boundaries of this area is conducted in 3.4.1.

According to 3.3.5.3, hinge length depends on both the slenderness ratio and specimen test. The formulation needed to consider a characteristic length only according to specimen depth is described in 3.4.2. Moreover, as one of the major uncertainties in a TPBT is the crack's position, a simple formulation for its consideration is presented in 3.4.3. Apreliminary study to justify the assumption of the linearity in compression is also made in 3.4.4

According to Bazant (Bazant, 1989), a fracture mechanics model needs to be able to reproduce the scale effect found in concrete for it to be validated. This is why an analytical study of the scale effect in conventional concrete, fibre-reinforced concrete with high fracture energy and UHPFRC is carried out (3.4.5) using the developed model.

3.4.1. Suitability of the non-linear hinge hypothesis

The developed non-linear hinge model is based on the fact that the boundaries of the non-linear hinge remain plane after deformation. However, the constant bending moment area in a TPBT is usually a D-region as the distance between rollers commonly falls within the specimen depth range. This is why one wonders about the suitability of a TPBT and the analysis of the constant bending moment area to describe the constitutive behaviour of UHPFRC.

As a TPBT assumes that the distance between load rollers is one-third the specimen length, the slenderness ratio ($\lambda = L/h$) plays a very important role. According to EN12390-5:2009, most TPBT tests use a L/h parameter that equals 3. The French UHPFRC guideline (AFGC, 2013) also proposes this relationship for FPBT in square cross-sectioned specimens with variable depths according to the length of fibres. In these cases, the constant bending moment area coincides with specimen depth. A decision to use two different slenderness ratios to develop the model was made. Therefore, it is developed not only for a slenderness ratio of 3, but also for a higher slenderness ratio of 4.5 for the following main reasons:

1. Specimens are still easy to handle if 100-mm-depth beams are used. The maximum fibre length used for UHPFRC is commonly 20 mm. Therefore, a 100 mm-depth specimen is suitable for characterising the commonest UHPFRCs.

2. Point loads create a disruption in the stress field close to the points where they are applied, whose influence is lower the higher the slenderness ratio is.

In order to prove this, a linear elastic 2D FEM model is carried out in SAP2000 to model the behaviour of a square 100-mm cross-section prism tested in a TPBT using a slenderness ratio of 3 and one of 4.5, with an elastic modulus of 48 GPa. The stress distribution field obtained in the central one-third is shown in Figure 3.21 (left). It can be derived from the S11 distribution that, in both cases, the hypothesis of the stress distribution profile being constant inside the central area is not completely right. Shear stresses also appear at any cross-section in this area, even though their sum is null. However, their value is low compared with the tensile strength of UHPFRC and can be neglected.

The non-linear hinge model works with the average deformational behaviour on the boundaries of the hinge which, in a first approach, can be considered the distance between load rollers no matter what the real state of the stresses inside it. So now the question is whether the linear elastic theory predicts the same average curvature and strain as the FEM model. As it is a linear FEM, the $\phi/\lambda P$ and $\varepsilon/\lambda P$ ratios are constant regardless of the slenderness ratio used and the load applied. Following the linear elastic theory, these ratios can be obtained following Eq. 3.37. The results are shown in Table 3.4. Figure 3.21 (right) shows the comparison between the $\varepsilon/\lambda P$ ratio along the specimen depth for the linear elastic beam theory (Eq. 3.37) and the 2D linear elastic FEM.

$$M = EI\phi = \frac{PL}{6} \quad \rightarrow \quad \frac{\phi}{\lambda P} = \frac{2}{Ebh^2}; \quad \frac{\varepsilon}{\lambda P} = \frac{1}{Ebh}$$

Eq. 3.37

Table 3.4 $\chi/\lambda P$ and $\varepsilon/\lambda P$ at the most compressed and tension face obtained from a 2D linear elastic FEM and its comparison with the linear elastic beam theory

	λ	$\phi/\lambda P \ (MN^{-1}m^{-1})$	$\varepsilon/\lambda P \ (MN^{-1})$ (compression)	$\varepsilon/\lambda P \ (MN^{-1})$ (tension)
Linear elastic beam theory		0.0417	0.00208	0.00208
2D linear FEM	3	0.0433	0.00224	0.00215
	4.5	0.0424	0.00215	0.00211

According to the results shown in Table 3.4 and Figure 3.21 (right), we can see that, as expected, the higher the slenderness ratio, the more accurate the linear elastic theory to the FEM.
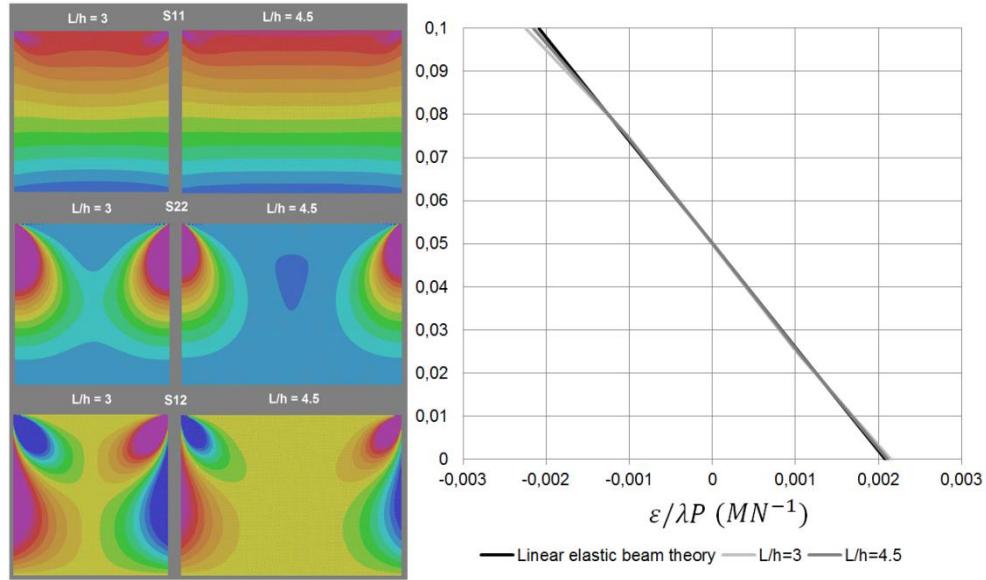
Figure 3.21 Qualitative linear elastic normal stresses in the longitudinal (S11) and transversal (S22) direction, and the shear stresses (S12) in the area between load rollers in a TPBT of a square cross-section 100-mm specimen depth.

Another way to see this is found Figure 3.22, which represents the normal stresses distribution on different layers. In Figure 3.22, $y = h$ at the most compressed layer. The results are plotted at a load of 50 kN when the slenderness ratio is 3 and load is 33.3 kN when it is 4.5 so as to keep the same level of stresses. We can also note from this figure that the maximum linear stress on the most tensioned layer is around 6.5% higher than the linear elastic beam theory with a slenderness ratio of 3, while it reduces to only 2% with a slenderness ratio of 4.5.

The use of a low slenderness ratio leads to a non-homogenous distribution of the stresses in the area between load rollers. Loads create a disruption of the stress distribution field, as predicted by the linear elastic beam theory since these regions are actually D-regions. However, the hypothesis of using the Navier-Bernoulli hypothesis inside this region is no further away from the real behaviour in average terms, as shown in Figure 3.22, and can be considered valid for characterisation purposes.
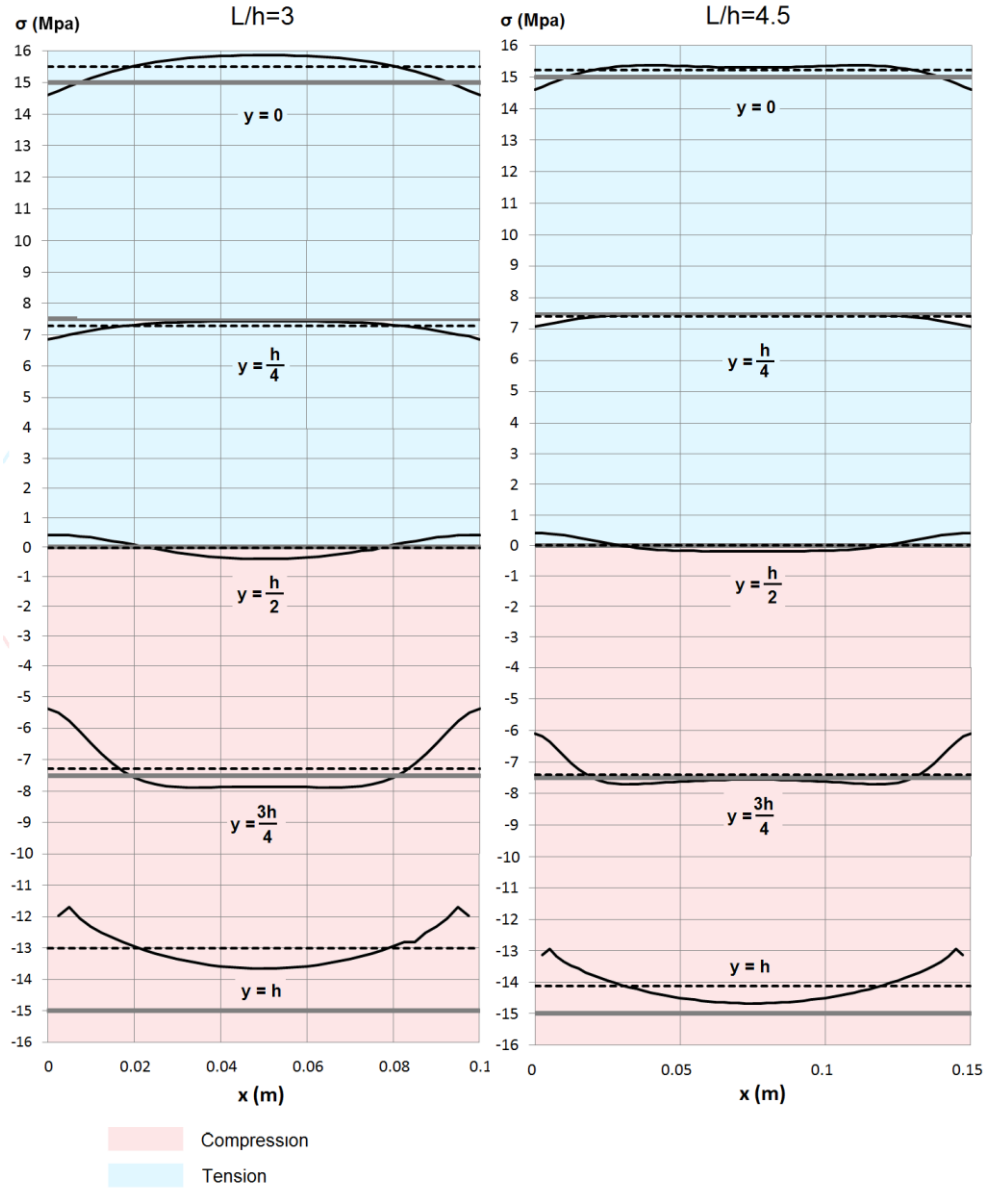
Figure 3.22 Distribution of the S11 stresses along the hinge length in FEM on different layers (black line). Average stress distribution from FEM (dashed line) and linear elastic beam theory hypothesis (grey line).

In addition, shear stress must be evaluated to ensure that the specimen does not undergo non-linear shear deformations. Eq. 3.38 shows the maximum shear stress according to the equivalent flexural strength (σ_{max}) and the slenderness ratio (λ) by assuming a parabolic distribution of the shear stresses along the depth at the support section (linear theory). When a flexural strength of 30 MPa is assumed, the maximum shear stresses at the support reach 7.5 MPa and 5 MPa for a slenderness ratio of 3 and one of 4.5, respectively. Note that at 7.5 MPa, the specimen could already be cracked due to shear forces, or be about to.

$$\tau_{max} = \frac{3\sigma_{max}}{4\lambda}$$

Eq. 3.38

3.   Friction and other phenomena on the supports are low due to the reduced flexural load. Using a slenderness ratio of 4.5, the maximum load lowers to 66%.

4.   Larger constant-moment areas improve the determination of multiple cracking and average crack spacing, and also enhance further studies to determine the influence of the crack position along the central one-third and the strain profile that surrounds the crack.

The above-described paragraphs show the influence of the slenderness ratio on non-linear hinge model performance. The selection of this ratio is important as it (i) affects the accurateness of the non-linear hinge model; (ii) has a huge influence on whether the linear behaviour of the specimen remains under shear forces; (iii) determines hinge length according to the curvature to deflection transformation in 3.3.5. A minimum slenderness ratio of 3 should be used for UHPFRC to keep the specimen uncracked under shear forces. This value agrees with existing test setup standards.

3.4.2. Modification of crack hinge length

An important issue that may be a matter of concern to some researchers is the fact that the considered characteristic length is according to not only specimen depth, but also to the slenderness ratio in line with Eq. 3.36. This assumption is the result of the curvature distribution assumption along the central one-third of the specimen, when the transformation of the displacement at mid-span into average curvature (ϕ) was developed. As all the kinematics properties refer to the central one-third length, the non-linear hinge length can be no other than the central one-third length. As the non-linear hinge model was developed for the TPBT, this length is always one third of the length. This hypothesis leads to a variable hinge length in accordance with the slenderness ratio and specimen height.

However, hinge length is not supposed to be in accordance with the slenderness ratio. The curvature distribution assumed while developing the deflection to curvature transformation is shown in Figure 3.23. It leads to an average curvature distribution at mid-span after maximum load as depicted in Figure 3.23 (left). Assuming a shorter

hinge length implies there having to be a shorter length around the crack, where the Bernoulli hypothesis can also be assumed. The minimum length in which that is true in a 1D model is the so-called characteristic length or the crack affection length (l_c) of the test.

Once crack localisation has taken place at the end of the hardening phase, the average curvature within the characteristic length (ϕ_{ch}) must be higher than ϕ (Figure 3.23, left), assuming that the characteristic length is always shorter than central one-third. On the crack affection zone edges, a curvature distribution following the unloading branch (ϕ_{ul}) (Figure 3.23, right) should be found. On the boundaries of the constant bending moment area, the average curvature must be ϕ. If we assume that this is true, the weighted average between these two curvatures, ϕ_{ch} and ϕ_{ul}, must be ϕ. This relationship is shown in Eq. 3.39.
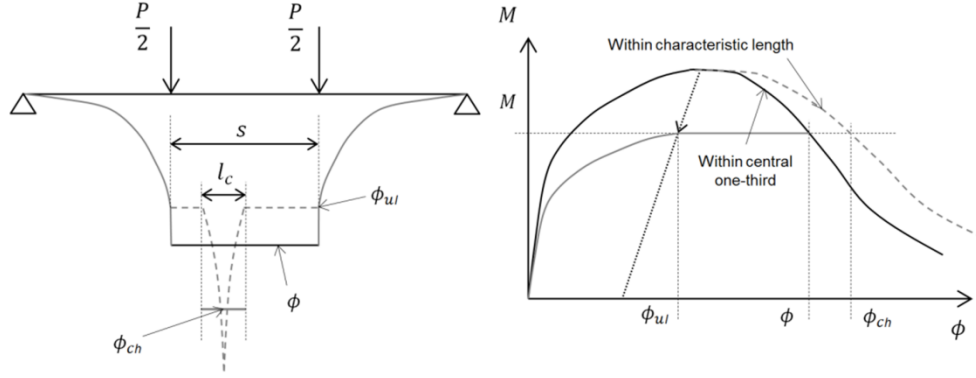
Figure 3.23 Curvature distribution along a beam (left) during a TPBT for bending moment "*M*" on the unloading branch (left); bending moment versus curvature relationship (right).

$$\phi = [\phi_{ul}\left(\frac{L}{3} - L_c\right) + \phi_{ch}l_c]\frac{3}{L}$$

<div align="right">Eq. 3.39</div>

Characteristic length is often expressed according to specimen depth, which is why parameter κ is introduced with the meaning shown in Eq. 3.40

$$l_c = \kappa h$$

<div align="right">Eq. 3.40</div>

If characteristic length were known, it would be possible to obtain the average curvature inside the cracking zone after the crack localisation point. Then it would be possible to obtain the bending moment – average curvature curve in the cracking zone (Figure 3.23, right), and also its corresponding stress-strain response. This process

would lead to an increased strain capacity of the hinge. In this case, hinge length would not be the central one-third any more, but the previously defined characteristic length (l_c).

From Eq. 3.39 and Eq. 3.40, a characteristic curvature (ϕ_{ch}) can be expressed, as pointed out in Eq. 3.41, where λ is the slenderness ratio (L/h).

$$\phi_{ch} = \phi_{ul} + \frac{\lambda}{3\kappa}(\phi - \phi_{ul})$$

Eq. 3.41

According to the linear elastic beam theory, the expression in Eq. 3.42 can be written for a TPBT.

$$\Delta\phi = \frac{2}{Eh}\Delta\sigma$$

Eq. 3.42

Using Eq. 3.42 and according to Figure 3.23 (right), the unloading curvature (ϕ_u) can be derived using Eq. 3.43, in which ϕ_{loc}, σ_{loc} and E^* are the average curvature and the equivalent strength at the crack localisation point; i.e. when the softening process starts, and the unloading modulus, respectively.

$$\phi_{ul} = \phi_{loc} - \frac{2}{E^*h}(\sigma_{loc} - \sigma)$$

Eq. 3.43

At this point it is important to bring back the deflection to curvature transformation developed in 3.3.5. In this case, the equivalent strength is used instead of the applied load to simplify the subsequent formulation. As the increase in curvature affects only the unloading branch, the logarithm transformation is used. It is shown in Eq. 3.44.

$$\phi = \frac{72}{5L}\left[\frac{\delta}{L} - \frac{\sigma}{6E}\left(\frac{L}{h}\right) - \frac{12\sigma}{25E}\left(\frac{h}{L}\right)\right]$$

Eq. 3.44

By introducing Eq. 3.43 and Eq. 3.44 into Eq. 3.41, a new curvature to deflection transformation beyond the maximum load can be derived. As this equation is too complicated, it is derived for three specific cases. It is always safe to use a slightly higher value for the unloading modulus than the real one. This is why it has been considered that the unloading modulus is one fifth of the elastic modulus for simplicity. This assumption agrees with the research conducted in (Wille et al., 2011). The three cases are described below and are governed by the equations in Table 3.5. Note that the cases in which characteristic length corresponds to the constant bending moment area,

the displacement to curvature transformation corresponds to the logarithm one developed in 3.3.5. The same process can be followed for other λ, κ values.

Table 3.5 Curvature to deflection transformation that takes into account the characteristic length in the TPBT

Curvature to deflection transformation			δ
Up to the end of the microcracking stage			$min\left\{\begin{array}{c} \dfrac{23L^2}{216}\phi + \dfrac{12\sigma L}{25E}\left(\dfrac{h}{L}\right) \\ \dfrac{5L^2}{72}\phi + \dfrac{\sigma L}{6E}\left(\dfrac{L}{h}\right) + \dfrac{12\sigma L}{25E}\left(\dfrac{h}{L}\right) \end{array}\right\}$
λ	κ	E^*	
3	1	$0.2\,E$	$\dfrac{5L^2}{72}\phi + \dfrac{\sigma L}{6E}\left(\dfrac{L}{h}\right) + \dfrac{12\sigma L}{25E}\left(\dfrac{h}{L}\right)$
	0.5	$0.2\,E$	$\dfrac{1}{2}\left[\dfrac{5L^2}{72}\phi + \dfrac{(1021\sigma - 823\sigma_{loc})L}{300E} + \delta_{loc}\right]$
4.5	1.5	$0.2\,E$	$\dfrac{5L^2}{72}\phi + \dfrac{\sigma L}{6E}\left(\dfrac{L}{h}\right) + \dfrac{12\sigma L}{25E}\left(\dfrac{h}{L}\right)$
	1	$0.2\,E$	$\dfrac{1}{3}\left[\dfrac{5L^2}{36}\phi + \dfrac{(3417\sigma - 2389\sigma_{loc})L}{600E} + \delta_{loc}\right]$
	0.5	$0.2\,E$	$\dfrac{1}{3}\left[\dfrac{5L^2}{72}\phi + \dfrac{(2646\sigma - 2389\sigma_{loc})L}{300E} + 2\delta_{max}\right]$

After applying this new curvature to displacement transformation, hinge length is no longer the distance between rollers, but now coincides with characteristic length and only depends on specimen depth.

3.4.2.1 Implications of the hinge length modification

The consequences of the previous assumption can be better explained with an analytical example. According to Figure 3.2, the curvature to displacement transformation is applied on the load–curvature curve, which is obtained from the closed-from load–curvature relationship. In order to do this, the simplified quadrilinear stress-strain relationship has to be previously obtained according to hinge length (or characteristic length). Note that the assumed hinge length modifies the quadrilinear

stress-strain relationship and determines the curvature to displacement transformation that must be used.

Let's assume a TPBT with a slenderness ratio of 4.5 and a 100-mm depth square cross-section specimen. The assumed constitutive behaviour is shown in Figure 3.24. According to the assumed non-linear hinge length (or characteristic length), the stress-strain response inside the hinge differs. The different quadrilinear stress-strain responses for a κ value of 1.5, 1 and 0.5 are depicted in Figure 3.25 according to Eq. 3.11 and Eq. 3.12. Note that the hinge length assumption does not affect the strain-hardening properties in the model.
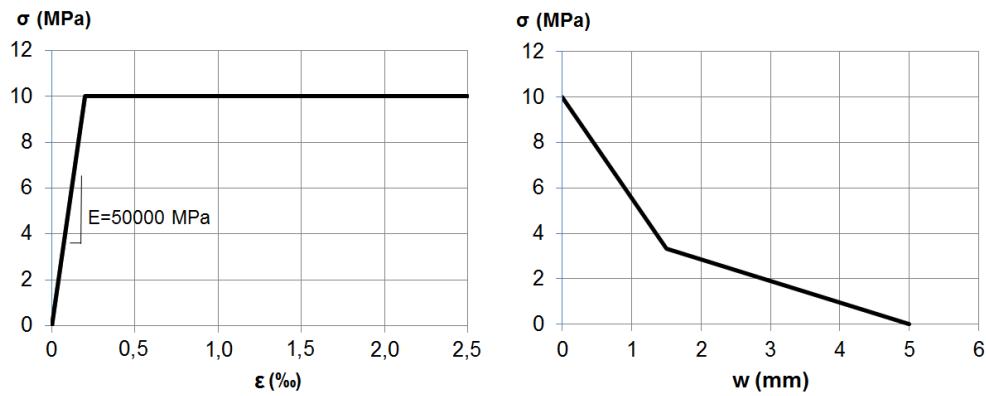
Figure 3.24 Typical constitutive behaviour for UHPFRC.

Using the closed-form formulation in Table 3.1 and Table 3.3, the equivalent bending strength versus curvature relationship can be easily derived from the three different stress-strain responses in Figure 3.25. These curves are plotted in Figure 3.26. Two important things can be derived from Figure 3.26. The most obvious one is the greater hinge length rotation capacity if a lower hinge length is assumed. The second one is less noticeable; it is the scale effect at the peak. In this figure, the influence of the first softening line on the maximum load is seen. More details about the scale effect can be found in 3.4.5. Note that this scale effect is not due to a variation in specimen depth, but to a variation in hinge length.

Once the equivalent strength versus curvature relationship is obtained, the load-deflection curve can be easily derived using the equations in Table 3.5. At this point it is worth remembering that no matter the selected hinge length, the average curvature measured on the constant bending moment area edges is always going to be ϕ. So as the average curvature controls the displacement at mid-span, the three curves in Figure 3.26 are expected to offer the same equivalent strength versus displacement at mid-span curve. The results are shown in Figure 3.27.
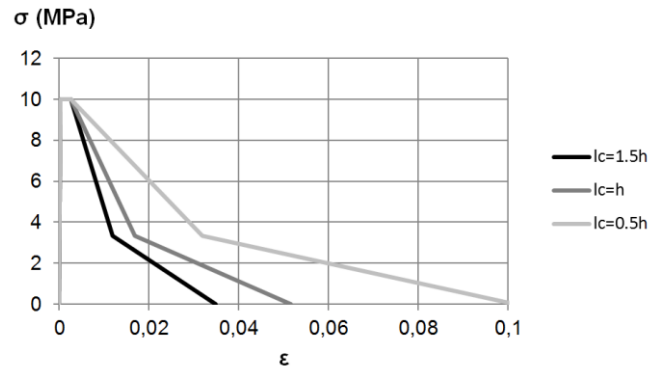
Figure 3.25 Stress-strain response according to characteristic length.
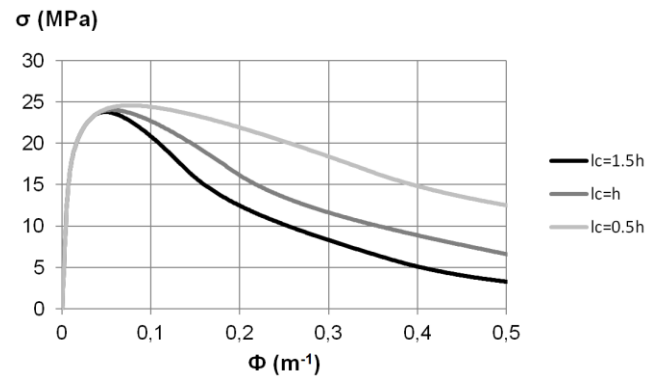
Figure 3.26 Equivalent strength versus curvature curves for the different hinge length assumptions.
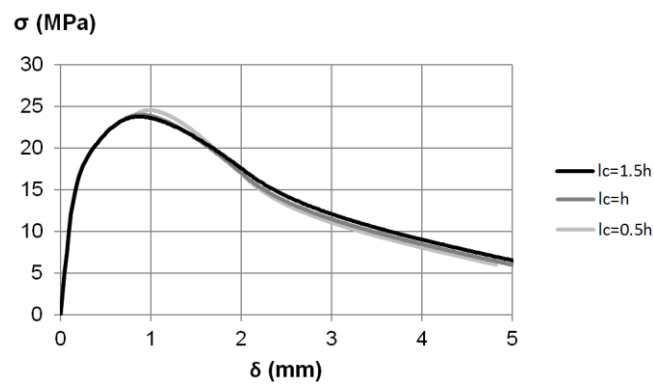
Figure 3.27 Equivalent strength versus displacement at mid-span for the different crack hinge length assumptions.

According to the developed model, these results have a very important implication for TPBTs: 'The crack hinge length assumption has little effect on the determination of the constitutive properties of a specimen tested in a TPBT in strain hardening materials'. However, this is not true for strain-softening materials in which the first softening line strongly influences the flexural bearing capacity, and hinge length greatly influences the flexural response. This fact is shown in 3.4.5.

3.4.3. The crack's position

The crack's position is one of the most important causes of variability in the unloading response in unnotched FPBTs. As noticed in (Chanvillard et al., 2003), for the same crack opening angle, the displacement measured at mid-span can be reduced up to a 66% if the crack appears on the border of the central one-third. Not considering this fact is probably one of the reasons that lead to replace the unnotched FPBT by the notched three-point bending test as a standard test to characterise the tensile properties of FRC. It is worth highlighting that German recommendations for FRC (DAfStB, 2015) still include FPBT as a standard, and remarking the wide variability obtained. Probably introducing a parameter that takes into account the crack's position inside the constant bending moment area would help reduce variability.

This correction parameter is easy to obtain by assuming that after crack localisation takes place, the two concrete blocks on each side of the crack behave like rigid bodies, as illustrated in Figure 3.28. Figure 3.28 represents two different cases: (i) the crack appears at the mid-span section; (ii) the crack appears in an arbitrary section within the central one-third. In both cases, the crack's rotation angle is the same and equals φ. The main purpose is to establish a relationship between the displacement at mid-span in both cases and the distance d, which indicates the crack's position.
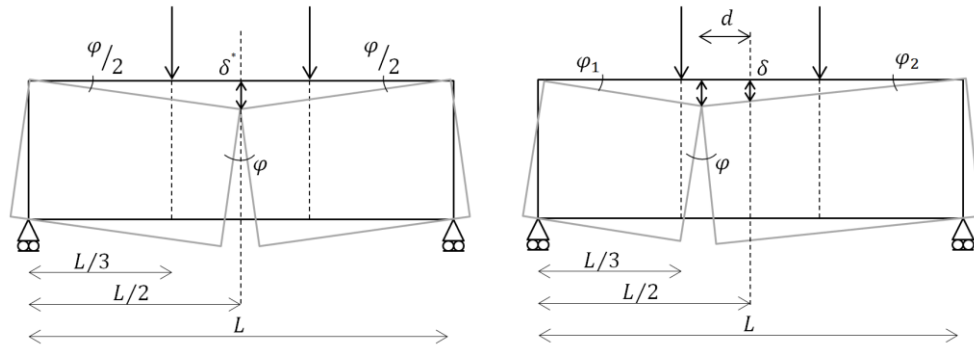
Figure 3.28 Deflection at the mid-span scheme when the crack appears at mid-span (left) and outside it (right).

From Figure 3.28 (left), displacement at mid-span can be written according to the rotation angle and specimen length is that shown in Eq. 3.45.

$$\delta^* = \frac{\varphi L}{4}$$

<div align="right">Eq. 3.45</div>

In Figure 3.28 (right), angles φ_1 and φ_2 are related by the expression in Eq. 3.46.

$$\varphi_1 \left(\frac{L}{2} - d \right) = \varphi_2 (\frac{L}{2} + d)$$

<div align="right">Eq. 3.46</div>

In addition, the crack's total rotation angle is the sum of these two angles, as pointed out in Eq. 3.47.

$$\varphi = \varphi_1 + \varphi_2$$

<div align="right">Eq. 3.47</div>

The displacement at mid-span in Figure 3.28 (right) can be expressed as in Eq. 3.48.

$$\delta = \frac{\varphi_2 L}{2}$$

<div align="right">Eq. 3.48</div>

Solving Eq. 3.46, Eq. 3.47 and Eq. 3.48 leads to Eq. 3.49.

$$\delta = \frac{\varphi}{2} (\frac{L}{2} - d)$$

<div align="right">Eq. 3.49</div>

Now the relationship between δ^* and δ can be established, as shown in Eq. 3.50.

$$\delta^* = \frac{1}{1 - 2 \left(\frac{d}{L} \right)} \delta$$

<div align="right">Eq. 3.50</div>

It is important to note that parameter d varies from 0 to L/6 and that the displacement which would have been measured if the crack had appeared at mid-span varies from 1 to 1.5 times the displacement at mid-span actually measured for an arbitrary crack location.

In order to allow a soft transition after the crack localises, a linear expression according to the stress level reached is introduced. It is considered that correcting the displacement due to the crack's position only affects the unloading branch, while the

loading branch remains the same no matter what the crack's position. The increase in displacement due to the crack's position is shown in Eq. 3.51. It is important to note that no correction factor is applied at the maximum load. When no load is applied, the correction factor coincides with the correction factor in Eq. 3.50. Note that the correction factor is given as an increase in displacement, which needs to be added to the displacement measured at mid-span.

$$\Delta\delta_{cp} = \left(1 - \frac{\sigma}{\sigma_{max}}\right)\left[\frac{1}{1 - 2\left(\frac{d}{L}\right)} - 1\right]\delta$$

<div align="right">Eq. 3.51</div>

In real experimental tests, a crack is not a straight line, and a measurement criterion should be provided. Parameter d is defined as the distance between the crack's location and mid-span, measured at the most compressed layer according to Figure 3.28.

Figure 3.29 illustrates the crack location correction proposed herein for the analytical example presented in 3.4.2.1. As equivalent strength versus deflection at mid-span is almost the same regardless of the selected crack hinge length, and a crack hinge length of 1.5 times specimen depth is used. An arbitrary d value of 50 mm is considered to show the effect of crack location correction.
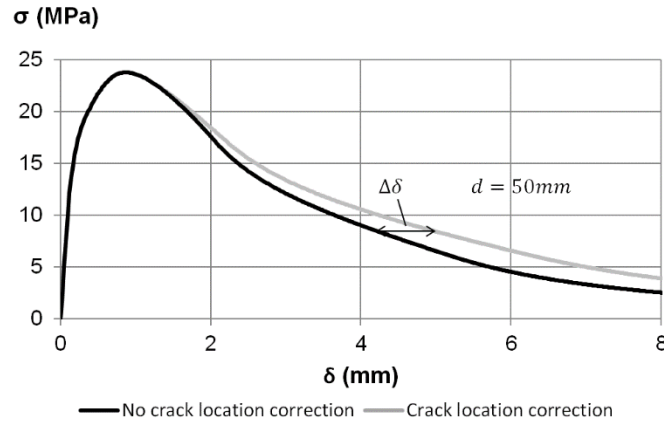
Figure 3.29 Effect of crack location correction on the stress-deflection response of a TPBT.

3.4.4. Influence of the linear elastic hypothesis in compression

The influence of the linear elastic hypothesis in compression has not been analytically studied. Instead the influence of this hypothesis has been studied for worst case scenarios. It is known that the influence of plastic UHPFRC behaviour in compression is stronger when: (i) the lesser the compressive strength; (ii) the greater the tensile strength; (iii) the smaller the specimen depth; (iv) the smaller the elastic modulus.

An analytical study has been conducted following the test setup configuration of the A TPBT with a slenderness ratio of 3 with 100-mm square cross section specimens. Behaviour in compression is considered elasto-plastic with an elastic modulus of 45 GPa. The end of the linear branch finishes when compressive strength is reached. Then a plastic branch up to a maximum strain value of 4‰ is used. After this value, linear softening is considered with an ultimate strain value of 10‰ at zero stress. Concretes with a compressive strength of 80, 100, 125 and 150 MPa are modelled. The parameters that define the tensile response are obtained from Figure 2.14, and corresponds to a 211 MPa compressive strength concrete with a 2% of 13/0.2 steel fibres. These parameters are: f_t =10 MPa; $f_{t,u}$ = 14 MPa; $\varepsilon_{t,u}$ = 8‰; w_d = 3 mm; w_c = 6.5 mm. A hinge length that equals specimen depth is used. These responses are compared to the hypothesis of linear elastic behaviour in compression. Note that in order to obtain the load-cuvature and load-strain curves of a material with non-linear behaviour in compression, the closed-form formulations in Table 3.1, Table 3.2 and Table 3.3 cannot be employed. For this case, a numerical model to obtain the sectional response is programmed in Matlab.

Figure 3.30 depicts the strain at the most compressed and tension faces within hinge length according to the flexural equivalent strength. Here we can see that there is a relevant difference in the strain determination at the most compressed face depending on the assumed constitutive behaviour in compression.
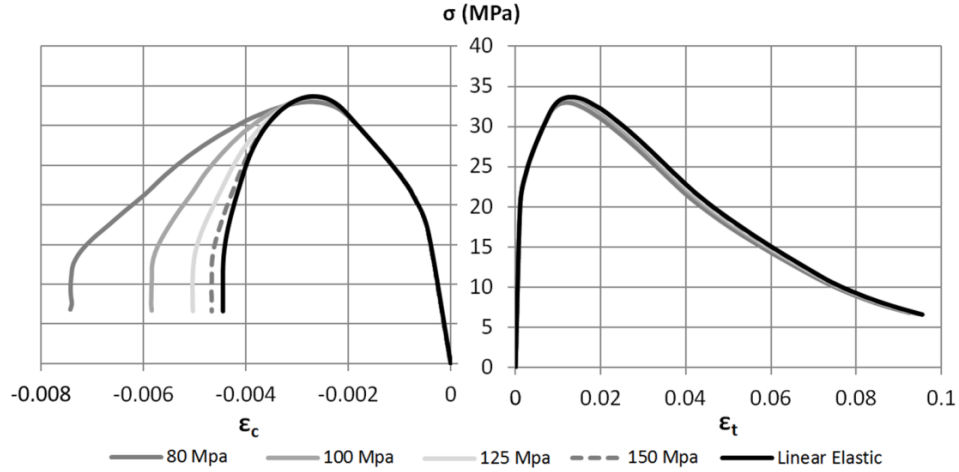
Figure 3.30 Strain at the most compressed (left) and tension (right) faces within hinge length for different constitutive behaviours in compression.

However, these differences are small when determining the strain at the most tensioned face. Note that the values in compression are much smaller than the values in tension. Therefore, the average curvatures inside the hinge must come close to each other for the different developed models. Note that the inverse analysis methodologies shown in

this work (Chapters 4 and 5) are based on the determination of the average curvature in the non-linear hinge. The linear relationship in compression can be considered valid if the load–curvature curve is similar for the different constitutive relationships. It is important to remark that an inverse analysis method based on the determination of the strain at the most compressed face, which assumes a linear relationship in compression, cannot be considered valid if a linear elastic behaviour in compression is contemplated. This is probably the reason why this type of inverse analysis method has not yet been developed.

As shown in Figure 3.31 (left), the stress-curvature relationships for the different hypotheses come very close to each other, as predicted from Figure 3.30. The biggest error in the determination of displacement at any point on the curve in Figure 3.31 is about 5.5%, and is 3% in the 80 and 100 MPa compressive strength model. When compressive strength is higher, the error is almost zero.

Since the hypotheses taken in this analysis are quite conservative, and as the compressive strength of UHPFRC is systematically greater than at least 125 MPa, the hypothesis of considering a linear elastic behaviour in compression is valid and no further correction factors are needed.
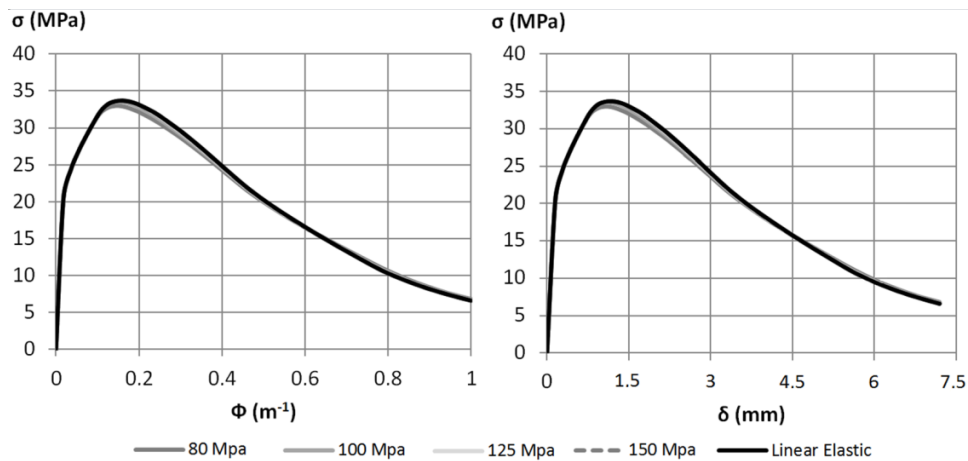
Figure 3.31 Curvature within hinge length (left) and displacement at mid-span (right) according to the equivalent flexural strength for different constitutive behaviours in compression.

3.4.5. Scale effect

According to Bazant (Bazant, 1989), for a fracture mechanics model to be validated, it has to be able to reproduce the scale effect found in concrete. This is why an analytical study of the scale effect in (i) conventional concrete, (ii) fibre-reinforced concrete with high fracture energy and (iii) UHPFRC is carried out in this section using the developed model.

The non-linear crack hinge model developed herein is able to reproduce the scale effect on concrete in both flexural strength and deformation. As previously mentioned, this model assumes that the crack hinge length is $\lambda h/3$, and a slenderness ratio that equals 3 is used for this particular case. Hence all the numerical results are shown for a crack hinge length that equals specimen depth.

Following the closed-form non-linear hinge model developed in a TPBT with a slenderness ratio of 3, the load versus displacement at mid-span curves is obtained for six different specimen depths, 100 mm, 150 mm, 200 mm, 500 mm, 1000 mm and 2000 mm. In the first step, it is necessary to define the tensile material properties, which can be assumed as intrinsic material properties if the fibre orientation effects and scale defects are neglected; i.e. if the statistical scale effect is neglected. If only considering a deterministic model, the tensile properties of UHPFRC can be defined by a stress-strain relationship up to the maximum tensile strength and a softening stress-crack opening relationship, according to Figure 3.3, for all the specimens, no matter what their size is.

Even though UHPFRC is already cracked in the hardening stage, it is commonly assumed that the strain-hardening phase itself is a material property and is not affected by scale effects; i.e., crack spacing is not influenced by specimen depth. Recent studies have proved that crack spacing varies according to specimen depth, even if the slenderness ratio remains constant (Nguyen et al., 2012). Nevertheless, these results may not be attributed to a deterministic scale effect, but to fibre orientation effects, which are more relevant the larger the cross-section area is.

As this phenomenon is still not fully understood, a decision was made to compare two different UHFPRCs with different stress-strain laws up to the peak (see Figure 3.32 and Figure 3.33). The softening stress-crack opening relationship used for both UHPFRC is the same. If the stress-strain behaviour up to peak is affected by a deterministic scale effect, the expected results can be found between the two UHPFRC responses.

A third concrete type, which corresponds to C30 according to MC2010 (Figure 3.34), is used to compare the results to a traditional scale effect formulation. The C30 tensile strength considered is 2.9 MPa and the crack opening at zero stress is 0.073 mm. The unloading modulus (E^*) used in the strain-hardening UHPFRC is 10 GPa. Elastic unloading is considered for strain-softening UHPFRC and C30 as no yielding is allowed in tension.

After defining the material's tensile behaviour, the stress-crack opening relationship is turned into stress-strain behaviour along the non-linear hinge length using Eq. 3.11 and Eq. 3.12. After obtaining the stress-strain behaviour, the bending moment-average curvature along the hinge length curve is derived using the formulation in Table 3.3. The load-deflection curve is then obtained using Table 3.5.
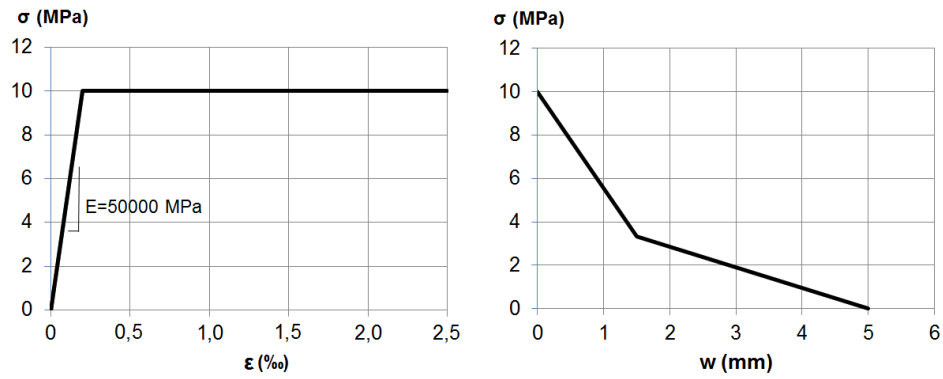
Figure 3.32 The constitutive tensile relationship considered for UHPFRC with hardening
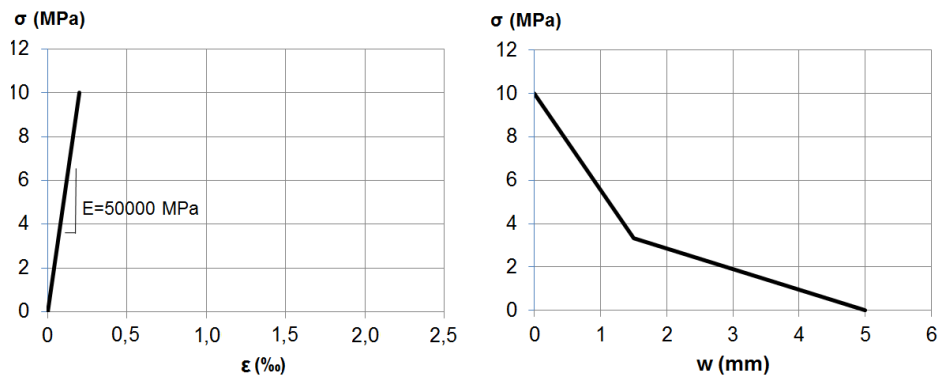
Figure 3.33 The constitutive tensile relationship considered for UHPFRC without hardening
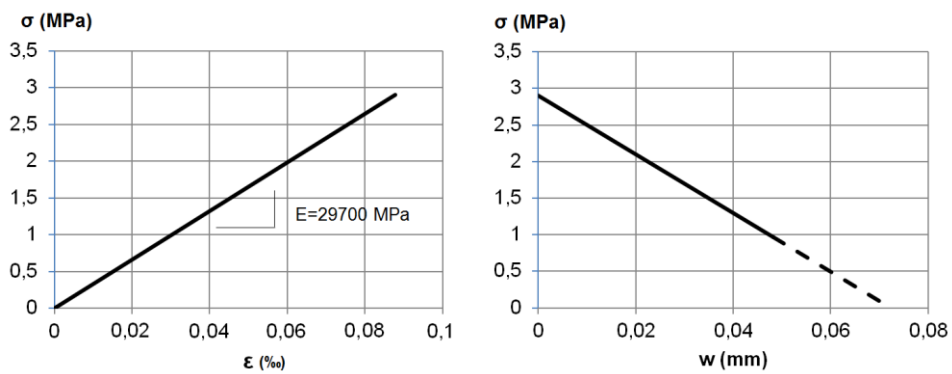
Figure 3.34 The simplified constitutive tensile relationship considered for C30 according to MC2010.

The scale effect is studied using the normalised strength and displacement in Eq. 3.52 and Eq. 3.53, where δ_{el} is the displacement at the end of the elastic stage according to Eq. 3.54, which can be derived from the linear elastic theory by adding the shear deflection term.

$$\sigma_{fl} = \frac{M}{W_{el}} = \frac{Pl}{bh^2}$$

Eq. 3.52

$$\delta_n = \frac{\delta}{\delta_{el}}$$

Eq. 3.53

$$\delta_{el} = \left[\frac{23}{108} \left(\frac{L}{h} \right)^2 + \frac{12}{25} \right] h \frac{f_t}{E}$$

Eq. 3.54

Figure 3.35 depicts the flexural $\sigma_{fl} - \delta_n$ response for the three different constitutive relationships in Figure 3.32, Figure 3.33 and Figure 3.34. Figure 3.35 (a) represents the flexural UHPFRC behaviour with a strain capacity of 2.5‰. Figure 3.35 (b) depicts a strain-softening UHPFRC with the same fracture energy. Figure 3.35 (c) illustrates the flexural behaviour expected for a C30 according to MC2010.

The results in Figure 3.35 agree with the experimental results found in the literature. Lepech and Li (Lepech et al., 2004) reported that the size effect on the flexural strength of engineered cement composites (ECCs) was negligible compared to reinforced concrete specimens given its high ductility. When comparing Figure 3.35 (a) and Figure 3.35 (b), it can be concluded that the strain-hardening branch significantly reduces the scale effect on strength compared to the same material without that plastic branch. Conversely, Nguyen et al. (Nguyen et al., 2014) reported a clear size effect on strength upon the peak using a 2% content in the volume of steel fibres, probably due to fibre orientation effects.
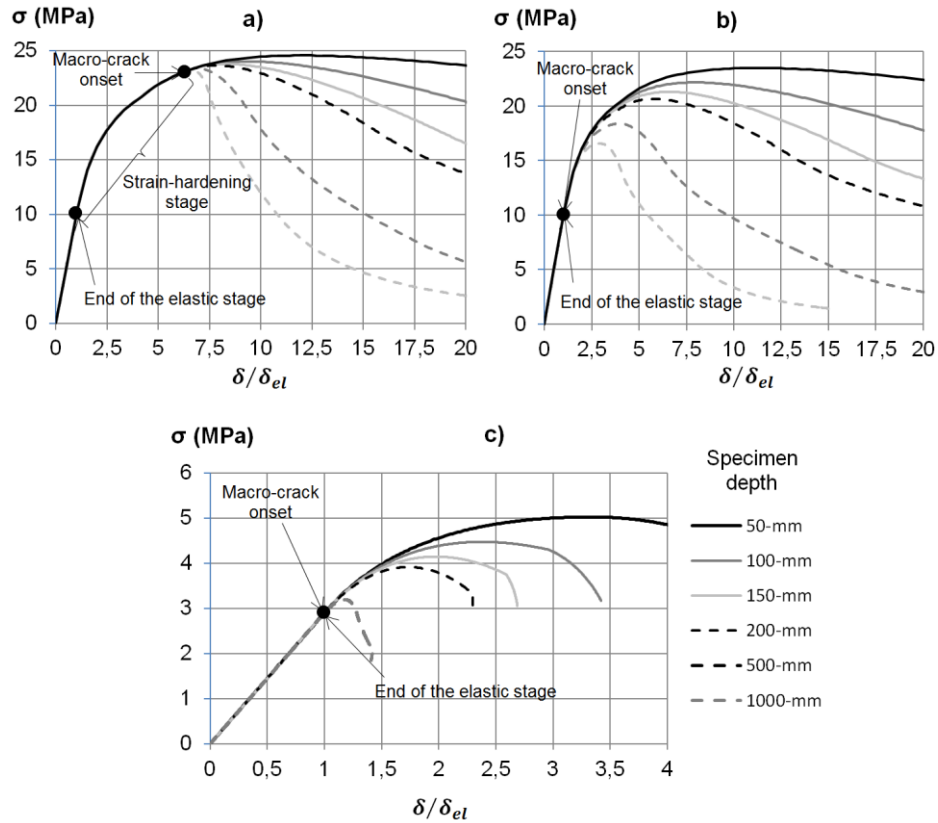
Figure 3.35 Normalised flexural strength *vs.* normalised displacement for different specimen depths and distinct tensile constitutive relationships: a) UHPFRC with hardening; b) UHPFRC without hardening; c) C30.

The model also agrees with Spasojevic et al. (Spasojevic et al., 2008), who discovered that UHPFRC, characterised by a strain capacity of 2-3‰, showed a reduced size effect on the flexural response. Our results also agree with Kim et al. (Kim et al., 2010), who found that the flexural strength and normalised deflection capacity for fibre-reinforced concretes (FRCs) increased as specimen size decreased.

It is worth emphasising that the pure (deterministic) size effect can be distorted by statistical effects, especially when fibre orientation is induced for any reason; e.g. specimen size and geometry, pouring system, etc. This could explain the dependence on the ratio between section width and depth that Reineck and Frettlohr found in the flexural strength capacity of UHFPRC (Reineck et al., 2010), and the clear size effect reported by Nguyen et al. (Nguyen et al., 2014).

When modelling strain-hardening materials, two limit cases are identified: (i) when considering elastic perfectly plastic material tensile behaviour, the maximum flexural capacity is 3 times the cracking strength, no macrocrack appears and no scale effect is detected; (ii) when considering elastic perfectly brittle material tensile behaviour, and when not considering linear elastic fracture mechanics, flexural strength coincides with tensile strength, brittle behaviour is expected in bending, and a macrocrack appears with a null tensile force transfer over the crack. Therefore, no scale effect is detected. The three different modelled concrete types fall between these two limit cases; therefore, the scale effect appears. Its magnitude depends on both strain-hardening and stress-crack opening behaviours. From the results offered in Figure 3.35, several conclusions about the scale effect phenomenon can be drawn:

- The developed non-linear hinge model can predict the scale effect found in concrete, regardless of its fracture energy and the tensile behaviour considered up to the peak
- The scale effect appears once the macrocrack starts developing. This scale effect appears in all existing concretes and becomes more pronounced the lower fracture energy considered
- The materials that display pronounced strain-hardening behaviour (higher than 2‰) have a less significant scale effect on both the strength and normalised deflection at the peak because macrocrack onset appears at over 95% of maximum flexural capacity
- If no strain-hardening behaviour is considered, the larger the fracture energy, the less significant the scale effect. In this case, if a bilinear softening stress-crack opening relationship is used, total fracture energy is not what really matters, but the initial slope of the stress-crack opening law. Obviously, these two parameters are related to each other, so the lower the initial slope, the greater the fracture energy and the less significant the scale effect.
- If the hardening phase turns out to be a scale effect parameter, UHPFRC behaviour should be somewhere between the results shown in Figure 3.35 (a) and Figure 3.35 (b). In this case, a significant difference in terms of cracking and ultimate load may be found, especially for high depth values.

The scale effect upon the peak is commonly used to describe this phenomenon. Figure 3.36 represents the scale effect on both normalised strength and deflection. As the deflection upon the peak is normalised by the deflection at the end of the elastic stage, it provides information about the size effect on ductility.
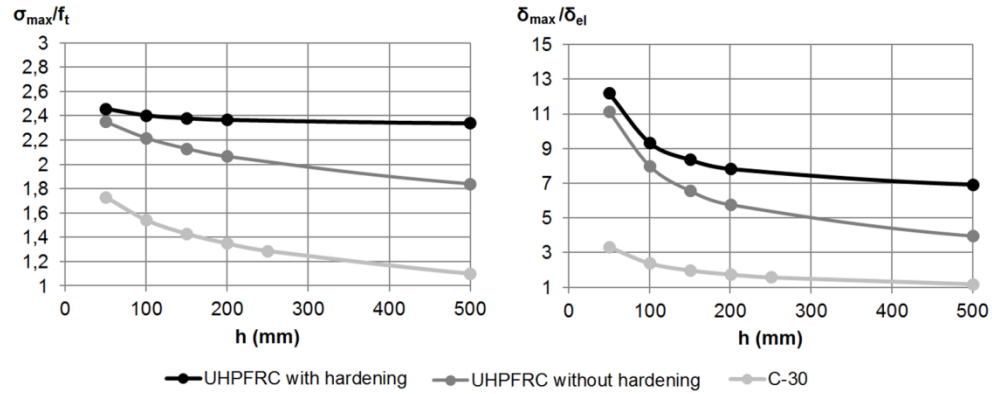
Figure 3.36 Scale effect on normalised strength (left) and deflection (right)

According to Figure 3.36, it is concluded that:

- Scale effect on strength is low for strain-hardening materials
- For strain-softening materials, this effect is more pronounced and increases as fracture energy decreases
- Strain-hardening materials are more ductile
- The greater the fracture energy, the greater ductility becomes
- Ductility significantly reduces as specimen depth increases for all concretes
- The scale effect on ductility is stronger on strain-softening materials with great fracture energy

3.4.5.1 Bazant size effect law

According to (Bazant, 1989), a basic criterion for the acceptability of non-linear fracture mechanics models for concrete is that they must describe the size effect law. The equation that describes the size effect according to Bazant is described in Chapter 2, and is reminded in Eq. 3.55.

$$\sigma_N = Bf_t \left(1 + \frac{h}{h_0} \right)$$

Eq. 3.55

Figure 3.37 depicts a logarithm representation of the size effect on the strength determined for UHPFRC with hardening, UHPFRC without hardening, but with the same fracture energy, and a C30 according to the developed hinge model.
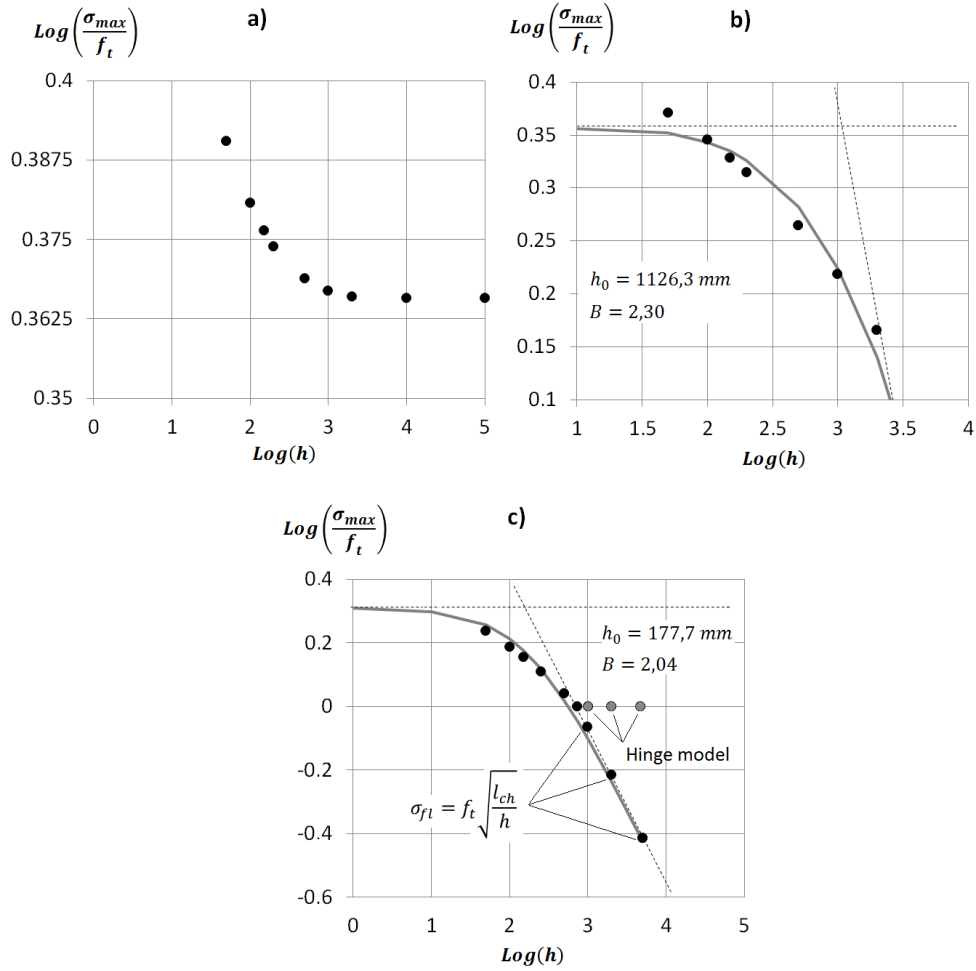
Figure 3.37 Logarithm representation of the scale effect for different specimen depths and distinct tensile constitutive relationships: a) UHPFRC with hardening; b) UHPFRC without hardening; c) C30.

For UHPFRC without hardening and C30, the results follow the size effect law proposed by Bazant, but UHPFRC with hardening does not. This is because the stress-strain hardening behaviour is considered size-independent as there is no information in the current literature about how the deterministic size effect on strain-hardening UHPFRC behaviour is.

A deterministic size effect on strain hardening UHPFRC behaviour probably exists. It can be determined by testing different specimens with distinct geometries. Although it has already been conducted in (Kim et al., 2010; Frettlöhr et al., 2011), it is quite

difficult to distinguish between a deterministic and a statistical (fibre orientation effect) size effect. However, it seems that the greater the specimen depth, the larger the spacing between cracks and, therefore, the lower the strain upon the peak. If this can be confirmed, a deterministic size effect for the hardening phase can be defined.

Although it is somewhat hidden behind the obtained results, the characteristic length, as defined in 2.3.1, plays an important role in the results and is strongly related to hinge length. Its influence is more clearly distinguishable in the C30 results. It is important to remember that the average stress-strain behaviour on the non-linear hinge is obtained from the stress-crack opening relationship following Eq. 3.56 with strain-softening material.

$$\varepsilon = \frac{\sigma}{E} + \frac{w}{s}$$

Eq. 3.56

As defined in Eq. 3.36, hinge length depends only on specimen depth if the slenderness ratio remains constant. This occurs in this analysis, where the slenderness ratio remains equal to 3, and hinge length corresponds to specimen depth. The main consequence of the hinge's average stress-strain behaviour is that the greater specimen depth, the steeper the softening stress-strain response and, up to a certain depth in which this response becomes a vertical line. This happens when hinge length coincides with characteristic length, as defined in Eq. 3.57; i.e. when the volumetric elastic energy stored in the hinge equals the fracture energy. The non-linear hinge model applied to a strain-softening material implies that once cracking strength is reached, the volumetric energy absorbed in the hinge is released and absorbed by the crack. Following the tensile parameters in Figure 3.34, the characteristic length for the analysed C30 is 742 mm. As hinge length coincides with specimen depth in the analysed cases, once specimen depth reaches characteristic length, the test exhibits brittle failure and flexural strength coincides with tensile strength.

$$l_{ch} = \frac{2EG_f}{f_t^2}$$

Eq. 3.57

If specimen depth is greater than characteristic length, once f_t is reached the available volumetric elastic energy in the hinge that can be released upon crack formation is greater than the fracture energy. According to Griffith's balance energy criterion (Griffith, 1921), crack growth stability is guaranteed if the available strain energy is lower than the fracture energy. Thus a reduction in flexural strength is required to accomplish Griffith's balance criterion if specimen depth is greater than characteristic length. However, the proposed hinge model considers that for the specimen depths that are larger than characteristic length, flexural strength coincides with cracking strength,

which may be wrong. The volumetric strain energy (G) per unit of area upon cracking strength can be expressed following Eq. 3.58.

$$G = \frac{f_t^2}{2E}\, s \leq G_F$$

<div align="right">Eq. 3.58</div>

If hinge length is longer than characteristic length, it is assumed that flexural strength follows the linear fracture mechanics theory, and that flexural strength is in accordance with the inverse of the square root of the depth according to Eq. 3.59. This is represented in Figure 3.37 (c). As the characteristic length on fibre reinforced concrete is much longer than the common representative dimensions of structures, this situation never takes place in either structures or characterisation tests.

$$G = G_F \;\leftrightarrow\; \frac{f_t'^2 s}{2E} = \frac{f_t^2 l_{ch}}{2E} \;\leftrightarrow\; f_t' = f_t \sqrt{\frac{l_{ch}}{s}} \;\;;\;\; s > l_{ch}$$

<div align="right">Eq. 3.59</div>

Note that the larger the considered hinge length, the lower the specimen depth at which the volumetric strain in the hinge equals the fracture energy. This is why hinge length selection is quite important for conventional concrete. Figure 3.38 shows the size effect on strength for C30 for different crack hinge lengths, where the size effect law can be seen to differ according to them. For those depths at which hinge length is longer than characteristic length, Eq. 3.59 is used.

The size effect law in the bending proposed in MC2010, which relates flexural strength to tensile strength for conventional concrete (Eq. 3.60), is also included in Figure 3.38. As we can see, the proposed hinge model and the MC2010 formulation offer a similar approach for a 100-500 mm specimen depth range. However, as we can see in Figure 3.38, left, the equation proposed in MC2010 does not follow the Bazant size effect law.

$$f_t = f_{ct,fl}\, \frac{0.06 h^{0.7}}{1 + 0.06\, h^{0.7}}$$

<div align="right">Eq. 3.60</div>
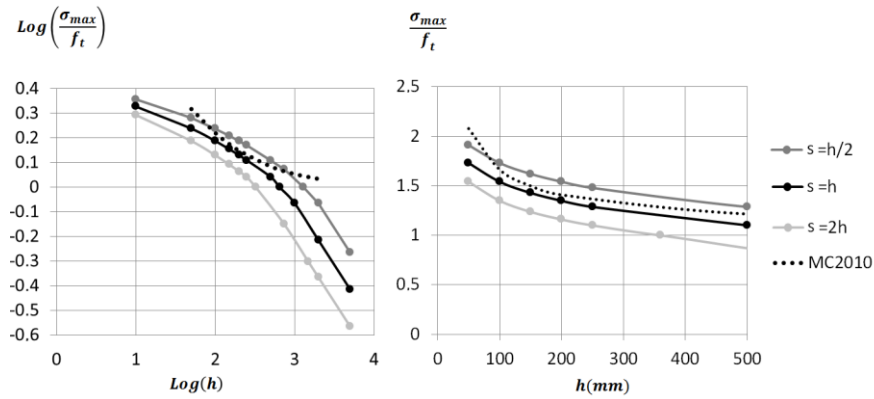
Figure 3.38 The size effect law according to the non-linear hinge model developed for different hinge length assumptions and its comparison to the size effect law in MC2010.

3.5. Summary

A closed-form non-linear hinge model has been developed specifically for modelling flexural UHPFRC behaviour in a TPBT. This new hinge model is a great step forward in the current non-linear hinge flexural models for the following reasons:

- Unlike most non-linear hinge models, this model is to be specifically applied to TPBTs instead of three-point bending tests
- It includes strain hardening UHPFRC behaviour
- It offers a closed-form analytical solution for the sectional and structural specimen behaviour for a selected hinge length.
- It includes the crack position consideration

This model has been developed by assuming the following hypotheses:

- Linear elastic behaviour in compression, proved suitable for UHPFRC
- A bilinear strain-hardening behaviour in UHPFRC tension
- A bilinear softening stress-crack opening behaviour in UHPFRC tension with a change in slope at one third the tensile strength
- The same elastic modulus in tension as in compression
- Unloading modulus equals one fifth the elastic modulus. It is only assumed when for the development of the curvature to deflection transformation when the considered hinge length differs from the constant bending moment area
- Rectangular cross-section
- Strain plane remains plane on the boundaries of the hinge during all the loading and unloading processes
- Linear elastic behaviour under shear forces, proved suitable if the slenderness ratio is higher than 3 for UHPFRC

The model requires the following inputs:

- TPBT geometry: slenderness ratio (λ), and either test span (L) or specimen depth (h). A suitable slenderness ratio for a UHPFRC characterisation purpose is either 3 or 4.5
- Material constitutive behaviour in tension given by: (i) a stress-strain relationship up to the maximum strength defined by cracking strength (f_t), elastic modulus (E), tensile strength ($f_{t,u}$) and its associate strain ($\varepsilon_{t,u}$); (ii) a stress-crack opening relationship defined by the crack opening upon change of slope (w_d) and characteristic crack opening (w_c)
- Crack hinge length must equal or be lower than the distance between load rollers. Hinge length selection has a huge influence on sectional UHPFRC behaviour determinations, but has a minor influence on structural load-deflection behaviour determinations. This is true for strain-hardening materials

Using these inputs, material constitutive behaviour must be turned into a stress-strain response inside the hinge using Eq. 3.11 and Eq. 3.12. Once the stress-strain response inside the hinge is obtained, the model enables the direct determination by a closed-form formulation of the following sectional responses curves associated with hinge length:

- Load – curvature response
- Load – strain at any layer
- Strain – curvature
- Load – crack depth
- Load – crack opening (macrocrack opening)

'Load' can also refer to the bending moment or equivalent flexural strength as they are linearly linked.

Among all the section responses of the hinge, the load–curvature response is used to determine the load–deflection at mid-span curve, which defines the specimen's structural behaviour. This is obtained by a curvature to displacement transformation. Even though this transformation has been obtained for different hinge length assumptions, it has been proved that the hinge length assumption has barely any influence on the load – deflection behaviour in a TPBT on strain-hardening materials such as UHPFRC.

The developed closed-form non-linear hinge is a powerful tool that will be used as the foundation of an iterative and a simplified inverse analysis methodology to derive the material properties from a load–deflection response obtained from a TPBT. The different sectional responses inside the hinge will be used to check them. These inverse analysis methods and their corresponding experimental validations are described in Chapter 4 and Chapter 5, respectively.

Chapter 4

Iterative Inverse Analysis Methods

4.1. Introduction

As indicated in Chapter 3, the closed-form non-linear hinge model description has been developed. The next step is how to use it to derive the tensile properties of UHPFRC knowing the load-displacement at mid-span response obtained from a TPBT. This is the main aim of an inverse analysis methodology. Using the closed-form $M - \phi$ formulation developed herein and the suggested δ to ϕ transformation, a load-curvature inverse analysis method can be easily proposed. In this chapter, two different load-curvature inverse analysis methods, according to the classification described in Figure 2.28, have been proposed based on the developed closed-form non-linear hinge model: (i) an iterative method and (ii) a point-by-point method. The procedure to carry out these inverse analysis methodologies are explained and an experimental programme is run to check that the non-linear hinge model offers results that agree with the experimental measurements taken from the tests. Even though the inverse analysis methodologies proposed in this chapter are not new, their use according to the support of a theoretical model has never been performed before. That is probably the main reason why these methods have always been suspected of not offering good solutions.

Finally, the major problems of these methodologies are highlighted, together with some ideas to overcome them, by the development of simplified inverse analysis methodologies.

4.1. Load–curvature inverse analysis methods

The iterative and point-by-point inverse analysis methods share the same initial steps. Firstly, the experimental load–displacement at mid-span must be obtained from a TPBT. For each experimental point $P_i - \delta_i$, the δ to ϕ transformation in Table 3.5 is applied to obtain the $P - \phi$ experimental curve. It is common to use either the equivalent flexural strength, σ_{fl}, instead of the applied load, or the moment at mid-span. The used transformations are shown in Eq. 4.1 for a rectangular cross-section and a TPBT setup.

$$\sigma_{fl} = \frac{6M}{bh^2} = \frac{PL}{bh^2}$$

Eq. 4.1

Precisely at this point, either an iterative or point-by-point inverse analysis method can be followed to obtain the average stress-strain relationship along the assumed hinge length. Afterwards, suitable transformations to derive the stress-crack opening constitutive relationship must be applied according to the hinge length used.

4.1.1. Iterative load-curvature inverse analysis method (I-IA)

Once the $P - \phi$ curve is obtained for a specifc hinge length using Table 3.5, an initial stress-strain tensile response inside the hinge has to be assumed. By employing the same curvature values obtained from the experimental curve, the $M - \phi$ relationship can be derived from the tensile response by assuming the $M - \phi$ closed form in Table 3.3. With Eq. 4.1, the bending moment can be converted into equivalent flexural stress, and the experimental and numerical values of σ_{fl} can be compared for each ϕ value.

Note that the $M - \phi$ obtained from the closed-form formulation (analytical curve) depends on the selected constitutive tensile parameters. Besides for each ϕ point, we have only one σ_{fl} point for each experimental and analytical curve. Thus the analytical curve can be fitted to the experimental curve by a numerical iterative process, and by varying the constitutive tensile parameters to achieve the minimal sum of the residual squares of the σ_{fl} for each curvature value (Figure 4.1).

Since the $\sigma_{fl} - \phi$ relationship is derived from a closed-form solution, the iterative process is truly effective and fast. A common and widely available tool for this process can be the Excel SOLVER tool. At the end of the process, the $\sigma - \varepsilon$ relationship that describes the sectional response of the non-linear hinge can be obtained. The inverse analysis procedure is summarised in Figure 4.1. Finally, the softening branch of $\sigma - \varepsilon$ must be turned into $\sigma - w$ using Eq. 3.11 and Eq. 3.12 according to the hinge length used. The unloading modulus (E^*) can be derived from a different test, considered one fifth of the elastic modulus, or its influence can be neglected if no data are available for simplicity reasons.
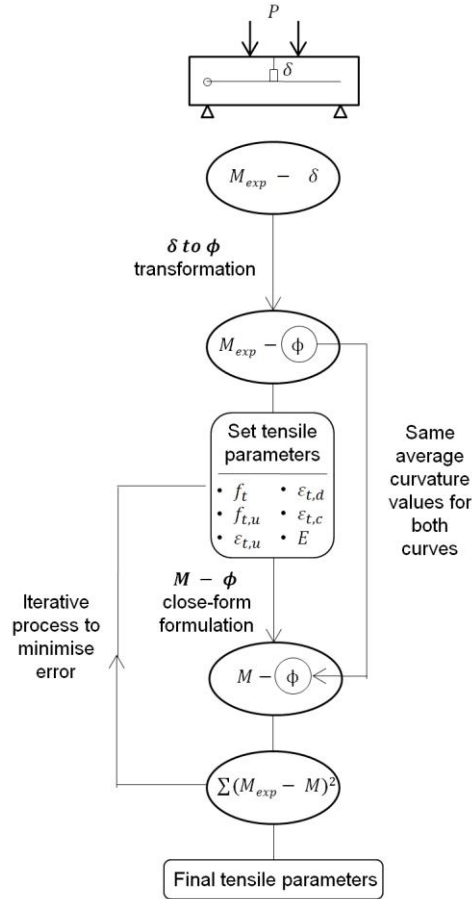
Figure 4.1 Scheme of the iterative load-curvature inverse anlaysis method (I-IA)

4.1.2. Point-by-point load-curvature inverse analysis method (PBP-IA)

As described in 2.6.1.4, point-by-point inverse analysis methods do not require having to assume any constitutive parameters in tension. Linear elastic behaviour is considered in compression. Once the experimental $M - \phi$ has been derived using the δ to ϕ transformation for a specific hinge length, a point-by-point inverse analysis, like that described in 2.6.1.4, can be directly applied. All the details needed for its application are described in that section. The result of its application is a rough $\sigma - \varepsilon$ curve in tension. However, it consists in a rough curve that is difficult to work with and must be simplified. Simplification consists in fitting a quadrilinear law to the obtained rough curve. The rough curve is fitted to a quadrilinear relationship with the criteria of keeping the same area under the curve and minimising the error between the two curves.

At the end of this method, the $\sigma - \varepsilon$ relationship that describes the sectional response of the non-linear hinge can be obtained. As in the iterative method, the last step is to convert the softening $\sigma - \varepsilon$ relationship into $\sigma - w$ according to the selected hinge length.

Note that the sectional simplified quadrilinear $\sigma - \varepsilon$ response that derives from the point-by-point inverse analysis does not have to accomplish the condition assumed in the non-linear hinge model, for which stress upon the change of the slope in the softening branch is one third of the maximum tensile stress. This is why the closed-form solution in Table 3.3 cannot be applied with the results obtained from the point-by-point inverse analysis.

4.1.3. Example of an application

An example of both the presented inverse analysis methods is shown in this section using the experimental load-deflection curve obtained in (Kanakubo, 2006) for the specimen BH-2 tested in a TPBT with a slenderness ratio of 3. It is considered that hinge length equals specimen depth according to the presented non-linear hinge model.

The first step is to determine the load-curvature curve from the experimental equivalent stress-deflection one. For this purpose, the equations in Table 3.5 are used to convert the displacement at mid-span into average curvature at the hinge, and those in Eq. 4.1 are used to convert load into equivalent flexural strength. The experimental $P - \delta$ at mid-span and the $\sigma - \phi$ curves are depicted in Figure 4.2.
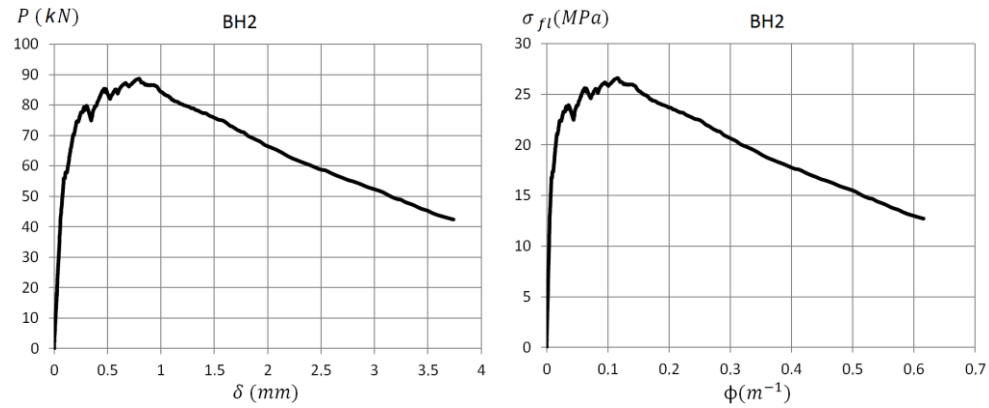
Figure 4.2 Experimental $P - \delta$ at mid-span of specimen BH-2 (Kanakubo, 2006) and the $\sigma - \phi$ curve derived from it according to the developed non-linear hinge model.

Once the $\sigma - \phi$ curve has been obtained, both the I-IA and PBP-IA methods can be applied to this curve to derive the $\sigma - \varepsilon$ relationship in uniaxial tension, which describes the sectional behaviour inside the hinge. The results are shown in Figure 4.3.

Once the quadrilinear $\sigma - \varepsilon$ relationship is obtained, the bilinear $\sigma - w$ can be derived using Eq. 3.11 and Eq. 3.12. As no data about the unloading modulus value are available, in this particular case it is considered to be one fifth of the elastic modulus. The results are represented in Figure 4.4, where we can see that both methods offer similar results. Note that for the $\sigma - w$ relationship, the iterative process, which is derived from the non-linear hinge model, establishes stress upon the change of slope in one third of the maximum tensile strength. However in the point-by-point inverse analysis, the method selects the point that best fits the point-by-point $\sigma - \varepsilon$ relationship, which corresponds to a slightly higher stress. As both methods are based on a minimum square adjust procedure, both methods offer similar results in fracture energy terms. The fracture energies obtained from both the I-IA and PBP-IA methods are $26.2 \ kJ/m^2$ and $27.9 \ kJ/m^2$. The maximum fibre length used in the BH-2 specimen is 15 mm, which is approximately double the characteristic crack opening (w_c) obtained in the inverse analysis (see Figure 4.4).
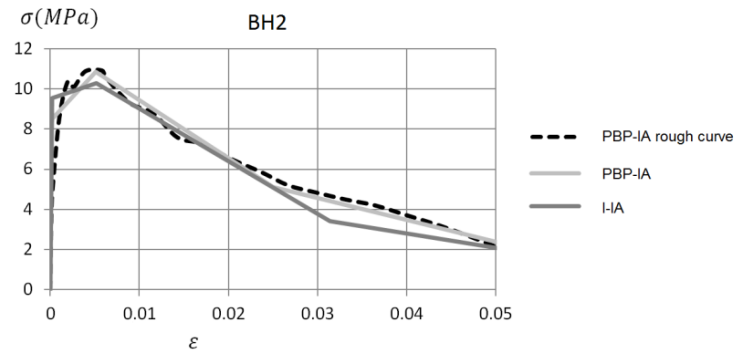
Figure 4.3 The $\sigma - \varepsilon$ relationship in uniaxial tension that describes the sectional behaviour inside the hinge using both I-IA and PBP-IA in specimen BH-2 (Kanakubo, 2006).
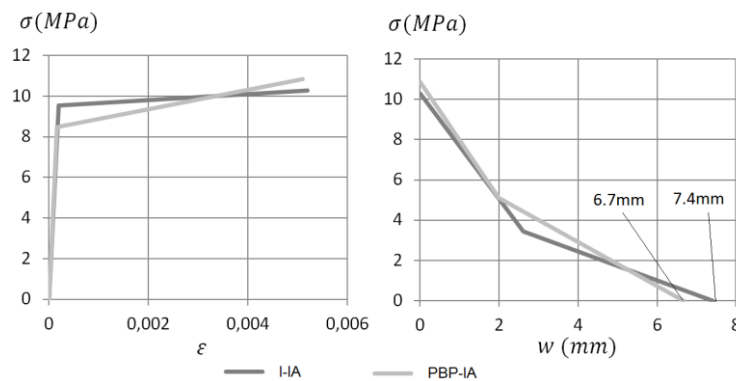
Figure 4.4 Complete description of the tensile behaviour of specimen BH-2 (Kanakubo, 2006).

In his tests, Kanakubo did not only measure deflection at mid-span, but also two strain measures on the boundaries of the central one third. These measures were taken at a distance from the top and bottom faces of 15 mm according to Figure 3.18, and provide information about the sectional response of the hinge, if it is considered equal to specimen depth.

As the constitutive behaviour obtained from the I-IA has the shape required to apply the non-linear hinge, it is possible to derive $\sigma - \delta$, $\sigma - \phi$ and $\sigma - \varepsilon(y)$ on different layers. For the constitutive behaviour obtained from PBP-IA, the numerical sectional analysis tool developed in Matlab is used. These curves can be compared to the experimental measures taken by Kanakubo in his tests. The comparisons of $\sigma - \delta$, $\sigma - \phi$ and $\sigma - \varepsilon(y)$ at a distance of 15 mm from both bottom and top faces are shown in Figure 4.5, Figure 4.6, Figure 4.7 and Figure 4.8, respectively.

Generally speaking, the results offer a good approach of the experimental results obtained in (Kanakubo, 2006). Despite there being a general trend to compare the uniaxial tensile test results to those obtained from flexural tests to validate inverse analysis procedures, what is really important for validation is to ensure that the inverse analysis methodology is able to reproduce the sectional behaviour of the failure section. The reason for this may be due to the fact that a higher or lower correspondence between uniaxial tests and the inverse analysis results lies in several factors, which go beyond the inverse analysis, such as specimen size, way of casting and fibre distribution.
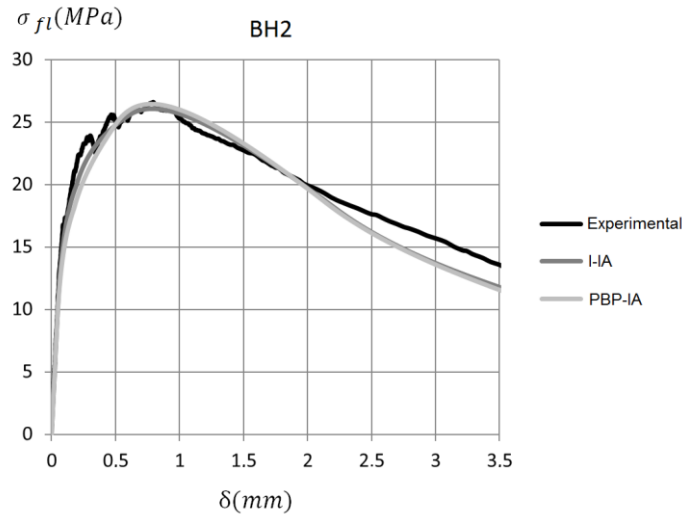
Figure 4.5 Experimental $\sigma - \delta$ at mid-span of specimen BH-2 (Kanakubo, 2006) and the approach obtained from the I-IA and PBP-IA methods.
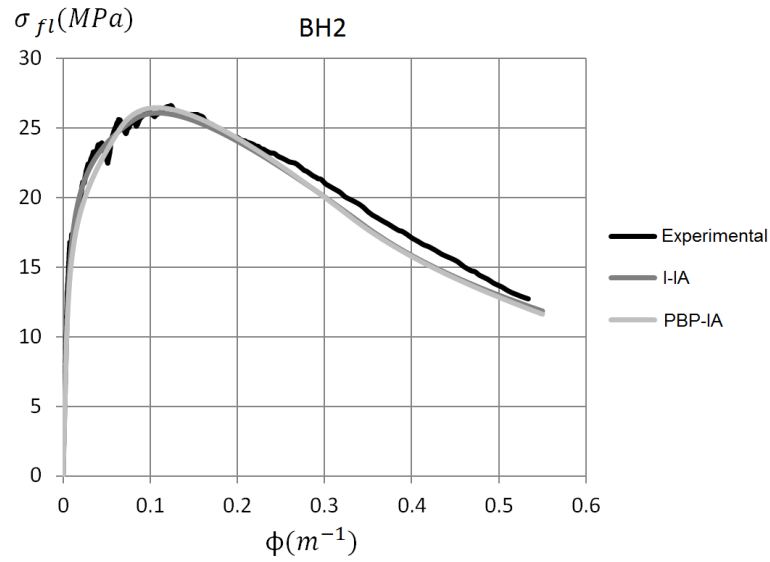
Figure 4.6 Experimental $\sigma - \phi$ of specimen BH-2 (Kanakubo, 2006) and the approach obtained from I-IA and PBP-IA.
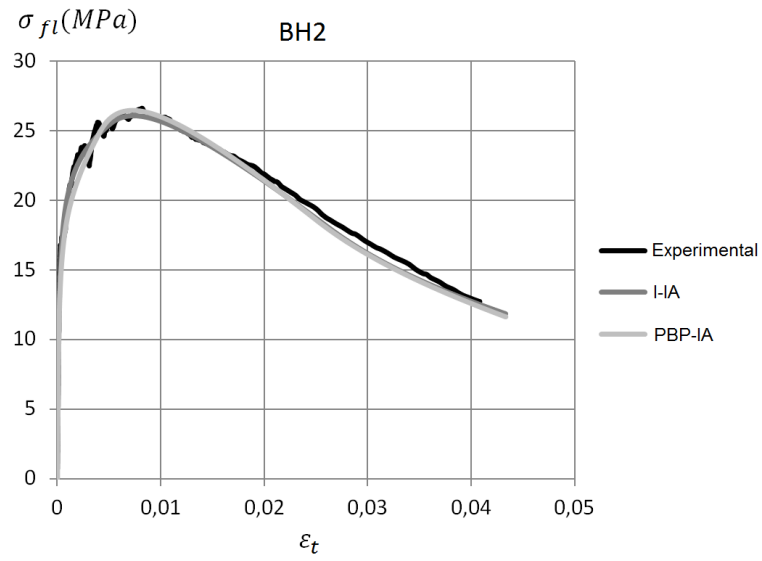
Figure 4.7 Experimental $\sigma - \varepsilon_t$ at 15 mm from the bottom face of specimen BH-2 (Kanakubo, 2006) and the approach obtained from I-IA and PBP-IA.
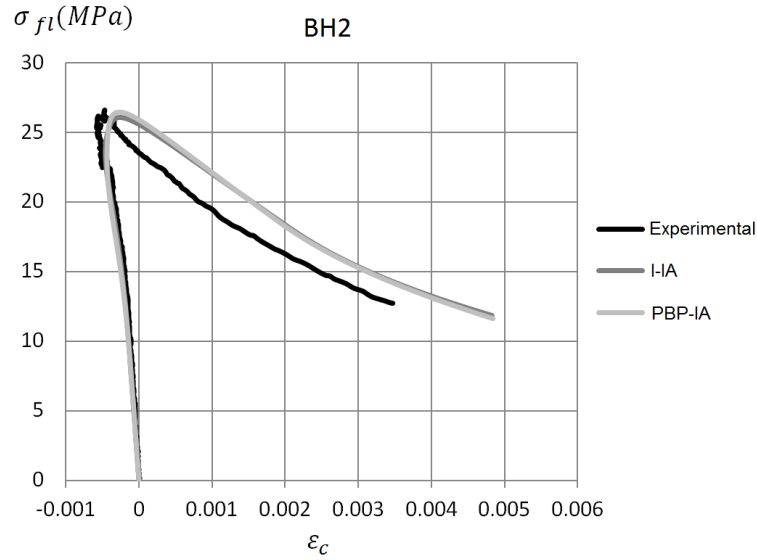
Figure 4.8 Experimental $\sigma - \varepsilon_t$ at 15 mm from the top face of specimen BH-2 (Kanakubo, 2006) and the approach obtained from I-IA and PBP-IA.

This is why the validation of both the non-linear hinge model and inverse analysis procedures should be done when knowing the experimental kinematic sectional behaviour on hinge lenght obtained from TBPTs, and by comparing to the predicted kinematic sectional behaviour that derives from the constitutive tensile parameters obtained from both inverse analysis procedures and the non-linear hinge model. In our case, hinge length is considered the central one third, and the kinematic sectional response is smeared in the constant bending moment area between load rollers.

A validation of both the non-linear hinge model and the inverse analysis methodologies according to the above-mentioned criteria is made in the following section.

4.2. Experimental validation

The experimental validation of the non-linear hinge requires a definition of the inverse analysis method to determine the constitutive *material properties* that derive from the bending test. As the non-linear hinge model requires a constitutive relationship in tension, which is *a priori* unknown, iterative and point-by-point inverse analyses are used to determine it. An experimental programme is run to validate the non-linear hinge model and the inverse analysis procedures by comparing the experimental measurements on the boundaries of the central one third to the expected sectional response offered by the non-linear hinge model, which is obtained from the constitutive behaviour that derives from inverse analysis methods. A general overview of the followed validation process is shown in Figure 4.9.

Moreover, the experimental programme is also used to experimentally check the scale effect results obtained in 3.4.5.
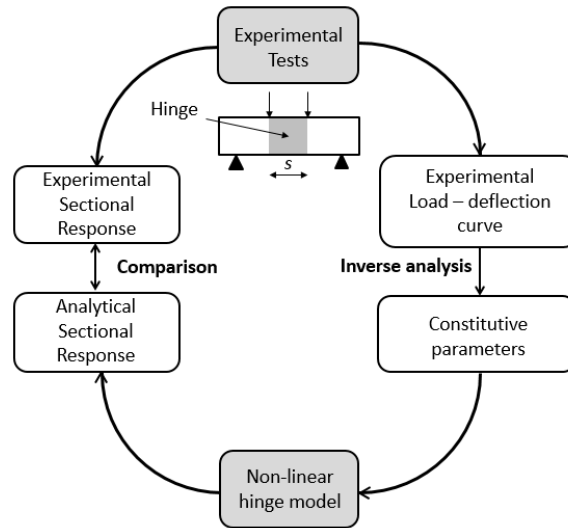
Figure 4.9 The experimental validation process

4.2.1. Experimental programme

For the purpose of validating the non-linear hinge model and the inverse analysis methods proposed, three different types of square cross-section specimens were prepared with a variable depth of 50, 100 and 150 mm. The L/h ratio was constant and equals 4.5 for them all. A 2% in volume of smooth-straight (13/0.20) steel fibres were used in an Ultra-High-Performance cementitious matrix with an average compressive strength of 169.89 MPa, obtained from 61 100-mm long cubes with a 4.78% coefficient of variation. Eight 50-mm and 100–mm specimens, and four 150-mm specimens, were made. The geometry of the specimens and the TPBT setup are shown

in Figure 4.10. Those cases in which the macrocrack appeared out of the central one third were not considered. The reason for the large number of specimens with the macrocrack out of the analysed area may be due to the fact that minor drillings were made to attach the displacement transducers, which weakened the section bearing capacity and forced unwished failures. The specimens are summarised in Table 4.1. The cells in red denote those specimens in which a macrocrack appears out of the central one third. More details can be found in Appendix I.

Table 4.1 Specimen naming

Depth (mm)	Number							
	1	2	3	4	5	6	7	8
50								
100								
150								
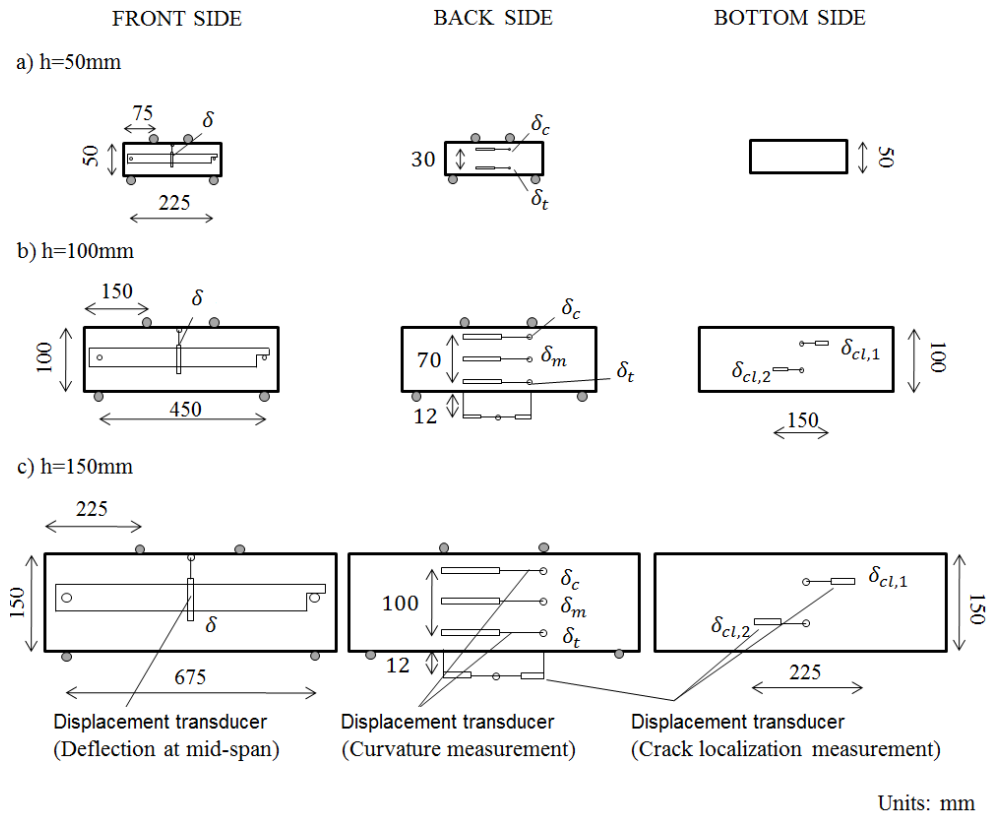
Figure 4.10 Specimen geometries and location of the displacement transducers used.

According to Figure 4.10, a displacement transducer was used to record the displacement at mid-span on the front side. Three displacement transducers were used on the rear side of the 100- and 150-mm specimens to obtain the experimental average curvature inside the central one third. With the 50-mm deep specimens, the shallower depth forced having to use only two displacement transducers. On the bottom side, two staggered extensometers were used at a distance of 12 mm from the specimen's tensile face. The setup configuration for the 50-mm deep specimens made impossible to place these displacement transducers.

4.2.2. Load–deflection results

The load-displacement at mid-span relationship for a TBPT setup that derives from the linear elastic theory can be rewritten as shown in Eq. 4.2 and Eq. 4.3. Accordingly, the experimental load-deflection results obtained from TPBT can be expressed according to two normalised parameters. If the L/h ratio remains constant, the load-deflection at mid-span curve can be expressed as the normalised bending strength (σ_{fl}) versus the normalised displacement at mid-span ($\delta_n = \delta/h$), which is not dependent on specimen depth. Thus variation in this normalised curve for different specimen heights shows the size effect on the flexural response, if it actually exists.

$$\frac{PL}{bh^2} = \left[\frac{23}{108}\left(\frac{L}{h}\right)^2 + \frac{36}{75}\right]^{-1} E\, \frac{\delta}{h}$$

Eq. 4.2

$$\sigma_{fl} = f\left(\frac{L}{h}\right) E\, \delta_n$$

Eq. 4.3

Normalised bending strength (σ_{fl}) versus normalised displacement at mid-span (δ_n) curves of the test series with the 50-, 100- and 150-mm square cross-sections are shown in Figure 4.11(a), (b) and (c). The average curves are depicted by a bold black line and are compared in Figure 4.11(d).

It is important to remark that for all the tested specimens, hinge length is in accordance with only specimen depth, and its value is always one half the specimen depth. This is why it is possible to compare the obtained results. Therefore, the constitutive properties that derive from the tested different specimens must be close to each other no matter what the specimen depth. The differences between them show the scale effect.
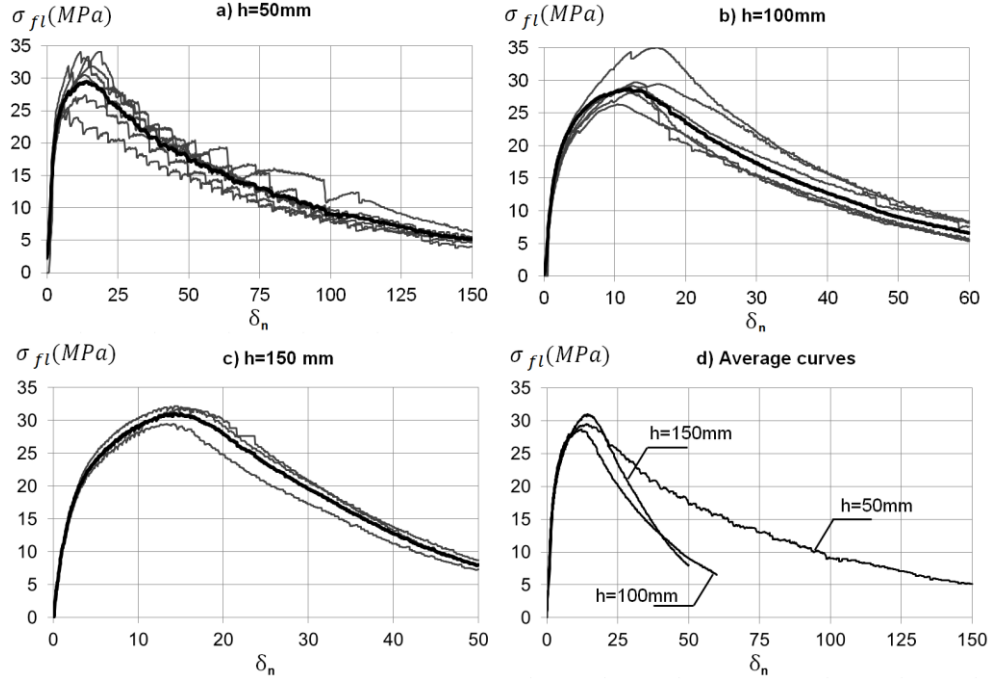
Figure 4.11 The normalised $\sigma_{fl}-\delta_n$ curves for the test series with the 50- (a), 100- (b) and 150- (c) mm square cross-sections; average curves in (d).

From the curves in Figure 4.11 (d), a clear size effect in deformation can be observed after the peak since the unloading slope is lower as specimen depth decreases. Figure 4.11 (d) shows how the three average curves for the different specimen depths offer close values for the maximum flexural strength, and also for the normalised displacement upon the peak. This is expected from a deterministic size effect point of view, according to the results in 3.4.5, but not from a fibre orientation effect point of view. Better fibre orientation is expected for smaller specimens with increased flexural capacity. However, this is not the case according to the obtained results. Therefore, favourable orientation of fibres cannot be concluded from these results.

4.2.3. Application of the inverse analysis

The parameters that define the stress-strain relationship on the hinge can be derived using the described iterative (I-IA) and point-by-point (PBP-IA) inverse analyses and from the $\delta - \phi$ transformation. According to these methodologies, constitutive tensile parameters are obtained for both methodologies. The average inverse analysis results for both methods are depicted in Figure 4.12. The stress-strain relationship values inside the hinge for each obtained specimen are shown in Appendix I.

Note that as the gage length of the displacement transducers corresponds to the central one third, the hinge length to depth ratio is the same and equals 1.5. This is the only feasible way to compare the experimental results to the results obtained by inverse analysis methods.

Both methods offer similar results regardless of specimen depth. I-IA assumes that stress $f_{t,d}$ is one third of the maximum tensile strength. This assumption proves to be a good approach for the concrete type tested, as derived from Figure 4.12 (a), (b) and (c).

Figure 4.12 Inverse analysis results for the test series with the 50- (a), 100- (b), 150- (c) mm square cross-sections using both PBP-IA and 5P-IA; scale effect on strain (d).

Figure 4.12(d) depicts the average inverse analysis results using both methods for the three different tested depth specimens. No scale effect is detected upon the peak in either stress or strain. However, a strong size effect at the $\sigma - \varepsilon$ sectional response of the hinge on the unloading branch after crack localisation is derived from the stress-strain relationship inside the hinge length, as shown in Figure 4.12 (d), as it was predicted in 3.4.5.

4.2.4. The displacement to curvature check

The equivalent bending strength (σ_{fl}) versus curvature on the boundaries of the non-linear hinge (ϕ) relationship can be obtained from three different sources: (i) the experimental data from the displacement transducer on the rare side of the specimen (see Figure 4.10); (ii) using the stress-strain sectional behaviour law that derives from I-IA and the non-linear hinge model; (iii) using the stress-strain sectional behaviour law that derives from PBP-IA with the help of the non-linear sectional analysis programme developed by the authors.

In case (i), the experimental curvature is obtained by the linear regression of the strain measurements of the three displacement transducers, δ_c, δ_m, and δ_t (see Figure 4.10), placed on the rare side of the 100-mm and 150-mm specimens. The experimental curvature in the 50-mm specimens is obtained following Eq. 4.4, where d_ϕ is the distance between the displacement transducer, and s is gage length or hinge length.

$$\phi_{50mm} = \frac{|\delta_t - \delta_c|/s}{d_\phi}$$

Eq. 4.4

In case (iii), the closed form formulation in Table 3.3 cannot be used because $f_{t,d}$ stress is not fixed at one third of $f_{t,u}$. This is why the numerical programme developed by the authors is used to obtain the $\sigma_{fl} - \phi$ relationship by assuming the stress-strain relationship that derives from PBP-IA. For each bending moment value, the average curvature and crack depth are determined by assuming that axial forces are null and the bending moment is known. Once the average curvature and crack depth are known, it is possible to obtain the average strain at any position along the specimen depth by following a similar process to that used in the non-linear hinge model.

The accuracy of both inverse analysis methods is determined from the deviation between the $\sigma_{fl} - \phi$ curves, obtained using these two methods and the experimental curve. Deviation is obtained by using Eq. 4.5, where n is the number of points of the $\sigma_{fl} - \phi$ curve; $\sigma_{fl_{exp,i}}$ is the equivalent experimental strength corresponding to the i curvature value, and $\sigma_{fl_{IA,i}}$ is the equivalent strength corresponding to the i curvature value obtained from methods (ii) and (iii) using the stress-strain law that derives from I-IA and PBP-IA. The deviation values are shown in Table 4.2. The "-" symbol indicates those specimens in which the average curvature cannot be obtained due to a bad measurement of the displacement transducers placed on the specimen's back side.

Figure 4.13 shows the three different σ_{fl} versus normalised average curvature ($\phi_n = \phi h$) curves obtained for six randomly selected specimens. Here we can see that the three curves are close to each other, which means that both the used inverse analyses offer a constitutive stress-strain sectional response, which accurately reproduces the

experimental curvature measured inside hinge length. The curves obtained for the other specimens are shown in Appendix I.
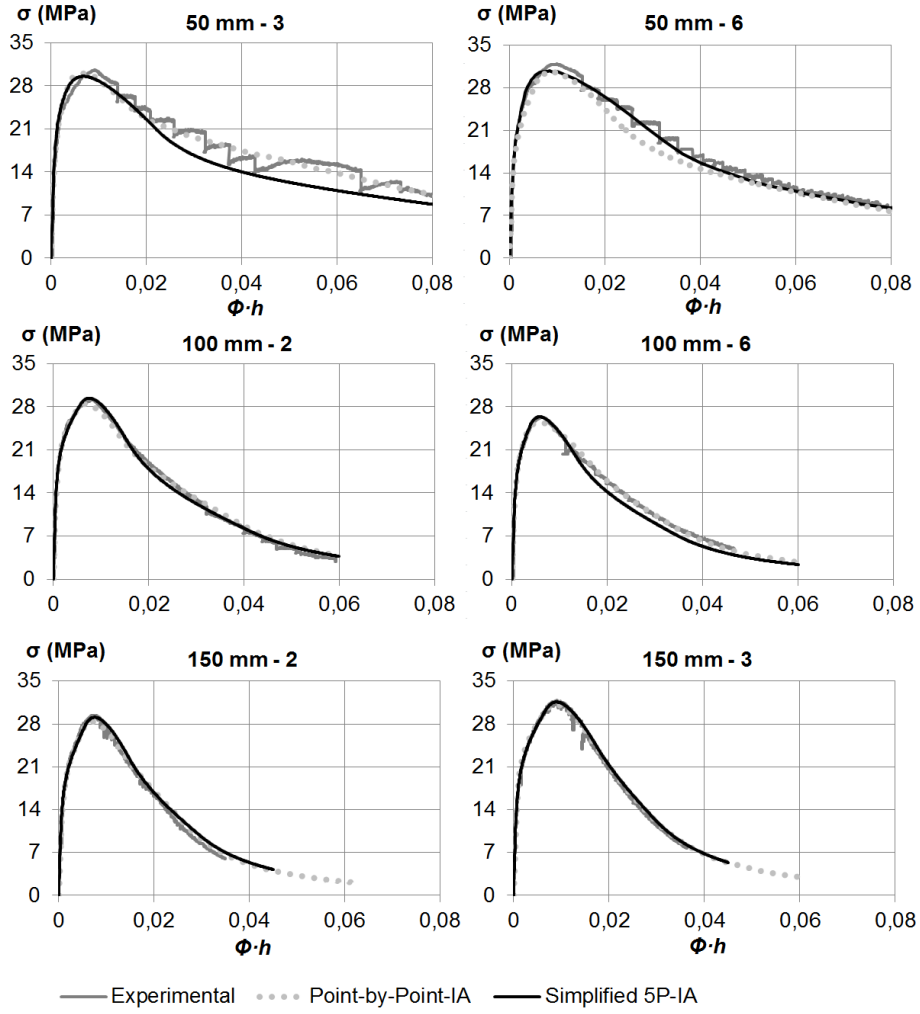
Figure 4.13 Comparison between the experimental σ_{fl}-$\bar{\phi}$ curve and those that derive from 5P-IA and PBP-IA for the test series with the 50- (specimens 3 and 6), 100- (specimens 2, 6), and 150- (specimens 2 and 3) mm depths.

$$s_d(MPa) = \sqrt{\frac{\sum_{i=1}^{n}\left(\sigma_{fl_{exp,i}} - \sigma_{fl_{IA,i}}\right)^2}{n-1}}$$

Eq. 4.5

Table 4.2 Curvature deviation values in MPa between the experimental and inverse analysis results

Specimen height	50 mm						100 mm						150 mm		
Specimen number	1	2	3	4	5	6	1	2	3	4	5	6	1	2	3
Deviation 5P-IA (MPa)	-	1.0	2.6	-	1.2	1.9	0.5	0.6	-	1.1	0.5	1.0	0.5	0.6	0.4
Deviation PBP-IA (MPa)	-	2.8	1.2	-	1.5	0.9	0.4	0.6	-	0.4	0.6	0.5	0.4	0.5	0.3

4.2.5. Analysis of the average strain profile inside the hinge

The experimental equivalent flexural strength versus the average strain on the non-linear hinge on different depth position curves are obtained using the displacement transducers placed on the back and bottom sides of the tested specimens. The average strain values ε_c, ε_m, and ε_t, represented in Figure 4.14, are obtained by dividing the δ_c, δ_m, and δ_t displacement transducer measurements by their gage length, which corresponds to the constant bending moment area. The ε_{cl} strain values are obtained as the average values of the δ_{cl1} and δ_{cl2} (see Figure 4.10) measurements divided by hinge length.

The average strain values at the different depth positions obtained from the experimental tests are compared to the values that derive from the constitutive law obtained by I-IA and the PBP-IA. As in the previous section, Eq. 4.5 is used to compare the experimental curves to those obtained using the two different proposed inverse analyses. The deviation values for each specimen and each depth position are shown in Table 4.3. The "-" symbol indicates those displacement transducers that recorded incorrect measures.

Figure 4.14 shows three different σ_{fl} versus the normalised average strain curves obtained for three randomly selected specimens at different depth positions. Here we can see that the three curves are close to each other in all cases, which means that both inverse analyses offer a constitutive stress-strain relationship which accurately reproduces not only the average curvature on the non-linear hinge, but also the average strain profile along specimen depth. A comparison for the other tested specimens is found in Appendix I. All these results show the good performance of both the inverse analysis methods and the non-linear hinge model proposed.
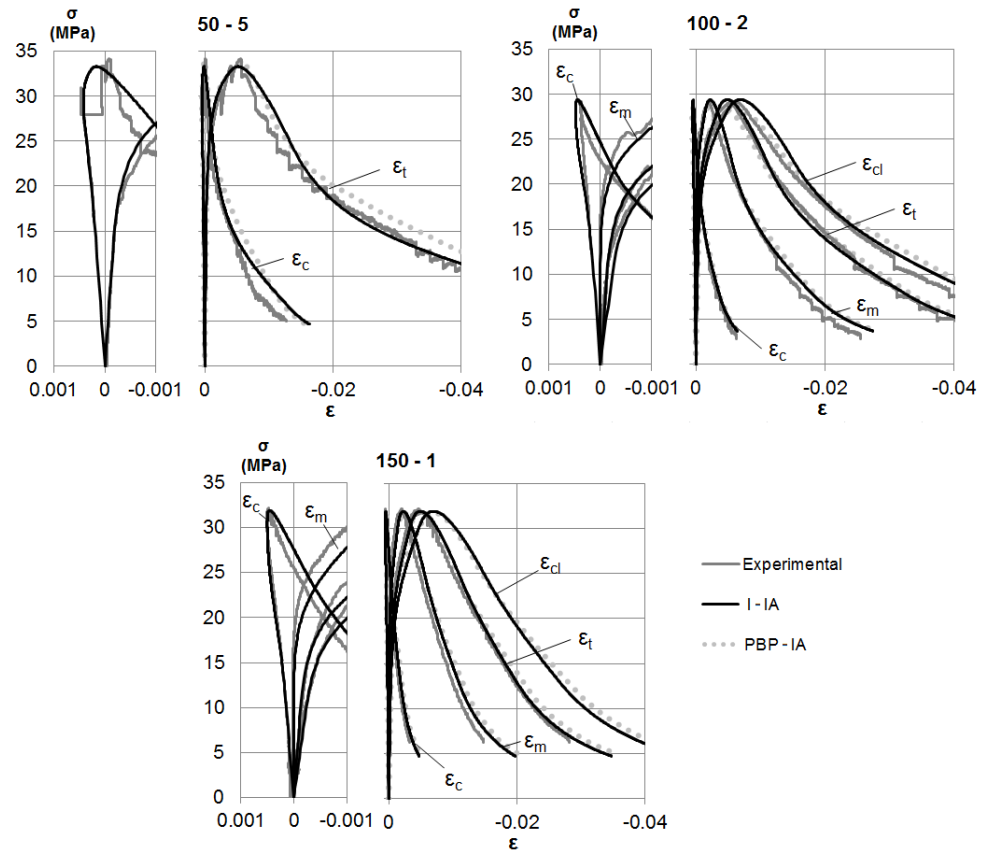
Figure 4.14 Comparison between the experimental I-IA and PBP-IA, and the equivalent flexural strength versus the average strain at the different height position curves for specimens 50-5, 100-2 and 150-1.

Table 4.3 Strain deviation values for the experimental and inverse analysis results.

| | Deviation (MPa) | | | | | | | |
| | Iterative Inverse Analysis | | | | Point-by-Point Inverse Analysis | | | |
	ε_c	ε_m	ε_t	ε_{cl}	ε_c	ε_m	ε_t	ε_{cl}
50-1	-		-		-		-	
50-2	1.24		0.65		0.47		1.85	
50-3	1.77		2.90		0.89		1.25	
50-4	2.61		-		1.42		-	
50-5	0.98		1.24		1.29		1.66	
50-6	1.18		1.37		1.47		0.67	
100-1	0.21	0.38	0.45	-	0.19	0.21	0.34	-
100-2	0.27	0.75	0.50	1.16	0.29	0.79	0.62	1.30
100-3	-	0.97	1.12	-	-	0.93	1.50	-
100-4	1.78	1.53	1.72	2.06	1.53	0.92	0.90	1.10
100-5	0.38	0.41	0.53	1.71	0.41	0.48	0.59	1.78
100-6	1.00	0.85	1.01	1.27	0.71	0.42	0.40	0.60
150-1	0.39	0.84	0.52	-	0.49	0.98	0.67	-
150-2	0.27	0.96	0.63	0.90	0.25	0.86	0.51	0.77
150-3	0.19	0.91	0.45	0.64	0.16	0.80	0.38	0.58

4.2.6. Constitutive tensile behaviour

Figure 4.15 shows the average constitutive tensile law obtained from I-IA for the three different specimens used. It includes the average spacing of microcracks at the end of the hardening phase (s_{av}) for each specimen depth. The values for each specimen are included in Appendix I. Using this parameter and the strain at the end of this phase, the average crack opening at the end of this phase can be determined. The results show that this value remains around 20 μm, showing the small crack opening before tensile softening despite the high deformation.

Figure 4.16 depicts the stress-crack opening relationship that derives from the stress-strain relationship plotted in Figure 4.12. We can see how the scale effect that appears on the softening branch in the stress-strain section response disappears when this law is transformed into a stress-crack opening. An average w_c value of 5.4 mm is obtained, which represents 42% of fibre length. The fracture energy obtained in Figure 4.16 is similar to that obtained by (Wille et al., 2014) in tension tests using a UHPFRC with similar compressive strength, and the same amount and type of steel fibres.
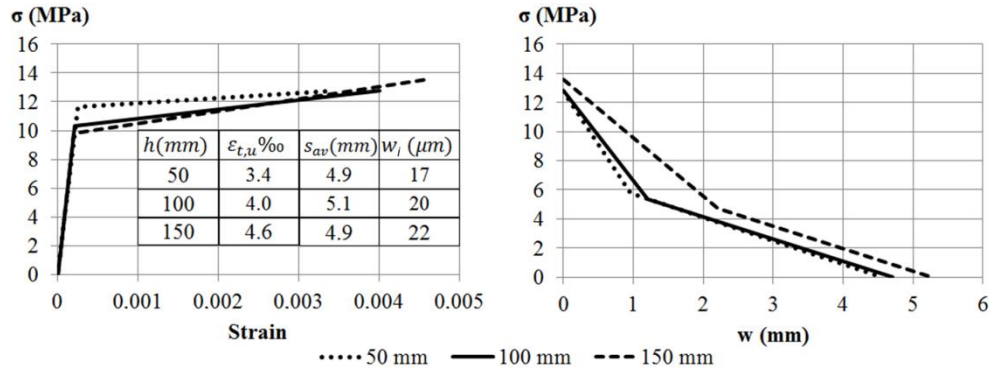
Figure 4.15 Constitutive tensile properties for the test series with the 50-, 100-, 150-mm square cross-sections using I-IA.

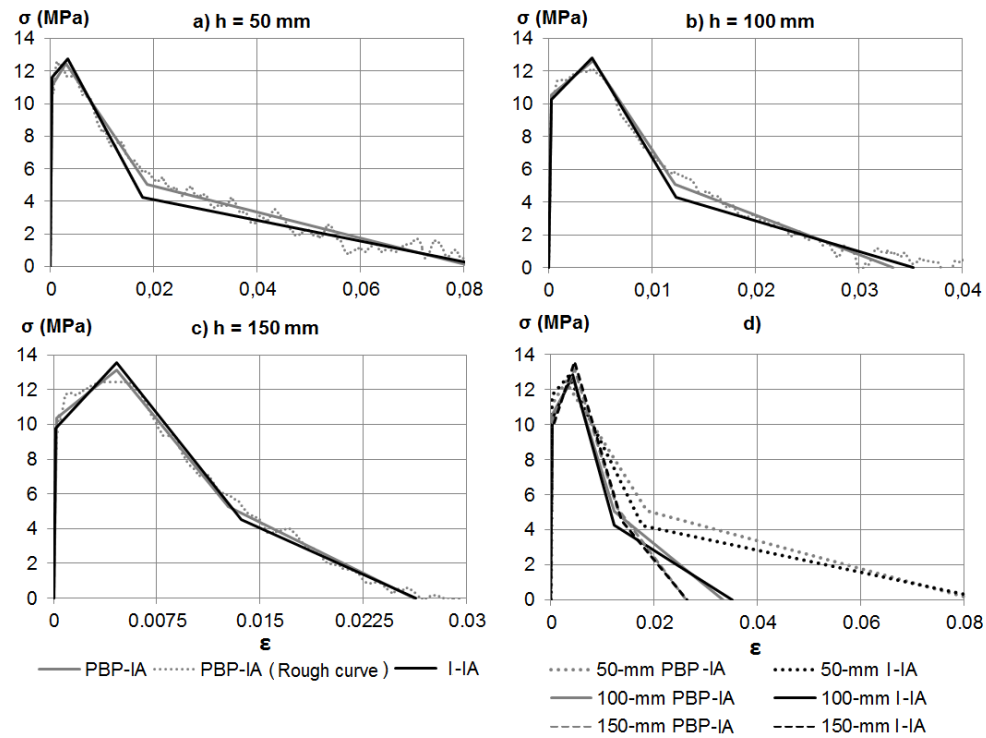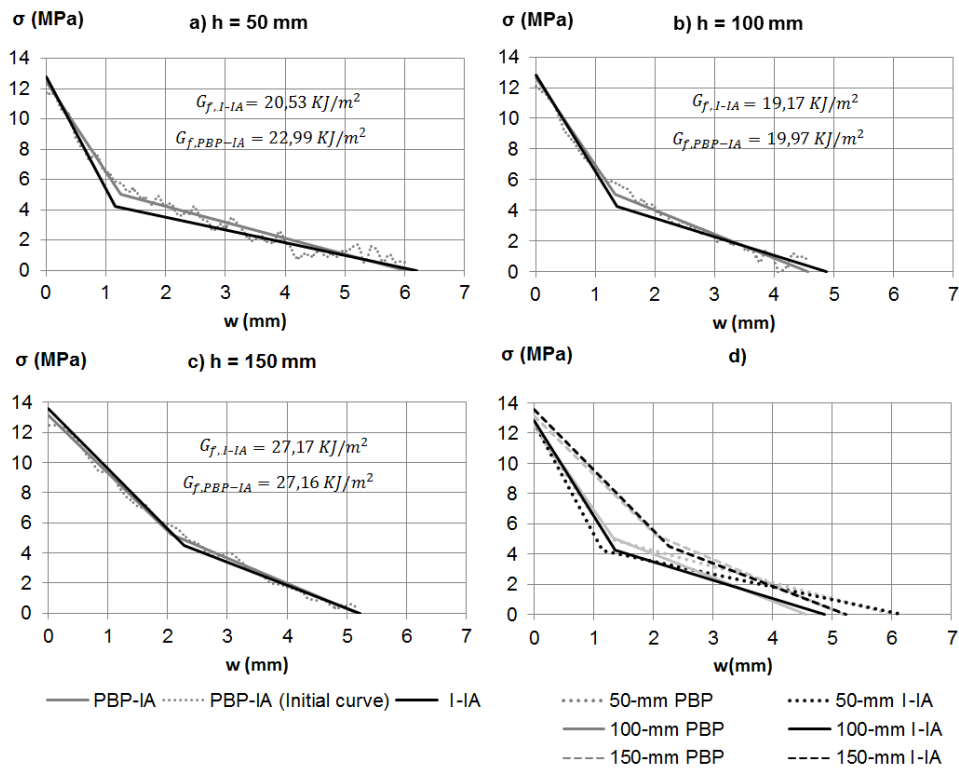Figure 4.16 A stress-crack opening relationship results for the test series with the 50- (a), 100- (b), 150- (c) mm square cross-sections using both PBP-IA and I-IA; a comparison made of all the stress-crack opening curves (d).

4.3. Summary

The closed form non-linear hinge model developed in Chapter 3 has been used as the basis to develop two different types of load-curvature inverse analysis methodologies, which only require the experimental load-deflection at mid-span measurement.

The results from both the inverse analysis methodologies were compared to the experimental sectional behaviour recorded at the edges of the constant bending moment area, which were employed as hinge length. From their comparison, it can be concluded that non-linear hinge model accurately reproduces the experimental sectional behaviour, such as the load-curvature and the load-strain profile along specimen depth. The non-linear hinge model requires having to determine a constituitive relationship in tension, obtained from the proposed inverse analysis methods. According to the obtained results, it can be stated that both the proposed inverse analysis methods can be considered suitable for their purpose.

The main problem of I-IA lies in the solution to the problem of minimising the sum of the residual squares of σ_{fl} for each curvature value as it may depend on the initial solution given to the software tool being used. PBP-IA offers precise sectional behaviour inside the hinge. However, it offers a rough curve that needs simplification. Simplification consists in fitting a quadrilinear law to the obtained rough curve. As it is another sum of the residual squares minimisation problem, it has the same problem as the iterative process. Informally speaking, after the fitting process one feels that it could have been done better.

Another major disadvantage of these methods is that they require a computational process, and cannot be carried out without the help of a computer. Even though the results seem accurate, they are not suitable inverse analysis methods to be included in either a characterisation standard or a design code. Apart from accuracy, a standard method must be simple and objective. A simplified method based on the objective selection of key points with no significant loss of accuracy is desirable for both design and quality control purposes, which is what is developed in Chapter 5.

Chapter 5

Simplified Five-Point Inverse Analysis Method

5.1. Introduction

Even though the closed-form non-linear hinge model developed in Chapter 3 enables the determination of the load-deflection response of a UHPFRC specimen in a TPBT, its main purpose was to set up the analytical basis to support subsequent inverse analysis methodologies. In this way, two load-curvature inverse analysis methodologies, according to the inverse analysis classification in Figure 2.28, were proposed in Chapter 4: (i) an iterative inverse analysis and (ii) a point-by-point inverse analysis. These methodologies can provide the complete description of UHPFRC material behaviour in tension from the experimiental load-deflection curve, and can accurately fit all the experimental measurements inside hinge length.

However, these methods lack simplicity and, to an extent, objectivity. This may not be a problem for a research purpose, and are probably the easiest and most accurate inverse analysis methodologies developed to date. Nevertheless, they seem unsuitable methods to form part of a design code or to be considered a characterisation standard. This is why a simplified objective inverse analysis methodology, that maintains the accuracy of more complex methodologies, would be desirable. This methodology is not currently available, and a new simplified proposal is presented and extensively validated.

This new simplified methodology is also based on the closed-form non-linear hinge model developed in Chapter 3. It entails having to select five specific key points, drawn from the experimental equivalent bending strength-displacement at mid-span curve. Using these points, the parameters that define the assumed quadrilinear stress-strain law inside the hinge can be determined by back-of-the-envelope calculation. This law is used to determine the constitutive tensile behaviour of UHPFRC. The parameters that define tensile behaviour are: cracking strength (f_t); ultimate tensile strength ($f_{t,u}$) and its corresponding strain ($\varepsilon_{t,u}$), crack opening upon change of slope (w_d), characteristic crack opening at zero stress (w_c) and the elastic modulus (E). The method developed herein assumes the same hypotheses as the non-linear hinge model developed in Chapter 3.

Unlike most existing inverse analysis methods, the simplified method developed herein is straightforward for implementation and does not strictly require using a computer. This method assumes a TPBT setup. It was developed only for a L/h ratio that equal 3 and 4.5, and can be used regardless of specimen depth. Therefore, the deterministic scale effect is included in its formulation.

The analytical basis of the method, the way the back-of-the-envelope formulation is derived, and the justification of the selection of the key points is explained in Section 5.2, together with an application example. The analytical and experimental validation of this method is found in Sections 5.3.1 and 5.3.2. For the analytical validation, the load-deflection results directly obtained by applying the non-linear hinge model presented in 3.4.2 are used. For the experimental validation, the constitutive tensile relationship obtained from the experimental load-deflection curve of sixteen 100-mm cross-section specimens using the PBP-IA are compared to the constitutive tensile relationship obtained from the simplified inverse analysis. Finally, more relevant results of this chapter are summarised in Section 5.4.

5.2. Simplified Five-Point Inverse Analysis method (5P-IA)

5.2.1. General assumptions

Figure 5.1 (a) depicts the constitutive $\sigma - \varepsilon$ law assumed, along with the notation of the six parameters employed to model UHPFRC behaviour. The elastic modulus (E) is considered the same in both compression and tension. The other five parameters that define the tensile law are: first cracking tensile strength (f_t), ultimate tensile strength ($f_{t,u}$) and its associate strain ($\varepsilon_{t,u}$), the strain at the intersection of the softening lines ($\varepsilon_{t,d}$), and the maximum strain with zero stress ($\varepsilon_{t,c}$). To simplify the formulation, four normalised parameters are introduced, as in the non-linear hinige model. They are α, β, μ, and γ, as defined in Eq. 5.1. The normalised stress-strain law is shown in Figure 5.1 (right).
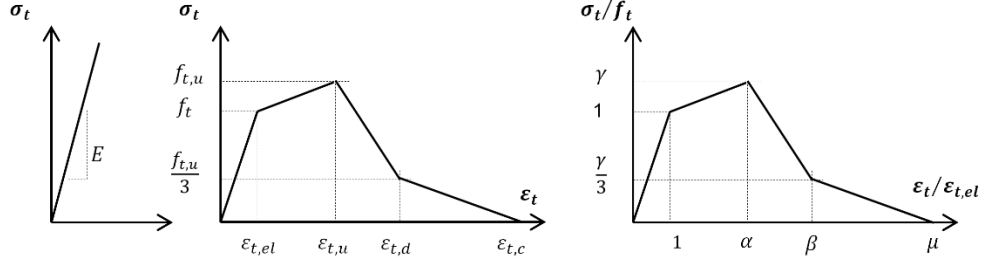
Figure 5.1 The stress-strain relationship assumed in tension (left); the normalised stress-strain relationship (right)

$$\varepsilon_{t,el} = \frac{f_t}{E}; \quad \alpha = \frac{\varepsilon_{t,u}}{\varepsilon_{t,el}}; \quad \beta = \frac{\varepsilon_{t,d}}{\varepsilon_{t,el}}; \quad \mu = \frac{\varepsilon_{t,c}}{\varepsilon_{t,el}}; \quad \gamma = \frac{f_{t,u}}{f_t}$$

Eq. 5.1

According to the non-linear hinge model developed in Chapter 3, the normalised load-deflection curve varies according to the slenderness ratio, as shown in Figure 5.2. Figure 5.2 depicts the normalised σ_{fl}-δ curve for a typical UHPFRC using the non-linear hinge model developed in Chapter 3 for three different L/h ratios and the same stress-strain sectional behaviour of the hinge. The equivalent flexural strength is normalised by the first cracking tensile stress and the displacement at mid-span by the displacement upon the first cracking tensile stress.

Note that the stress-strain law is used instead of the stress-crack opening law. This means that the curves plotted in Figure 5.2 correspond to different UHPFRCs constitutive stress-crack opening behaviour in tension as hinge length varies according to the slenderness ratio. In this case, the different constitutive behaviour displays the same deformational behaviour of the hinge as the stress-strain used was the same. This fact is very important and was intentional. The reason lies in the fact that in a simplified inverse analysis, the deformational behaviour in the hinge is firstly obtained from the experimental load-deflection behaviour. After obtaining the stress-strain behaviour, the stress-crack opening behaviour can be derived according to the assumed hinge length. Therefore, the only purpose of Figure 5.2 is to prove that for different slenderness ratios, distinct formulations are required to derive the deformational behaviour of the non-linear hinge. As it is too complicated to develop a general formulation according to the slenderness ratio, a different formulation must be developed for each slenderness ratio.

It is important to remark that the normalised σ_{fl}-δ shown in Figure 5.2 remains identical if specimen width and depth vary, but only if the slenderness ratio (L/h) remains constant. This is why the method developed herein is completely independent

of the cross-section size if the slenderness ratio remains constant. This curve is also independent of f_t and E if normalised parameters α, β, μ, and γ remain constant.
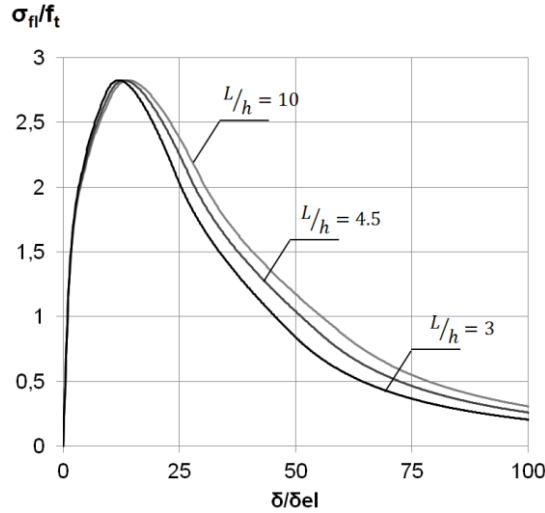
Figure 5.2 Normalised σ_{fl}-δ for a typical UHPFRC with a rectangular cross-section and $\gamma = 1.2 \, ; \alpha = 20; \beta = 75; \mu = 175$

5.2.2. Simplified Five-Point Inverse Analysis methodology derivation (5P-IA)

In a first step, the simplified inverse analysis must allow the determination of deformation behaviour (stress-strain relationship) inside hinge length. As the method to be developed is 'simplified', this behaviour must be derived from the specific key points obtained from the experimental load-deflection curve. Afterwards, the equations described in Chapter 3, which link the stress-strain behaviour to the stress-crack opening one (Eq. 3.11 and Eq. 3.12), can be used to derive the constitutive behaviour of UHPFRC. So the keys of the simplified method are: (i) the selection of the key points and (ii) the determination of a simple formulation that links these points to the parameters that define the deformational behaviour of the hinge.

From the non-linear hinge model, the analytical load–deflection curves from a TPBT with a specific slenderness ratio can be obtained from a hypothetical stress-train response of the hinge. By varying the stress-strain parameters, different analytical strain-hardening behaviour concretes ($\gamma \geq 1$) can be modelled. For each set of tensile parameters (f_t, E, α, β, γ, μ), the analytical σ_{fl}-δ curve can be obtained according to the developed non-linear hinge model. From these curves, a set of points (δ_i, $\sigma_{fl,i}$) can be extracted and statistically analysed to establish the relationships between these points and the tensile parameters. As the non-linear hinge model has a closed-form solution, the procedure can be fast and vast quantities of data can be easily obtained and analysed. The procedure used to collect these data is summarised in Figure 5.3.
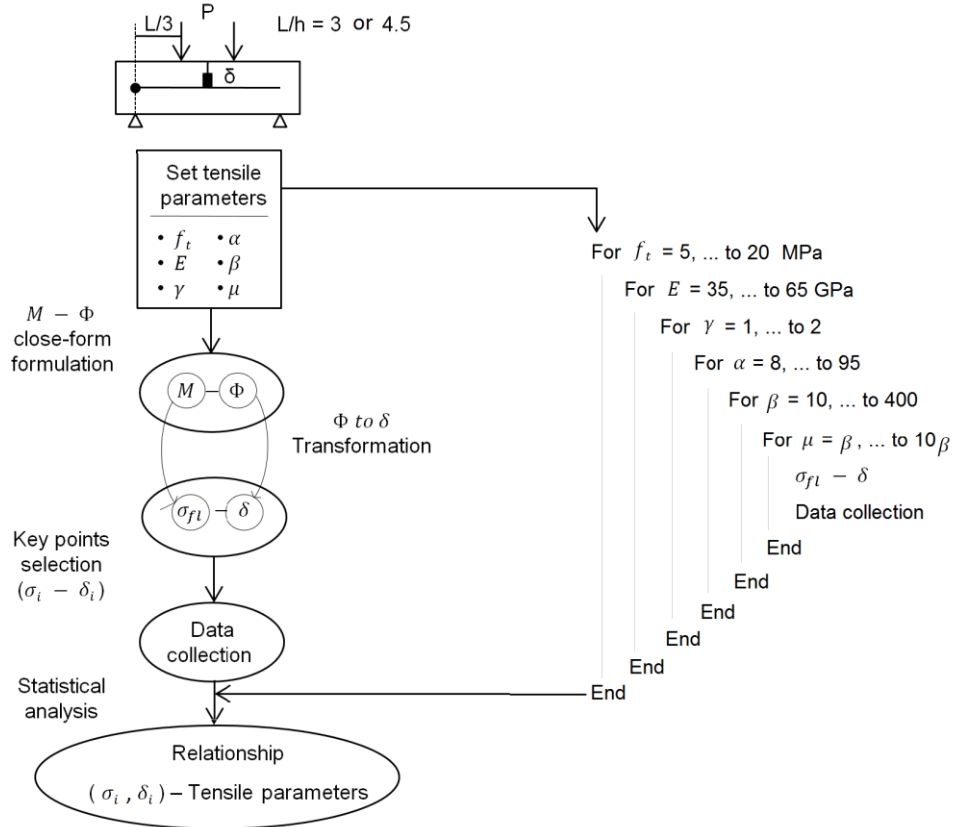
Figure 5.3 The data collection methodology scheme

Constitutive tensile parameters were varied to cover a wide range of theoretical strain-hardening concretes. The intervals in the normalised constitutive parameters that were varied are:

- $f_t \in [5, 6, 7, \dots, 18, 19, 20]\, MPa$ (16 different values)

- $E \in [35, 40, \dots, 60, 65]\, GPa$ (7 different values)

- $\gamma \in [1, 1.05, 1.10, \dots, 1.90, 1.95, 2.00]$ (21 different values)

- $\alpha \in [8, 10, \dots, 28, 30, 35, \dots, 85, 95]$ (25 different values)

- $\beta \in [10, 20, \dots, 90, 100, 150, \dots, 350, 400]$ (16 different values)

- $\mu \in [\beta, 1.5\beta, \dots, 4.5\beta, 5\beta, 6\beta, \dots, 9\beta, 10\beta]$ (13 different values)

Around 12 million different concretes were modelled. Only the concretes that met the following restrictions were considered:

- $\varepsilon_{t,u} \in [0.001,\ 0.015]$

- $\varepsilon_{t,d} \in [\varepsilon_{t,u},\ 0.05]$

- $\varepsilon_{t,c} \in [(1.5\ \varepsilon_{t,d} - 0.5\ \varepsilon_{t,c}),\ 0.4]$

Note that these intervals not only represent UHPFRC behaviour, but also all the HPFRCCs whose hardening behaviour can be described with a bilinear assumption and characterised by a declining softening curve. This behaviour is generally found when steel or high modulus fibres are used (Naaman et al., 2003).

5.2.2.1 Determination of stage 1. Linear elastic state.

The determination of the first crack point in bending is no easy task (Barr et al., 1996), and much less so in ductile material like UHPFRC. Traditionally in plain concrete, the relationship between flexural tensile strength and tensile strength has been established by (Hillerborg et al., 1976) with the Fracture Mechanics Theory to fit a model according to specimen depth. The deeper the specimen depth, the more brittle the specimen becomes, and flexural tensile strength and tensile strength come closer. As mentioned in Chapter 2, this is the so-called size effect, which takes place after a macrocrack appears (Baby et al., 2012; Hillerborg et al., 1976; Spasojevic, 2008). This method was maintained in MC2010 for normal-strength concretes.

Despite having been developed for brittle materials, the same formulation has been proposed by (AFGC, 2013) to determine the tensile strength of UHPFRC with a slight modification to a parameter value (Chanvillard et al., 2003). This formulation does not consider flexural tensile strength, but strength that corresponds to loss of linearity. Using this criterion, two problems arise: (i) this strain-hardening concrete leads to a soft deflection curve under bending, and loss of linearity point cannot be objectively identified as it depends on the scale that the curve is seen at, and also on personal judgement; (ii) the way the method is used substantially changes the hypothesis on which it is based because flexural strength is replaced with loss of linearity strength. This is why this method should be reviewed.

The Swiss standard draft proposed identifying crack strength to the point that corresponds 1% loss of stiffness. Even though this is a more objective criterion, loss of stiffness is so small that is too complicated to be obtained in the right way. However, the loss of stiffness criterion seems a good one to obtain cracking strength. This is the method proposed in this work, but by using of different loss of stiffness ratios. More detailed information about the above-mentioned methods is described in 2.6.2.2 and 2.6.2.3.

Figure 5.4 shows the theoretical normalised curve for three different strain-hardening constitutive tensile laws. The drawn black point indicates the crack localisation point; i.e. the end of the hardening phase. Three lines are also represented: the S_0 line represents initial curve stiffness; the other two lines represent secant stiffness at 75%, and 40% of the initial one. Figure 5.4 indicates that before the crack localisation point, only parameters α and γ influenced the shape of the normalised σ_{fl}-δ, while β and μ had no influence at all. This can be deduced from the equations that define Stages I and II of the M-ϕ relationship in Table 3.3. However, an initial region seems to appear where the influence of parameters α and γ can be neglected by assuming a low error. In this area, only the elastic modululs and cracking strength have a strong influence. Accordingly, the simplified methodology to determine the first cracking strength is based on this region.
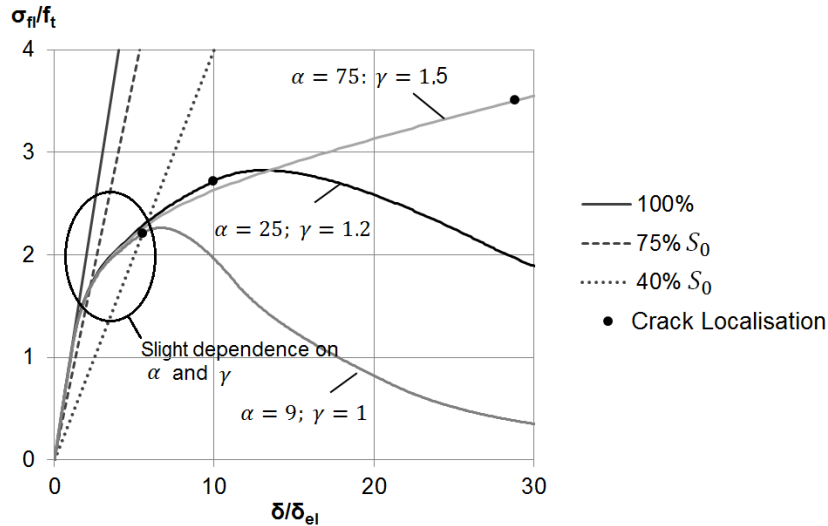
Figure 5.4 Normalised stress at 75% and 40% of the initial stiffness for very different concretes: $\beta = 3\alpha; \mu = 7\alpha$.

It is impossible to derive a simple accurate equation that relates cracking strength to the equivalent strength at a certain loss of stiffness. However, it is possible to do this using two equivalent strength values that correspond to two different secant stiffness values on the σ_{fl}-δ curve.

The closer to the initial stiffness, the slighter the influence of α and γ, and the more difficult it is to extract a suitable point from the experimental curve due to the low intersection angle between the two curves. A secant stiffness of 75% of the initial one is suggested as a compromise solution, instead of one of 99% as proposed in the Swiss standard draft.

The stiffness of the second line plays a very different role. The further away from the stiffness of the first line, the higher the correlation value that can be obtained, but the smaller the quantity of the different types of concretes that can be modelled. This is due to the fact that for a given secant stiffness, the strength that corresponds to it may be above the strength at the crack localisation point for a set of strain-hardening concretes. Hence the method cannot be applied. Figure 5.5 shows the regions that could not be modelled if secant stiffnesses of 40%, 45% and 50% were used when considering a slenderness ratio of 4.5. Similar results would be obtained for a slenderness ratio of 3.
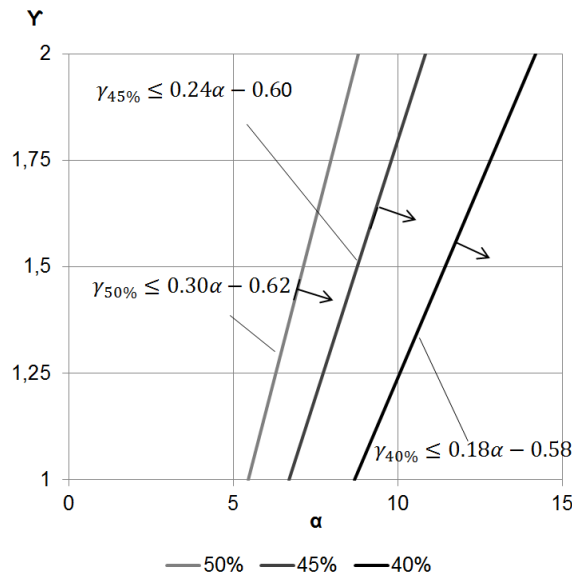
Figure 5.5 Secant stiffness influences the concrete types that can be modelled. The concretes that can be modelled are found to the right of the lines.

A secant stiffness of 40% of the initial one is proposed. According to Figure 5.5, this assumption implies that parameter α has to be higher than 10 as a reference value so that this method can be applied. For a common UHPFRC with $af_t = 10\ MPa$; $E = 50\ GPa$, $\varepsilon_{t,u}$ should be higher than 2.0‰ as a reference value. For lower $\varepsilon_{t,u}$, values, the strength at the crack localization point may be lower than the strength that corresponds to a secant stiffness of 40% of the initial one. So it is not possible to apply the method. It is noteworthy that Figure 5.4 shows a concrete with parameters $\alpha = 9$ and $\gamma = 1$ located precisely on this boundary. Here can see that the line with a 40% initial stiffness intersects the curve immediately at the crack localisation point.

Using these secant stiffnesses, another condition arises: all the concretes in which the crack localisation stress is below the stress correspond to a secant stiffness of 40% of the initial one are ruled out.

A statistical analysis of the strength values that correspond to a secant stiffnesses of 75% (σ_{75}) and 40% (σ_{40}) was carried out for the TPBT setup with $L/h = 4.5$ and $L/h = 3$. Figure 5.6 shows that it is possible to define a simple accurate relationship between secant stiffness strengths at 75%, 40%, and the first cracking strength, which disregards the influence of α and γ. According to the results in Figure 5.6, the first cracking strength can be obtained following Eq. 5.2 and Eq. 5.3
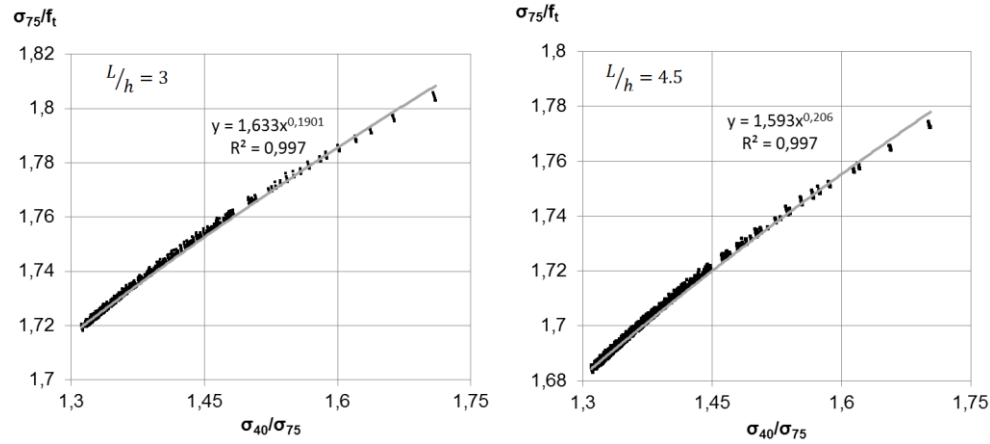
Figure 5.6 The statistical relationship between secant stiffness strengths 75%, 40% and the first cracking strength

$$f_t = \frac{\sigma_{75}}{1.63}\left(\frac{\sigma_{75}}{\sigma_{40}}\right)^{0.19} \qquad if \ L/h = 3$$

Eq. 5.2

$$f_t = \frac{\sigma_{75}}{1.59}\left(\frac{\sigma_{75}}{\sigma_{40}}\right)^{0.21} \qquad if \ L/h = 4.5$$

Eq. 5.3

It is important to remark that it was possible to decide using the equivalent stress that corresponds to a different loss of stiffness. It probably would have obtained a different formulation, leading to a similar cracking strength value. No single solution exists. The solution presented in this work is a compromise solution among (i) accuracy, (ii) low deviation in the determination of the stress values that correspond to the selected loss of stiffness and (iii) the amount of concretes that can be modelled.

5.2.2.2 Determining stage 2. Hardening state.

For strain and stress determinations at peak, simplified methods use flexural strength to this end. Nonetheless, flexural strength is reached after crack localisation, as demonstrated in Chapter 3. Therefore, these methods tend to overestimate strength and strain at peak. Despite being easy to implement, the simplified methods developed to date offer a poor approach and should be improved.

Determining ε_{tu} and $f_{t,u}$ requires using the crack localisation point because it is the border point between the hardening and softening stages. Both normalised deflection and strength at the crack localisation point were recorded during the data collection process. According to the results in Figure 5.7, the strain at the ultimate tensile strength, $\varepsilon_{t,u}$, can be obtained following Eq. 5.4 and Eq. 5.5, where δ_{loc} corresponds to the displacement at the crack localisation point, and δ_{75} is the displacement at the point with a secant stiffness of 75% of the initial one.
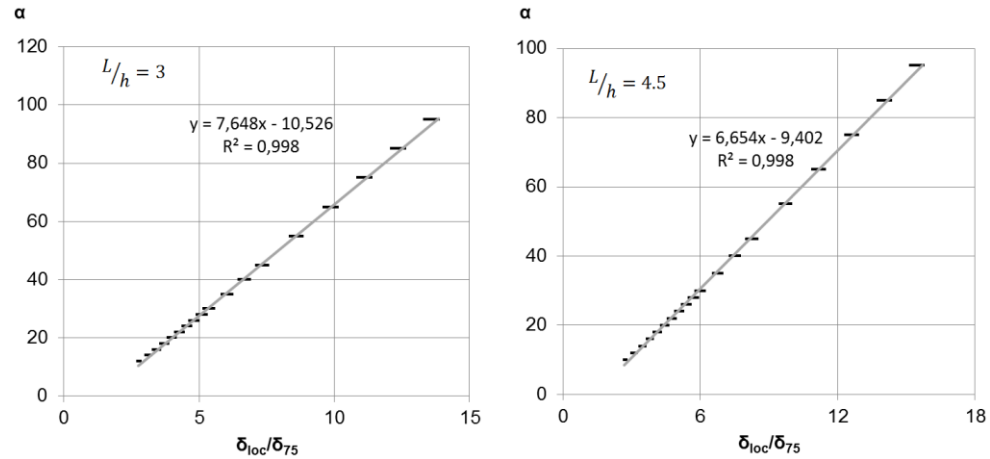
Figure 5.7 Statistical relationship between parameters α and δ_{loc} and δ_{75}

$$\varepsilon_{t,u} = \left(7.65 \frac{\delta_{loc}}{\delta_{75}} - 10.53\right) \frac{f_t}{E} \qquad if \ {}^L\!/_h = 3$$

Eq. 5.4

$$\varepsilon_{t,u} = \left(6.65 \frac{\delta_{loc}}{\delta_{75}} - 9.40\right) \frac{f_t}{E} \qquad if \ {}^L\!/_h = 4.5$$

Eq. 5.5

According to the results in Figure 5.8, ultimate tensile strength $f_{t,u}$ can be obtained following Eq. 5.6 and Eq. 5.7, where σ_{loc} corresponds to the stress at the crack localisation point.

$$f_{t,u} = \alpha^{-0.18} \left(2.46 \frac{\sigma_{loc}}{\sigma_{75}} - 1.76 \right) f_t \quad if \ {}^L\!/_h = 3$$

<div align="right">Eq. 5.6</div>

$$f_{t,u} = \alpha^{-0.17} \left(2.24 \frac{\sigma_{loc}}{\sigma_{75}} - 1.55 \right) f_t \quad if \ {}^L\!/_h = 4.5$$

<div align="right">Eq. 5.7</div>
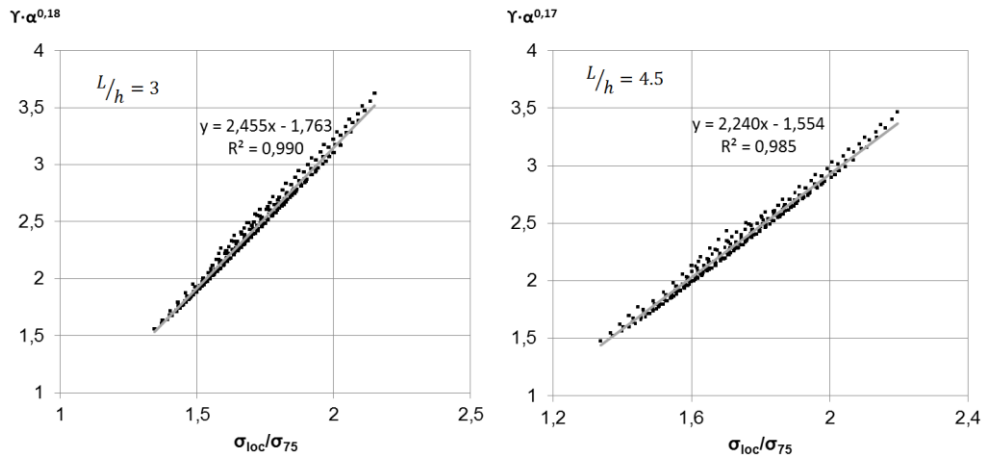
Figure 5.8 Statistical relationship between parameters γ and σ_{loc} and σ_{75}

The major problem arises when attempting to identify the crack localisation point on the experimental load-deflection curve. It is only known that this point is found before flexural strength is achieved, but the experimental curve does not give any clear signal to recognise it. This is why its identification is subjected to a certain degree of subjectivity.

The data collection process from all the modelled concretes shows that the analytical crack localisation point can vary between 75% and 100% of flexural strength (Figure 5.9). Figure 5.9 depicts the probability distribution of this relationship. According to Figure 5.9, the crack localisation point in 70% of the modelled concretes is above 95% of maximum strength. The more frequent value at which the crack localisation point takes place is at 97% of flexural strength. This is why using this value to obtain the crack localisation point is proposed herein as this criterion allows an objective value to be identified. Remember that an objective criterion is what is needed for a characterisation standard.

This method can be improved by using a more complex test setup based on the scheme in Figure 5.10, as proposed in (Baby et al., 2012) and included in (AFGC, 2013). This setup helps distinguish the onset of the bifurcation of the cracking process with crack

localisation over one of the gauge lengths, while cracking remains diffuse over the other gauge length. The criteria to be adopted to obtain the crack localisation point from these measurements are explained for three different cases in (Baby et al., 2012). This method requires measuring the strain on the bottom fibre by two LVDTs and more test setting efforts. However, these two LVDTs help to not only identify the crack localisation point, but to also determine the unloading modulus (5.2.2.3).

Another simpler alternative is to consider that the crack localisation point takes place once the macrocrack becomes visible to the naked eye.

The last two above-described methods are probably unsuitable methods to be included in characterisation standards as they both depend on a subjective point selection criterion.
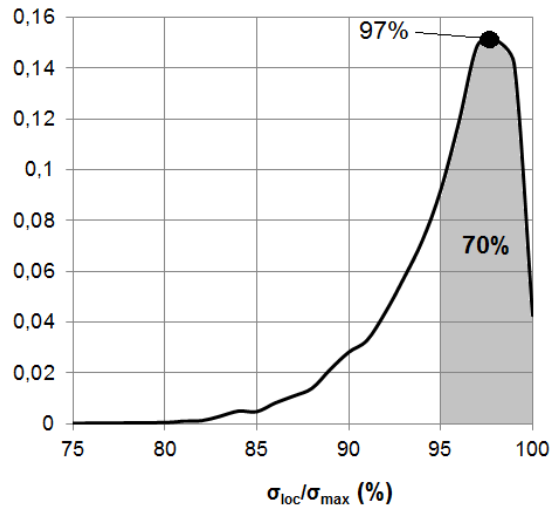
Figure 5.9 The probability function of $\sigma_{loc}/\sigma_{max}$

Figure 5.11 offers the experimental results of a 100-mm square cross-section UHPFRC specimen in a TBPT with a slenderness ratio of 4.5. The strain on the most tensioned fibre was measured according to Figure 5.10. Displacement transducers were placed at a distance of 12 mm from the bottom side of the specimen (δ_{DT}). The crack localisation point was obtained according to the three above-described methods.

As seen in Figure 5.11, a remarkable difference was found between the strain at the crack localisation point depending on the method used, while the strength value was less sensitive to it.
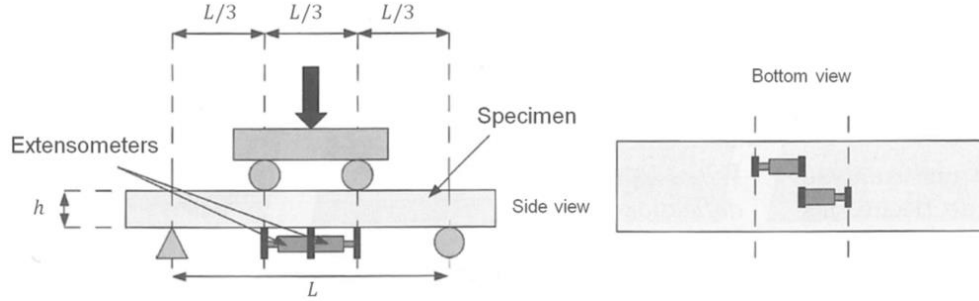
Figure 5.10 The crack localisation measurement staggers the extensometers on the tensile face (AFGC, 2013).
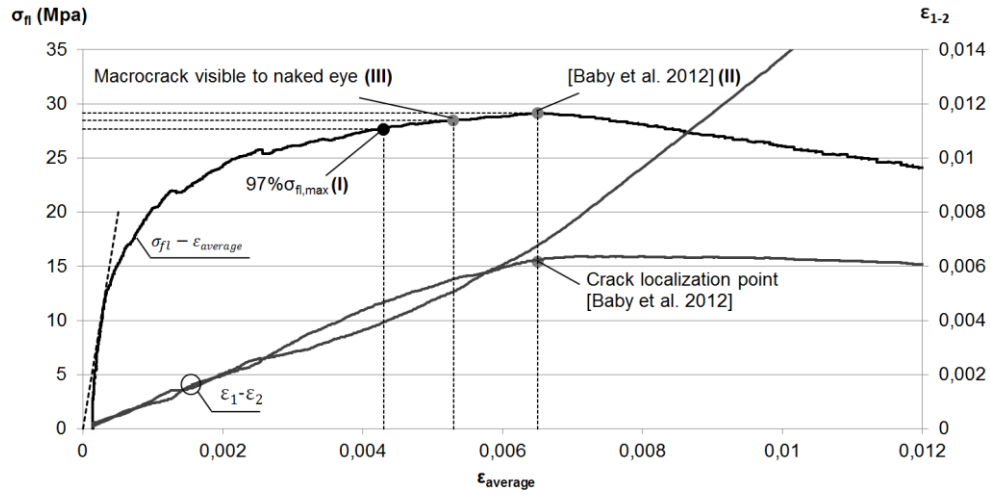
Figure 5.11 Determination of crack localisation point using the three proposed methods.

5.2.2.3 Determination of softening stages.

The softening deformational behaviour of the hinge is defined only by parameters $\varepsilon_{t,d}$ and $\varepsilon_{t,c}$ since the strength at the intersection of both softening lines is considered to be one third of $f_{t,u}$.

The initial slope of the descending branch is the most important parameter in the stress-crack opening relationship since it has been closely related to material brittleness (Spasojevic, 2008) and size effect, and determines, together with the hardening phase, the ratio between bending strength and direct tensile strength (Hillerborg, 1986). In order to make a good estimation of the initial slope of the descending tensile branch, a point close enough to the peak should be selected. On the contrary, the strain at zero stress should remain far from this point.

The two points selected to determine the descending branch were the points at flexural strengths of 80% and 30% of the crack localisation strength on the unloading branch. According to the analytical model, maximum load always took place after crack localisation, which means that this point already belonged to the descending branch in uniaxial tension. This is why the selected points on the unloading branch were defined as a percentage of crack localisation strength instead of a percentage of maximum load, which seemed more intuitive.

According to the results in Figure 5.12, the strain at the intersection of the softening lines, $\varepsilon_{t,d}$, can be obtained following Eq. 5.8 and Eq. 5.9, where δ_{80u} corresponds to the displacement at 80% of the crack localisation strength on the descending branch.
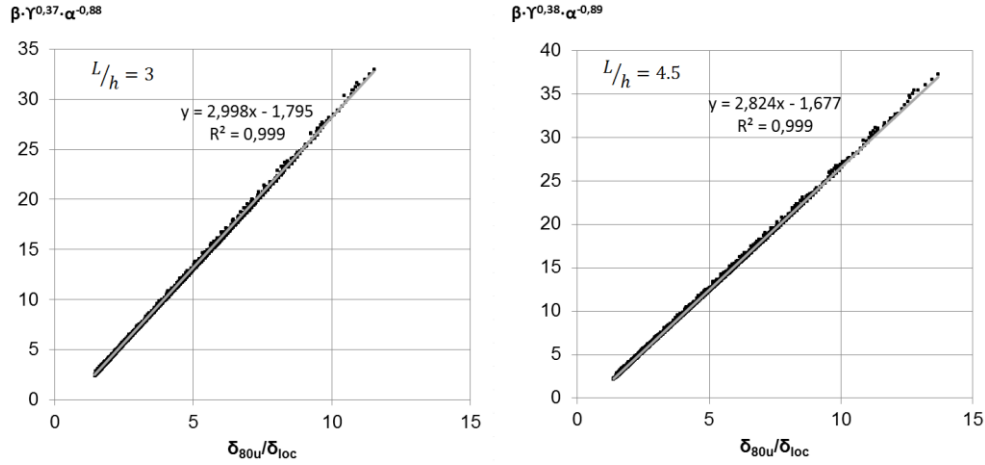
Figure 5.12 Statistical relationship between among β, γ, α, δ_{80u} and δ_{loc}

$$\varepsilon_{t,d} = \gamma^{-0.37}\alpha^{0.88}\left(3.00\frac{\delta_{80u}}{\delta_{loc}} - 1.80\right)\frac{f_t}{E} \quad if \ {}^{L}/{}_{h} = 3$$

Eq. 5.8

$$\varepsilon_{t,d} = \gamma^{-0.38}\alpha^{0.89}\left(2.82\frac{\delta_{80u}}{\delta_{loc}} - 1.68\right)\frac{f_t}{E} \quad if \ {}^{L}/{}_{h} = 4.5$$

Eq. 5.9

According to the results in Figure 5.13, the maximum strain at zero stress, $\varepsilon_{t,max}$, can be obtained following Eq. 5.10 and Eq. 5.11, where δ_{30u} corresponds to the displacement at 30% of the crack localisation strength on the unloading branch.

$$\varepsilon_{t,c} = 2.81\beta^{-0.76}\gamma^{-0.19}\alpha^{1.42}\left(\frac{\delta_{30u}}{\delta_{loc}}\right)^{1.85}\frac{f_t}{E} \quad if\ ^{L}/_{h} = 3$$

<div align="right">Eq. 5.10</div>

$$\varepsilon_{t,c} = 2.17\beta^{-0.76}\gamma^{-0.26}\alpha^{1.48}\left(\frac{\delta_{30u}}{\delta_{loc}}\right)^{1.86}\frac{f_t}{E} \quad if\ ^{L}/_{h} = 4.5$$

<div align="right">Eq. 5.11</div>
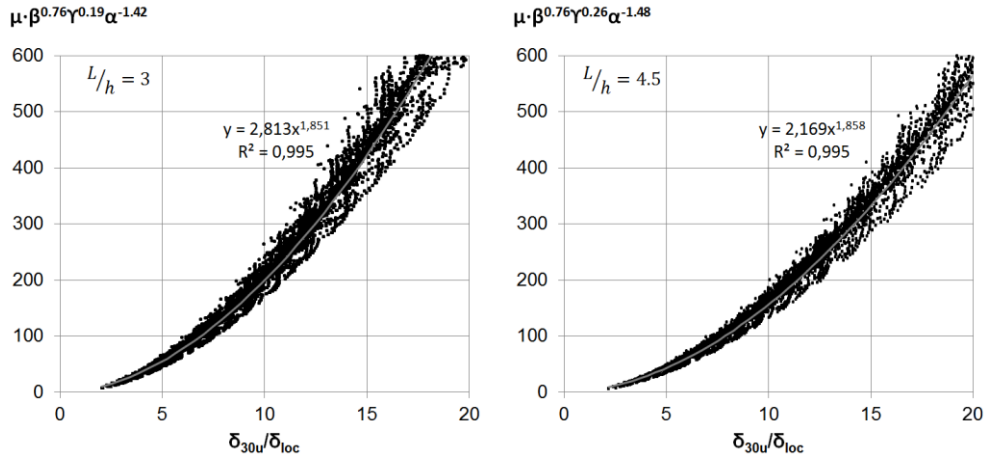
Figure 5.13 Statistical relationship among parameters μ, β, γ, α, δ_{30u} and δ_{loc}

Even though the correlations shown in Figure 5.12 and Figure 5.13 are both good, the correlation of parameter $\varepsilon_{t,c}$ can be called into question. The reason why this correlation is less accurate than the others is found in Figure 3.6. Determination of parameter $\varepsilon_{t,d}$ is sought in the unloading at 80% of the crack localisation stress. At this point, all the modelled concretes are in Stage III according to Figure 3.6. This is why the obtained correlation is so good. However, determination of parameter $\varepsilon_{t,c}$ is more complex. It requires a point on the unloading branch that remains in Stage IV according to Figure 3.6. If this point is selected above 30% of the crack localisation stress, this point belongs to Stage III for a large amount of concrete. If, however, this point is selected below 30% of the crack localisation stress, the point quite likely belongs to Stage V. A compromise solution was found at 30% of the crack localisation stress, which offered an accurate enough solution.

The determination of these two points on the experimental load-deflection curve is clearly shown in 5.2.6.

5.2.2.4 Determination of the unloading modulus

According to 3.3.3, determination of the stress-crack opening relationship requires knowledge of the unloading modulus (E^*). The experimental tests applied to the UHPFRC specimens showed that this term of the equation could represent around 10% of the crack opening at the intersection of the softening lines, and 5% of the crack opening at zero stress. If no additional data are available, unloading can be considered completely rigid, and can remain on a conservative side. In this case, a crack opening underestimation would be obtained since the increase in crack opening due to closing microcracks would be neglected. According to the results obtained from (Wille et al., 2014), it is safer and more accurate to use an unloading modulus of 20% of the elastic one.

If the unloading modulus needs to be precisely determined, the experimental setup in Figure 5.10 should be used. If the experimental strain at the most tensioned fibre versus flexural strength is plotted, a similar curve to that shown in Figure 5.14 is obtained. In one of the two displacement transducers, the multi-cracking process remains diffuse during unloading, which allows the unloading modulus (E^*) to be determined. This parameter can be established following Eq. 5.12, where δ_{DT}, is the distance from the displacement transducer to the bottom face of the specimen, and $\Delta\varepsilon$, and $\Delta\sigma$ are defined in Figure 5.14.

$$E^* = -\frac{\Delta\sigma}{\Delta\varepsilon}\left(1 + \frac{2\delta_{DT}}{h}\right)$$

Eq. 5.12

The way Eq. 5.12 is obtained is done by the linear elastic theory. According to it, the elastic modulus can be straightforwardly obtained from the $M - \phi$ relationship from two points on the linear elastic branch using Eq. 5.13, in which I is the momentum of inertia and ΔM, $\Delta\phi$ are the bending moment and curvature variation between the two points selected. $\Delta\sigma$ is the equivalent strength variation between these two points.

$$E = \frac{\Delta M}{I\,\Delta\phi} = \frac{2\Delta\sigma}{h\Delta\phi}$$

Eq. 5.13

The two staggered displacement transducers offer the strain measured at a distance δ_{DT} from the displacement transducer to the bottom face of the specimen. In a linear regime, an increase in curvature can be expressed according to the strain measured following Eq. 5.14, where $\Delta\varepsilon$ is the increase in the strain measured by the displacement transducer placed in the unloading area. Solving Eq. 5.13 and Eq. 5.14 provides Eq. 5.12, which enables the determination of the unloading modulus from a monotonic TPBT.

$$\Delta\phi = \frac{\Delta\varepsilon}{(\frac{h}{2} + \delta_{DT})}$$

<div align="right">Eq. 5.14</div>
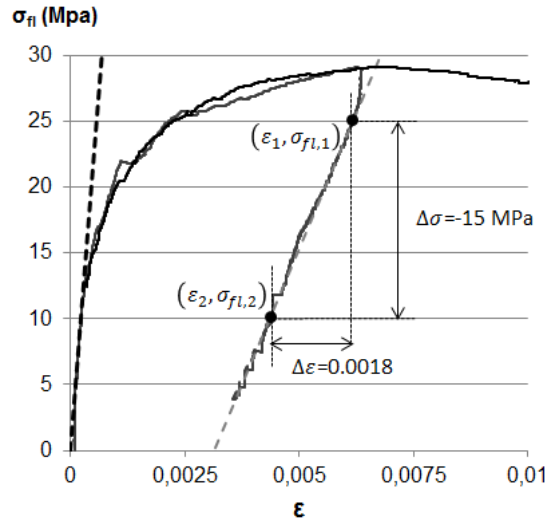
Figure 5.14 The $\sigma_{fl} - \varepsilon$ curve to determine the unloading modulus

According to Eq. 5.12 and the results shown in Figure 5.14, an unloading modulus of 10.3 GPa is obtained, which corresponds to 20% of the elastic one.

5.2.3. Crack position correction in the simplified 5P-IA

The crack position correction in the simplified 5P-IA can be made directly from the displacement measured at Points 4 and 5. Then corrected displacements $\delta_{80,u}{}^*$ and $\delta_{30,u}{}^*$ can be obtained using Eq. 5.15, where $\Delta\delta_{cp,i}$ is obtained using Eq. 3.51, and i parameter corresponds to 80 and 30.

$$\delta_{i,u}{}^* = \delta_{i,u} + \Delta\delta_{cp,i}$$

<div align="right">Eq. 5.15</div>

By applying Eq. 3.12 for the stress level at Point 4 and Point 5, Eq. 5.16 and Eq. 5.17 can be derived to obtain the corrected $\delta_{80,u}{}^*$ and $\delta_{30,u}{}^*$.

$$\delta_{80,u}{}^* = \delta_{80,u}\left(1 + \frac{9d}{20(L - 2d)}\right)$$

<div align="right">Eq. 5.16</div>

$$\delta_{30,u}{}^* = \delta_{30,u}\left(1 + \frac{71d}{50(L - 2d)}\right)$$

<div align="right">Eq. 5.17</div>

5.2.4. Adaptation of the hinge length assumption to the simplified 5P-IA

A general method to consider a different hinge length than the central one third developed in 3.4.2 cannot be directly applied to the simplified five-point inverse analysis straightforwardly as the correlation equations to determine the sectional response paramaters in 5.2.2 were obtained by assuming that hinge length equals one third the TPBT span. Its adaptation to the simplified method requires specific adaptation, which is developed in this subsection.

As shown in 3.4.2.1, from a load-displacement curve, only one single constitutive behaviour is derived regardless of the hinge length assumed in strain-hardening materials. So what is the reason for this subsection? Considering different hinge lengths offers different sectional stress-strain responses after crack localisation takes place. Minor variation in hinge length offers a vast variation in the stress-strain softening behaviour of the hinge. However, the obtained stress-crack opening relationship must be the same regardless of the assumed hinge length.

Note that the simplified inverse analysis works with the sectional stress-strain behaviour of the hinge. From 3.4.2.1, it is known that the simplified inverse analysis from different hinge length assumptions must lead to the same constitutive behaviour, otherwise the method is not right. Assuming different hinge lengths allows the simplified inverse analysis method to be validated for quite different sectional responses, which can be obtained from one single test. Hence the only reason for this subsection is to allow the extensive validation of the simplified inverse analysis method with only a few tests.

Hinge length modification affects only the determination of points 4 and 5 in the simplified 5P-IA. This modification can be modelled as an increase in the displacement measured at points 4 and 5. According to 3.3.5, the curvature to displacement transformation at the central one third beyond the crack localisation point is shown in Eq. 5.18. It is worth remembering that it corresponds to the logarithm curvature to the displacement transformation developed in 3.3.5.

$$\delta = \frac{5L^2}{72}\phi + \frac{P}{6Eb}\left(\frac{L}{h}\right)^3 + \frac{12P}{25Eb}\left(\frac{L}{h}\right)$$

<div align="right">Eq. 5.18</div>

For the developed simplified inverse analysis, it is necessary to find the increase in displacement at points 4 and 5 which makes the curvature value associated with the new displacement value the characteristic curvature (ϕ_{ch}). If this were possible, the stress-strain response obtained from it would correspond to the moment-curvature

relationship inside the selected hinge (or characteristic) length (Figure 3.23, right). The displacement at mid-span according to the average curvature in the central one third is shown in Eq. 5.18, while displacement due to a characteristic curvature can be obtained according to Eq. 5.19. Note that the only difference between Eq. 5.18 and Eq. 5.19 is the curvature value.

$$\delta_c = \frac{5L^2}{72}\phi_{ch} + \frac{P}{6Eb}\left(\frac{L}{h}\right)^3 + \frac{12P}{25Eb}\left(\frac{L}{h}\right)$$

<div align="right">Eq. 5.19</div>

Increase in displacement can be obtained following Eq. 5.20. Eq. 5.20 results in Table 5.1 when the λ, κ values are set and the unloading modulus is considered one fifth of the elastic modulus. Remember that ϕ_{ch} can be derived from Eq. 3.41 and Eq. 3.43.

$$\Delta\delta_c = \delta_c - \delta = \frac{5L^2}{72}(\phi_{ch} - \phi)$$

<div align="right">Eq. 5.20</div>

<div align="center">Table 5.1 Increase in displacement according to the assumed hinge length</div>

λ	κ	E^*	$\Delta\delta_c$
3	1	$0.2\,E$	0
	0.5	$0.2\,E$	$\delta - \delta_{loc} + \dfrac{823h}{100E}(\sigma_{loc} - \sigma)$
4.5	1.5	$0.2\,E$	0
	1	$0.2\,E$	$\dfrac{1}{2}(\delta - \delta_{loc}) + \dfrac{7167h}{800E}(\sigma_{loc} - \sigma)$
	0.5	$0.2\,E$	$2(\delta - \delta_{loc}) + \dfrac{7167h}{200E}(\sigma_{loc} - \sigma)$

In 5P-IA the stress at points 4 and 5 is expressed according to the crack localisation strength, which is a 97% of the maximum flexural strength. These conditions can be imposed to the equations in Table 5.1 to derive the displacement increase at points 4 and 5, which needs to be added to the displacement value measured to take into account the selected characteristic length. The final formulation is summarised in Table 5.2.

Table 5.2 Correction factors to be applied to displacement measured at points 4 and 5

Point	λ	κ	$\Delta\delta_c$
4	3	0.5	$\delta_{80,u}{}^* - \delta_{loc} + 1.65h\dfrac{\sigma_{loc}}{E}$
5			$\delta_{30,u}{}^* - \delta_{loc} + 5.76h\dfrac{\sigma_{loc}}{E}$
4	4.5	1	$\dfrac{1}{2}\left(\delta_{80,u}{}^* - \delta_{loc}\right) + 1.79h\dfrac{\sigma_{loc}}{E}$
5			$\dfrac{1}{2}\left(\delta_{30,u}{}^* - \delta_{loc}\right) + 6.27h\dfrac{\sigma_{loc}}{E}$
4	4.5	0.5	$2\left(\delta_{80,u}{}^* - \delta_{loc}\right) + 7.16h\dfrac{\sigma_{loc}}{E}$
5			$2\left(\delta_{30,u}{}^* - \delta_{loc}\right) + 25.08h\dfrac{\sigma_{loc}}{E}$

The parameters $\delta_{80,u}{}^*$, $\delta_{30,u}{}^*$ in Table 5.2 correspond to the displacement measured at Points 4 and 5 after the crack position correction (see 5.2.3) has been done. Note that when applying the non-linear hinge model, the curvature to displacement at mid-span transformation according to the considered hinge length is applied prior to the crack position correction.

However while applying the inverse analysis method, it has to be done exactly in the opposite way: the crack position correction must be done before considering hinge length.

Finally, the global correction to be applied to the displacement measured at points 4 and 5 is shown in Eq. 5.21 and Eq. 5.22. The first term of these equations is the crack position correction according to 5.2.3.

$$\delta_{80,u}{}^{**} = \delta_{80,u}{}^* + \Delta\delta_c$$

Eq. 5.21

$$\delta_{30,u}{}^{**} = \delta_{30,u}{}^* + \Delta\delta_c$$

Eq. 5.22

5.2.5. Simpified 5P-IA summary

As a first step of the inverse analysis method, the experimental curve should be corrected so that the initial straight line that defines the elastic stage phase passes through the origin. A similar process to that pointed out in (ASTM C1609/C1609M-

10.) can be followed. After correcting the experimental curve, the elastic modulus (E) can be obtained following Eq. 5.23 for either $L/h = 3$ or $L/h = 4.5$. This expression can be obtained from the elasticity theory and should include shear deflection to better estimate the elastic modulus (Graybeal, 2006).

Eq. 5.23 leads to Eq. 5.24 and Eq. 5.25 when L/h is 3 or 4.5, respectively. The k parameter is used to define the lines that represent a certain loss of initial stiffness ($k \leq 1$). The straight lines that define initial stiffness S_0, secant stiffness S_{75} and S_{40} in Figure 5.4 can be obtained from Eq. 5.24 and Eq. 5.25 when considering that $k = 1$, $k = 0.75$ and $k = 0.40$, respectively.

$$\delta = \frac{\sigma_{fl} h}{E} \left[\frac{23}{108} \left(\frac{L}{h} \right)^2 + \frac{12}{25} \right]$$

Eq. 5.23

$$\sigma_{fl_i} = k \frac{E \delta_i}{2.40 h} \quad if \; {}^L/_h = 3$$

Eq. 5.24

$$\sigma_{fl_i} = k \frac{E \delta_i}{4.79 h} \quad if \; {}^L/_h = 4.5$$

Eq. 5.25

The way that the five key point parameters were defined allows the objective determination of the inverse analysis input parameters. Having defined the five key points on the experimental curve, the formulation in Table 5.3 has to be used to determine the complete stress-strain response inside the chosen hinge length. Thus the proposed inverse analysis method consists in identifying five key points from the experimental $\sigma_{fl} - \delta$ following objective criteria, and in applying simple equations. Unlike most of the inverse analysis methodologies found in the literature, this procedure does not strictly require a computer.

Table 5.3 The simplified inverse analysis formulation to determine the stress-strain relationship from the five key points drawn from the $\sigma_{fl} - \delta$ experimental curve.

	$L/h = 3$	$L/h = 4.5$
f_t	$\dfrac{\sigma_{75}}{1.63} \left(\dfrac{\sigma_{75}}{\sigma_{40}} \right)^{0.19}$	$\dfrac{\sigma_{75}}{1.59} \left(\dfrac{\sigma_{75}}{\sigma_{40}} \right)^{0.21}$
$\varepsilon_{t,u}$	$\dfrac{f_t}{E} \left(7.65 \dfrac{\delta_{loc}}{\delta_{75}} - 10.53 \right)$	$\dfrac{f_t}{E} \left(6.65 \dfrac{\delta_{loc}}{\delta_{75}} - 9.40 \right)$

$\boldsymbol{f_{t,u}}$	$\alpha^{-0.18}\left(2.46\dfrac{\sigma_{loc}}{\sigma_{75}}-1.76\right)f_t$	$\alpha^{-0.17}\left(2.24\dfrac{\sigma_{loc}}{\sigma_{75}}-1.55\right)f_t$
$\boldsymbol{\varepsilon_{t,d}}$	$\gamma^{-0.37}\alpha^{0.88}\left(3.00\dfrac{\delta_{80u}^{**}}{\delta_{loc}}-1.80\right)\dfrac{f_t}{E}$	$\gamma^{-0.38}\alpha^{0.89}\left(2.82\dfrac{\delta_{80u}^{**}}{\delta_{loc}}-1.68\right)\dfrac{f_t}{E}$
$\boldsymbol{\varepsilon_{t,c}}$	$2.81\beta^{-0.76}\gamma^{-0.19}\alpha^{1.42}\left(\dfrac{\delta_{30u}^{**}}{\delta_{loc}}\right)^{1.85}\dfrac{f_t}{E}$	$2.17\beta^{-0.76}\gamma^{-0.26}\alpha^{1.48}\left(\dfrac{\delta_{30u}^{**}}{\delta_{loc}}\right)^{1.86}\dfrac{f_t}{E}$

From the stress-strain response inside hinge length and using Eq. 5.26 and Eq. 5.27, which directly derive from Eq. 3.11 and Eq. 3.12, the stress-crack opening relationship can be obtained.

$$w_d = \left(\varepsilon_{t,d} - \varepsilon_{t,u} - \frac{2f_{t,u}}{3E^*}\right)s$$

Eq. 5.26

$$w_c = \left(\varepsilon_{t,c} - \varepsilon_{t,u} - \frac{f_{t,u}}{E^*}\right)s$$

Eq. 5.27

At the end of the inverse analysis method, the constitutive tensile law must be defined by a stress-strain relationship up to the peak, and a stress-crack opening relationship from this point onwards.

In order to avoid a scale effect in tension, the tensile characterisation of strain-hardening materials with a stress-crack opening relationship is absolutely necessary after crack localisation takes place.

As the crack opening values during strain-hardening behaviour are too low to be included in a stress-crack opening relationship, a stress-strain relationship might be more appropriate to characterise the ascending tensile branch. According to this criterion, the uniaxial tensile law for strain-hardening materials should look like Figure 5.15. Following this procedure, both the hardening and crack-opening stages can be determined from the same single test. An example of applying the proposed inverse analysis method is found in 5.2.6.
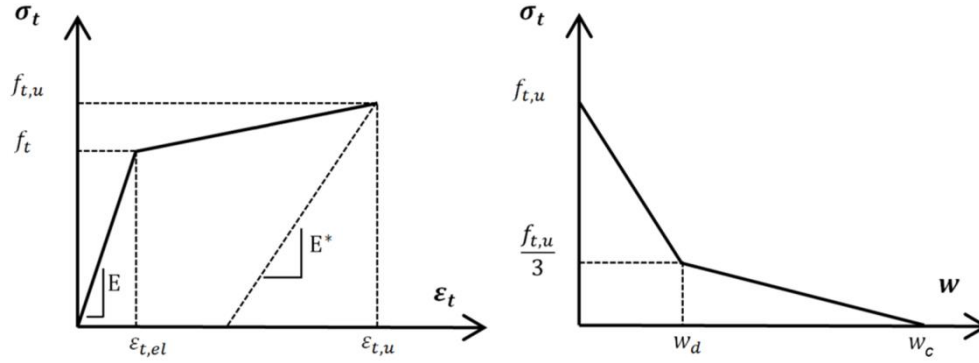
Figure 5.15 The bilinear σ-w relationship considered for UHPFRC behaviour.

5.2.6. Example of applying 5P-IA

An example of the proposed simplified inverse analysis method was applied to the TPBT $\sigma_{fl} - \delta$ curve (see Figure 5.16) and corresponds to the same specimen shown in Figure 5.11. The results were compared to the point-by-point inverse analysis.

Figure 5.16 shows the $\sigma_{fl} - \delta$ curve obtained from a TPBT with a $L/h = 4.5$ and a 100-mm-square cross-section in a UHPFRC specimen with an average compressive strength of 170MPa, which contained a 2% volume of steel fibres 13/0.2 (López et al., 2015). For simplicity reasons, hinge length equals one and a half the specimen depth (central one-third length) and centered crack hypothesis is assumed.

The simplified inverse analysis procedure proposed herein can be summarised in seven steps:

1. Correction of the $\sigma_{fl} - \delta$ to force it to pass through the origin, if necessary.

2. Establishment of the elastic modulus following Eq. 5.24 or Eq. 5.25.

3. Definition of the 75% and 40% loss of stiffness lines (S_{75} and S_{40}) according to Eq. 5.24 or Eq. 5.25, depending on the slenderness ratio, by considering that $k = 0.75$ and $k = 0.40$, respectively.

4. Determination of key points 1 and 2 as the intersection points between the loss of stiffness lines and the $\sigma_{fl} - \delta$ curve. These points define parameters σ_{75}, δ_{75}, and σ_{40}.

5. Definition of the crack localisation point, key point 3, that defines parameters σ_{loc} and δ_{loc}. Three different methods have been considered:

    i. 97% of flexural strength on the loading branch.

    ii.   The process pointed out in (Baby et al., 2012) using two staggered LVDTs at the most tensioned fibre (Figure 5.10 and Figure 5.11).

    iii.   Point when the macrocrack becomes visible to the naked eye.

6. Determination of key points 4 and 5 as 80% and 30% of the crack localisation point on the unloading branch. These points define parameters δ_{80u} and δ_{30u}.

7. Application of the back-of-the-envelope formulation in Table 5.3 and Eq. 5.26 and Eq. 5.27 to determine the tensile constitutive parameters.
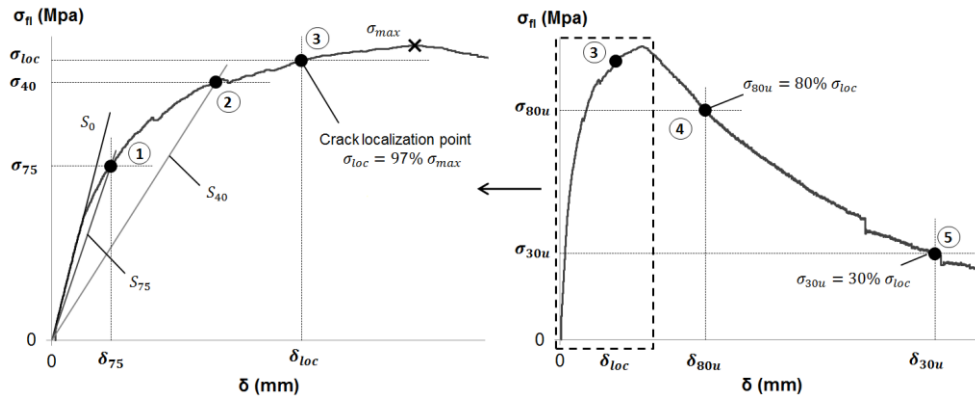
Figure 5.16 The five proposed key points obtained from the $\sigma_{fl} - \delta$ curve

The seven input parameters obtained from the experimental curve in Figure 5.16 are shown in Table 5.4, and correspond to the five key points. Table 5.5 presents the values of the constitutive parameters that resulted from applying the back-of-the-envelope formulation. Figure 5.17 shows the stress-strain results for different crack localisation points and a comparison to the point-by-point inverse analysis results.

Table 5.4 Input parameters for the simplified inverse analysis method obtained from Figure 5.16 and the different crack localisation criteria from Figure 5.11.

Key Point	1		2	3		4	5
Parameter	σ_{75} (MPa)	δ_{75} (mm)	σ_{40} (MPa)	σ_{loc} (MPa)	δ_{loc} (mm)	δ_{80u} (mm)	δ_{30u} (mm)
I (97% of σ_{max})				27.67	0.87	2.28	5.78
II (Baby et al, 2012)	17.2	0.205	25.5	29.12	1.25	2.14	5.68
III (visible to the naked eye)				28.46	1.02	2.23	5.75

Table 5.5 Output parameters from the simplified 5P-IA inverse analysis.

	$E(MPa)$	$f_t(MPa)$	$f_{t,u}(MPa)$	$\varepsilon_{t,u}$	$\varepsilon_{t,d}$	$\varepsilon_{t,c}$
I (97%)			12.46	0.0034	0.0130	0.0380
II (Baby et al, 2012)	54000	9.96	12.53	0.0057	0.0113	0.0443
III (visible to the naked eye)			12.46	0.0044	0.0128	0.0410

Figure 5.17 shows that the simplified inverse analysis offers a similar constitutive law to that obtained from the point-by-point inverse analysis. Crack localisation point selection becomes the weakest point of this new simplified procedure because clearly distinguish this point is not possible. Note that it is not easy to define the strain at tensile strength from the PBP-IA results due to the fluctuation of the resulting curve.

Figure 5.18 shows the crack pattern at the bottom of the specimen after the test. An average crack spacing of 4.7 mm is estimated. According to Figure 5.14 and Eq. 5.12, an unloading modulus of 10.33 GPa is also obtained. These values come close to those obtained in (Wille et al., 2014) for a UHFPRC with 2% steel fibres.
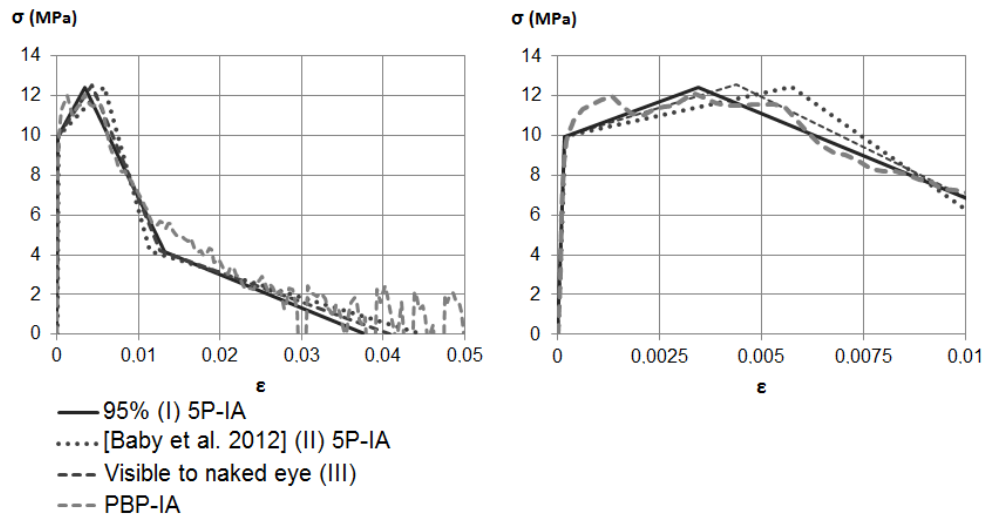
Figure 5.17 5P-IA for three different crack localisation point criteria and its comparison with the point-by-point inverse analysis.

The stress-crack opening relationship was derived using these data. Figure 5.19 shows the complete constitutive law in tension: a stress-strain relationship before crack localisation; and a stress-crack opening relationship after that point. The stress-strain

sectional behavoiur that derives from the simplified inverse analysis that corresponds to method (I) for the crack localisation point estimation is represented.

It is worthy noting that the stress-crack opening behaviour shown in Figure 5.19 comes close to the behaviour of other UHPFRCs with the same content of fibres tested in a uniaxial tensile test, as shown in Figure 2.14 and Figure 2.15 (included in Chapter 2).
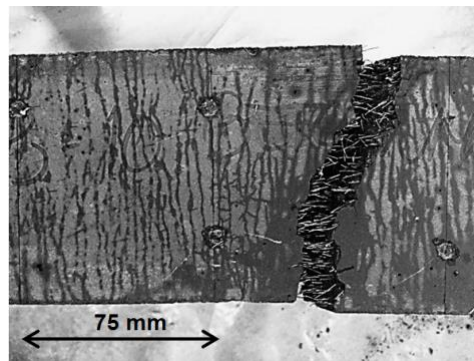
Figure 5.18 Average crack spacing after a TPBT (bottom view of the specimen)
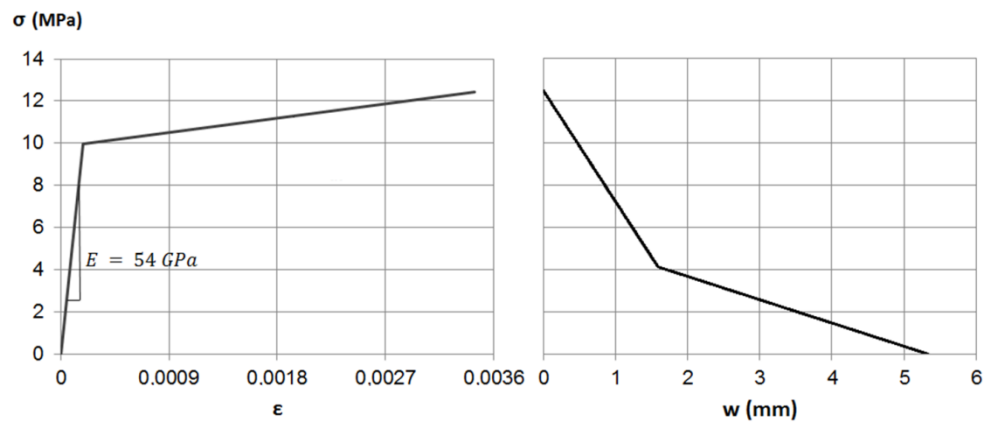
Figure 5.19 Constitutive law in tension using the simplified inverse analysis method.

5.3. Validation of 5P-IA

The validation of the simplified 5P-IA is done by comparing the results obtained using 5P-IA and PBP-IA. Chapter 4 checks that PBP-IA, together with the non-linear hinge model, offers accurate results compared to the experimental results. As the combined use of the non-linear hinge model and PBP-IA works, the validation of 5P-IA can be done by directly comparing the results obtained from PBP-IA.

Two different validation analyses were performed. The first one consists in applying the inverse analysis procedure to the analytical example shown in 3.4.2. The analytical load-deflection curve is used to derive the constitutive properties, which are actually known. These inverse analysis methods can be validated by comparing the inverse analysis results obtained from 5P-IA and PBP-IA to the initial constitutive properties.

For the second validation analysis, the experimental programme described in Appendix II was carried out, in which 16 specimens were tested following a TPBT with slenderness ratios of 3 and 4.5. From the experimental results, it was impossible to know the *real* constitutive properties. However, as it was considered that PBP-IA offers an accurate enough constitutive relationship, and the results obtained from 5P-IA were compared to it. To widen the validation range of the proposed method, different crack hinge length sectional responses hypotheses are used. The influence of considering crack position is also analysed. Finally, this experimiental programme enables us to obtain the variation coefficients in the determination of each parameter that defines UHPFRC constitutive behaviour.

5.3.1. Analytical validation

An analytical validation is done using the analytical example shown in 3.4.2. The inverse analysis method only requires the load–deflection curve. Then the results in Figure 3.27 are used. 5P-IA is applied by considering three different hinge lengths: (i) one and a half the specimen depth; (ii) the specimen depth; and (iii) half the specimen depth. According to the non-linear hinge model in Chapter 3, the final constitutive behaviour must be the same for all cases, no matter the assumed hinge length. The 5P-IA results are compared to the constitutive relationship in Figure 3.24, and also to the results obtained from PBP-IA.

When applying 5P-IA, that crack localisation (key point 3) is considered to take place at 97% the flexural strength. The results are shown in Table 5.6. From them, it can be concluded that despite its simplicity, 5P-IA offers close results for the initial constitutive behaviour. Greater deviation takes place while determining $\varepsilon_{t,u}$, with an error of 14%. This deviation is due to the fact that the crack localisation point for this particular case occurs at 98% of the flexural strength instead of at 97%. As already mentioned, crack localisation point determination is the major drawback of this method. Even though the selection of this point is not exact, the criterion is objective and offers accurate results.

Table 5.6 The 5P-IA results from the load-deflection curve in Figure 3.27 for a crack localisation strength that equals 97% of flexural strength

	f_t (MPa)		$f_{t,u}$ (MPa)		$\varepsilon_{t,u}$‰		E (GPa)		w_d (mm)		w_c (mm)	
Analytical Figure 3.24	10		10		2.5		50		1.50		5.00	
l_c	Value	Error (%)	Value	Error (%)	Value	Error (%)	Value	Error (%)	Value	Error (%)	Value	Error (%)
1.5h									1.41	5.9	4.32	13.6
h	9.9	1.1	10.2	1.8	2.16	13.7	50	0	1.37	8.9	4.64	7.1
0.5h									1.33	11.2	5.15	3.1

Table 5.7 offers the results obtained from 5P-IA when the crack localisation point is the right one. In this case, deviation is not due to the selection of the key points, but to the deviation of the method itself. As seen, the deviation values are low, which means that the method is quite accurate.

Table 5.7 The 5P-IA results from the load-deflection curve in Figure 3.27 using the analytical crack localisation point

	f_t (MPa)		$f_{t,u}$ (MPa)		$\varepsilon_{t,u}$‰		E (GPa)		w_d (mm)		w_c (mm)	
Analytical Figure 3.24	10		10		2.5		50		1.50		5.00	
l_c	Value	Error (%)	Value	Error (%)	Value	Error (%)	Value	Error (%)	Value	Error (%)	Value	Error (%)
1.5h									1.37	8.6	4.47	10.5
h	9.9	1.1	10.2	1.8	2.53	1.2	50	0	1.32	11.9	4.80	4.0
0.5h									1.33	11.3	5.33	6.6

Regarding stress-crack opening behaviour, we can see that 5P-IA provides results with a deviation that falls within a 4-14% range. A major deviation is found while determining the characteristic crack opening (w_c), which is expected as statistical adjustment in Figure 5.13 is the worst of them all. Despite the crack opening values being assumed to be the same regardless of the assumed hinge length, it seems that characteristic crack opening increases when a shorter hinge length. This is only due to the poorer accuracy achieved during the statistical adjustment. Crack opening at the change of slope (w_d) remains pretty much constant for each hinge length used. The results come close to each other no matter what the assumed hinge length. It means that

5P-IA can be used for a wide range of stress-strain sectional responses. Remember that 5P-IA was fitted to around 12 million different stress-strain sectional responses.

The 5P-IA results can also be compared to those obtained from the point-by-point inverse analysis. These results are shown in Figure 5.20 for the three different crack hinge lengths used.
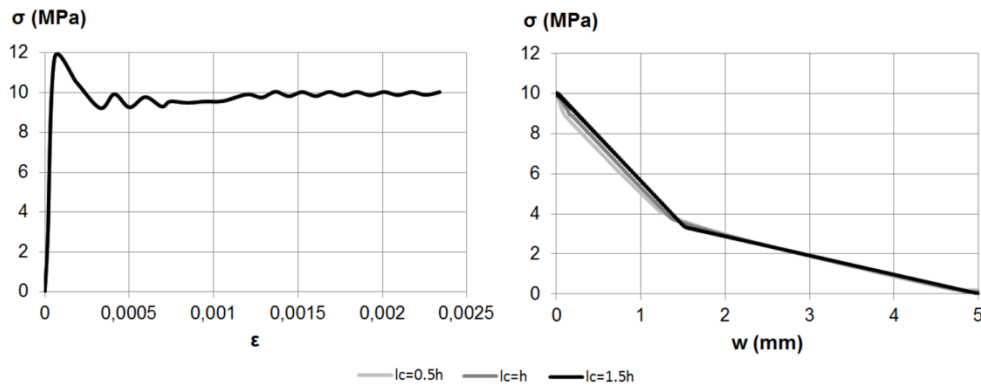
Figure 5.20 Point-by-point results from the load-deflection curve in Figure 3.27

As seen in Figure 5.20, a point-by-point inverse analysis reproduces with absolute accuracy the stress-crack opening behaviour. However, this is not the case of the stress-strain relationship. This method offers greater cracking strength of 12 MPa and a slight drop after it. It is important to know that this commonly happens when this inverse analysis method is used, so there is no need to be scared of the obtained results, nor of slight drops it they appear.

5.3.2. Experimental validation

An experimental programme was specifically carried out to validate the results obtained by applying 5P-IA for it to be compared to the results obtained from PBP-IA. The experimental programme is fully described in Appendix II. Sixteen TPBTs on 100-mm square cross-section specimens are shown. Half were tested with a slenderness ratio of 3, and the other half with a slenderness ratio of 4.5. The only experimental measurements taken were the displacement at mid-span and its associated load. The used UHPFRC had an average compressive strength of 169.89MPa, obtained from sixty-one 100 mm-long cubes with a 4.78% coefficient of variation. A fibre amount of 2% of 13/0.2 steel fibres in volume was used. The test setup configuration is shown in Figure 5.21.

Specimens were cast in eight different batches by casting two specimens per batch. One specimen from each batch was tested with a slenderness ratio of 3, and the other with a slenderness ratio of 4.5. The naming is "D$i\lambda$j", where i is the batch number and

j is the slenderness ratio. Specimens were turned 90º degrees from their casting position for testing.
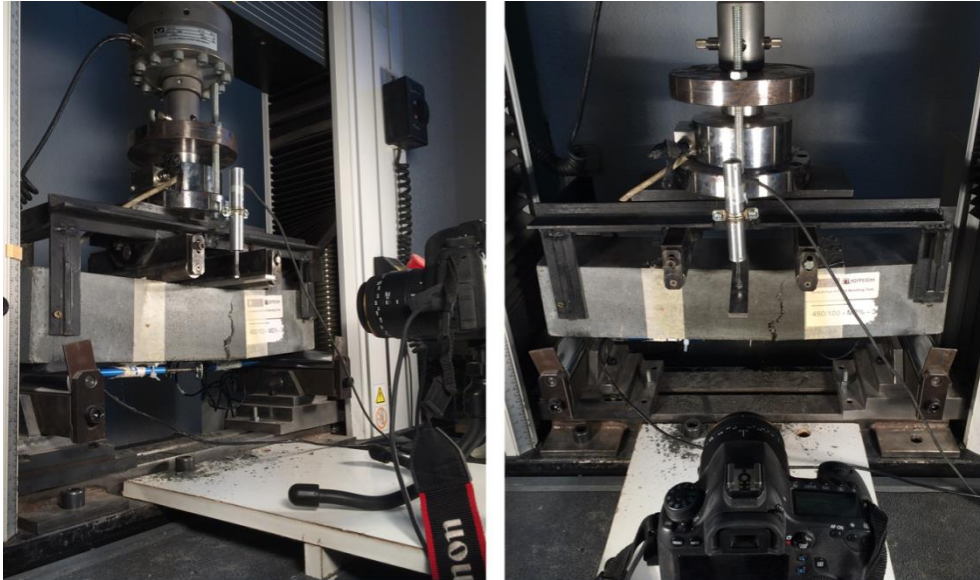
Figure 5.21 Experimental test setup for a TPBT of a 100-mm square cross-section specimen with a slenderness ratio of 4.5.

The main objectives of this experimental programme are to: (i) validate 5P-IA by comparing it to the PBP-IA results; (ii) evaluate the influence on the consideration of crack position; (iii) evaluate the influence of the slenderness ratio on UHPFRC material behaviour; (iv) determine the coefficient of variation for each parameter. The analysis of the results is offered in subsequent subsections.

5.3.2.1 Crack position correction

The equivalent strength versus displacement at mid-span curves are obtained directly from TBPTs. According to Figure 3.28, the measurement of parameter d,according to for each tested specimen is shown in Table 5.8. These values range from 0 to 50 mm if the slenderness ratio is 3, and from 0 to 75 mm if it is 4.5; i.e. from 0 to $L/6$.

Table 5.8 Measurement of parameter d

d (mm)	D1	D2	D3	D4	D5	D6	D7	D8
$\lambda 3$	30	50	5	35	0	25	5	0
$\lambda 4.5$	75	20	15	75	70	35	75	50

Figure 5.22 and Figure 5.23 show the average equivalent strength *versus* the displacement at mid-span curves for a slenderness ratio of 3 and one of 4.5,

respectively. The average curve is depicted in black, while the grey lines represent the maximum and minimum values obtained in the tests for the same displacement at mid-span. From these figures, we can see that variation lessens when curves are corrected if crack position is taken into account. In fact the average coefficient of variation goes from 32% to 18% when the slenderness ratio is 3, and from 18% to 10% when it is 4.5.
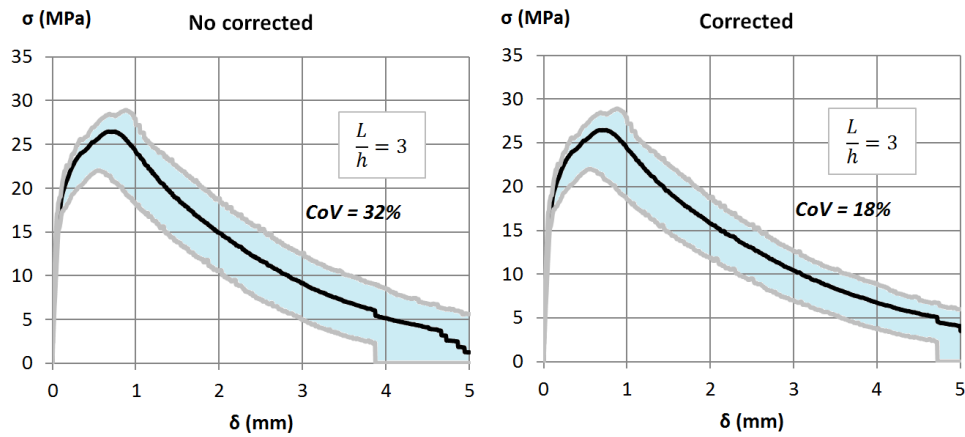
Figure 5.22 Equivalent strength *versus* displacement on the mid-span average curve and its variability, both with (right) and without (left) crack location correction.
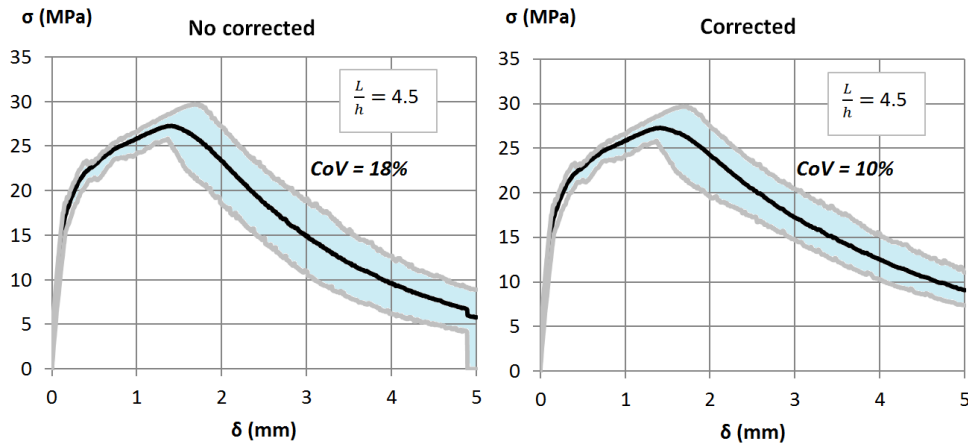
Figure 5.23 The equivalent strength *versus* the displacement on the mid-span average curve and its variability, both with (right) and without (left) crack location correction.

The crack position correction acts from the maximum load onwards. After its application, the parallelism between softening curves increases. This fact leads to a less variability in the determination of UHPFRC constitutive tensile properties.
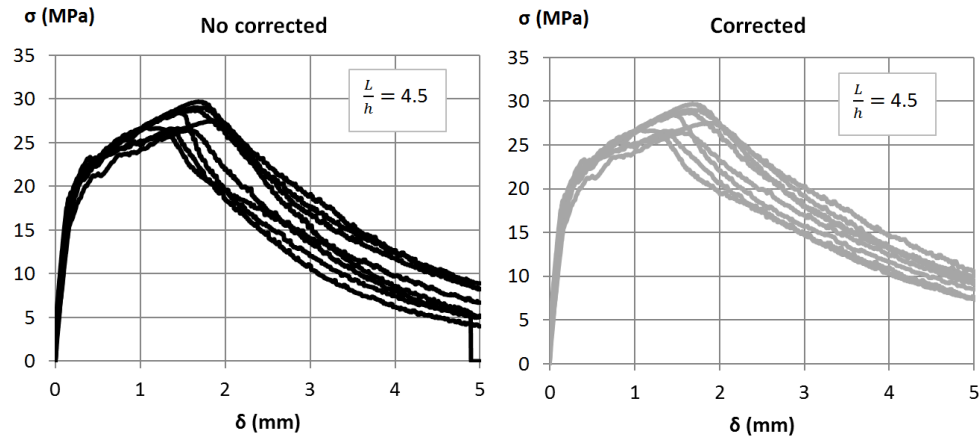
Figure 5.24 Equivalent strength versus displacement at mid span experimental curves for a slenderness ratio of 4.5, with (right) and without (left) crack location correction.

The increase in the parallelism after the crack position correction is noted in Figure 5.24, in which the equivalent strength *versus* the displacement at mid-span curves for a slenderness ratio of 4.5 are shown. Crack position is probably the most relevant cause of variability in the TPBT. In order to evaluate this, 5P-IA was applied to the equivalent strength curves in Figure 5.24, and also to the curves that correspond to a slenderness ratio of 3, both with and without the crack position correction. The analysis was done using a hinge (or characteristic) length that equals specimen depth. As the crack position correction only affects the unloading branch, only the stress-crack opening results were plotted. Figure 5.25 depicts the stress-crack opening relationship obtained for different cases. A black line represents the average curve, while a grey line represents the upper and lower bounds obtained. Variability in the results significantly lessens when crack position is taken into account.

The average stress–crack opening results are plotted in Figure 5.26, both with and without the crack position correction. Here we can see that the results come closed to each other regardless of the slenderness ratio used. Table 5.8 shows how crack deviates more from mid-span for the tested specimens with a slenderness ratio of 4.5 in the test that was run. This leads to worse UHPFRC performance if crack position is not taken into account, which is shown in Figure 5.26 (left). However when crack position is considered, both tests offer similar results, which is why crack position must be taken into account in TPBTs.
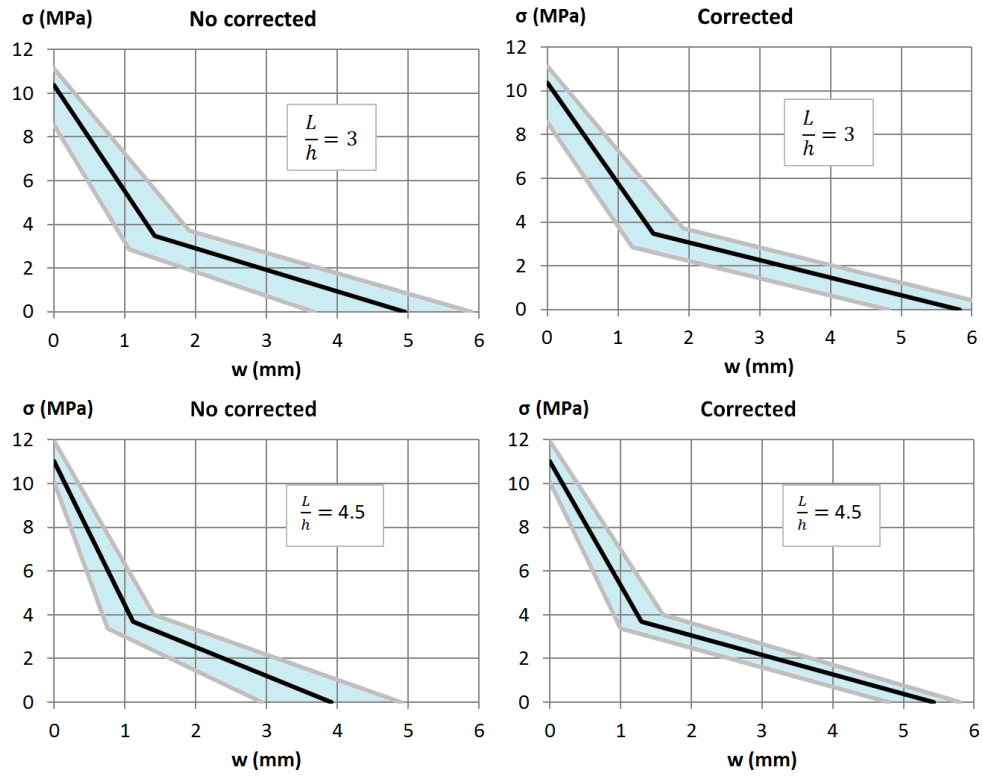
Figure 5.25 The stress-crack opening relationship obtained from 5P-IA for different slenderness ratios, both with and without crack location correction.
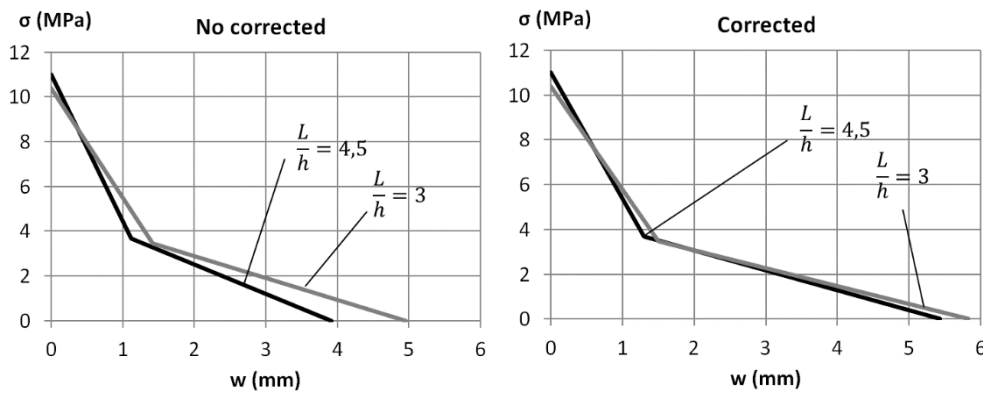
Figure 5.26 The average stress-crack opening responses for a hinge length equals to the specimen depth when crack location is considered (right) and when is not (left).

5.3.2.2 Crack hinge length

As pointed out in 3.4.2, the stress-crack opening relationship must be the same regardless of the assumed hinge length. This property can be used to check 5P-IA that was developed. Tests with a slenderness ratio of 3 were analysed by considering a hinge length equal to the specimen depth and half the specimen depth. Tests with a slenderness ratio of 4.5 have been analysed when considering that hinge length equals one and a half the specimen depth, the specimen depth, and half the specimen depth. In this subsection, the results were analysed with the corresponding crack position corrections.

To gain a better understanding of the effect of the crack hinge length hypothesis on the moment-rotation capacity of the hinge, Figure 5.27 is plotted. It depicts the experimental equivalent strength versus deflection at mid-span originally obtained and corrected according to the d value in Table 5.8 for specimen D4λ 4.5. Having completed the crack position correction, the displacement to the curvature transformation in Table 3.5 can be used to derive the equivalent strength *versus* the curvature curve for the different assumed hinge lengths. The results are shown in Figure 5.27 (right).

The higher the curvature values, the shorter the characteristic length considered, and the $\varepsilon_{t,d}$ and $\varepsilon_{t,c}$ values that determine the stress-strain sectional response of the hinge are also higher. However, they are multiplied by a shorter hinge length, as shown in Eq. 5.26 and Eq. 5.27, to obtain crack opening values. At the end of the process, the stress-crack opening relationship must be the same no matter what hinge length is used.
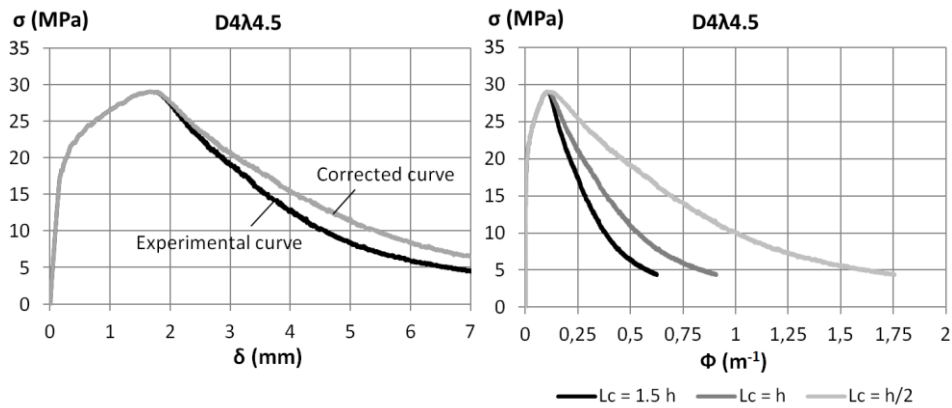
Figure 5.27 The crack position correction (left) and the different characteristic length hypotheses (right) for specimen D4λ4.5.

However, Figure 5.28 shows that characteristic crack opening (w_c) is greater the shorter the selected hinge length, which was the case in the example shown in 5.3.1.

This occurs for both slenderness ratios. The crack opening at the change of slope (w_d) remains almost the same in all cases regardless of the hinge length hypothesis.

Even though variability is less when determining the characteristic crack opening for a specific hinge length, the differences found in the different hinge length assumptions reveal that the characteristic crack opening determination is not altogether reliable. Considering that characteristic crack opening can be estimated as half the fibre length (6.5 mm in our case), it can be stated that 5P-IA is safe and tends to underestimate the expected value. This does not occur for the crack opening upon the change of slope, whose determination seems stable and reliable no matter what hinge length is used.
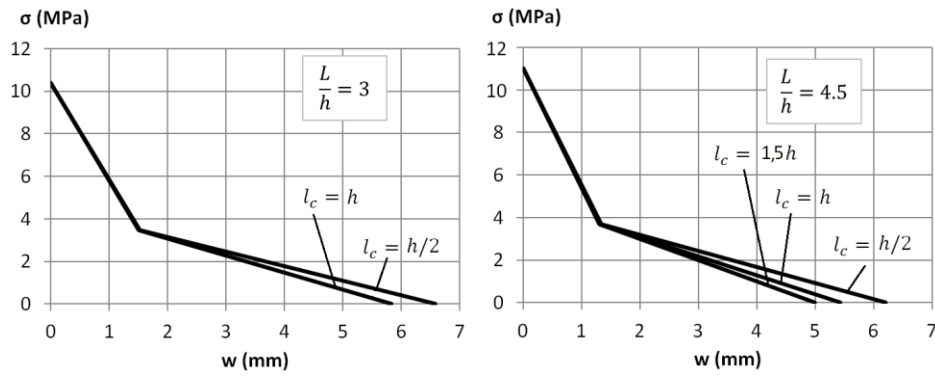
Figure 5.28 The average stress-crack opening relationship obtained from 5P-IA for different characteristic length hypotheses.

5.3.2.3 Comparing 5P-IA and PBP-IA

An analysis of the inverse analysis results is divided into two steps: (i) analysis of the stress-strain response up to the peak; and (ii) an analysis of the stress-crack opening relationship. Finally in a third step (iii), the differences found between these two methods are explained.

(i)   Stress-strain relationship results

The parameters that define average UHPFRC stress-strain behaviour up to the peak obtained from 5P-IA and PBP-IA are shown in Table 5.9 and Table 5.10. The complete results are shown in Appendix II. Table 5.11 provides the deviation of the 5P-IA results from PBP-IA as a %. Green cells indicate an underestimation of 5P-IA, while red cells denote an overestimation of 5P-IA compared to PBP-IA.

From Table 5.9 and Table 5.10 we can see that the coefficient of variation is small in the determinations of cracking strength (f_t), ultimate tensile strength ($f_{t,u}$) and the elastic modulus (E). However, the coefficient of variation in the determination of the strain associated with ultimate tensile strength falls within the 15%-20% range. It may highlight the difficulties found when determining the strain upon the peak in both

methods. With 5P-IA, we can assume that the crack localisation point at 97% of flexural strength leads to some variability in the results. With PBP-IA, the point-by-point curve shows that the end of strain-hardening cannot be clearly distinguishable.

Table 5.9 The average stress-strain results from 5P-IA in MPa

5P-IA									
	L/h = 3					L/h = 4,5			
	f_t	f_{tu}	ε_{tu}	E		f_t	f_{tu}	ε_{tu}	E
AVERAGE	10,4	10,4	0,0062	53738	AVERAGE	11,1	11,0	0,0058	50650
ST.DEV	0,8	0,9	0,0012	5196	DESV	0,4	0,6	0,0010	3615
COV %	7,8	8,4	20,0	9,7	COV %	3,2	5,8	17,7	7,1

Table 5.10 The average stress-strain results from PBP-IA in MPa

PBP-IA									
	L/h = 3					L/h = 4,5			
	f_t	f_{tu}	ε_{tu}	E		f_t	f_{tu}	ε_{tu}	E
AVERAGE	10,0	10,1	0,0063	53738	AVERAGE	10,5	10,7	0,0062	50650
ST.DEV	0,9	0,9	0,0014	5196	DESV	0,4	0,4	0,0012	3615
COV %	8,8	8,7	21,3	9,7	COV %	4,1	3,3	19,1	7,1

Table 5.11 Deviation as a % of the average result obtained from 5P-IA compared to those obtained by PBP-IA

DEVIATION							
	L/h = 3				L/h = 4.5		
	f_t	f_{tu}	ε_{tu}		f_t	f_{tu}	ε_{tu}
AVERAGE	-3,6%	-3,2%	1,8%	AVERAGE	-5,9%	-2,5%	6,0%

When comparing the deviation of the 5P-IA results with those obtained with PBP-IA, it turns out that 5P-IA systematically tends to overestimate parameters f_t and $f_{t,u}$ and within only a range of 3%-4% for the values obtained with PBP-IA, which is a very good approximation. Taking into account the variability of the parameter $\varepsilon_{t,u}$, it seems to be good that the 5P-IA tends to underestimate if compared to PBP-IA, showing that the hypothesis of considering the key Point 3 at a 97% of the flexural strength is suitable.

(ii)   The stress-crack opening relationship results

In order to suitably compare the stress-crack opening results between these two methods, the fitting process to derive the quadrilinear stress-strain response of the hinge from the point-by-point curve was modified, which means that the stress upon the change of slope coincides with one third the specimen depth. It was done only for these tests. Comparison of the average results obtained from 5P-IA and PBP-IA are shown inTable 5.12 to Table 5.17. The complete results are offered in Appendix II.

These tables allow us to draw the conclusion that 5P-IA offers similar characteristic crack opening (w_c) values to PBP-IA for any assumed hinge length with a maximum average deviation value of about 7%. However, deviation in the crack opening at the change of slope value (w_d) increases the shorter the assumed hinge length. This wider variation, which falls within the 15%-25% range, has a lot to do with the assumption of establishing stress upon the change of slope at one third the maximum tensile strength in PBP-IA.

Table 5.12 The average stress-crack opening results for λ=3 from 5P-IA

5P-IA L/h=3					
Lc = h			Lc = h/2		
	w_d	w_c		w_d	w_c
AVERAGE	**1,50**	**5,83**	**AVERAGE**	**1,52**	**6,58**
DESV	0,20	0,51	**DESV**	0,20	0,58
CV %	13,4	8,8	**CV %**	13,2	8,8

Table 5.13 The stress-crack opening results for λ=3 from PBP-IA

PBP-IA L/h=3					
Lc = h			Lc = h/2		
	w_d	w_c		w_d	w_c
AVERAGE	**1,78**	**5,62**	**AVERAGE**	**2,00**	**6,18**
DESV	0,26	0,50	**DESV**	0,20	0,56
CV %	14,5	8,8	**CV %**	10,1	9,1

Table 5.14 Deviation as a % of the results obtained from 5P-IA compared to those obtained by PBP-IA for λ=3

DEVIATION L/h=3					
Lc = h			Lc = h/2		
	w_d	w_c		w_d	w_c
AVERAGE	15,7%	-3,8%	AVERAGE	23,6%	-6,5%

Table 5.15 The stress-crack opening results for λ=4.5 from 5P-IA

5P-IA L/h=4.5								
Lc = 1,5h			Lc = h			Lc = h/2		
	w_d	w_c		w_d	w_c		w_d	w_c
AVERAGE	1,31	4,99	AVERAGE	1,30	5,43	AVERAGE	1,33	6,20
DESV	0,22	0,29	DESV	0,18	0,31	DESV	0,17	0,38
CV %	16,8	5,8	CV %	13,7	5,6	CV %	12,9	6,1

Table 5.16 The stress-crack opening results for λ=4.5 from PBP-IA

PBP-IA L/h=4.5								
Lc = 1,5h			Lc = h			Lc = h/2		
	w_d	w_c		w_d	w_c		w_d	w_c
AVERAGE	1,30	4,86	AVERAGE	1,58	5,31	AVERAGE	1,76	6,12
DESV	0,26	0,35	DESV	0,24	0,38	DESV	0,10	0,49
CV %	20,4	7,2	CV %	15,3	7,1	CV %	5,8	8,0

Table 5.17 Deviation in % of the results obtained from the 5P-IA in comparison to those obtained by PBP-IA for λ=4.5

DEVIATION L/h=4.5								
Lc = 1,5h			Lc = h			Lc = h/2		
	w_d	w_c		w_d	w_c		w_d	w_c
AVERAGE	-1,0%	-2,6%	AVERAGE	17,6%	-2,2%	AVERAGE	24,0%	-1,3%

(iii)   Source of deviation

Specimen D5λ4.5 offers the greatest deviation between 5P-IA and PBP-IA. The deviation for individual specimens is found in Appendix II. The stress-strain inverse analysis results obtained from PBP-IA and 5P-IA are plotted in Figure 5.29, Figure 5.30 and Figure 5.31 for specimen D5λ4.5, in an attempt to identify and understand the source of variation in the determination of the tensile parameters between both inverse analysis procedures.

Figure 5.29, Figure 5.30 and Figure 5.31 show the stress-strain relationship for specimen D5λ4.5 obtained from 5P-IA and PBP-IA for different hinge length values. The figures on the left and right represent the same curve, but on a different scale. It is worth remembering that the quadrilinear stress-strain law obtained from PBP-IA is derived from the minimum square adjustment to the point-by-point law.
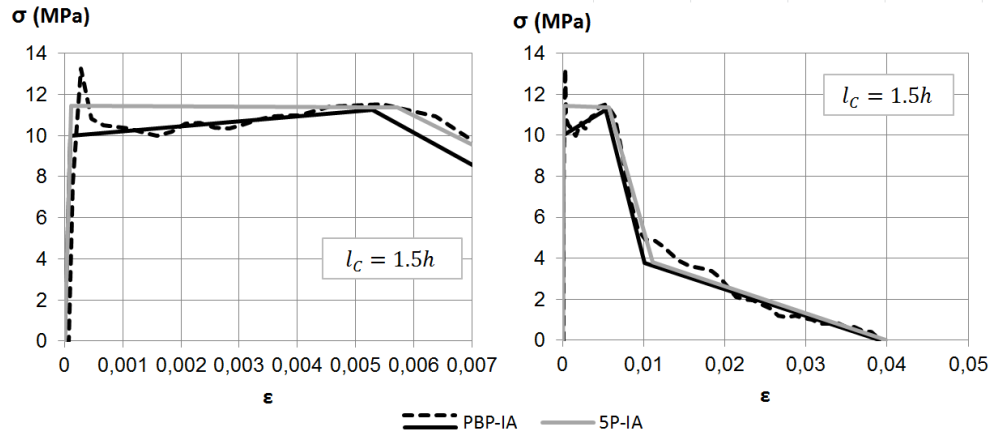
Figure 5.29 The stress-strain relationship for specimen D5λ4.5 obtained according to 5P-IA and the PBP-IA for a characteristic length that equal 1.5 h.

It is simple to note in these figures how each inverse analysis works. As in 5.3.1, PBP-IA gives a higher cracking strength value, followed by a slight drop. As this area is small, the quadrilinear fitted line tends to neglect the peak and offers a lower cracking strength value than the average in this area. This is why 5P-IA systematically offers higher cracking strength values than PBP-IA.

Regarding the softening sectional response, 5P-IA better estimates the slope after crack localisation takes place regardless of the assumed hinge length. Note that as hinge length shortens, the hinge's strain capacity increases. As the strain capacity increases, PBP-IA finds a less steeper slope than the real one, which makes the sum of the squares in the overall stress-strain response a minimum. This is the reason to explain that the w_d value is systematically higher the shorter hinge length becomes if using PBP-IA.
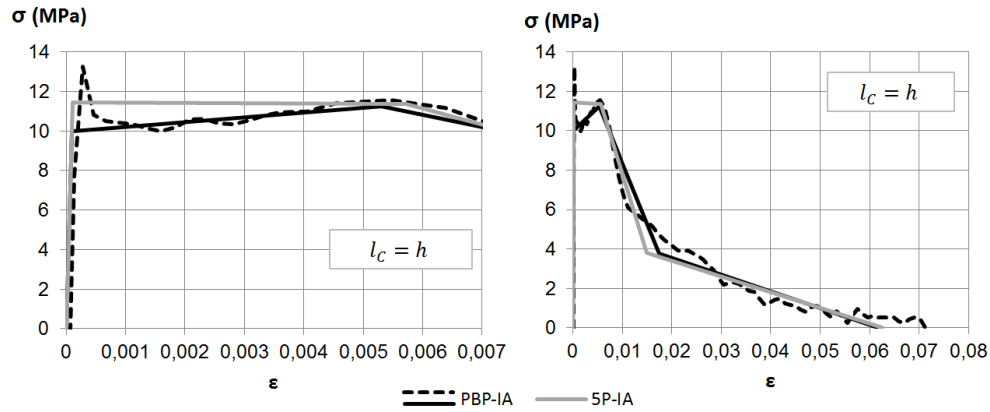
Figure 5.30 The stress-strain relationship for specimen D5λ4.5 obtained according to 5P-IA and PBP-IA for a characteristic length that equals h.
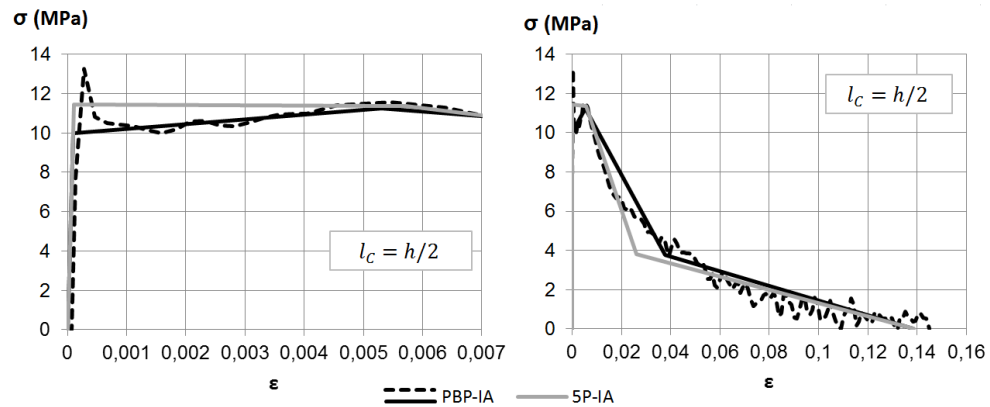
Figure 5.31 The stress-strain relationship for specimen D5λ4.5 obtained according to 5P-IA and the PBP-IA for a characteristic length that equals h/2.

Finally, the average inverse analysis results obtained from 5P-IA and PBP-IA are plotted in Figure 5.32 and Figure 5.33 for a slenderness ratio of 4.5 and one of 3, respectively. From these results, we can see that the characteristic crack opening value (w_c) is systematically higher the shorter the hinge length assumed for both slenderness ratios and for both methods. We expected 5P-IA to be according to what happened in the analytical validation in 5.3.1, but we did not expect PBP-IA to be according to the analytical validation in 5.3.1. If we look at Figure 5.29, Figure 5.30 and Figure 5.31 and pay special attention to the end of the point-by-point curve, it is quite difficult to state which suitable strain value corresponds to a zero level of stress. If the stress upon the change of slope is not forced to be one third of tensile strength, it is evident that this

value can become higher, therefore the characteristic strain (ε_c) will be lower. Nonetheless, is this happened for the whole hinge length, it will be more significant the shorter hinge length becomes as the slope of the stress-strain curve is less steep the shorter the assumed hinge length. This fact is probably the reason for the different w_c values obtained from PBP-IA.

σ (MPa) $\lambda = 4.5$

σ (MPa) $l_c = 1.5h$

σ (MPa) $l_c = h$

σ (MPa) $l_c = h/2$

PBP-IA   5P-IA
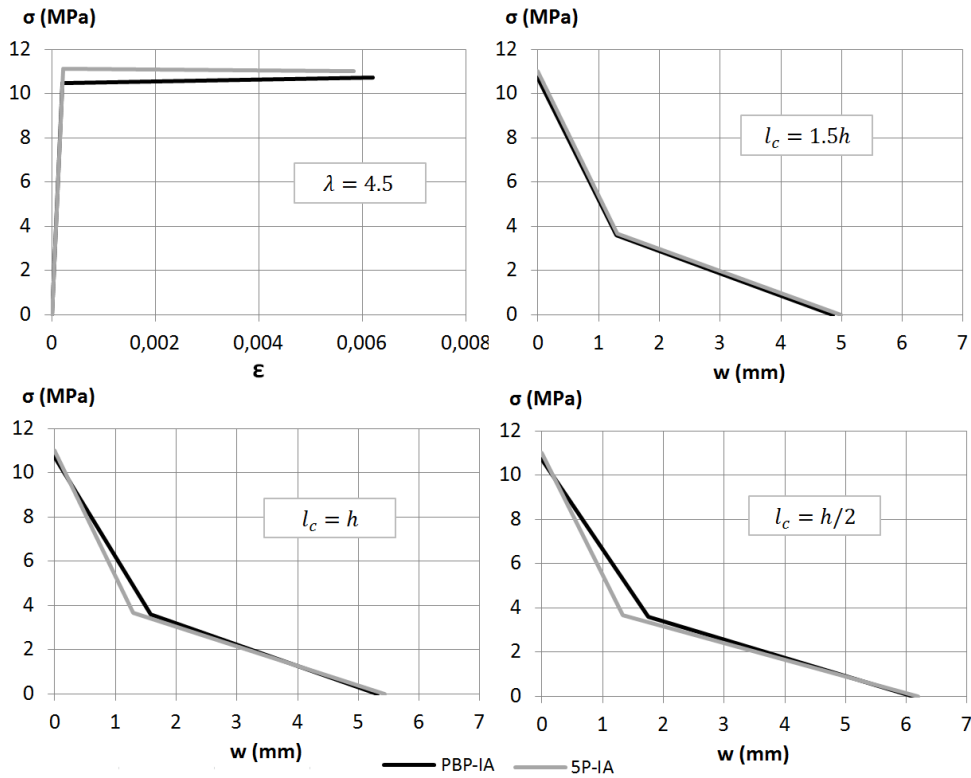
Figure 5.32 The average inverse analysis results for the specimens tested with a slenderness ratio of 4.5 for the different characteristic length values obtained with PBP-IA and 5P-IA.

In Figure 5.32 and Figure 5.33 we can see that the results come close to each other regardless of hinge length when the inverse analysis method and the slenderness ratio are used. This means that 5P-IA can be used as a reliable alternative to PBP-IA. However, 5P-IA is much simpler than PBP-IA. While it is necessary to obtain the corrected load-displacment curve according to crack position in PBP-IA, and afterwards the moment-curvature relationship according to the hinge length selected before performing the inverse analysis, 5P-IA is based on the determination of five key points in the equivalent strength *versus* the displacement at mid-span and the application of a back-of-the-envelope formulation. Crack position and characteristic

length correction can be done by increasing the displacement measured at Points 4 and 5. Even though, a computer would facilitate this process, and 5P-IA does not strictly require having to use one. Therefore, 5P-IA arises as a suitable method to characterise UHPFRC tensile performance in a TPBT. The proposed final characterisation test setup and inverse analysis procedure, and adapted to the required design parameters, are described in Chapter 6.
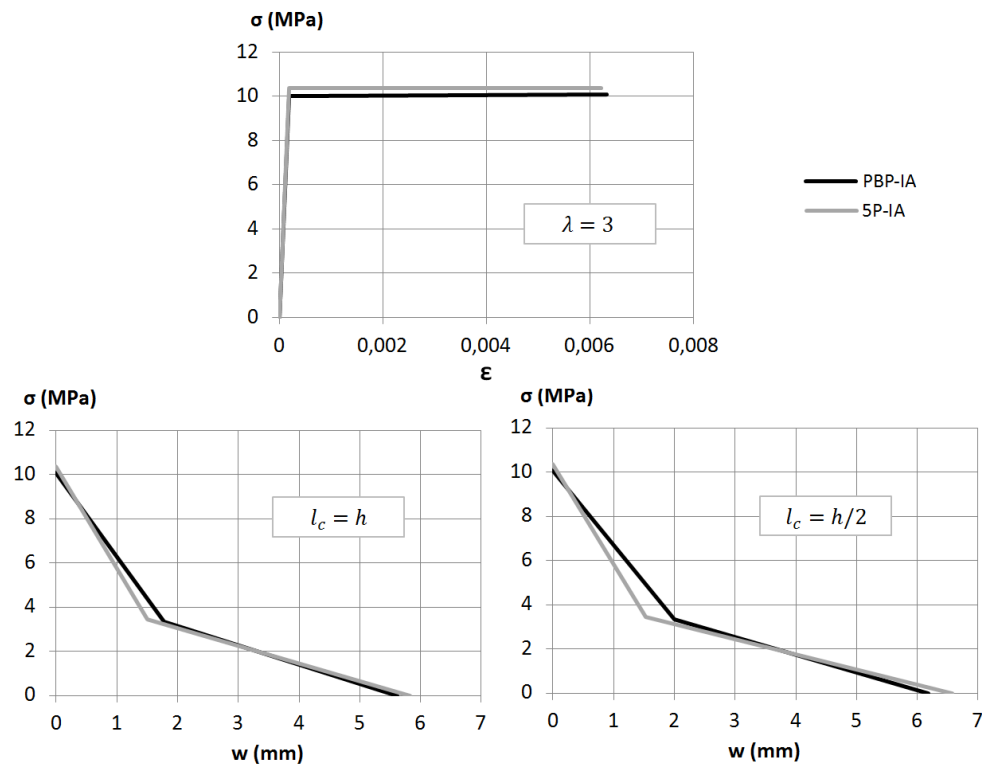
Figure 5.33 The average inverse analysis results for the specimens tested with a slenderness ratio of 3 for the different characteristic length values obtained from PBP-IA and 5P-IA.

5.4. Summary

A new simplified five-point inverse analysis method (5P-IA) to determine the tensile properties of UHPFRC from TPBT has been successfully developed for slenderness ratios (L/h) of 3 and 4.5. The proposed method takes the crack position into account and can be used for three different characteristic (or hinge) lengths: one and a half the specimen depth, the specimen depth and half the specimen depth. The proposed method assumes that the unloading modulus is one fifth the elastic one. This new methodology can be used for any specimen size and depth.

This method assumes linear elastic behaviour in compression, a bilinear stress-strain behaviour in tension up to the peak, and bilinear stress-crack opening behaviour in the softening in which the stress upon the change of slope is set at one third the maximum tensile strength. This method can also be extended to other HPFRCC, in which hardening behaviour can be fitted to a bilinear curve and characterised by descending softening behaviour. Generally speaking, this simplified method can be applied to all HPFRCC that use steel or high modulus fibres.

The proposed method requires eight input parameters, which derive from only five key points taken from the experimental flexural strength *versus* the displacement at mid-span curve obtained from a TPBT. The method's output generates the six constitutive parameters that define UHPFRC constitutive behaviour. The suggested selection of points and equations has been properly justified.

The required parameters are represented in Table 5.18. The definition of these parameters is provided below. The independent parameters are defined in black, while the dependant ones are defined in grey.

- σ_{75}: Equivalent strength at a secant stiffness of 75% the initial one
- σ_{40}: Equivalent strength at a secant stiffness of 40% the initial one
- σ_{max}: Flexural strength
- σ_{loc}: 97% of flexural strength
- σ_{80u}: 80% of σ_{loc}
- σ_{30u}: 30% of σ_{loc}
- δ_{75}: Corresponding displacement at σ_{75}
- δ_{max}: Corresponding displacement at σ_{max}
- δ_{loc}: Corresponding displacement at σ_{loc}
- δ_{80u}: Corresponding displacement at σ_{80u}
- δ_{30u}: Corresponding displacement at σ_{30u}

The inverse analysis procedure is summarised in Table 5.18 and Table 5.19. Using these tables, the parameters that define UHPFRC constitutive behaviour can be determined.

The new 5P-IA offers a very simple alternative to the inverse analysis procedures used to date. This procedure does not strictly require a computer as it is based on both simple formulation and the determination of the five key points on the experimental curve. Note that by assuming a different characteristic length from the central one third requires using a sixth point, the flexural strength point, since displacement at flexural strength is required. However, it has been demonstrated that with the strain-hardening materials tested in a TPBT, the results are the same no matter what the hinge length used. 5P-IA also offers accurate results compared to PBP-IA and can be used as a simpler alternative to it.

Table 5.18 Simplified 5P-IA. Part I.
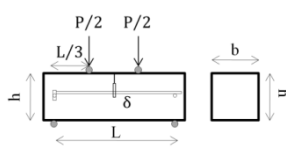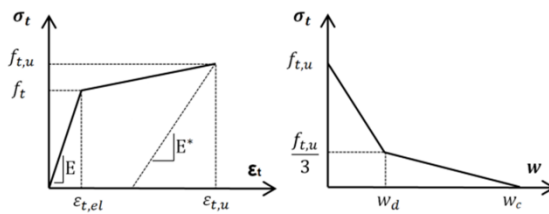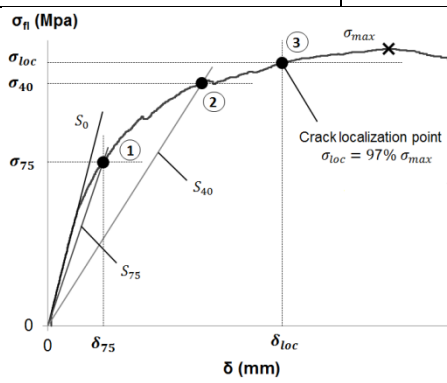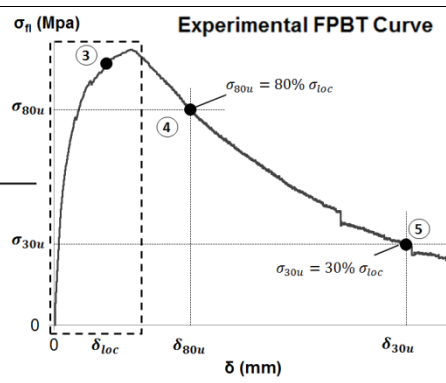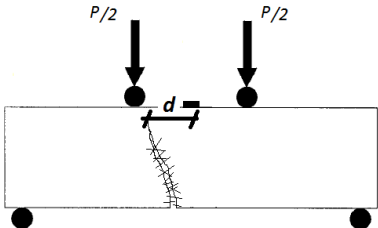
Test Setup

$$\sigma_{fl} = \frac{PL}{bh^2}$$

Constitutive Tensile Parameters

Experimental FPBT Curve

$\sigma_{loc} = 97\% \, \sigma_{max}$ (Crack localization point)

$\sigma_{80u} = 80\% \, \sigma_{loc}$

$\sigma_{30u} = 30\% \, \sigma_{loc}$

		$L/h = 3$	$L/h = 4.5$	$k_0 = 1$ $k_{75} = 0.75$ $k_{40} = 0.40$
Stress-Strain	S_i	$\sigma_{fl} = k_i \dfrac{E\delta}{2.40h}$	$\sigma_{fl} = k_i \dfrac{E\delta}{4.79h}$	
	f_t	$\dfrac{\sigma_{75}}{1.63}\left(\dfrac{\sigma_{75}}{\sigma_{40}}\right)^{0.19}$	$\dfrac{\sigma_{75}}{1.59}\left(\dfrac{\sigma_{75}}{\sigma_{40}}\right)^{0.21}$	Normalised parameters
	$\varepsilon_{t,u}$	$\dfrac{f_t}{E}\left(7.65\dfrac{\delta_{loc}}{\delta_{75}} - 10.53\right)$	$\dfrac{f_t}{E}\left(6.65\dfrac{\delta_{loc}}{\delta_{75}} - 9.40\right)$	$\varepsilon_{t,el} = {f_t}/{E}$
	$f_{t,u}$	$\alpha^{-0.18}\left(2.46\dfrac{\sigma_{loc}}{\sigma_{75}} - 1.76\right)f_t$	$\alpha^{-0.17}\left(2.24\dfrac{\sigma_{loc}}{\sigma_{75}} - 1.55\right)f_t$	$\alpha = {\varepsilon_{t,u}}/{\varepsilon_{t,el}}$
Stress-Crack Opening	$\varepsilon_{t,d}$	$\gamma^{-0.37}\alpha^{0.88}\left(3.00\dfrac{\delta_{80u}^{**}}{\delta_{loc}} - 1.80\right)\dfrac{f_t}{E}$	$\gamma^{-0.38}\alpha^{0.89}\left(2.82\dfrac{\delta_{80u}^{**}}{\delta_{loc}} - 1.68\right)\dfrac{f_t}{E}$	$\gamma = {f_{t,u}}/{f_t}$
	$\varepsilon_{t,c}$	$2.81\beta^{-0.76}\gamma^{-0.19}\alpha^{1.42}\left(\dfrac{\delta_{30u}^{**}}{\delta_{loc}}\right)^{1.85}\dfrac{f_t}{E}$	$2.17\beta^{-0.76}\gamma^{-0.26}\alpha^{1.48}\left(\dfrac{\delta_{30u}^{**}}{\delta_{loc}}\right)^{1.86}\dfrac{f_t}{E}$	$\beta = {\varepsilon_{t,d}}/{\varepsilon_{t,el}}$
	w_d	$\left(\varepsilon_{t,d} - \varepsilon_{t,u} + \dfrac{10f_{t,u}}{3E}\right)l_c$		
	w_c	$\left(\varepsilon_{t,c} - \varepsilon_{t,u} + \dfrac{5f_{t,u}}{E}\right)l_c$		

Table 5.19 Simplified 5P-IA. Part II.

<table>
<tr><td colspan="5" align="center">Crack position correction</td></tr>
<tr>
<td colspan="3">$\delta_{80,u}{}^{*} = \delta_{80,u}\left(1 + \dfrac{9d}{20(L-2d)}\right)$</td>
<td colspan="2" rowspan="2"></td>
</tr>
<tr>
<td colspan="3">$\delta_{30,u}{}^{*} = \delta_{30,u}\left(1 + \dfrac{71d}{50(L-2d)}\right)$</td>
</tr>
<tr><td colspan="5" align="center">Characteristic length assumption</td></tr>
<tr>
<td align="center">L/h</td>
<td align="center">l_c</td>
<td align="center">$\delta_{80,u}{}^{**}$</td>
<td colspan="2" align="center">$\delta_{30,u}{}^{**}$</td>
</tr>
<tr>
<td align="center">3</td>
<td align="center">h</td>
<td align="center">$\delta_{80,u}{}^{*}$</td>
<td colspan="2" align="center">$\delta_{30,u}{}^{*}$</td>
</tr>
<tr>
<td align="center">3</td>
<td align="center">$h/2$</td>
<td align="center">$2\delta_{80,u}{}^{*} - \delta_{loc} + 1.65h\dfrac{\sigma_{loc}}{E}$</td>
<td colspan="2" align="center">$2\delta_{30,u}{}^{*} - \delta_{loc} + 5.76h\dfrac{\sigma_{loc}}{E}$</td>
</tr>
<tr>
<td align="center">4.5</td>
<td align="center">1.5h</td>
<td align="center">$\delta_{80,u}{}^{*}$</td>
<td colspan="2" align="center">$\delta_{30,u}{}^{*}$</td>
</tr>
<tr>
<td align="center">4.5</td>
<td align="center">h</td>
<td align="center">$\dfrac{3\delta_{80,u}{}^{*} - \delta_{loc}}{2} + 1.79h\dfrac{\sigma_{loc}}{E}$</td>
<td colspan="2" align="center">$\dfrac{3\delta_{30,u}{}^{*} - \delta_{loc}}{2} + 6.27h\dfrac{\sigma_{loc}}{E}$</td>
</tr>
<tr>
<td align="center">4.5</td>
<td align="center">$h/2$</td>
<td align="center">$3\delta_{80,u}{}^{*} - 2\delta_{loc} + 7.16h\dfrac{\sigma_{loc}}{E}$</td>
<td colspan="2" align="center">$3\delta_{30,u}{}^{*} - 2\delta_{loc} + 25.08h\dfrac{\sigma_{loc}}{E}$</td>
</tr>
</table>

Chapter 6

UHPFRC classification and characterisation test proposal

6.1. Introduction

Fibre-reinforced concrete evolution showed us that development of both characterisation test and design methods have to go hand in hand and have to be treated simultaneously because they are interrelated. It is common in current design guidelines that those parameters required for design that cannot be obtained indirectly from other parameters are those parameters used to classify the material. Structures are designed according to them. In the construction stage, a suitable quality control is performed according to standard characterisation tests to check that the parameters required in design are guaranteed during construction. This is why standard characterisation tests must provide those parameters used to classify the material used.

The work conducted from Chapters 3 to 5 has focused on developing a simple, objective and accurate tool to determine UHPFRC tensile behaviour from a TPBT for the main purpose of developing a standard characterisation test setup and methodology which allow those tensile parameters strictly required for design purposes to be obtained; i.e. for UHPFRC classification. However, what are these parameters?

The UHPFRC classification proposal is not a pure scientific task, but includes a very important engineering part. Both science and engineering must work together to reach a compromise solution between accuracy and simplicity. The use of very complex models, formulations and theories moves away from the interest of most engineers. However, too simple methods can lead to either oversized or unsafe structures.

This chapter presents a review of the UHPFRC constitutive relationship proposed for design by current UHPFRC standards in both SLS and ULS and the parameters needed to define them. Taking into account the current UHPFRC classification, a new UHPFRC classification has been proposed that considers the current classification for conventional concrete, FRC, and the classifications already proposed for UHPFRC. This classification encompasses the current classifications for concrete and FRC, and offers an integrated view of concrete. This is what it is described in Section 6.2

The parameters used to classify UHPFRC must be provided by a characterisation test and methodology. Even though the 5P-IA method developed in Chapter 5 arises as a simple tool to derive tensile UHPFRC properties from TPBTs, it is probably still too complicated to be proposed as a standard methodology to be included in a design code, and must be simplified according to the classification parameters. Section 6.33 describes a more simplified methodology to derive tensile UHPFRC properties from a proposed TPBT setup.

6.2. UHPFRC classification

Traditionally, the design process of concrete structures has been determined by one single parameter: the concrete compressive strength. This parameter has been found to be crucial as it can correlate with other mechanical parameters required for a project, such as bond strength, tensile strength or flexural strength. That is why compressive strength is the only strength parameter in concrete descriptions. However this is not the only parameter required for design. Other required parameters are: (i) exposure environment, which determines the permissible crack opening, covering and durability properties of concrete; (ii) maximum aggregate size, which determines the distance between rebars; (iii) concrete workability, which determines the casting procedure according to the structure design. Using these parameters it is possible to develop any concrete project using current codes.

With FRC, concrete tensile behaviour cannot be explained using compressive strength, and additional information must be provided to take into account tensile performance in design. This is why MC2010 includes two parameters that correspond to tensile residual strength at two CMOD values obtained from EN-14651. These parameters describe the stress-crack opening behaviour of FRC and allow the consideration of its tensile performance in both ULS and SLS.

As with FRC, it is necessary to identify the UHPFRC tensile properties required for design and which cannot be derived from any other parameter. It seems reasonable to keep compressive strength, exposure environment and concrete workability as UHPFRC project parameters. However, this may not be the case for maximum aggregate size. According to current codes, maximum aggregate size is limited to 1-2 mm. Notwithstanding, it is known that certain types of UHPFRC or VHPFRC use maximum aggregate sizes of 6-8 mm. A larger aggregate size is not used since the

commonest fibre length used is 13, and it would affect the fibre to matrix bond. This is why the distance between rebars is determined by fibre length instead of maximum aggregate size. Therefore in the specific case of UHPFRC, it seems more convenient to use fibre length instead of maximum aggregate size. This could also be valid for FRC.

Regarding UHPFRC tensile parameters, a brief summary of the properties required in the French and Swiss standard is described below. A decision was made to include this summary in this chapter rather than in the state-of-the-art review to make its reading easier. From these standards, some conclusions have been drawn to determine the minimum required properties for design, which will also determine the characterisation test method used.

6.2.1. The classification of French and Swiss standards

The French standard proposed a classification of UHPFRC tensile performance into three classes:

- T1: those UHPFRC in which both the average and characteristic value of $f_{t,u}$ is lower than f_t.
- T2: those UHPFRC in which the characteristic value of $f_{t,u}$ is lower than f_t, but not the average value.
- T3: those UHPFRC in which both the average and characteristic value of $f_{t,u}$ are higher than f_t.

Depending on the UHPFRC tensile class, a different tensile constitutive law is used. The parameters required to determine the tensile law are derived from either notched three-point bending tests for class T1 and T2 and the associated inverse analysis procedure, which includes the disadvantages mentioned in 2.5.2.1, or an unnotched four-point bending test for class T3. The required parameters are summarised in Table 6.1.

No matter what the class type, the French standard requires two different tests: a first one to determine cracking strength and a second one to determine the other tensile parameters. Moreover, it does not consider the softening stress-crack opening branch in class T3. This consideration may make sense for unreinforced thin-slabs in which ductility depends on both UHPFRC behaviour and structure redundancy, but how is it supposed to design for thin slabs combined with reinforcement? In this case when reinforcement is considered at a deformation value beyond its yielding, what is the contribution of UHPFRC? Probably, a softening law is required no matter what the class in tension, as considered for FRC.

Another important feature is that the specimen geometry for characterisation tests depends on either fibre length or structure size. A quality control of that structure would imply different beams sizes and would prove rather messy depending on the controlled structure element. It seems more reasonable to do what MC2010 proposes:

one single test setup regardless of the structure size and fibre orientation correction factors in the design according to the structure geometry, fibre type and pouring system. However, as these factors have not yet been developed, the angle of the French standard is understandable.

Table 6.1 The tensile parameters needed for classes T1 and T2 according to the French standard.

Class	Parameter	Determination
T1 & T2	f_t	Unnotched FPBT
	w_{peak}: crack opening that corresponds to the local peak or 0.3 mm if there is no peak.	Notched three-point bending test. Specimen size according to fibre length and structure dimensions.
	$w_{w1\%}$: crack opening that corresponds to 1% of the specimen depth under flexure	
	w_{lim}: one fourth of the maximum fibre length.	According to fibre length
T3	f_t	Unnotched FPBT
	$\varepsilon_{t,u}$: strain on the tensile face that corresponds to maximum flexural strength	Unnotched FPBT in specimen of the same thickness of the structure or 3 times the fibre length.

The Swiss standard, which was more specifically developed for thin UHPFRC structures, classified UHPFRC into three classes, U0, UA and UB, according to the values in Table 6.2.

Table 6.2 The UHPFRC classification according to the Swiss standard

CLASS	U0	UA	UB
$f_{t,k}$ (MPa)	≥ 7	≥ 7	≥ 8.5
$f_{t,u,k}/f_{t,k}$	>0.7	>1.1	>1.2
$\varepsilon_{t,u,k}$ (‰)	f_t/E	>1.5	>2

As seen in Table 6.2, the Swiss standard requires a minimum characteristic cracking strength value of 7 MPa. No hardening is considered in the calculations if the ratio between the characteristic ultimate strength and the characteristic cracking strength is lower than or equals 1.1, with a limiting factor of 0.7 for being considered UHPFRC. As shown in the experimental programme in Chapter 5, the hardening value 1.1 may be

too restrictive because this value for common UHPFRC is 1 (see 5.3.2). However, the fact that the standard test setup proposed in this guideline has a thickness of only 30 mm must be taken into account, which may explain the factor of 1.1 required. As previously shown, a minimum strain value of 1.5‰ may be too low, especially for thin specimens. As in the French standard, no UHPFRC softening behaviour is considered.

6.2.2. Proposed UHPFRC constitutive models

The parameters used to classify UHPFRC must allow the determination of the constitutive behaviour proposed in both ULS and SLS. It seems convenient to define the constitutive behaviour in the UHPFRC tension proposed for both limit states. Note that current design guidelines define the ULS constitutive relationship using the design values (subscript d) and the SLS one using the characteristic values (subscript k). Design and characteristic values must be defined in the specific design guidelines, which is not an issue of this work. Fibre orientation effects (K coefficients) were not considered in the proposed definition of the constitutive relationships as they do not influence the purpose of this section, which is to define the minimum number of parameters required to define UHPFRC constitutive tensile behaviour.

Two new parameters are added to define UHPFRC constitutive behaviour compared to the Swiss standard. Parameter γ refers to the hardening ratio and is defined as the ratio between f_t and $f_{t,u}$. Parameter w_o is the intersection of the line defined by the initial slope of the stress − crack opening law and its intersection to the w axis. By using these two new parameters, the constitutive law in the tension of UHPFRC at SLS is represented in Figure 6.1 for two different cases of γ.
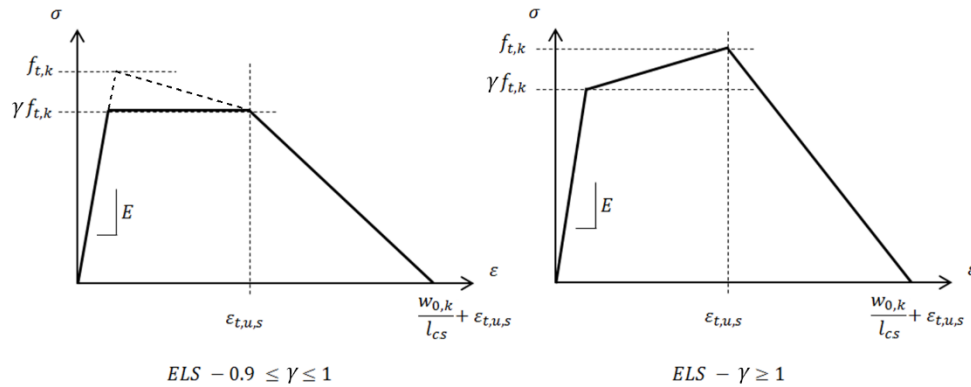

Figure 6.1 The constitutive behaviour proposed for SLS without considering statistical scale effects.

The most complicated parameter to be defined is parameter $\varepsilon_{t,u,s}$, which corresponds to the *structural* maximum strain prior to crack localisation in the service limit state. The experimental results have shown that average values that fall within the 4‰-6‰ range

are frequently obtained from TPBTs. However, when UHPFRC is combined with steel rebars, is it possible for UHPFRC to remain in a microcracking stage up to a strain value within this range with yielded steel rebars? What is the interaction between the concrete and steel rebars in these cases? Is parameter $\varepsilon_{t,u}$ a material or a structure parameter? Probably, a solution to these questions has not yet been found. What it is true is that the characteristic strain at peak $\varepsilon_{t,u,k}$ derives from characterisation tests and structural $\varepsilon_{t,u,s}$ must be related to each other in some way.

The softening branch has also been represented in Figure 6.1. Sometimes, SLS cases may lead to a sectional response in which the maximum strain is below $\varepsilon_{t,u,s}$. In these cases, this section can be considered to remain in a microcracking stage. However, the sectional strain reached at SLS can also be higher. In these cases, crack opening calculations require the softening branch. As crack opening is limited to 0.3 mm for the least aggressive environmental conditions, there is no reason to use a bilinear softening stress-crack opening relationship. A linear relationship is proposed, for which only the first line of the bilinear equation is used. As change of slope was defined as one third of the maximum tensile strength, parameter w_o can be easily obtained from w_d with Eq. 6.1.

$$w_o = \frac{3}{2} w_d$$

<div align="right">Eq. 6.1</div>

As a sectional calculation is made using a stress-strain relationship, crack opening has to be converted into strain, as shown in Figure 6.1. The effect of unloading was not considered as its influence on design is negligible.

The calculation in ULS generally involves a sectional analysis in which steel rebars deformation is high, and further away from its yielding, thus ensuring the rotational capacity of the hinge and a certain degree of force redistribution. Figure 6.2 depicts different possible hypotheses for ULS calculations.

Considering a characteristic structural length, as proposed in the French standard, which corresponds to 66% of the structural element depth and a 200-mm depth beam, an estimated crack opening of 1.33 mm is obtained for a maximum strain deformation of 10‰. According to the results presented in Chapter 5, this point comes close to the change of slope in the bilinear stress-crackopening approach. Depending on concrete type, it can be either before or after the peak. This is why two different alternatives are presented in Figure 6.2: a linear unloading branch, as depicted in Figure 6.2 (a) and Figure 6.2 (c); a bilinear unloading branch, as shown in Figure 6.2 (b) and Figure 6.2 (d). Moreover, strain-hardening behaviour may be neglected as it has barely any influence on the global section response in ULS. Constitutive models with (Figure 6.2 (a) and Figure 6.2 (b)) and without (Figure 6.2 (c) and Figure 6.2 (d)) a strain-hardening consideration is also included. In ULS the area in an elastic regime has

barely any effect on the sectional response. This is why it was neglected as it is considered in MC2010 for FRC. As in Figure 6.1, the crack opening for the proposed strain transformation neglects the unloading consideration.
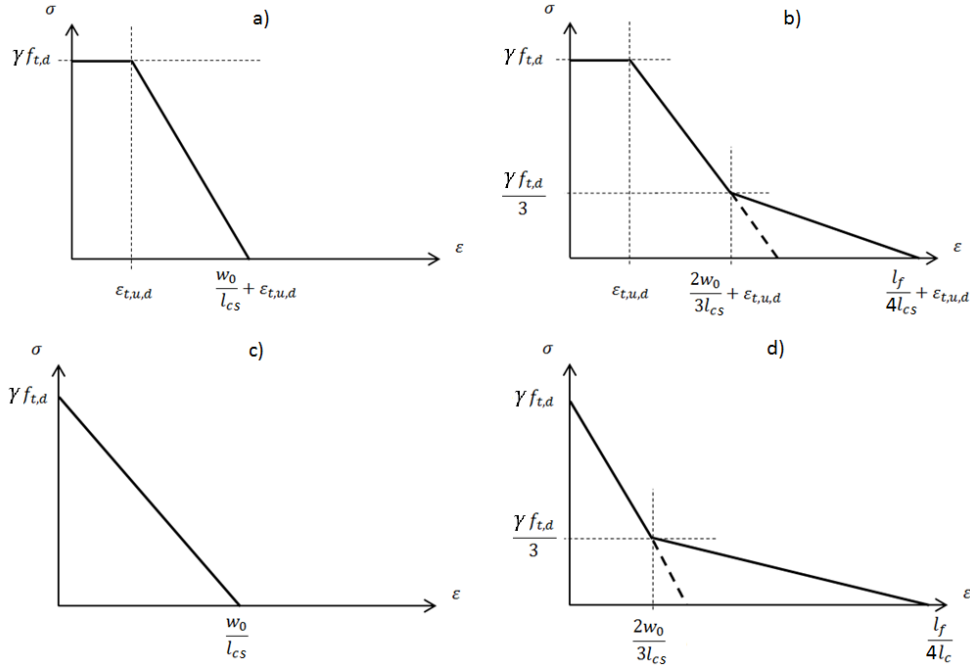
Figure 6.2 Different ULS constitutive models proposals for UHPFRC without considering statistical scale effects.

According to the results obtained in Chapter 5, a rigid plastic model with constant residual strength probably does not make much sense for UHPFRC. Instead Figure 6.2(c) may be the simpler choice to determine the UHPFRC sectional response in ULS when it contains steel rebars. Note that this constitutive equation is similar to the linear model proposed in MC2010 for FRC. However, the two points of the constitutive equation that define it have a different meaning: in FRC the two points are somewhere in the middle of the linear branch, while the two points are exactly on the intersection to the axes in the proposed model.

If needed, a more complex, but still simple, bilinear model is proposed in Figure 6.2 (d). Note that in Figure 6.2 (b) and (d), the strain at zero stress corresponds to a crack opening of one fourth the fibre length. It has always been stated that half the fibre length is a suitable assumption for this value. However, as this area is not to be used frequently and in order to keep on the safety side, one fourth the fibre length was chosen, and it is proposed in the French standard for UHPFRC.

Using the constitutive models in both Figure 6.1 and Figure 6.2 requires the definition of five parameters, which must be included in the definition of UHPFRC. These parameters are: f_t, γ, $\varepsilon_{t,u}$, w_0 and l_f. Note that the defined constitutive stress-strain behaviour takes into account the deterministic scale effect by introducing the structural characteristic length (l_{cs}), which must be related to crack spacing, crack depth or specimen depth.

6.2.3. The proposed UHPFRC classification

According to previous subsections, UHPFRC can be defined according to the following description:

$$\text{UHPFRC -} f_{c,k} \text{ / W / FL / EE}$$

$$\text{SX -} f_{t,k} \text{ / } \gamma_k \text{ / } \varepsilon_{t,u,k} \text{ / } w_{0,k}$$

where W is the workability type of UHPFRC; FL is the maximum fibre length; EE is environmental exposure. The definition of these classes does not correspond to this work. Only the UHPFRC classification is dealt with according to its tensile constitutive law. Parameter SX can be either SS, which means strain-softening, or SH, which means strain-hardening, as not all UHPFRC must be strain-hardening materials. If SS comes into play, only $f_{t,k}$ and $w_{0,k}$ are required as γ_k and $\varepsilon_{t,u,k}$ describe the strain-hardening behaviour.

A minimum characteristic cracking strength value of 5 MPa seems reasonable for UHPFRC. It implies an average value of around 6 MPa, which is reasonable for low fibre content UHPFRCs.

The minimum ductility condition for UHPFRC included in the French standard is shown in Eq. 6.2. Eq. 6.2 can be expressed as in Eq. 6.3 following the notation and constitutive relationship in Figure 6.2(c), when w_{lim} equals 0.3 mm and $K=1.25$ is in accordance with the French standard. The worst case scenario takes place when γ and f_t take a minimum value. Let's assume a minimum value of 0.9 and 5 MPa, respectively. For this specific unfavourable case, w_0 must be higher than 1.0 mm. Therefore, the minimum material ductility requirement according to the French standard can be accomplished by demanding a minimum $w_{0,k}$ of 1.0 mm.

$$\frac{1}{K w_{lim}} \int_0^{w_{lim}} \sigma(w) dw \geq \max(0.4 f_t; 3 \ MPa)$$

Eq. 6.2

$$\frac{\gamma f_t}{1.25} \left(1 - \frac{0.15}{w_0}\right) \geq \max(0.4 f_t; 3 \ MPa)$$

Eq. 6.3

Establishing minimum $\varepsilon_{t,u,k}$ and γ_k values is no easy task because, in some way, setting them determines the border between a strain-softening and a strain-hardening concrete. Even though the international research community agrees on its qualitative definition according to Figure 2.17, establishing a quantitative criterion is not easy as concrete behaviour is much more complex than that and the tools used for its determinations are not 100% reliable. This is why any criteria assumed for this purpose can be questioned and discussed in-depth.

The experimental test shows that a microcracking process is ensured when the $\varepsilon_{t,u}$ value is higher than approximately 2.5‰. The coefficient of variation on its determination is around 20%. Accordingly, it seems reasonable to consider a minimum $\varepsilon_{t,u,k}$ value of 2‰ to guarantee UHPFRC strain-hardening behaviour, which implies an average $\varepsilon_{t,u}$ value of around 3‰.

Hardening parameter γ depends on the determination of f_t, and $f_{t,u}$. It is commonly assumed that strain-hardening behaviour appears when a specimen exhibits microcracking. (ISO/TC 71/SC 6 Working draft, 2016) proposes that exhibiting strain-hardening behaviour in a four-point bending test requires the formation of *plural* cracks. This term is defined as two independent cracks or more that are visible to the naked eye and occur in the pure bending span before a maximum load is observed, thus ensuring deflection hardening behaviour and gradual load decreasing after the maximum load. The visual criterion shown in Figure 6.3 is proposed. Even though these concretes are assumed to exhibit strain-hardening behaviour, the specimen examples shown in Figure 6.3 do not seem to quite represent what a strain-hardening response may be considered.

In UHPFRC, it is common that only one single macro-crack appears after tests. Other minor cracks can be seen only by wetting the surface or using special coatings. Two examples of microcracking in UHPFRC are shown in Figure 6.4, which depicts the differences in the number of cracks to the specimens in Figure 6.3. If the microcracking response is the criterion used to determine UHPFRC strain-hardening behaviour, what minimum number of cracks would be required? Is determining the number of cracks objective? These questions are probably not easy to answer. This is why it is believed that whether strain-hardening behaviour exists or not must be determined from experimental recordings, which are at least objective measurements.

What it is commonly assumed is that if a specimen exhibits multi-microcracking, it is due to the fact that concrete has been able to hold cracking stress at higher strain deformations. Therefore, exhibiting microcracking during tests ensures that the hardening parameter is higher than 1.
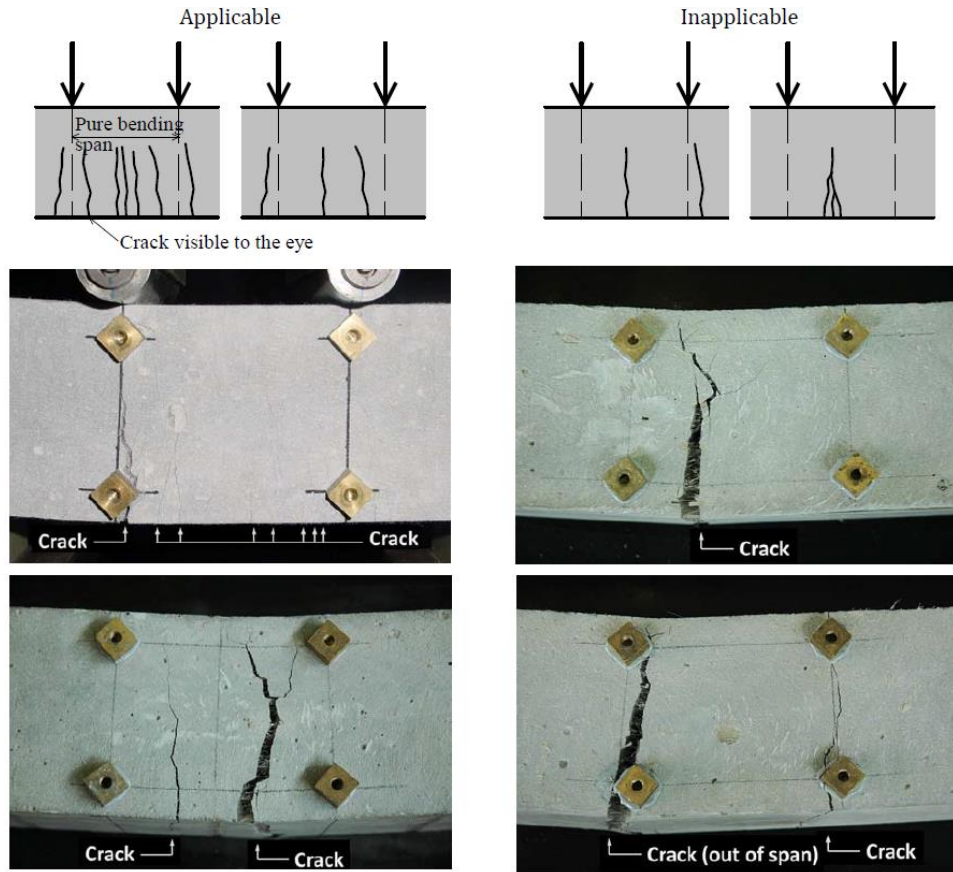
Figure 6.3 The visible criterion to determine the applicability of the inverse analysis method for FRCC according to (ISO/TC 71/SC 6 Working draft, 2016).

Figure 6.4 Microcracks pattern on two different UHPFRC specimens

At this point, the characterisation test setup and methodology play an important role. According to the results in Chapter 5, hardening ratio (γ) is commonly 0.85 to 1.10 using a TPBT and 5P-IA. In those cases in which the hardening ratio is lower that 1, a microcracking process similar to that shown in Figure 6.4 was observed. So, can the UHPFRC tested be considered a strain-hardening material? In an attempt to answer this, the results obtained from the inverse analysis are shown in Table 6.3.

Table 6.3 The inverse analysis results obtained from 5P-IA from specimens with a slenderness ratio of 4.5, as described in Chapter 5.

	$f_t(MPa)$	$f_{t,u}(MPa)$	γ	$\varepsilon_{t,u}$	w_o
D1λ4.5	11.2	11.9	1.07	0.0068	1.99
D2λ4.5	11.0	10.3	0.94	0.0073	2.07
D3λ4.5	10.5	10.6	1.01	0.0059	2.05
D4λ4.5	10.7	11.6	1.09	0.0063	2.51
D5λ4.5	11.4	11.4	1.00	0.0057	1.35
D6λ4.5	11.6	10.7	0.92	0.0035	1.91
D7λ4.5	11.2	11.5	1.03	0.0058	2.19
D8λ4.5	11.3	10.1	0.89	0.0055	1.62
AVERAGE	11.1	11.0	**0.99**	0.0058	1.96
DESV	0.4	0.6	0.1	0.0010	0.33
CV %	3.2	5.8	7.1	17.7	16.8
Characteristic value	**10.4**	**9.8**	0.86	**0.0039**	**1.34**

Table 6.3 describes the inverse analysis results from the specimens with a slenderness ratio of 4.5 shown in Chapter 5. Note that the characteristic γ value is 0.86, while the average value is 0.99. All the specimens exhibited multi-microcracking. As a bilinear stress-strain relationship is always a simplification of real UHPFRC behaviour, deviation in the determination of strain-hardening parameters due to the followed inverse analysis procedure may lead to a hardening ratio that is below 1, even for specimens that exhibit multi-microcracking. To gain a better understanding of this fact, Figure 6.5 was plotted. Figure 6.5 shows the PBP-IA and 5P-IA results obtained from specimen D8λ4.5. In this case, the γ value is clearly lower than 1. However, this is due to both an overestimation of f_t and an underestimation of $f_{t,u}$, as the simplified method has some errors. Therefore, even though the γ value obtained in a TPBPT from 5P-IA can be lower than 1, the specimen can exhibit a strain-hardening response.

By assuming that the inverse analysis method induces some errors in the hardening ratio determination, what would the minimum hardening ratio be for considering

strain-hardening behaviour in UHPFRC by assuming the deviation of the inverse analysis? Once again, this is no easy question.
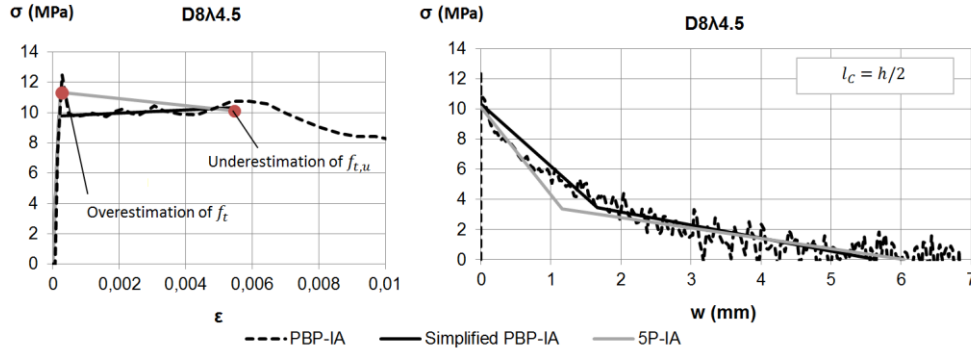
Figure 6.5 The inverse analayis results obtained from specimen D8λ4.5 (see Appendix II)

In the light of the obtained results (see Appendix II), establishing the following condition seems a good choice: for being considered a strain-hardening material, the average hardening ratio value obtained from a TPBT and 5P-IA must be at least 0.9. That is to say, if the characteristic hardening value is no higher than 1, it suffices that the average value is at least 0.9. In this case, the constitutive hypothesis in Figure 6.1 (left) must be used, in which tensile capacity is reduced. The use of a higher hardening ratio in design requires achieving this specific characteristic value in TPBTs. Note that this criterion depends only on the characterisation test setup and methodology used. It reinforces the idea that both the classification and characterisation proposals must go hand in hand.

If after UHPFRC characterisation all the specimens exhibit a deflection hardening response, whose experimental curve accomplishes the conditions to apply 5P-IA, i.e., Point 2 is below Point 3, but $\varepsilon_{t,u,k}$ is lower than 2‰ or the average γ value is lower than 0.9, then the hardening branch cannot be used and UHPFRC must be treated as a strain-softening material. In this case, UHPFRC would be described according to the following description:

$$SS - f_{t,k} / w_{0,k}$$

Note that the softening UHPFRC description can be compared to the FRC description given by MC2010. It consists of two parameters: (i) a strength value ($f_{R,1}$ or $f_{t,k}$), and a second value that gives the slope of the stress-crack opening line ($f_{R,3}/f_{R,1}$ or $w_{0,k}$). It is important to remark that all the FRCs that exhibit deflection hardening in bending and Point 2 is below Point 3 in its load–deflection response can be characterised by this test method. However, this method is not for application to deflection softening results.

If $f_{t,k}$ is lower than 5 MPa or $w_{o,k}$ is lower than 1.0 mm, then the material cannot be considered UHPFRC and must be characterised as common FRC following EN-14651.

The final UHPFRC proposal is summarised in Table 6.4. Additional conditions are imposed when UHPFRC is used as a structural material to ensure a minimum degree of ductility, even in compression.

Table 6.4 Summarised UHPFRC classification

Parameter	SS-UHPFRC	SH-UHPFRC
$f_{t,k}$	≥ 5 MPa	≥ 5 MPa
$w_{o,k}$	≥ 1.0 mm	≥ 1.0 mm
$\varepsilon_{t,u,k}$	-	≥ 2‰
γ	-	≥ 0.9 (average value)
Additional conditions	Deflection-hardening response in bending	
	Point 2 below Point 3	

According to previous considerations, the possible variation ranges of these parameters for UHPFRC are:

$f_{t,k}(MPa) \rightarrow [5,6,7,8,9,10,12,14]$

$\gamma_k \rightarrow [0.9^*, 1, 1.2, 1.4]$, * means average value

$\varepsilon_{t,u,k}(‰) \rightarrow [2, 4, 6, 8, 10]$

$w_{0,k}(mm) \rightarrow [1, 1.5, 2, 3, 4]$

These ranges were established by taking into account the variability expected for these parameters. A 10% coefficient of variation was considered for f_t, γ, and one of 20% was considered for $\varepsilon_{t,u}$, w_0, according to the experimental results in Chapter 5. The average value of a specific class was considered to be between the characteristic values of the next two classes. The relationship between the average and characteristic values is shown in Eq. 6.4, for which a student coefficient that corresponded to six experimental results and a probability of exceedance that equalled 95% were contemplated.

$$f_k = f_m(1 - 2.015 \, COV\%)$$

Eq. 6.4

To gain a better understanding of the proposed classification, three examples are shown. Only the tensile classification was considered:

	SX	$f_{t,k}$	γ	$\varepsilon_{t,u,k}$	$w_{0,k}$
UHPFRC 1	SH	8	0.9	2	1
UHPFRC 2	SH	8	1.1	4	2
UHPFRC 3	SS	6	-	-	1

UHPFRC 1 is characterised by a characteristic cracking strength of 8 MPa; an *average* hardening coefficient of 0.9; a characteristic ultimate strain of 2‰; and a crack opening at the intersection to the w axis of 1 mm. A constitutive relationship shape coincides with Figure 6.1, left.

UHPFRC 2 is characterised by a characteristic cracking strength of 8 MPa; a *characteristic* hardening coefficient of 1.1; a characteristic ultimate strain of 4‰; and a crack opening at the intersection to the w axis of 2 mm. A constitutive relationship shape coincides with Figure 6.1, right.

UHPFRC 3 is characterised by a characteristic cracking strength of 6 MPa and a strain-softening behaviour with a crack opening at the intersection to the w axis of 1 mm.

According to the results in Table 6.3, and taking into account a student coefficient for 8 specimens of 1.895, UHPFRC can be classified following the description below.

$$SH - 10 / 0.9 / 2 / 1$$

6.3. Proposed standard test setup and methodology

The use of a given standard test setup and methodology to characterise the mechanical behaviour of a material can be very different depending on its evolution stage. With UHPFRC, it can be distinguished between current novel design methods followed for UHPFRC and the way design tools must work in the near future once UHPFRC has finally settled in the civil engineering field.

Nowadays, it is common to use characterisation tests as a starting point in the design process. Hence structural design is based on the constitutive parameters that derive from them. This approach is quite different compared to the way conventional concrete structures are devised, and also to the FRC design proposed in MC2010. A natural process involves an existing classification of the material used. This classification entails having to assume certain UHPFRC design parameters and the structure's environmental exposure. After defining and classifying them all, engineers pick a specific set of these parameters for design purpose according to specific loads and limit state checks. During construction, it is necessary to check that material used fits the project requirements by means of standard characterisation test setups in a quality

control process. For FRC, these standard tests are described in EN-12390 and EN-14651 to determine concrete compressive strength and the residual tensile strength parameters, respectively.

Therefore, characterisation tests can be used in two different approaches depending on the material's level of evolution: (i) contemplating them as characterisation tools for design, which can be considered a novel approach; (ii) contemplating them as a quality control tool, which can be considered a more consolidated approach. The latter requires a UHPFRC classification based on design parameters and is more suitable if design recommendations for engineers are to be developed. This is the point of the current French and Swiss UHPFRC design guidelines, which already propose a certain UHPFRC classification.

Although the second approach is more desirable for engineers, the low level of widespread use and scarce knowledge acquired by engineers, architects and precasting companies mean that the UHPFRC structure design is commonly devised knowing the constitutive behaviour of the specific UHPFRC that is intended to be used beforehand. In this case, characterisation test setups are conducted prior to structure design. As the material becomes more consolidated in the civil engineering field, an evolution from approach (i) to approach (ii) is expected, which implies an evolution from 'what we have' to 'what we need'. The characterisation test setup and methology proposed in the following subsections can be used whatever the approach followed to design.

6.3.1. Specimen preparation and test setup

The proposed test method to determine UHPFRC tensile properties is the unnotched Third-Point Bending Test (TPBT). The size and geometry of the standard specimen are not in accordance with structure size, but depend on fibre length. For FRC, considering a minimum prism side that is 3 times the fibre length is common practice. In EN-14651, is 2.5 times the fibre length as the maximum fibre length allowed is 60 mm and the specimen side is 150 mm. However in UHPFRC, using short 13-mm fibres is quite common. In this case, it may be pointless to use 40-mm square cross-section specimens. This is why the limitation is extended to either 5 times the fibre length, as also proposed in the French standard, or 100 mm, the more restrictive value. This assumption leads to the limitation shown in Table 6.5.

Table 6.5 Relationship between fibre length and the square cross-section specimen side

Fibre length (mm)	Specimen side (mm)
≤ 20	100
$20 < l_f \leq 30$	150

Fibres shorter than 20 mm are commonly short straight fibres, while fibres longer than 20 mm can be either hooked-end or straight fibres. It is not common to use fibres longer than 30 mm for UHPFRC. However, if that were the case, a 150 mm-square cross-section specimen could also be used up to a 60 mm fibre length according to EN-14651.

For the slenderness ratio, using a 4.5 slenderness ratio when the specimen depth is 100 mm is recommended. The reasons for this are explained in 3.4.1. If specimen depth is 150 mm specimen, it is more convenient to use a slenderness ratio of 3 so that specimens are easier to handle.

If a slenderness ratio of 3 is used, the minimum specimen length must be 4 times the specimen depth. In this case, the span is 3 times the specimen depth. If a slenderness ratio of 4.5 is used, the minimum specimen length must be 5.5 times the specimen depth and the span must be 4.5 times the specimen depth.

If UHPFRC is flowable, specimens should be cast using a movable pouring point in order to avoid its longitudinal flow. The process must start on the specimen edge. Then the pouring point is moved to the other edge at a constant speed, which coincides with the concrete flowing speed. This process has to be repeated after reaching the other edge until the specimen is completely filled. With this system concrete is poured in layers. It is absolutely necessary that a new layer does not simply lie in the previous one. It must break the previous layer and blend with it to avoid fibre alignment. The specimen must be tested by turning it 90 degrees from its casting position. If UHPFRC is not flowable, the pouring system shown in EN-14651 must be followed.

Tests should be run at a constant frame displacement of 0.05 mm/min up to the maximum load. It may be increased up to 0.2 mm/min from this point onwards. The test finishes when a load that equals 75% of the maximum is reached on the unloading branch.

The support and bearing rollers must allow the degrees of freedom shown in Figure 6.6. This is an absolutely necessary condition that must be guaranteed to avoid overestimating UHPFRC tensile performance and macro-crack formation out of the constant bending moment area.

The position of the rollers must be ensured with a precision of 2 mm. Two LVDTs with a minimum precision of 0.01 mm must be placed on each side of the specimen to record the displacement at the mid-span using a similar device to that shown in Figure 6.7. Together with the displacement at the mid-span, the distance from the crack to the mid-span measured on the top face (d) must also be recorded (see Figure 6.8). The tests in which the crack appears out of the central one third must be eliminated. After the test, the specimen depth and width must be measured at the failure section with a ruler that guarantees a precision of 0.1 mm.
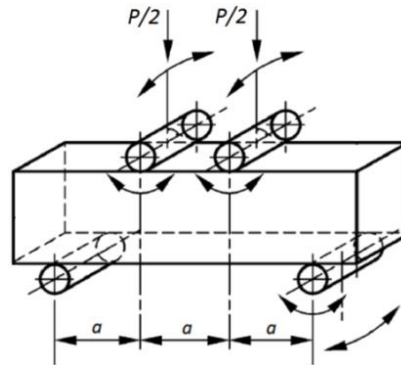
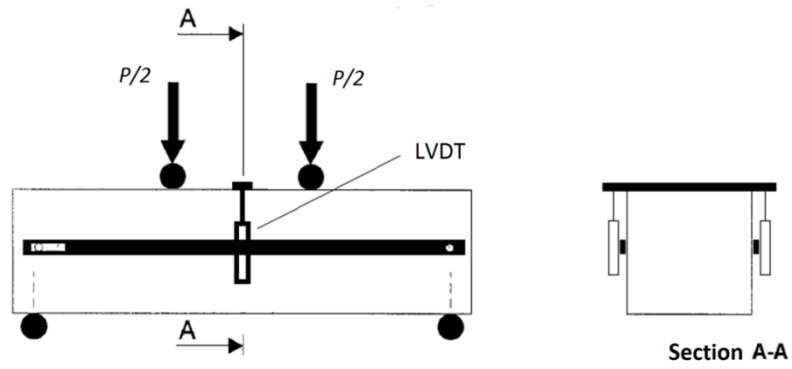Figure 6.6 Degrees of freedom of the load and bearing rollers

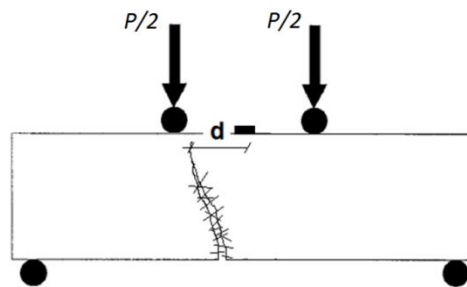Figure 6.7 Displacement at the mid-span measurement by means of two LVDTs

Figure 6.8 Measurement of the distance from the crack to the mid-span

6.3.2. Analysis of the results

After performing the test, load must be converted into an equivalent flexural strength following Eq. 6.5.

$$\sigma_{fl} = \frac{PL}{bh^2}$$

<div align="right">Eq. 6.5</div>

If the extension of the linear elastic slope of the $\sigma_{fl} - \delta$ curve intersects the δ axis at point δ_c that differs from 0, every measured δ value must be corrected following Eq. 6.6.

$$\delta_{corr} = \delta - \delta_c$$

<div align="right">Eq. 6.6</div>

After this correction, the new $\sigma_{fl} - \delta$ is obtained. This curve must be drawn. Now the four key points required to determine f_t, γ, $\varepsilon_{t,u}$ and w_o can be obtained. The procedure to obtain these four key points is explained in three steps.

(i) If the displacement correction is properly made, a point in the linear elastic part of the curve must be chosen $P_l(\delta_l, \sigma_l)$. The slope of line $\overline{OP_l}$ defines the initial stiffness of the curve (S_o), where O is the point with coordinates $(0,0)$. Its slope (m) can be derived by Eq. 6.7.

$$m = \frac{\sigma_l}{\delta_l}$$

<div align="right">Eq. 6.7</div>

(ii) On the experimental corrected curve, two lines are drawn:

S_{75}: A line passing through the origin with a slope equal to $0.75\ m$.

S_{40}: A line passing through the origin with a slope equal to $0.40\ m$.

(iii) Key points 1, 2, 3 and 4 are defined as follows. Their graphical definition is shown in Figure 6.9.

P_1 is defined as the intersection between S_{75} and the experimental curve. P_1 is defined by (δ_1, σ_1).

P_2 is defined as the intersection between S_{40} and the experimental curve. P_2 is defined by (δ_2, σ_2).

P_3 is defined as 97% of the flexural strength on the loading experimental curve. P_3 is defined by (δ_3, σ_3).

P_4 is defined as 80% of σ_3 on the unloading experimental curve. Displacement at this point is defined as δ_4. In order to take the crack location effect into account, Eq. 6.8 has to be used.

$$\delta_4^{\,*} = \delta_4 \left(1 + \frac{9d}{20(L - 2d)}\right)$$

Eq. 6.8

After this transformation, P_4 is defined by ($\delta_4^{\,*}$, σ_4). It is important to remark that the transformation that takes into account the characteristic length of the test is neglected as the determination of parameter w_d is not affected by the characteristic length consideration when using 5P-IA, according to the results in 5.3.2, in stran-hardening materials. Therefore, a hinge length of one third the specimen length, which corresponds to the central one third, is used.

Point 5 is not necessary to be determined because a characteristic crack opening (w_c) can be easier to obtain from fibre length. As fibre length is required for the UHPFRC classification, there is no need to determine the characteristic crack opening (w_c) by the inverse analysis method.
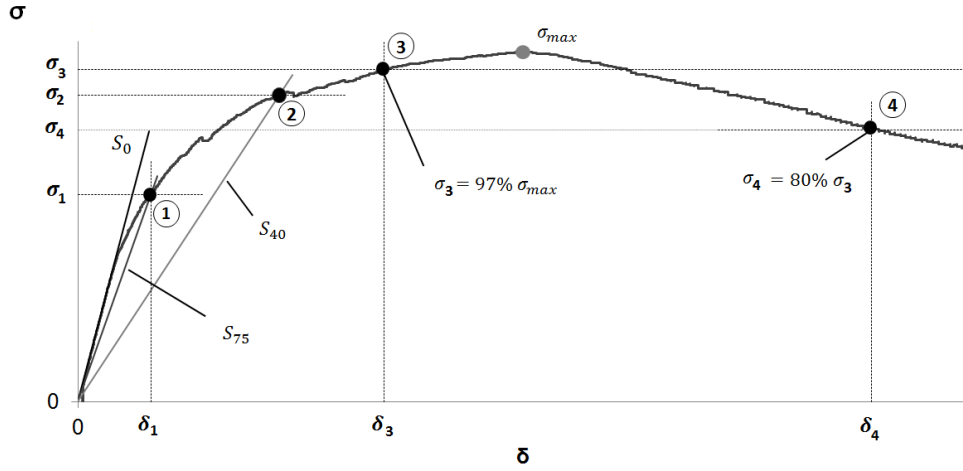
Figure 6.9 Definition of the four key points on an experimental $\sigma_{fl} - \delta$ curve.

The proposed constitutive model for UHPFRC is depicted in Figure 6.10, defined according to six parameters: the elastic modulus (E) cracking strength (f_t); ultimate cracking strength ($f_{t,u}$) and its associated strain ($\varepsilon_{t,u}$); crack opening at the intersection of the line that defines the initial slope to the w axis (w_o); the characteristic crack opening ($l_f/4$). Only the first five are determined by this procedure. Note that a

conservative value for w_c of one fourth the fibre length is proposed according to the French standard.
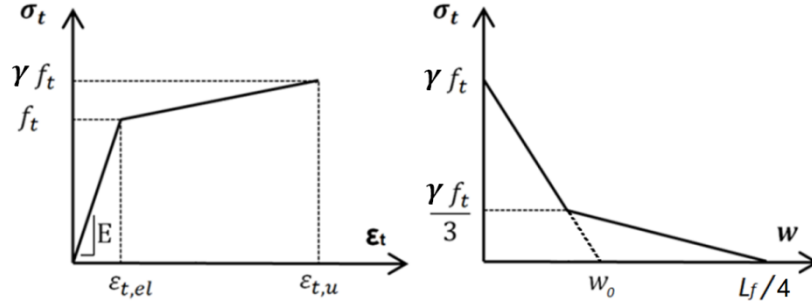
Figure 6.10 The proposed constitutive model for UHPFRC

The inverse analysis formulations to determine these five parameters are summarised in Table 6.6 for the two slenderness ratios considered, these being 3 and 4.5. Its application only requires the four previously defined key points.

Table 6.6 The inverse analysis formulations for slenderness ratios of 3 and 4.5

	$\frac{L}{h} = 3$	$\frac{L}{h} = 4.5$	Normalised parameters
E	$2.40\,h\,m$	$4.79\,h\,m$	
f_t	$\frac{\sigma_1}{1.63}\left(\frac{\sigma_1}{\sigma_2}\right)^{0.19}$	$\frac{\sigma_1}{1.59}\left(\frac{\sigma_1}{\sigma_2}\right)^{0.21}$	
$\varepsilon_{t,u}$	$\frac{f_t}{E}\left(7.65\frac{\delta_3}{\delta_1} - 10.53\right)$	$\frac{f_t}{E}\left(6.65\frac{\delta_3}{\delta_1} - 9.40\right)$	
γ	$\alpha^{-0.18}\left(2.46\frac{\sigma_3}{\sigma_1} - 1.76\right)$	$\alpha^{-0.17}\left(2.24\frac{\sigma_3}{\sigma_1} - 1.55\right)$	$\alpha = \varepsilon_{t,u}E/f_t$
$\varepsilon_{t,d}$	$\gamma^{-0.37}\alpha^{0.88}\left(3.00\frac{\delta_4^{*}}{\delta_3} - 1.80\right)\frac{f_t}{E}$	$\gamma^{-0.38}\alpha^{0.89}\left(2.82\frac{\delta_4^{*}}{\delta_3} - 1.68\right)\frac{f_t}{E}$	
w_0	$\left(\varepsilon_{t,d} - \varepsilon_{t,u} + \frac{10\gamma f_t}{3E}\right)\frac{3h}{2}$	$\left(\varepsilon_{t,d} - \varepsilon_{t,u} + \frac{10\gamma f_t}{3E}\right)\frac{9h}{4}$	

Note that coefficient $3/2$ found in the determination of w_0 when the slenderness ratio equals 3 is the same coefficient shown in Eq. 6.1. Coefficient $9/4$ takes into account the same w_d to w_0 transformation in Eq. 6.1 and also the fact that characteristic length is one and a half the specimen depth. This transformation assumes an unloading modulus that equals 20% the elastic modulus.

A detailed application of this method in an experimental test carried out with a slenderness ratio of 3 and a 100 mm-square cross-section specimen is shown below to offer a better understanding of the proposed procedure.

6.3.3. Example of the application

A UHPFRC specimen was tested in a TPBT with the following geometry: $h = 100\ mm$; $b = 100\ mm$; $l = 300\ mm$; $L = 500\ mm$; $d = 10\ mm$.

The recorded load is transformed into the equivalent flexural strength following Eq. 6.5. Experimental $\sigma_{fl} - \delta$ is depicted in Figure 6.11.
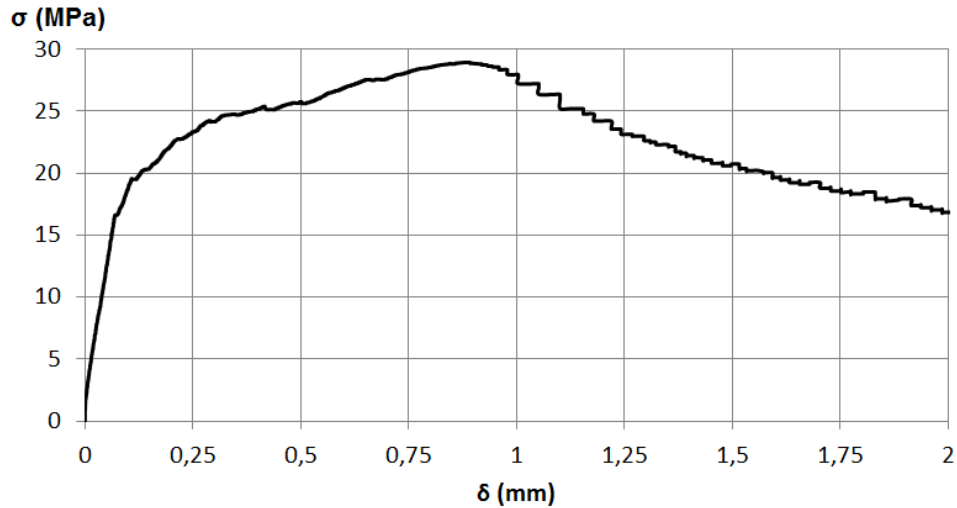
Figure 6.11 The experimental equivalent flexural strength versus displacement at mid-span in a third-point bending test with a slenderness ratio of 3.

As seen in Figure 6.12, left, the line that defines the elastic behaviour does not go through the origin. According to Figure 6.12, parameter δ_c equals -0.0089 mm. The experimental curve is corrected with Eq. 6.6. The corrected curve is shown in Figure 6.12, right. We can see how the line that defines the linear elastic behaviour passes through the origin.
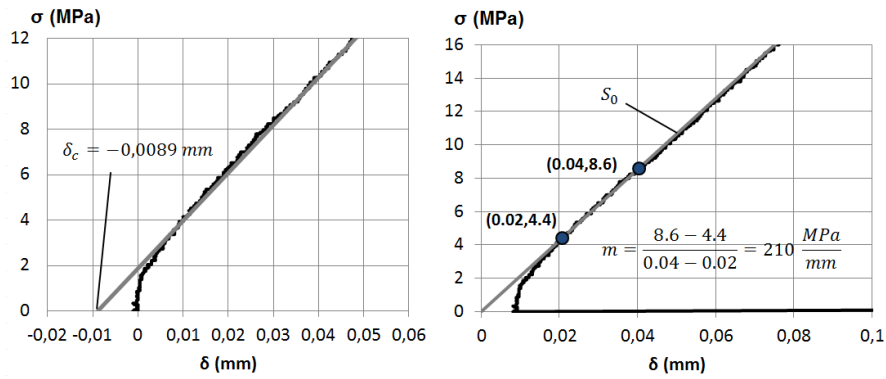
Figure 6.12 Correcting the experimental curve to make it pass through the origin.

In this particular case, the determination of the initial slope is done out using two points in the linear part of the curve. Determination of the slope is shown in Figure 6.12, right. After obtaining the slope, line S_0 can be easily drawn. Afterwards, lines S_{75} and S_{40} are drawn. Their slope is $0.75\,m$ and $0.40\,m$, respectively, as shown in Figure 6.13. After drawing these lines, the four key points can be determined. The points are defined in Table 6.7 and shown in Figure 6.14.
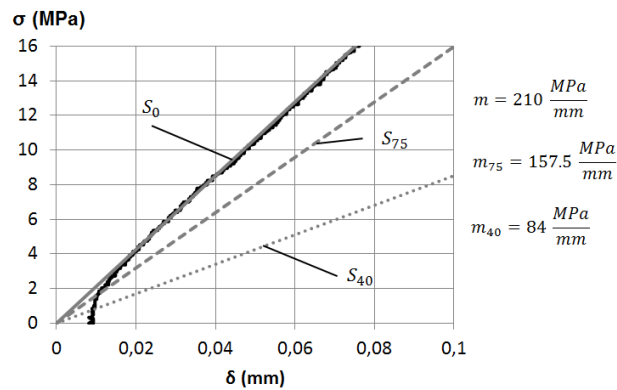
Figure 6.13 Representation of lines S_0, S_{75}, and S_{40} and their corresponding slopes.

Table 6.7 Definition of the four key points

POINT	$\delta\ (mm)$	$\sigma\ (MPa)$
P_1	0.12	19.0
P_2	0.28	23.6
P_3	0.75	28.1
P_4	1.33	22.4
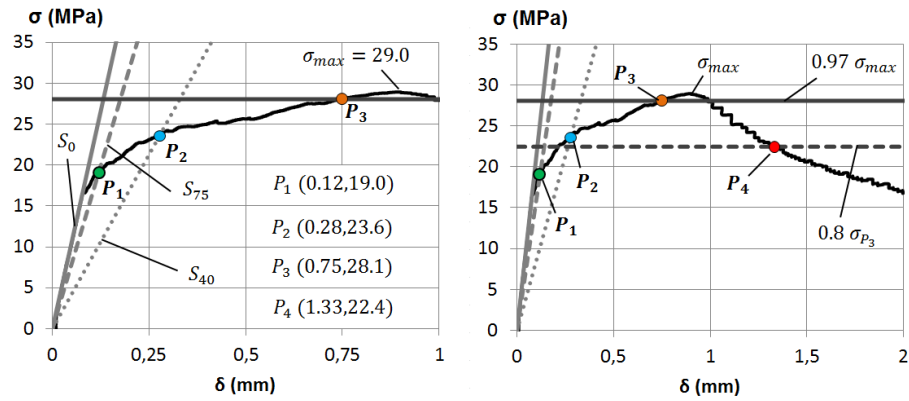
Figure 6.14 Determination of the four key points

Using the key points and the equations in Table 6.6 for a slenderness ratio of 3, the constitutive parameters in tension that correspond to the tested specimen can be obtained. Determining the elastic modulus is done in accordance with the initial slope and the specimen depth according to Table 6.8

Table 6.8 Determination of E

h	Geometry data	100	mm
m	Initial slope	210	MPa/mm
E	2.40 $h\,m$	50400	MPa

Cracking strength is determined in accordance with σ_1 and σ_2 according to Table 6.9

Table 6.9 Determination of f_t

σ_1	P_1	19.0	MPa
σ_2	P_2	23.6	MPa
f_t	$\dfrac{\sigma_1}{1.63}\left(\dfrac{\sigma_1}{\sigma_2}\right)^{0.19}$	11.19	MPa

The strain that corresponds to maximum tensile strength is determined in accordance with δ_1 , δ_3, f_t and E according to Table 6.10

Table 6.10 Determination of $\varepsilon_{t,u}$

δ_1	P_1	0.12	mm
δ_3	P_3	0.75	mm
f_t	Already obtained	11.19	MPa
E	Already obtained	50400	MPa
$\boldsymbol{\varepsilon_{t,u}}$	$\dfrac{f_t}{E}\left(7.65\dfrac{\delta_3}{\delta_1}-10.53\right)$	8.28‰	

Maximum tensile strength is determined in accordance with α, σ_3, σ_1 and f_t according to Table 6.11

Table 6.11 Determination of γ

α	$\left(7.65\dfrac{\delta_3}{\delta_1}-10.53\right)$	37.28	
σ_3	P_3	28.1	MPa
σ_1	P_1	19.0	MPa
$\boldsymbol{\gamma}$	$\alpha^{-0.18}\left(2.46\dfrac{\sigma_3}{\sigma_1}-1.76\right)$	0.979	MPa

Parameter w_0 is determined in accordance with $\varepsilon_{t,d}$ according to Table 6.12

Table 6.12 Determination of w_0

d	Crack location	10	mm
l	Geometry data	300	mm
δ_4	P_4	1.33	mm

$\delta_4{}^*$	$\delta_4{}^* = \delta_4\left(1 + \dfrac{9d}{20(L-2d)}\right)$	1.35	mm
δ_3	P_3	0.75	mm
α	Already obtained	37.28	
γ	Already obtained	0.979	
f_t	Already obtained	11.19	MPa
E	Already obtained	50400	MPa
$\varepsilon_{t,d}$	$\gamma^{-0.37}\alpha^{0.88}\left(3.00\dfrac{\delta_4{}^*}{\delta_3} - 1.80\right)\dfrac{f_t}{E}$	19.45‰	
$\varepsilon_{t,u}$	Already obtained	8.28‰	
E	Already obtained	50400	MPa
h	Geometry data	100	mm
w_0	$\left(\varepsilon_{t,d} - \varepsilon_{t,u} + \dfrac{10\gamma f_t}{3E}\right)\dfrac{3h}{2} = 1.82$	1.78	mm

6.4. Summary

A UHPFRC classification is proposed in this chapter after taking into account the current classification for conventional concrete and the classifications already proposed for UHPFRC. The proposed classification differs from the conventional concrete classification as the maximum aggregate size is substituted for the maximum fibre length and the tensile parameters required for design are introduced.

Traditional FRC classifications include two residual tensile strength values, which provide an idea of the softening stress-crack opening behaviour of concrete. However, a design with UHPFRC requires more parameters to contemplate its strain-hardening response. The proposed classification uses four parameters that allow the determination of complete UHPFRC tensile constitutive behaviour. These parameters refer to a specific test setup that can be obtained by a specific simplified inverse analysis methodology. These parameters are: characteristic cracking strength ($f_{t,k}$); characteristic hardening coefficient (γ_k); characteristic strain upon peak ($\varepsilon_{t,u,k}$);

characteristic crack opening at the intersection of the line that defines the initial slope of the stress-crack opening behaviour to the w axis ($w_{o,k}$). For all these parameters, different classes are proposed according to the expected coefficient of variation in the determination of these parameters from the standard test. Minimum values are also proposed that establish the border between a strain-hardening and a strain-softening UHPFRC and the border between what can be considered a UHPFRC or not.

In order to be considered a UHPFRC, minimum $f_{t,k}$ and $w_{o,k}$ values of 6 MPa and 0.5 mm must be guaranteed. If UHPFRC fulfils this criterion, it can be considered a strain-hardening material represented by acronym SH, but only if $\varepsilon_{t,u,k}$ is higher than or equals 2‰, and if the average hardening coefficient (γ) is higher than or equals 0.9. Otherwise, UHPFRC will be considered a strain-softening material represented by the acronym SS. In this case, parameters $\varepsilon_{t,u,k}$ and γ_k are not required for its classification. Specimens that go beyond these criteria should be considered FRC, and be characterised and classified by EN-14651.

The tensile parameters used to classify UHPFRC are obtained from a TPBT that is proposed as a standard test for UHPFRC instead of EN-14651. All the required parameters for design can be derived accurately from it by a simple back-of-the-envelope formulation. An example of an application has shown how easy its application is as it only requires minimum knowledge of maths and geometry. This is a huge achievement compared to current inverse analyses.

The size of proposed standard square beam does not depend on the structural element size. Instead it is considered that the fibre orientation effect is introduced into the design phase, which affects the constitutive relationship as fibre orientation is a structural parameter. However, beam size is considered according to fibre length. Two different specimen depths are proposed depending on fibre length: (i) 100-mm beam depth up to a fibre length of 20 mm and (ii) 150-mm beam depth for a fibre length that falls within the 20-60 mm range. Although the slenderness ratio can be either 3 or 4.5, using a slenderness ratio of 4.5 for the 100-mm depth specimens and one of 3 for the 150-mm depth specimens is recommended.

The proposed standard test only requires measuring both the displacement at the mid-span on both specimen sides and crack position. The way specimens should be cast is also defined.

A characterisation test setup and its associated inverse analysis methodology have been developed according to the parameters required for design in a bold attempt to reproduce the extensive work developed by RILEM TC 162-TDF, which resulted in the development of EN-14651 and the current design methods for FRC.

Chapter 7

Conclusions and future work

7.1. Conclusions

According to the characterisation test setup and methodology proposed in Chapter 6, it can be stated that the main objective of this work, which is "*to develop a suitable characterisation test setup and methodology for being proposed as a standard that enables the determination of those tensile parameters required for the UHPFRC classification and the design of UHPFRC structures",* has been fulfilled. In fact the test setup and methodology proposed in Chapter 6 are already proposed to become a Spanish UNE standard in the near future. The UHPFRC classification and some of the constitutive relationships for design in both ULS and SLS also shown in that chapter are to be included in the Spanish Recommendations for UHPFRC developed by Committee 1.6 of ACHE (Spanish Scientific and Technical Association for Structural Concrete).

Several conclusions have been drawn throughout the document. To facilitate its summary and reading, they have been arranged into six groups: (i) constitutive UHPFRC behaviour; (ii) characterisation test setup and methodology; (iii) non-linear hinge model; (iv) inverse analysis methods; (v) experimental programme; (vi) test setup and methodology standardisation. While groups (i) and (ii) describe the main conclusions reached from the analysis of the current state of the art, the rest of the groups show the most relevant findings of the conducted work.

(i)   Constitutive UHPFRC behaviour

The study of the state of the art in Chapter 2 reveals that constitutive UHPFRC behaviour in tension can be modelled by a bilinear stress-strain relationship up to tensile strength and a bilinear stress-crack opening behaviour from this point onwards. Note that the proposed constitutive model is the same as MC2010, suggested for plain concrete. Even though the constitutive law's shape is the same, the values that define it are much higher in UHPFRC than in plain concrete, or even in fibre-reinforced concrete (FRC).

Note that the constitutive behaviour proposed in tension respects the concrete modelling tradition by offering an integrated view in which plain concrete and FRC are included in a broader group. Figure 7.1 offers a simplified not-scaled view of the different concrete types. With plain concrete and FRC, strain-hardening behaviour is not often considered because its influence in design is too slight in both cases. However, its consideration is important for UHPFRC. Differences in the softening behaviour of distinct concrete types are due to fracture energy. As fracture energy is so small in plain concrete, its influence is always neglected in design, but is always considered in FRC and UHPFRC.
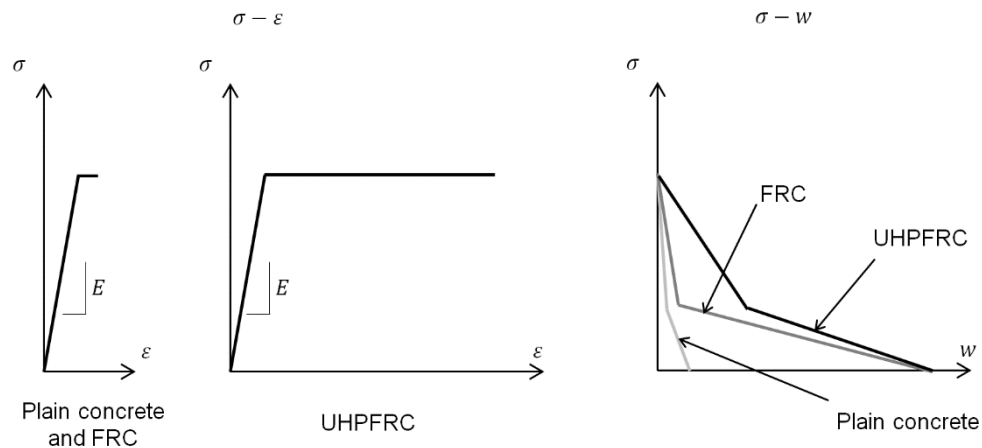

Figure 7.1 The constitutive tensile law for different concrete types.

According to previous literature, the stress at the change of slope has been established as one third the ultimate strength for UHPFRC, and remains on the safety side and with no significant loss of accuracy. This value agrees with both the experimental tests carried out and the conventional values used for plain concrete.

This work has not dealt with UHPFRC compressive constitutive behaviour. However for a characterisation purpose in a TPBT, it has been proved that linear elastic

constitutive behaviour can be assumed in compression if material compressive strength is at least 100 MPa.

(ii)   Characterisation test and methodology

UHPFRC tensile behaviour substantially differs from conventional concrete and FRC in terms of energy dissipated. This is why it has been properly justified that newer characterisation test setups are required.

A direct tensile test has been ruled out as a suitable test for being standardised given the difficulties encountered when performing it. In addition, no bending test setup that provides both stress-strain hardening behaviour and softening stress-crack opening UHPFRC behaviour is currently available.

It has been proved that the test setup proposed in EN-14651 (notched three-point bending test) is not suitable for UHPFRC because it is impossible to properly determine strain-hardening UHPFRC behaviour. The four-point bending test allows UHPFRC strain-hardening behaviour to be determined thanks to the constant bending moment area. This type of test arises as the best choice to characterise tensile UHPFRC behaviour and, generally speaking, of strain-hardening materials. However, the determination of the softening stress-crack opening from it requires having to use fracture mechanics models.

The commonest four-point bending test is the third-point bending test (TPBT), which follows the setup configuration in Figure 7.2. This work was specifically undertaken for this type of test and agrees with existing standards to characterise plain concrete behaviour.
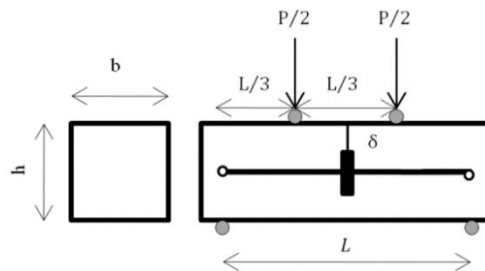

Figure 7.2 The third-point bending test (TPBT) setup.

(iii)   Non-linear hinge model

The determination of UHPFRC softening behaviour from bending tests requires using fracture mechanics models. In a compromise solution between simplicity and accurateness to model load-deflection UHPFRC behaviour in a TPBT, the non-linear hinge fracture mechanic model arises as the best solution. This model allows the major achievements listed below:

- An equation to relate the constitutive stress-crack opening to the sectional stress-strain behaviour inside the hinge according to hinge length has been successfully developed for UHPFRC.
- A closed-form bending moment according to sectional curvature formulation has been successfully developed, which is a specific adaptation of existing closed-from solutions to UHPFRC.
- A new closed-form curvature to displacement at mid span transformation has been successfully developed for a TPBT, and has improved the existing transformations found in the literature by considering non-linear curvature distribution and shear effects.
- Both closed-form bending moment-curvature equations and curvature to displacement at mid-span transformation are the pillars on which the whole non-linear hinge model is based. It allows the analytical determination of displacement at mid-span according to the constitutive tensile parameters in a TPBT.

After developing the general non-linear hinge model, additional studies have been conducted to validate it and to fully comprehend it. Major achievements are listed below:

- The non-linear hinge model has been successfully modified to include the crack position in the constant bending moment area.
- The non-linear hinge model has been successfully modified to allow the consideration of any desired characteristic length.
- The non-linear hinge model has been specifically developed for a characteristic length that equals one and a half the specimen depth, the specimen depth and half the specimen depth.
- For a given constitutive behaviour in tension, load-deflection at mid-span remains the same regardless of the hinge length considered in strain-hardening materials.
- It has been demonstrated that the developed non-linear hinge model reproduces the deterministic scale effect.

Finally, the non-linear hinge model was experimentally validated by comparing the expected sectional response after applying an inverse analysis procedure and the obtained experimental sectional response.

(iv) *Inverse analysis procedure*

The developed closed-form non-linear hinge is a powerful tool that has been used as the foundation of an iterative (I-IA) and simplified inverse analysis methodology (5P-IA) to derive the material properties from a load-deflection response obtained from a TPBT. The different sectional responses inside the hinge were used to check them.

An iterative load-curvature inverse analysis procedure has been developed and validated by comparing it to the load-curvature point-by-point inverse analysis method. This method allows the determination of complete UHPFRC tensile behaviour, but requires a computer to solve a least square problem. It has become a good simple method to derive the tensile properties from a TPBT, but is not simple enough to be included in a standard. However, it is suitable for research purposes.

The first step to develop a simplified inverse analysis method was to conduct a parametric study of the closed-form non-linear hinge model of around 12 million different stress-strain sectional hypotheses. It showed that it is possible to relate five specific points on the experimental load-deflection curve to the complete UHPFRC constitutive behaviour for slenderness ratios of 3 and 4.5. These simple equations allow the development of what has been called the five-point inverse analysis method (5P-IA). The major achievements of 5P-IA are listed below:

- The selection criteria of the key points are objective. After determining these points, a back-of-the-envelope calculation is used to determine the constitutive tensile parameters of UHPFRC.
- 5P-IA does not strictly require computer use as only basic knowledge in maths and geometry is needed, which makes the 5P-IA method suitable for being standardised.
- 5P-IA's accurateness has been evaluated by comparing it to the load-curvature point-by-point inverse analysis method, which reveals the method's suitability.

Given 5P-IA's simplified nature, it can be applied only if the following requirements are fulfilled:

- Using a TPBT
- Slenderness ratio of either 3 or 4.5 used in the TPBT.
- The experimental deflection-hardening behaviour obtained from a TPBT.
- Greater equivalent flexural stress at key point 3 than the equivalent flexural stress at key point 2. This condition is the equivalent to saying that the ultimate strain at tensile strength is greater than approx. 1.5-2‰.
- The constitutive behaviour of the tested material can be modelled by bilinear stress-strain behaviour up to tensile strength, and by decreasing bilinear stress-crack opening behaviour, similarly to that shown in Figure 7.1.

Finally, the validation of 5P-IA has been made by comparing it to the results obtained for an already validated and more complex inverse analysis method. No significant differences were found between these two methods, which demonstrates that 5P-IA is not only a simplify method, but also an accurate one.

(v)   Experimental programmes

Two different experimental programmes were run for the main purpose of validating the developed closed-form non-linear hinge model and the inverse analysis methods. The following conclusions were drawn from the obtained results:

- A wide source of variability in four-point bending tests is the non-consideration of crack position.
- The coefficients of variation of cracking strength (f_t) and ultimate tensile strength $(f_{t.u})$ lower than 10% are taken as reference values.
- Ultimate strain values $(\varepsilon_{t,u})$, crack opening at the slope change (w_d) and characteristic crack opening (w_c) present lower coefficients of variation than 25%, taken as a reference value.
- Strain-hardening behaviour can appear even if the ultimate tensile strength obtained from 5P-IA is lower than tensile strength due to both the complex behaviour in tension of UHPFRC and the simplifications assumed by the method.
- Generally speaking, UHPFRC can be considered to exhibit strain hardening behaviour if the strain at maximum tensile strength is higher than 2‰.
- Determining crack opening at zero stress (w_c) from inverse analysis procedures is difficult. Even though the obtained results are always below half the fibre length, i.e. conservative, they cannot be considered reliable. For simplicity and accuracy sake, its determination from fibre length makes more sense.

(vi)   Test setup and methodology standardisation

The constitutive tensile parameters obtained from the standard test methodology must offer the tensile parameters that are strictly required for design. Those parameters required for design are the same parameters used for its classification. This is why a UHPFRC classification has been proposed after taking into account the current classification for conventional concrete, FRC and the classifications already proposed for UHPFRC.

The proposed tensile classification uses four parameters that allow complete UHPFRC tensile constitutive behaviour to be determined. These parameters are: cracking strength (f_t); hardening coefficient (γ) and its corresponding strain $(\varepsilon_{t,u})$; and crack opening at the intersection of the line which defines the initial slope of the stress-crack opening behaviour to the w axis (w_o).

For all these parameters, different classes have been proposed according to the expected coefficient of variation while determining these parameters from the standard test proposed. Minimum required values have also been proposed. They establish the border between strain-hardening and strain-softening UHPFRC, and also the border between what can be considered UHPFRC or not.

Remember that design and characterisation must be developed together. This is why all the parameters used to classify UHPFRC can be obtained from the proposed standard standard test. The tensile parameters used to classify UHPFRC are obtained from a specific TPBT, proposed as a standard test for UHPFRC instead of EN-14651. The proposed test and methodology allow the determination of the four tensile parameters defined using a single test type. The proposed standard test setup has the following main features:

- The size of the proposed standard square beam does not depend on structural element size. Instead it is considered that fibre orientations effects must be introduced into the design.
- Standard beam size has been considered according to fibre length in order to avoid a significant fibre orientation influence on the characterisation test, and to allow specimens to continue being easy to handle.
- The proposed standard test only requires having to measure both displacement at mid-span on both sides of the specimen and crack location. The way specimens should be cast has also been defined.

The methodology to determine the four previously defined tensile parameters was based on 5P-IA. It includes some properly justified simplifications that enable the simplification of the test setup and methodology which, in turn, make them suitable for being included in a standard.

7.2. Future works

In line with the main purpose of this work, that of fostering the development of suitable UHPFRC design guidelines for engineers, some future works are proposed. Some of the works that need to be achieved are described below.

As mentioned in 6.2.2, the relationship between the strain at the crack localisation point ($\varepsilon_{t,u}$) in a standard TPBT (material level) and the structural strain at the crack localisation point value in both SLS and ULS ($\varepsilon_{t,u,s}$ and $\varepsilon_{t,u,d}$) is still unclear when reinforcement is used. This relationship is probably in accordance with specimen depth, the reinforcement ratio, rebars diameter, compressive concrete strength and material parameter $\varepsilon_{t,u,k}$. However, further investigation is required to define this link.

Another important parameter is the analysis of the fibre orientation effect. Current recommendations on UHPFRC only consider fibre orientation effect in a very basic manner, which is why using specific prototypes and testing to guarantee the fibre orientation in the structure are required most of the time. This fact makes the competitiveness of UHPFRC structures difficult. An ambitious research programme should be conducted to define reliable fibre orientation coefficients that allow engineers the easy safe design of UHPFRC structures that keeps costs low. These coefficients must take into account: fibre type, structure geometry, pouring system and

directions of forces. This is no easy task, but it is absolutely essential to foster the structural use of UHPFRC in the near future, as this is the most important step from material to structure.

There is still some uncertainty as to the relationship that links fibres types and amount, crack spacing and strain prior to macrocrack localisation. This uncertainty comes over even more clearly when concrete interacts with rebars. Further studies are required to shed some light onto these issues, and to improve knowledge of UHPFRC, and generally speaking, of strain-hardening materials.

Bibliography

ACI 549R-97. (n.d.). *State-of-the-Art Report on Ferrocement.* ACI Committee 549.

Adeline, R., Lachemi, M., & Blais, P. (1998). Design and behaviour of the Sherbrooke footbridge. *Proceedings of the International Symposium on High Performance and Reactive Powder Concretes*, (pp. 59-63). Sherbrooke University.

AFGC. (2013). *Ultra High Performance Fiber Reinforced Concretes. Recommendations.*

AFGC-Sétra. (2002). *Ultra High Performance Fiber Reinforced Concretes. Interim Reccomendations.*

Aïtcin, P. (2000). Cements of yesterday and today Concrete of tomorrow. *Cement and Concrete Research, 30*, 1349-1359.

Amin, A., Foster, S., & Muttoni, A. (2015). Derivation of the σ-w relationship for SFRC from prism bending tests. *Journal of Structural Concrete, 16*(1), 93-105.

ASTM C1609/C1609M-10. (n.d.). *Standard test method for flexural performance of fiber-reinforced concrete (using beam with third-point loading). American Society of Testing Materials.*

Baby, F., Graybeal, B., Marchand, P., & Toutlemonde, F. (2012). Proposed Flexural Test Method and Associated Inverse Analysis for Ultra High Performance Fiber Reinforced Concrete. *ACI Materials Journal, 109*(5), 545-556.

Baby, F., Graybeal, B., Marchand, P., & Toutlemonde, F. (2013). UHPFRC tensile behaviour characterization: inverse analysis of four-point bending test results. *Materials and Structures, 46*, 1337-1354.

Bache, H. (1981, June 10-12). Densified cement ultra-fine particle-based materials. *Second International Conference on Superplasticizers in Concrete.*

Bache, H. (1987). Compact Reinforced Composite. Basic principles. *Aalborg Portland, Cement-og Betonlaboratoriet, CBL report 41.*

Barr, B., Gettu, R., Al-Oraimi, S., & Bryars, L. (1996). Toughness measurement - the need to think again. *Cement & Concrete Composites, 18*, 281-297.

Bazant, Z. (1976). Instability, ductitlity, and size effect in strain-softening concrete. *Journal of Engineering Mechanics, 102*(2), 331-344.

Bazant, Z. (1984). Size effect in Blunt Fracture: Concrete, Rock, Metal. *Journal of Engineering Mechanics. ASCE., 110*(4), 518-535.

Bazant, Z. (1989). *Fracture Mechanics of Concrete: Concepts, Models and Determination of Material Properties.* Report by ACI Committee 446, Fracture Mechanics.

Bazant, Z. (2002). Concrete fracture models: testing and practice. *Engineering Fractuer Mechanics, 69*, 165-205.

Berard, A. (1874). *Patent No. 157 903.* Oakland, California.

Blais, P., & Couture, M. (1999). Precast, Prestressed Pedestrian Bridge - World's first reactive powder concrete structure. *PCI Journal, 44*, 60-71.

Branson, D. (1977). *Deformation of concrete structures.* New York: Mc Graw Hill.

Calavera, J. (2003). *Cálculos y conceptos en la historia del horimgón armado.* Biblioteca Insular Arrecife (Lanzarote). Discursos académicos.

Camacho, E. (2013). *Dosage optimization and bolted connections for UHPFRC ties.* Valencia: PhD Thesis. Universitat Politècnica de València.

Casanova, P., & Rossi, P. (1996). Analysis of metallic fibre-reinforced concrete beams subjected to bending. *Materials and Structures, 29*, 354-361.

Casanova, P., & Rossi, P. (1997). Analysis and design of steel fiber reinforced concrete beams. *ACI Structural Journal, 94*(5), 595-602.

Cavill, B., & Chirgwin, G. (2003). The worlds first Ductal road bridge Shepherds gully creek bridge, NSW. *21ème conférence biennale de l'institut du béton d'Australie, Brisbane.*

CEB-FIP. (1979). *Bulletin Nº 134. Non linear analysis of concrete structures.*

Chanvillard, G. (2000). Characterisation of fibre reinforced concrete mechanical properties: a review. *Proceedings of the fifth international RILEM symposium on fibre-reinforced concretes*, (pp. 29-50).

Chanvillard, G., & Rigaud, S. (2003). Complete Characterisation of Tensile Properties of Ductal UHFPRC according to the French recommendations. *Proceedings of the 4th International Symposium on High Performance Fiber Reinforced Concretes (HPFRCC4)*, 21-34.

Coignet, F. (1855). Constructions économiques en béton pisé. *Exposition universelle. Extrait du journal l'ingénieur.*

Collins, M., & Mitchell, D. (1980). Shear and torsion design of prestressed and nonprestressed concrete beams. *P.C.I. Journal.*

de Larrard, F., & Sedran, T. (1994). Optimization of Ultra-High-Performance Concrete by the Use of a Packing Model. *Cement and Concrete Research, 24*(6), 997-1009.

de Montaignac, R., Massicotte, B., Charron, J., & Nour, A. (2012). Design of SFRC structural elements: post-cracking tensile strength measurement. *Materials and Structures, 45*(4), 609-622.

Denarié, E., & Brühwiler, E. (2015). Cast-on site UHPFRC for improvement of existing structures - achievements over the last 10 years in practice and research. *Proceedings of the 7th International Symposium on High Performance Fiber Reinforced Cement Composites, HPFRCC-7. Stuttgart, Germany*, 473-480.

Densit, a. s. (n.d.). *www.densit.com.*

di Prisco, M., Colombo, M., & Ferrara, L. (2007). Chapter 2. FRC and HPFRC material properties. In M. di Prisco, *Fibre-Reinforced Concrete for Stron, Durable and Cost-Saving Structures and Infraestructures.* Starrylink Editrice.

Fehling, E., Schmidt, M., Bunje, K., & Schreiber, W. (2004). Ultra High Performance Composite Bridge across the River Fulda in Kassel - Conceptual Design, Calculations and Invitation to Tender. *Proceedings of the International Symposium on Ultra High Performance Concrete*, (pp. 69-75). Kassel University.

Fernández-Cánvoas, M. (1981). *Hormigones reforzados con fibras de acero.* Instituto Eduardo Torroja (IET). Informes de la Construcción/342.

FHWA. (2013). Ultra-High Performance Concrete: A State-of-the-art Report for the bridge community. *FHWA-HRT-13-060.*

FHWA. (2014). Design and Construction of Field-Cast UHPC Connections. *FHWA-HRT-14-084.*

Frettlöhr, B., Reineck, K., & Reinhardt, H. (2011). Size and Shape Effect of UHPFRC Prisms Tested under Axial Tension and Bending. *Proceedings of the 6th International Symposium on High Performance Fiber Reinfroced Cement Composites (HPFRCC 6)*, 365-372.

Freyssinet, E. (1928). *Patent No. 680547.* France.

Gambarova, P. (2007). Chapter 1. Introduction. In M. d. Prisco (Ed.), *Fibre-Reinforced Concrete for strong, durable and cost-saving structures and infrastructures.* Starrylink Editrice.

DAfStB. (2015). Deutscher Ausschuss Für Stahlbeton - Commentary on the DAfStb Guideline "Steel Fibre Reinfrced Concrete".

Gopalaratnam, V., & Gettu, R. (1995). On the Characterization of Flexural Toughness in Fiber Reinforced Concretes. *Cement and Concrete Composites, 17*, 239-254.

Gowripalan, N., & Gilbert, I. (2000). Design Guidelines for Ductal Prestressed Concrete Beams. *School of Civil and Environmental Engineering. The University of New South Wales*.

Graybeal, B. (2006, August). Material Property Characterization of Ultra-High Performance Concrete. *Federal Highway Administration FHWA-HRT-06-103*.

Graybeal, B. (2013). UHPC in the U.S. highway infrastructure: experience and outlook. *Proceedings of the International Symposium on Ultra-High Performance Fibre-Reinforced Concrete, UHPFRC-2013. Marseille, France*.

Graybeal, B., & Baby, F. (2013). Development of direct tension test method for UHPFRC. *ACI Material Journal, 110*(2), 177-186.

Graybeal, B., Baby, F., Marchand, P., & Toutlemonde, F. (2012). Direct and Flexural Tension Test Methods for Determination of the Tensile Stress-Strain Response of UHPFRC. *Proceedings of the 3rd International Symposium on UHPC (HIPERMAT)*, 395-402.

Griffith, A. (1921). The phenomenon of rupture and flow in solids. *Phil. Trans. Roy. Soc. London A 221, pp. 163-198*.

Groeger, J., N.V., T., & Wille, K. (2012). Bending behaviour and variation of flexural parameters of UHPFRC. *Proceedings of the 3rd International Symposium on UHPC and Nanotechnology for High Performance Construction Materials*, (pp. 419-426). Kassel, Germany.

Hajnal-Kónyi, K. (1956). The use of high tensile steel as reinforcement of concrete. *IABSE congress report*.

Heilmann, H., Hildsdorf, H., & Finsterwalder, K. (1969). Festigkeit und Verformung von Beton unter Zugspannungen. *Deutscher Aussechuss für Stahl-beton, Heft 203, W. Ernst & Sohn, Berlin*.

Hillerborg, A. (1983). Concrete Fracture Energy Tests Performed by 9 Laboratories according to a draft RILEM Recommendation. *Report to RILEM TC50-FMC*.

Hillerborg, A. (1985). The theoretical basis of a method to determine the fracture energy Gf of concrete. *Materials and Structures, 18*, 291-296.

Hillerborg, A. (1986). Determination and significance of the fracture toughness of steel fiber concrete. In S. Shah, & A. Skarendahl, *Steel fiber concrete (U.S.-Sweden joint seminar, 1985)* (pp. 257-271). London, England: Stockholm/Elsevier Applied Science Publishers.

Hillerborg, A., Modéer, M., & Petersson, P. (1976). Analysis of crack formation and crack growth in concrete by means of fracture mechanics and finite elements. *Cement and Concrete Research, 6*, 773-782.

Hughes, B., & Chapman, G. (1966). The complete stress-strain curve for concrete in direct tension. *Bulletin RILEM, No 30, pp. 95-97*.

ISO/TC 71/SC 6 Working draft. (2016). *Test methods for fibre-reinforced cementitious composites - Bending moment - curvature curve by four-point bending test.*

JSCE. (2006). Recommendations for design and construction of ultra high-strength fiber reinforced concrete structures (draft). *JSCE Guidelines for Concrete No. 9.*

JSCE. (2008). Recommendations for Design and Construction of High Performance Fiber Reinforced Cement Composites with Multiple Fine Cracks (HPFRCC).

Jungwirth, J., & Muttoni, A. (2004). Structural behavior of tension members in UHPC. *Prceedings of the Symposium of Ultra High Performance Concrete. Kassel*, 533-544.

Kanakubo, T. (2006). Tensile Characteristics Evaluation Method for Ductile Fiber-Reinforced Cementitious Composites. *Journal of Advanced Concrete Technology, 4*(1), 3-17.

Kim, D., Naaman, A., & El-Tawil, S. (2008). Comparative flexural behavior of four fiber reinforced cementitious composites. *Cement and Concrete Composites, 30*, 917-928.

Kim, D., Naaman, A., & El-Tawil, S. (2010). Correlation between tensile and bending behavor of FRC composites with scale effect. *Proceedings of the fracture mechanics of concrete and concrete structures - FraMCos-7. Korea Concrete Institute*, (pp. 1379-1385).

Krenchel, H. (1964). *Fiber Reinforcement.* Copenhagen: Akademisk Forlag.

Kupfer, H. (1964). Extension to the truss analogy of Mörsch using the principle of minimum potencial energy. *CEB. Bulletin d'Information Nº 40.*

Lankard, D. (1984). Slurry Infiltrated Fiber Concretes (SIFCON): Properties and Applications. *MRS Online Proceeding Library 42.*

Lepech, M., & Li, V. (2004). Size effect in ECC Structural Members in Flexure. *Proceedings of Fracture Mechanics of Concrete and Concrete Structures (FramCOs-5)*, (pp. 1059-1066).

López, J., Serna, P., Navarro-Gregori, J., & Camacho, E. (2014). An inverse analysis method based on deflection to curvature transformation to determine the tensile properties of UHPFRC. *Materials and Structures, 48*, 3703-3718.

López, J., Serna, P., Camacho, E., Coll, H. & Navarro-Gregori, J. (2014b). First Ultra-High-Performance Fibre-Reinforced Concrete footbridge in Spain: Design and Construction. *Journal of the International Association for Bridge and Structural Engineering (IABSE), 24:1, 101-104*

López, J., Serna, P., Navarro-Gregori, J., & Coll, H. (2015). Comparison between inverse analysis procedure results and experimental measurements obtained from UHPFRC Four-Point Bending Tests. *Proceedings of the 7th RILEM Workshop on High Performance Fiber Reinforced Cement Composites (HPFRCC7)*, (pp. 185-192). Stuttgart, Germany.

López, J., Coll, H., Serna, P., & Galán, F. (2016a). The UHPFRC pedestrian bridge above the V-21 Highway in Puzol, Valencia: Design, Construction and Cost. *Proceedings of the 4th International Symposium on UHPC. Kassel, Germany*.

López, J., Serna, P., Navarro-Gregori, J., & Coll, H. (2016b). Characterisation of the strain-hardening behaviour of UHFPRC using the Third-Point-Bending Test. *Proceedings of the 4th HIPERMAT International Symposiun on UHPC. Kassel*.

Maalej, M., & Li, V. (1994). Flexural strength of fiber cementitious composites. *Journal of Materials in Civil Engineering (ASCE), 6*, 390-406.

Mahmud, G., Yang, Z., & Hassan, A. (2013). Experimental and numerical studies of size effects on ultra high performance steel fibre reinforced Concrete (UHPFRC) beams. *Construction and Building Materials, 48*, 1027-1034.

Markovic, I. (2006). High-Performance Hybrid-Fibre Concrete. Development and utilisation. *PhD-Thesis, TU-Delft*.

Massicotte, B., & Bischoff, P. (2000). Fibre Reinforced Concrete: a structural perspective. *Proceedings of the 5th International RILEM Symposium on Fibre-Reinforced Concretes. BEFIB 2000*, 193-202.

Mayer, M. (1926). *Die Sicherheit der Bauwerke und ihre Berechnung nach Grenzkräften anstatt nach zulässigen Spanungen.* Verlag von Julius Springer.

MC1990. (1990). *CEB-FIP model code.*

MC2010. (2010). *CEB-FIP model code.*

McKee, H. (1973). *Introduction to Early American Masonry - Stone, Brick, Mortar and Plaster.* National Trust for Historic Preservation, Columbia University.

Naaman, A. (2007). Tensile strain-hardening FRC composites: Historical evolution since the 1960. In *Advances in Construction Materials* (pp. 181-202). Springer.

Naaman, A., & Reinhardt, H. (2003). Setting the stage: toward performance based classification of FRC composites. *Proceedings of the 4th RILEM symposium on high performance fiber reinforced cement composites (HPFRCC4)*, 1-4.

Naaman, A., & Reinhardt, H. (2006). Proposed classification of HPFRC composites based on their tensile response. *Materials and Structures, 39*, 547-555.

Naaman, A., & Wille, K. (2012). *The path to Ultra-High Performance Fiber Reinforced Concrete (UHP-FRC): Five Decades of Progress.* Kassel: Proceedings of the 3rd International Symposium on UHPC.

Nedwell, P., & Swamy, R. (1994). *Ferrocement: Proceedings of the Fifth International Symposium on Ferrocement UMIST.* Manchester.

NF P18-470. (2016). Bétons - Bétons fibrés à Ultra Hautes Performances - Spécification, performance, production et conformité.

NF P18-710. (2016). Calcul des structures en béton: règles espécifiques pour les Bétons Fibrés à Ultra-Hautes Peformances (BFUP).

Nguyen, D., Kim, D., Ryu, G., & Koh, K. (2012). Size effect on flexural behavior of ultra-high performance hybrid fiber-reinforced concrete. *Composites Part B: Engineering, 45*(1), 1104-1116.

Nguyen, D., Ryu, G., Koh, K., & Kim, D. (2014). Size and geometry dependent tensile behavior of ultra-high-performance fiber-reinforced concrete. *Composites Part B: Engineering, 58*, 279-292.

Nielsen, M. (1984). *Limit analysis and concrete plasticity.* New Jersey: Prentice-Hall.

Olesen, J. (2001). Fictitious crack propagation in fiber-reinforced concrete beams. *Journal of Engineering Mechanics, 127*(3), 272-280.

Ostergaard, L., Walter, R., & Olesen, J. (2005). Method for Determination of Tensile Properties of Engineered Cementitious Composites (ECC). *Proceedings of ConMar'05.* Vancouver, Canada.

Paez, A., & Torroja, E. (1952). *La determinación del coeficiente de seguridad en las distintas obras.* Instituto Técnico de la Construcción y el Cemento.

Park, S., Kim, D., Ryu, G., & Koh, K. (2012). Tensile behavior of ultra high performance hybrid fiber reinforced concrete. *Cement and Concrete Composites, 34*, 172-184.

Parra-Montesinos, G., Reinhardt, H., & Naaman, A. (2011). High Performance Fiber Reinforced Cement Composites 6 (HPFRCC6). *RILEM Bookseries*.

Paul, B., & Pama, R. (1978). *Ferrocement.* International Ferrocement Information Center.

Pedersen, C. (1996). New productioin processes, materials and calculation techniques for Fiber-Reinforced Concrete pipes. *PhD thesis. Department of Structural Engineering and Materials. Technical University of Denmark, Series R, no. 14.*

Petersson, P. (1981). Crack growth and development of fracture zones in plain concrete and similar materials. *PhD Lund Universitiy. Division of Building Materials Lund Institute of Technology.*

Planas, J., Elices, M., & Guinea, G. (1992). Measurement of the fracture energy using three-point bend tests: Part 2 - Influence of bulk energy dissipation. *Material and Structures, 25*, 305-312.

Qian, S., & Li, V. (2007). Simplified Inverse Method for Determining the Tensile Strain Capacity of Strain Hardening Cementitious Composites. *Journal of Advanced Concrete Technoology, 5*(2), 235-246.

Randl, N., Mészöly, T., & Harsányi, P. (2016). Load bearing behaviour of slender UHPC beam members in shear. *Proceedings of the 4th International Symposium on UHPC. Kassel, Germany.*

Reichel, M., Freytag, B., & Sparowitz, L. (2009). Road Bridge Wild-UHPFRC for a segmental arch structure. *Proceedings of the International Symposium on Ultra-High Performance Fibre Reinforced Concrete, UHPFRC 2009. Marseille, France.*

Reineck, K., & Frettlör, B. (2010). Test on scale effect of UHPFRC under bending and axial forces. *3rd Fib International Congress*, (p. 40). Washington DC.

Reinhardt, H., Parra-Montesinos, G., & Garrecht, H. (2015). *Proceedings of the 7th RILEM Workshop on High Performance Fiber Reinforced Cement Composites (HPFRCC7).* RILEM Publications S.A.R.L.

Resplendino, J., & Toutlemonde, F. (2013). The UHPFRC revolution in structural design and construction. *Proceedings of the International Symposium on*

Ultra-High Perfromance Concrete. UHPFRC 2013, October 1-3 2013, Marseille, France.

Richard, P., & Cheyrezy, M. (1995). Composition of Reactive Powder Concrete. *Cement and Concrete Research, 25*(7), 1501-1511.

Rigaud, S., Chanvillar, G., & Chen, J. (2011). Characterization of Bending and Tensile Behavior of Ultra-High Performance Concrete Containing Glass Fibers. *6th International Symposium on High Performance Fiber Reinforce Cement Composites*, 373-380.

RILEM 49TFR. (1984). Testing methods for fibre reinforced cement-based composites. *Materials and Structures, 17*, 441-456.

RILEM TC 162-TDF. (2001). Test and design methods for steel fiber reinforced concrete. Uni-axial tension test for steel fibre reinforced concrete. *Materials and Structures, 34*(235), 3-6.

RILEM TC 162-TDF. (2002). Test and design methods for steel fibre reinforced concrete. Design of steel fibre reinforced concrete using the σ-w method: principles and applications. *Materials and Structures, 35*, 262-278.

RILEM TC 162-TDF. (2003a). Round-robin analysis of the RILEM TC 162-TDF uni-axial tensile test: Part 1. *Materials and Structures, 36*, 265-274.

RILEM TC 162-TDF. (2003b). Test and design methods for steel fibre reinforced concrete. Round-robin analysis of the RILEM TC 162-TDF beam-bending test: Part 1 - Test method evaluation. *Materials and Structures, 36*, 609-620.

RILEM TC 162-TDF. (2003c). Test and design methods for steel fibre reinforced concrete: σ-ε design method. *Materials and Structures, 36*, 560-567.

RILEM TC50. (1985). Determination of Fracture Energy of Mortar and Concrete by means of three-point bend tests on notched beams. *Materials and Structures, 18*(106), 285-290.

Rokugo, K., Iwasa, M., Suzuki, K., & Koyanagi, W. (1989). Testing methods to determine tensile strength strain-softening curve and fracture energy of concrete. In H. Mihashi, H. Takahashi, & F. Wittmann (Eds.), *Fracture toughness and fracture energy: test methods for concrete and rock* (pp. 153-163). Rotterdam: Balkema.

Romualdi, J., & Mandel, J. (1964). Tensile Strength of Concrete Affected by Uniformly Distributed Closeley Spaced Short Length of Wire Reinforcement. *ACI Journal, 61*(6), 657-662.

Rossi, P. (2000). Ultra-High Performance Fibre Reinforced Concrete: an overview. *Proceedings of the International Symposium of Fibre-Reinforced Cocnrete BEFIB' 2000*, 87-100.

Sakai, K. (2013). Sustainability in fib Model Code 2010 and its future perspective. *Structural Concrete. Journal of the fib, DOI: 10.1002/suco.201300012*.

Schlaich, J., Scháfer, K., & Jennewein, M. (1987). Towarsd a Consistent Design of Structural Concrete. *PCI Journal*.

Serna, P. (1984). Una aportación al conocimiento del hormigón de fibras metálicas, en su concepción, propiedades y comportamiento mecánico. *Tesis Doctoral. Universidad Politécnica de Valencia.*

Serna, P., López, J., Camacho, E., Coll, H., & Navarro-Gregori, J. (2014). Footbridge over the ovejas ravine in Alicante: an economical alternative made only of Ultra-High Performance Fibre-Reinforced Concrete (UHPFRC). *Proceedings of the 2nd FRC International workshop (1st ACI-FIB Joint Workshop). Montreal, Canada.*

SETRA-AFGC. (2002). Ultra High Performance Fiber Reinforced Concretes. Interim Reccomendations.

SIA 2052: 2014-12. (n.d.). Béton Fibré Ultra-Performant (BFUP): Matériaus, dimensionnement et exéctuion. Draft.

Soranakom, C., & Mobasher, B. (2007). Closed-Form Moment-Curvature Expressions for Homogenized Fiber-Reinforced Concrete. *ACI Materials Journal, M39*(104).

Soranakom, C., & Mobasher, B. (2008). Correlation of tensile and flexural responses of strain softening and strain hardening cement composites. *Cement & Concrete Composites, 30*(6), 465-477.

Spasojevic, A. (2008, April). Structural Implication of Ultra High Performance Fibre Reinforced Concrete in Bridge Design. *PhD-Thesis, École Polytechnique Fédérale de Lausanne*.

Spasojevic, A., ReDaelli, D., Fernandez-Ruiz, M., & Muttoni, M. (2008). Influence of tensile properties of UHPFRC on size effect in bending. *Proceedings of the 2nd international symposium on ultra-high performance concrete*, (pp. 303-310). Kassel, Germany.

Stang, H. (2000). A fracture mechanics based design approach to FRC. *Proceedings of the Fifth International Symposium on Fibre-Reinforced Concrete (BEFIB 2000)*, 315-324.

Stang, H., & Olesen, J. (1998). On the interpretation of bending tests on FRC-materials. *Proceedings of the 3rd international conference on fracture mechanics of concrete and concrete structures (FramCOs3)*, (pp. 511-520). Freiburg, Germany.

Steinman, D. (1935). Isteg Steel for Concrete Reinforcement. *ACI Journal Proceedings, 32*(11), 183-194.

Switzerland. (1903). *Provisorische Normen für Prejektierung, Ausführung und Kontrolle von Baute armiertem Beton (EMPA9.*

Tailhan, J., Rossi, P., & Parant, E. (2004, September 20-22). Inverse Numerical Approach to Determine the Uniaxial Tensile Behaviour of a Stress Hardening Cement Composite From its Bending Behaviour. *6th RILEM Symposiium on Fibre-Reinforced Concretes (FRC) - BEFIB 2004*, (pp. 913-924). Varenna, Italy.

Tailhan, J., Rossi, P., & Parant, E. (2012). Tensile and bending behaviour of a strain hardening cement-based composite: Experimental and numerical analysis. *Cement & Concrete Composites, 34*(2), 166-171.

Tailhan, J.-L., Rossi, P., & Parant, E. (2004, September 20-22). Inverse Numerical Approach to Determine the Uniaxial Tensile Behaviour of a Stress Hardening Cement Composite From its Bending Behaviour. *6th RILEM Symposiium on Fibre-Reinforced Concretes (FRC) - BEFIB 2004*, 913-924.

Tanaka, Y. e. (2013). The innovation and application of UHPFRC bridges in Japan. *Designing and Building with UHPFRC - State of the Art and Development, ISTE Ltd 2011, chapter 12, pp. 149-187.*

Tanigawa, Y., Mori, H., Yonezawa, T., Izumi, I., & Mitsui, K. (1990). Evaluation of the flowability of high-stregth concrete by L-flow test. *Proceedings of the Annual Conference of the Architectural Institute of Japan.*

Tirimanna, D., & Falbr, J. (2013). FDN modular UHPFRC bridges. *Proceedings of the International Symposium on Ultra-High Performance Fibre Reinforced Concrete, UHPFRC 2013. Marseille, France.*

Ulfkjaer, J., Krenk, S., & Brincker, R. (1995). Analytical Model for Fictitious Crack Propagation in Concrete Beams. *Journal of Engineering Mechanics, 121*(1), 7-15.

Vitek, J., Kalný, M., & Coufal, R. (2015). Cable stayed footbridge made of UHPC. *Proceedings of the 7th Internationaly Symposium on High Performance Fiber Reinforced Cement Composites, HPFRCC7. Stuttgart, Germany.*

Walraven, J. (2009). High performance fiber reinforced concrete: progress in knowledge and design codes. *Materials and Structures, 42*, 1247-1260.

Walraven, J. (2012, March 7-9). On the way to international design recommendations for Ultra High Performance Fibre Reinforced Concrete. *Proceedings of the 3rd International Symposium on UHPC and Nanotechnology for High Performance Construction Materials*, (pp. 51-58). Kassel, Germany.

Wille, K., El-Tawil, S., & Naaman, A. (2014). Properties of strain hardening ultra high performance fiber reinforced concrete (UHP-FRC) under direct tensile loading. *Cement and Concrete Composites, 48*, 53-66.

Wille, K., Kim, D., & Naaman, A. (2011). Strain-hardening UHP-FRC with low fiber contents. *Materials and Structures, 44*, 583-598.

Wittmann, F., Rokugo, K., Brühwiller, E., Mihashi, H., & Simopnin, P. (1988). Fracture energy and strain softening of concrete as determined by compact tension specimens. *Material and Structures, 21*, 21-32.

Appendix I:
Experimental Programme I

AP.I.1 Experimental programme

Experimental programme described in this appendix was carried out with the main purpose of validating the non-linear hinge model and the inverse analysis methods proposed. Three different types of square cross-section specimens were prepared with a variable depth of 50, 100 and 150 mm. The L/h ratio was constant and equals to 4.5 for all of them.

UHPFRC admixture used is shown in Table AP.I. 1. Compressive strength was obtained from 100-mm cubes. A total of 61 specimens were tested. An average compressive strength of 169.89 MPa with a coefficient of variation of 4.78% was obtained. All specimens were stored at 20ºC and at a relative humidity of 100%. Specimens were tested at one year of its casting in a time period of one week.

Table AP.I. 1 UHPFRC dosage used

	Kg/m^3
Cement 42.5 R/SR	800
Quartz flour	225
Silica Fume	175
Silica Sand 0.8 mm	562
Silica Sand 0.4 mm	302
Sika Viscocrete 225	10
Water	175
Straight steel fibres 13/0.2 mm	160

A total of eight 50 mm and 100 mm and four 150 mm specimens were made. Their size is shown in Figure AP.I. 1. Specimens are summarised in Table AP.I. 2. Cells in red point out those specimens in which macro-crack appeared out of the central one-third. Those cases in which the macro-crack appeared out of the central one-third were not considered.

Table AP.I. 2Specimen naming

Depth (mm)	Number							
	1	2	3	4	5	6	7	8
50	🟩	🟩	🟩	🟩	🟩	🟩	🟥	🟥
100	🟩	🟩	🟩	🟩	🟩	🟩	🟥	🟥
150	🟩	🟩	🟩	🟥	⬜	⬜	⬜	⬜

Three different types of square cross-section specimens were prepared with a variable depth of 50, 100 and 150 mm. The L/h ratio was constant and equals to 4.5 for all of them. A 2% in volume of smooth-straight (13/0.20) steel fibres were used in an Ultra-High-Performance cementitious matrix with an average compressive strength of 170 MPa, obtained from 100-m length cubes. A total of eight 50 mm and 100 mm and four 150 mm specimens were made. Those cases in which the macro-crack appeared out of the central one-third were not considered. Specimens are summarised in Table AP.I. 2. Cells in red point out those specimens in which macro-crack appeared out of the central one-third.

The geometry of the specimens and the FPBT set-up are shown in Figure AP.I. 1. On the front side, a LVDT was used to record the displacement at mid span. Three LVDT's were used in the back side of the 100 and 150 mm specimen to obtain the experimental average curvature inside the central one third. In the case of the 50 mm depth specimens, the smaller depth forced to use only two LVDT's. At bottom side two staggered extensometers were used at a distance of 12 mm from the tensile face of the specimen. Setup configuration for 50 mm depth specimens made impossible to place those LVDT's.

FRONT SIDE BACK SIDE BOTTOM SIDE

a) h=50mm

b) h=100mm

c) h=150mm

LVDT
(Deflection at mid-span)

LVDT
(Curvature measurement)

LVDT
(Crack localization measurement)

Units: mm
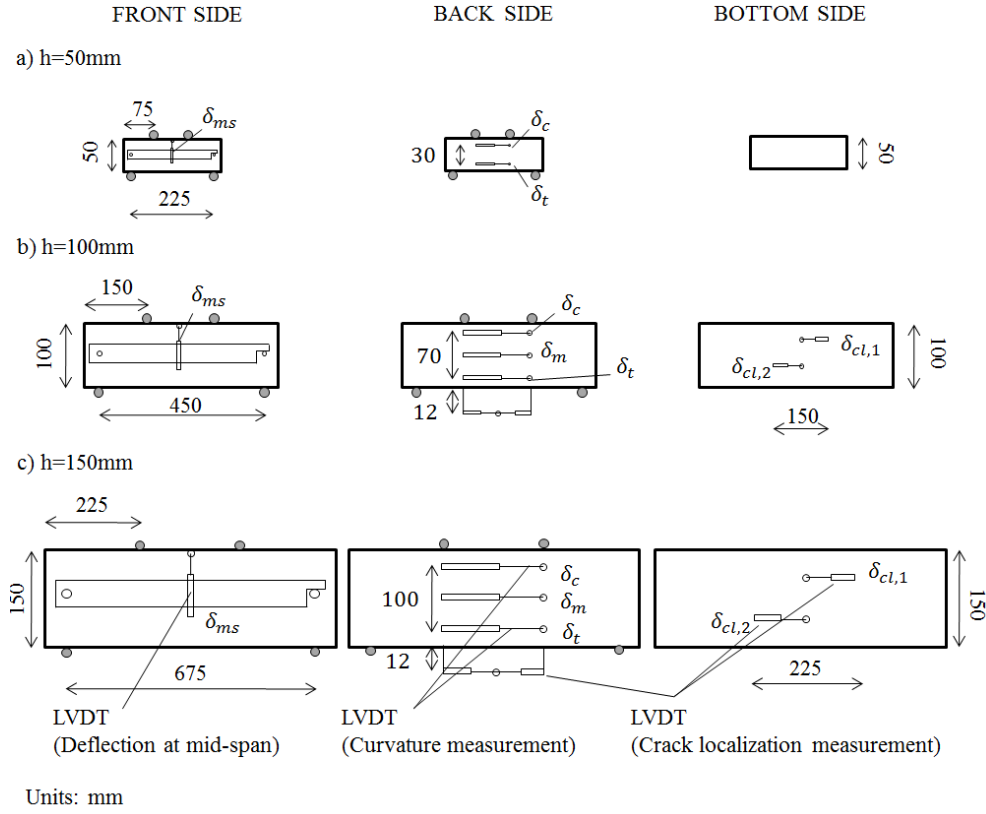
Figure AP.I. 1 Specimen geometries and location of LVDT's used.

For each specimen tested, the experimental load – deflection, load – curvature, load – strain at different layers (δ_c, δ_m, δ_t, δ_{cl})curves are shown, together with the stress-strain behaviour in the hinge obtained from the inverse analysis procedures described in Chapter 4 for a hinge length equal to constant bending moment area.

While the deflection and starin at different layers are direct measurements, average curvature at the central one-third was obtained according to the following criteria:

- Average curvature of 50-mm depth specimens was obtained following Eq. AP.I.1, in which *s* is 75 mm and *d* is 30 mm according to Figure AP.I. 1

$$\phi = \frac{|\delta_c - \delta_t|}{sd}$$

Eq. AP.I.1

- Average curvature of 100-mm and 150-mm depth specimens was obtained by a linear regression of δ_c, δ_m and δ_t LVDT measurements

AP.I.2 Summary of results

Specimens were described by its depth in mm (50, 100 or 150) following by a number. Results are summarised for those specimen in which the crack appeared inside the constant bending moment area. Specimens 50-7, 50-8, 100-7, 100-8, 150-4 were neglected.

Experimental results obtained from each specimen are shown below. For each specimen a data sheet is shown. Each data sheet contains five figures in three different rows. Figure in first row shows the experimental load – deflection curve. Second row shows the load – strain curve at different layers (left) and the load – curvature curve (right). Experimental results and those derived from the I-IA and PBP-IA are shown in this row. Finally, in the third row the inverse analysis results from both I-IA and PBP-IA methods are shown. In case of PBP-IA results, both rough and quadrilinear fitted curves are shown.

50-1
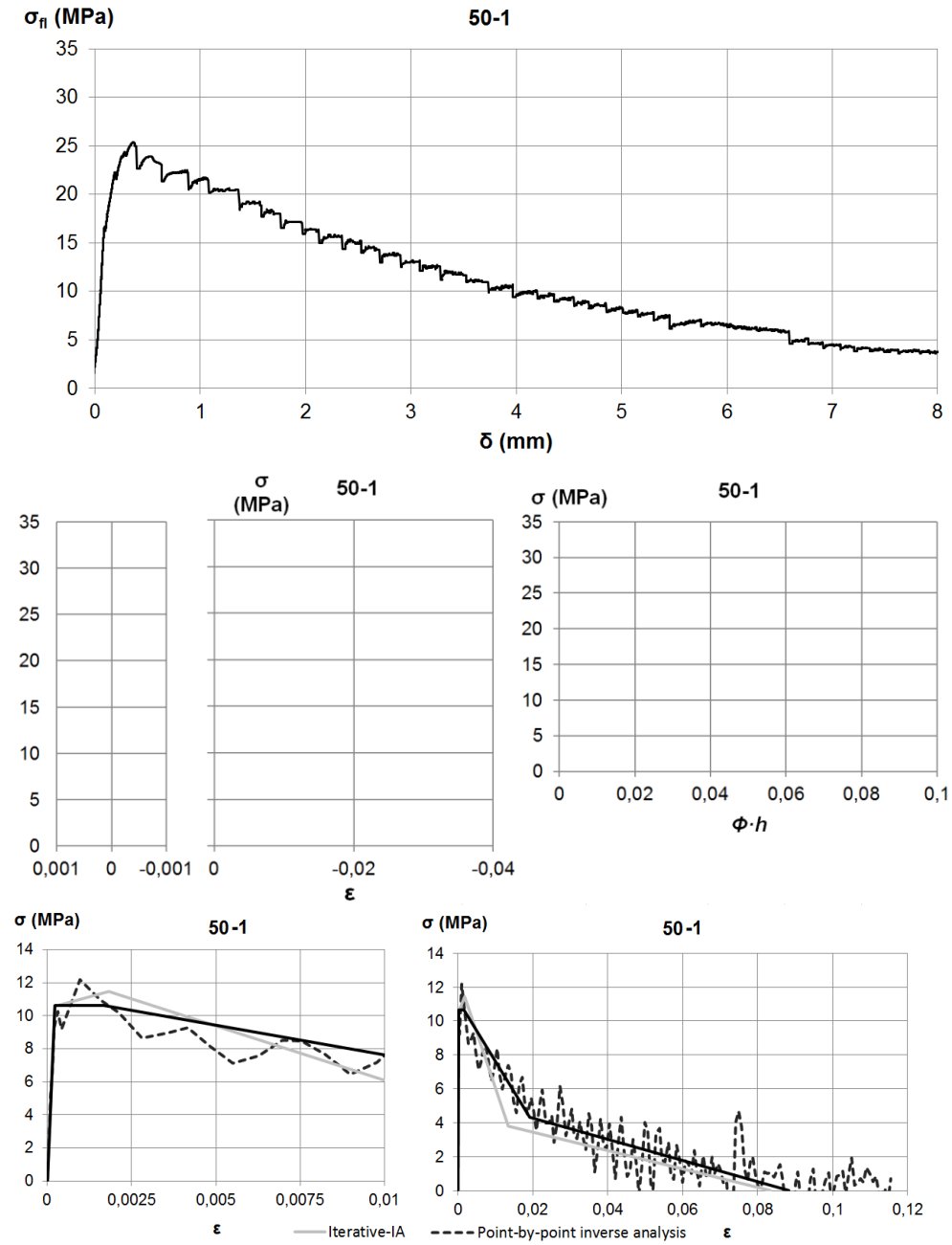
50-2
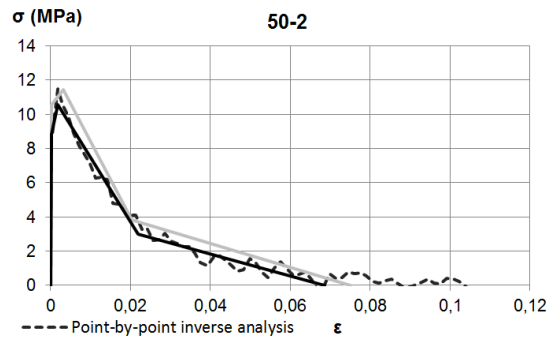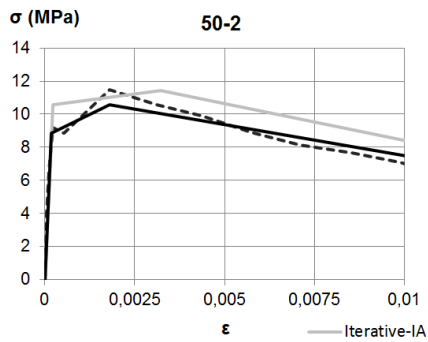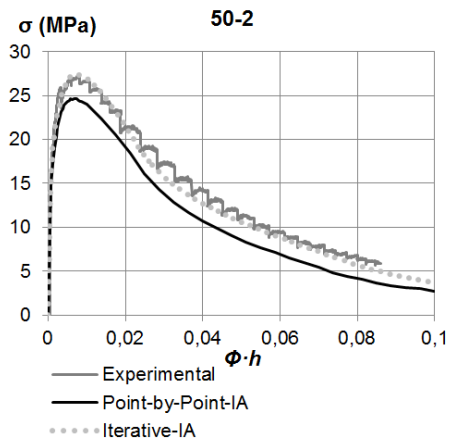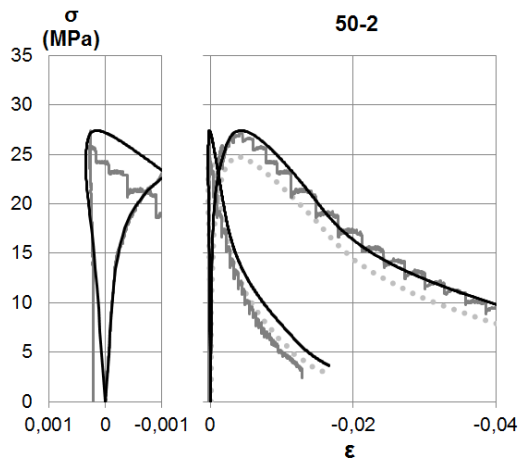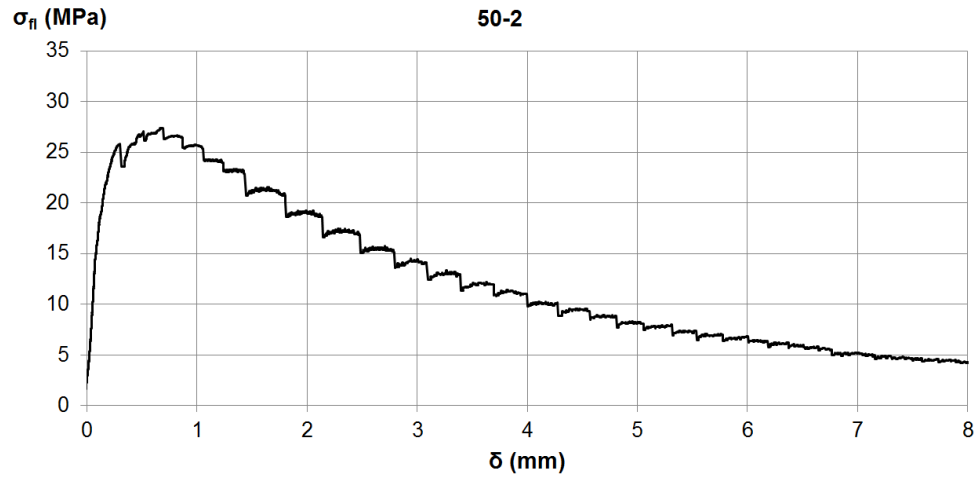
50-3
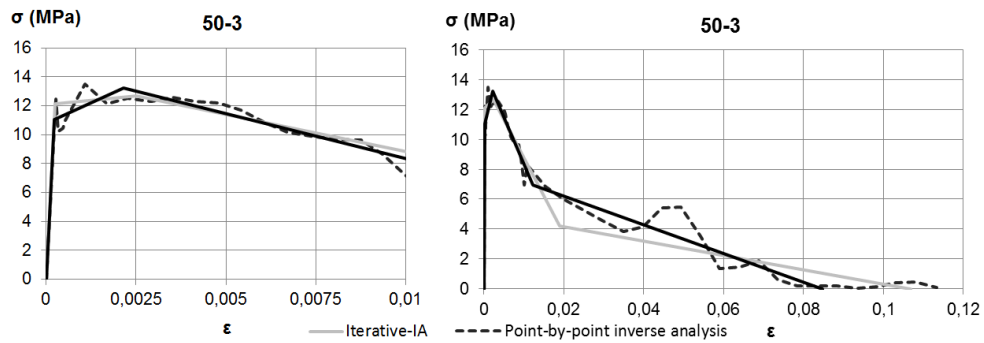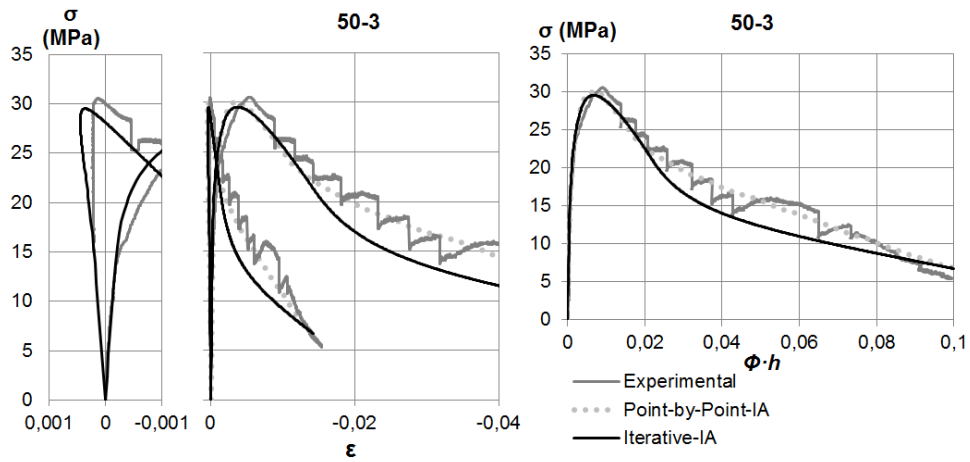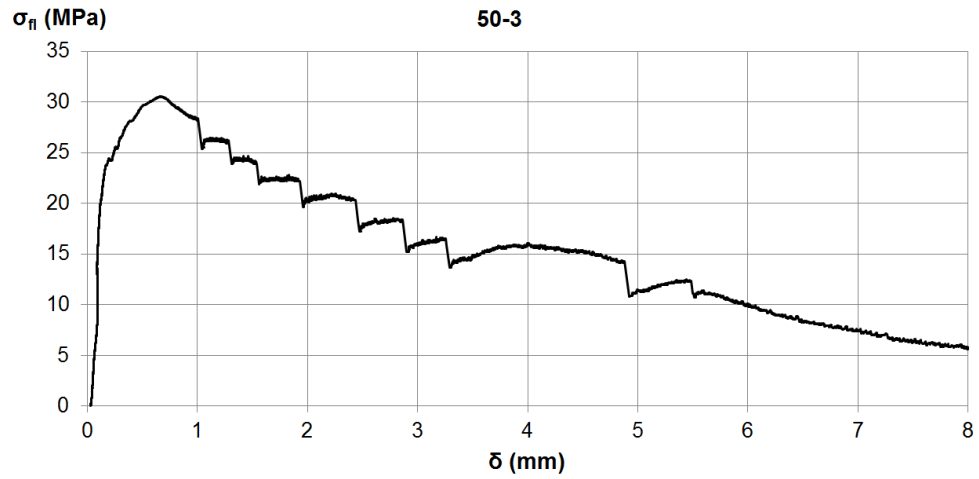
50-4
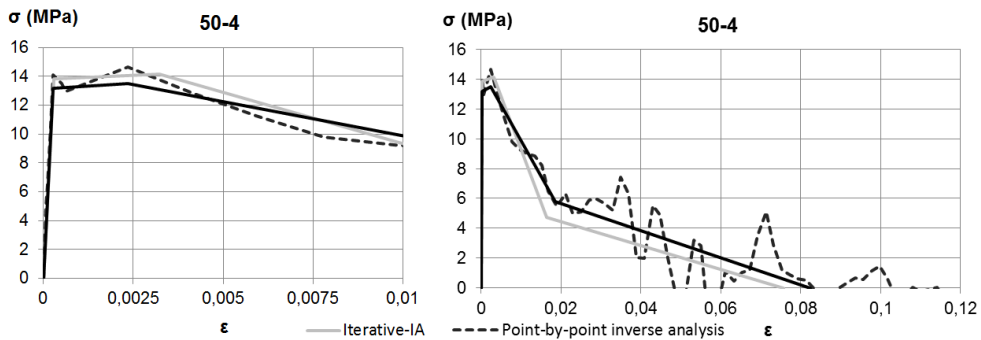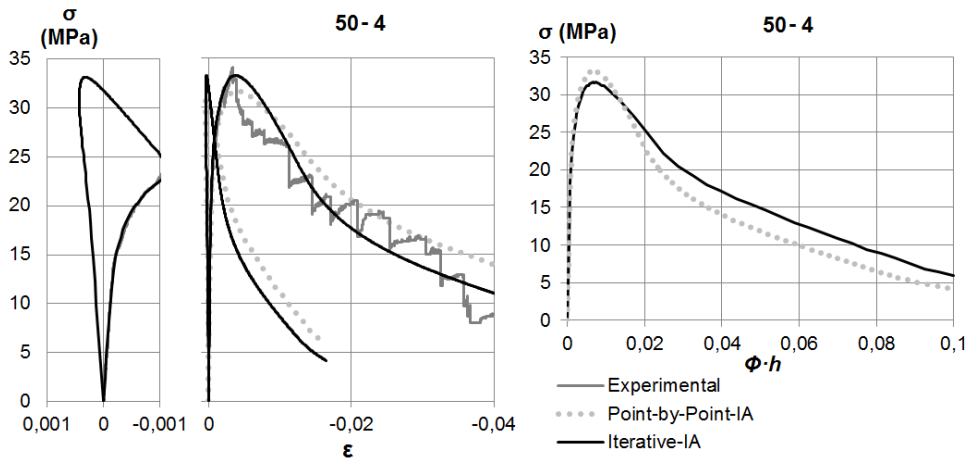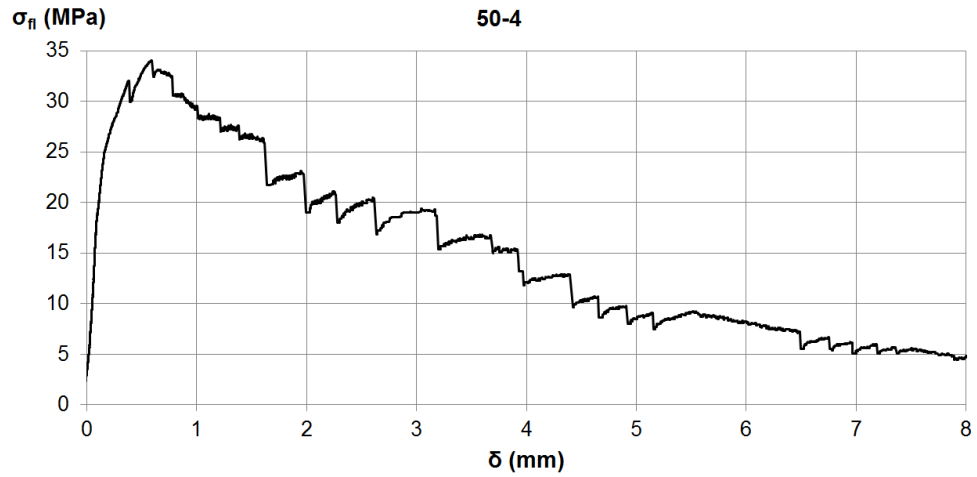
50-5
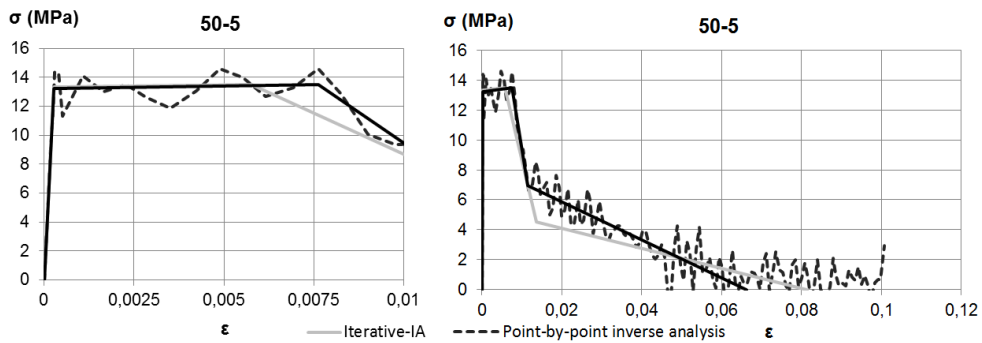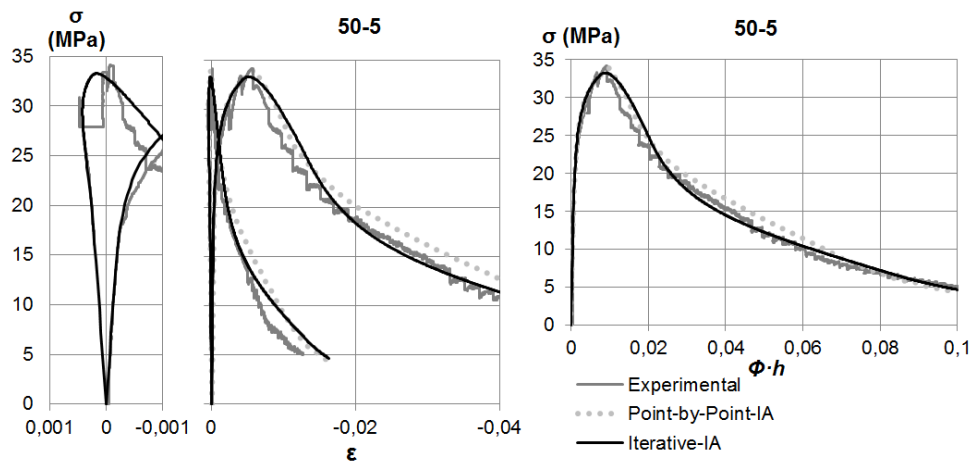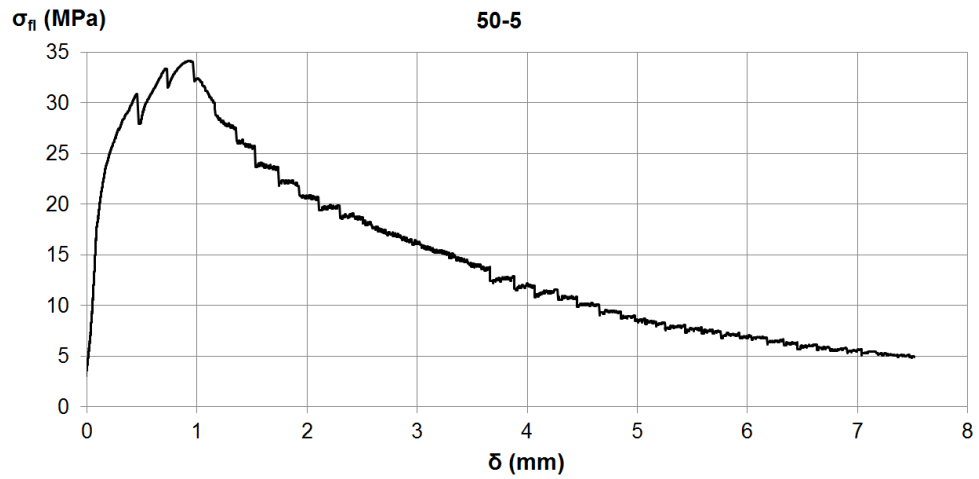
50-6
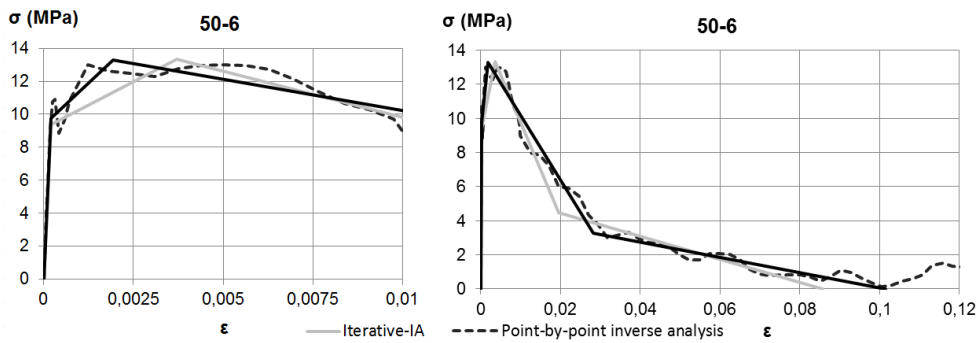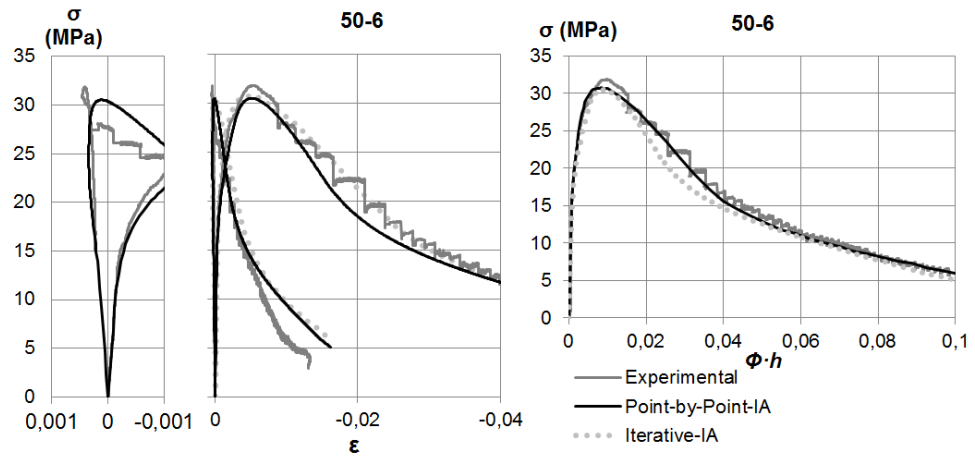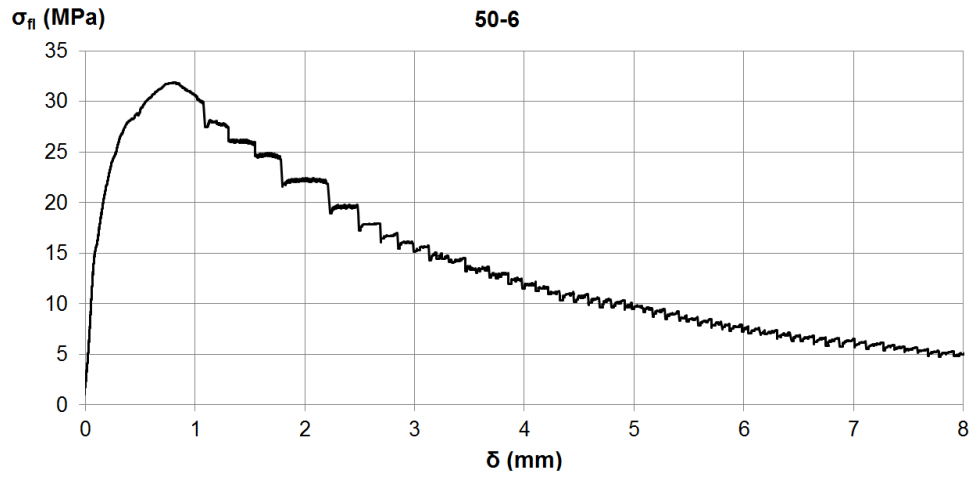
100-1
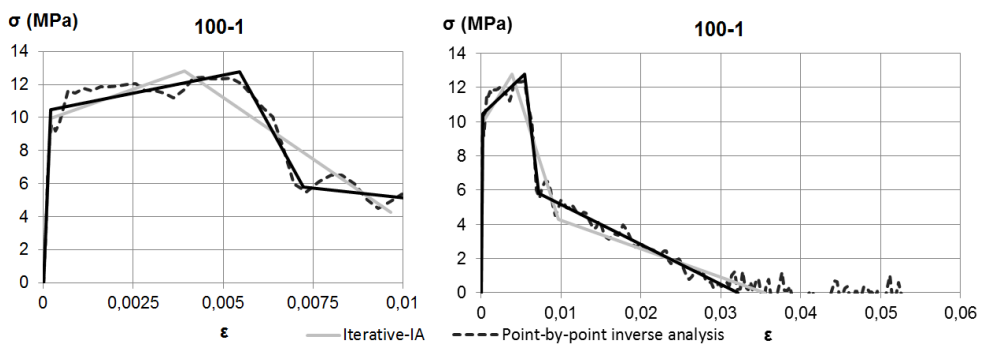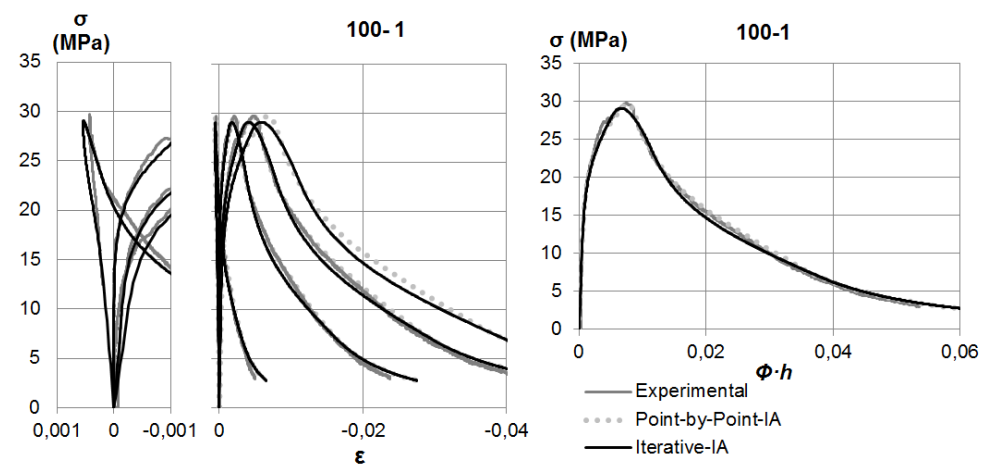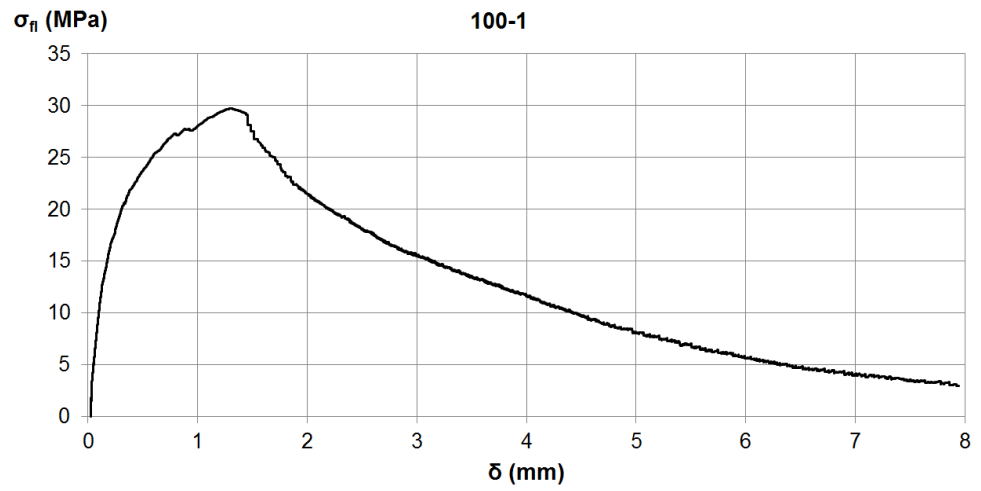
100-2
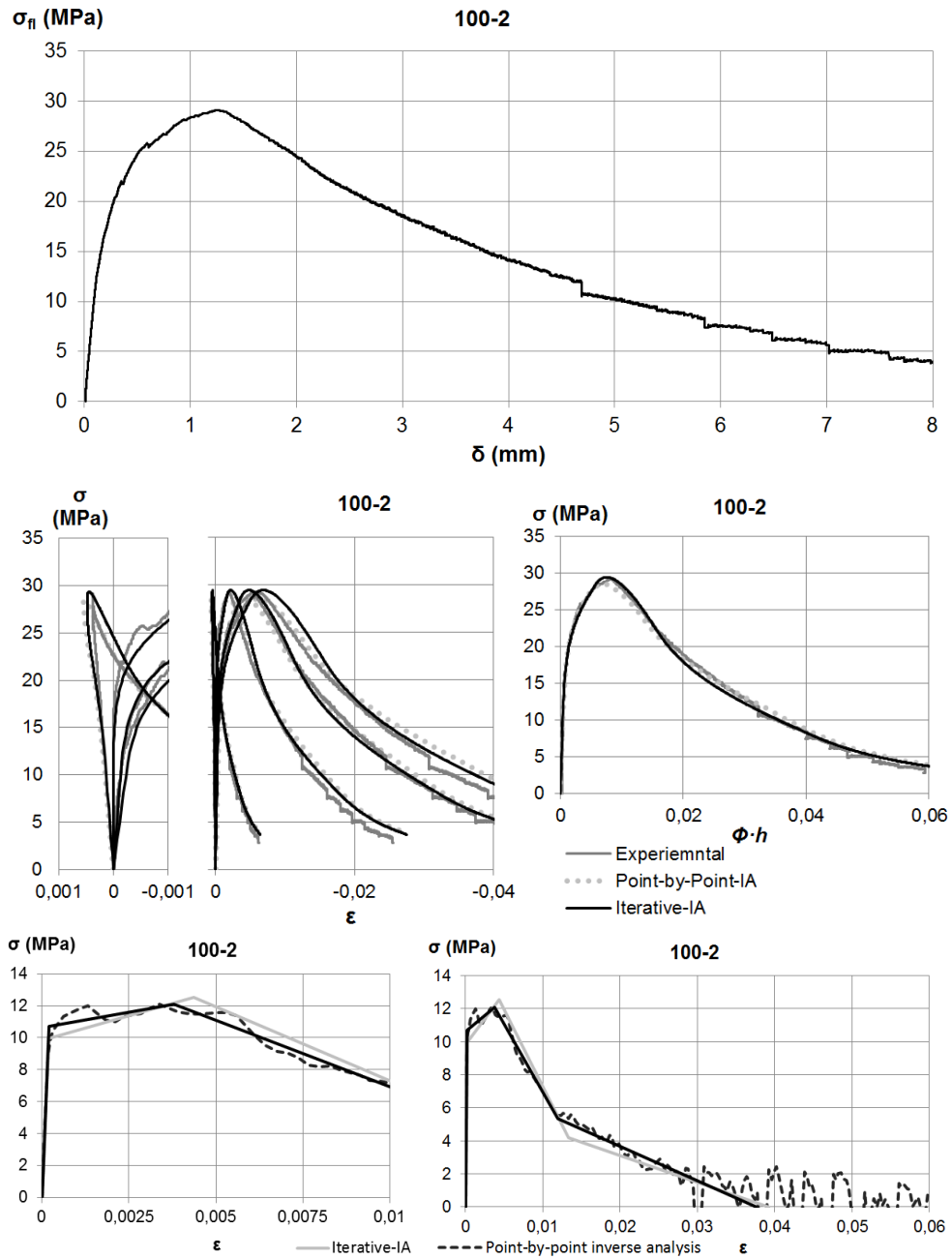
100-3
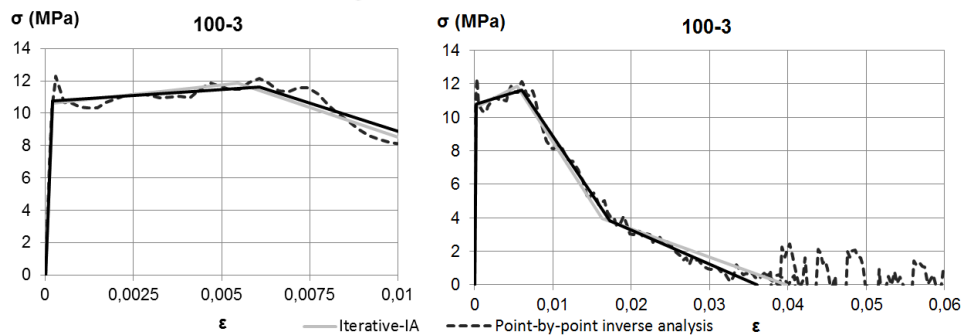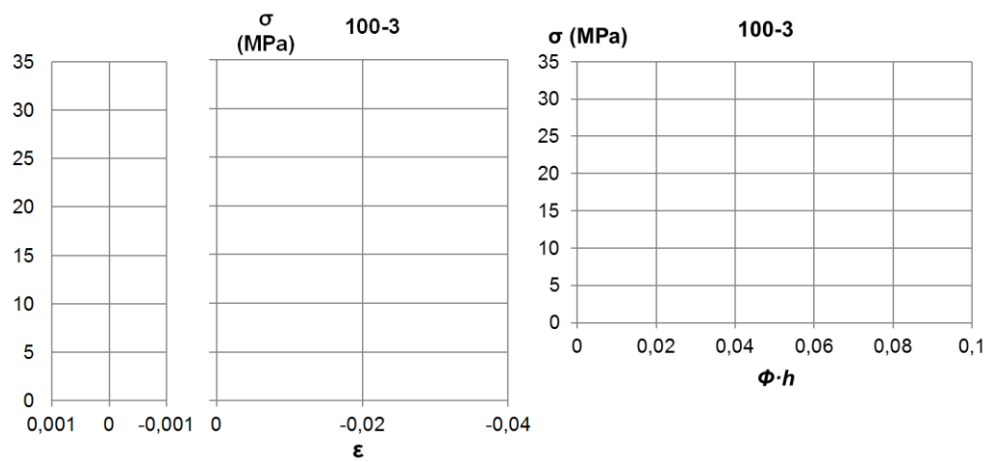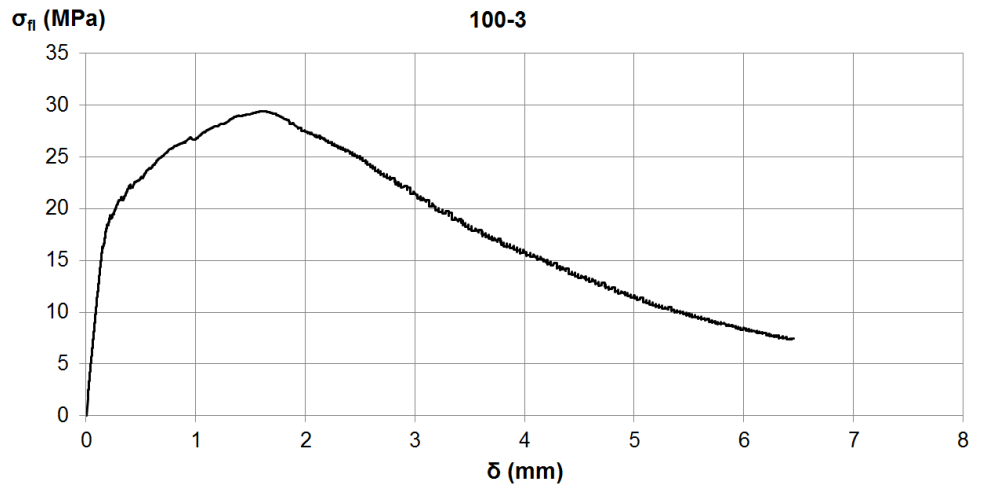
100-4
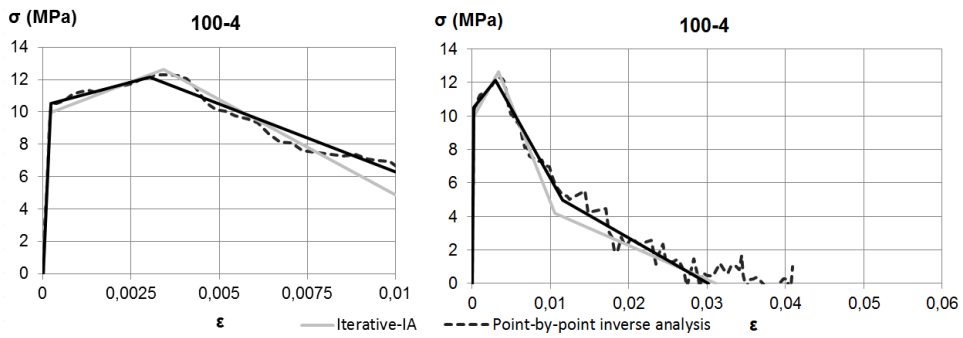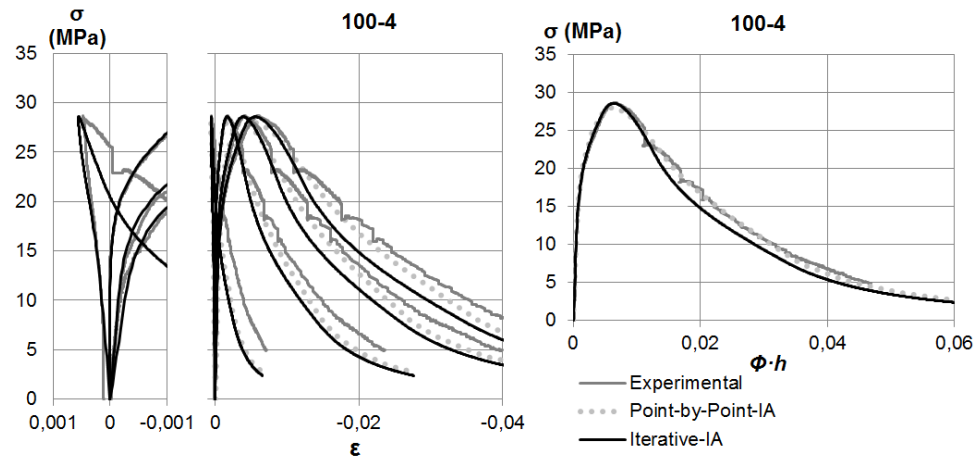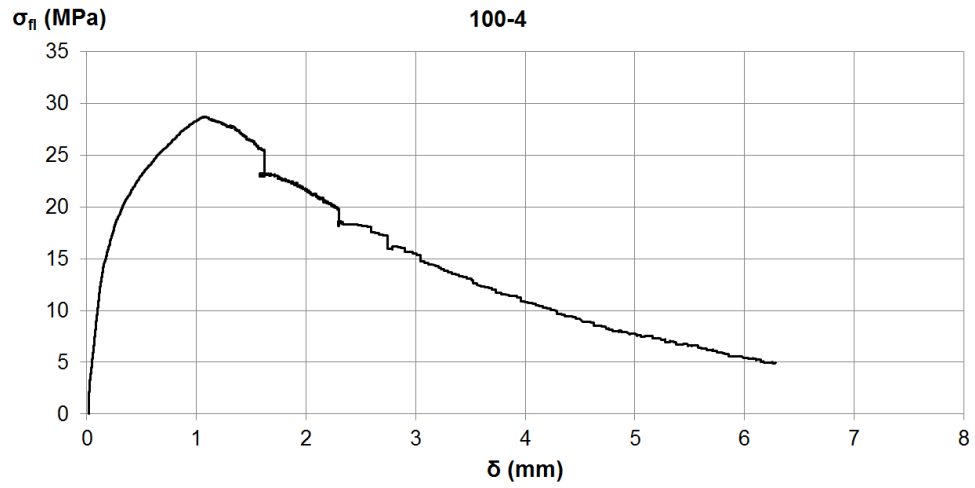
100-5
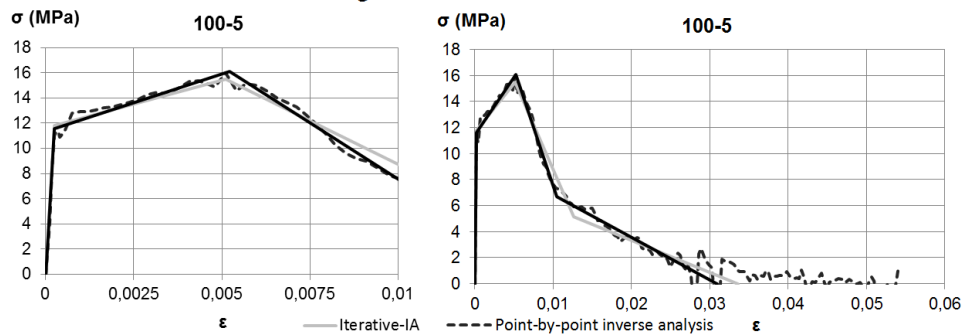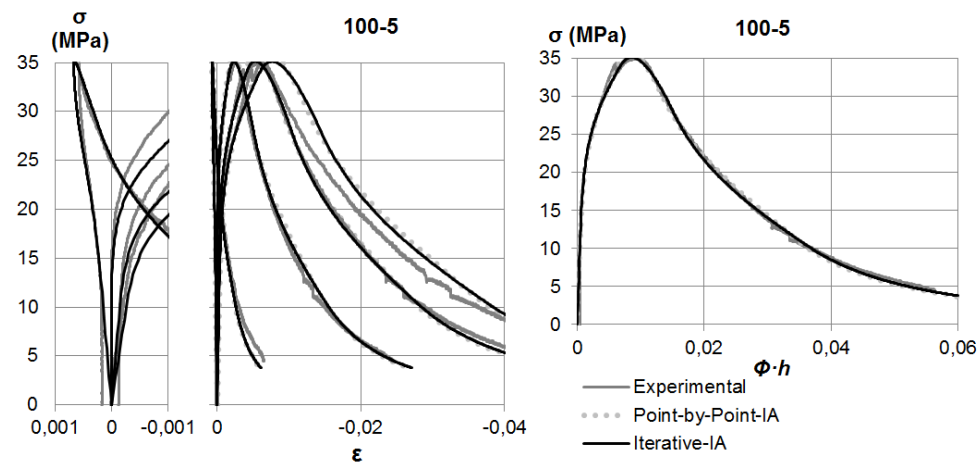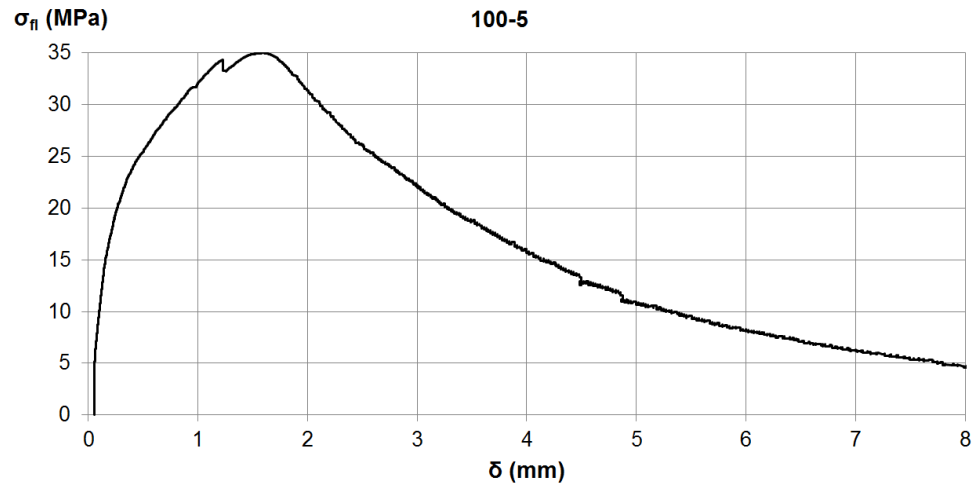
100-6
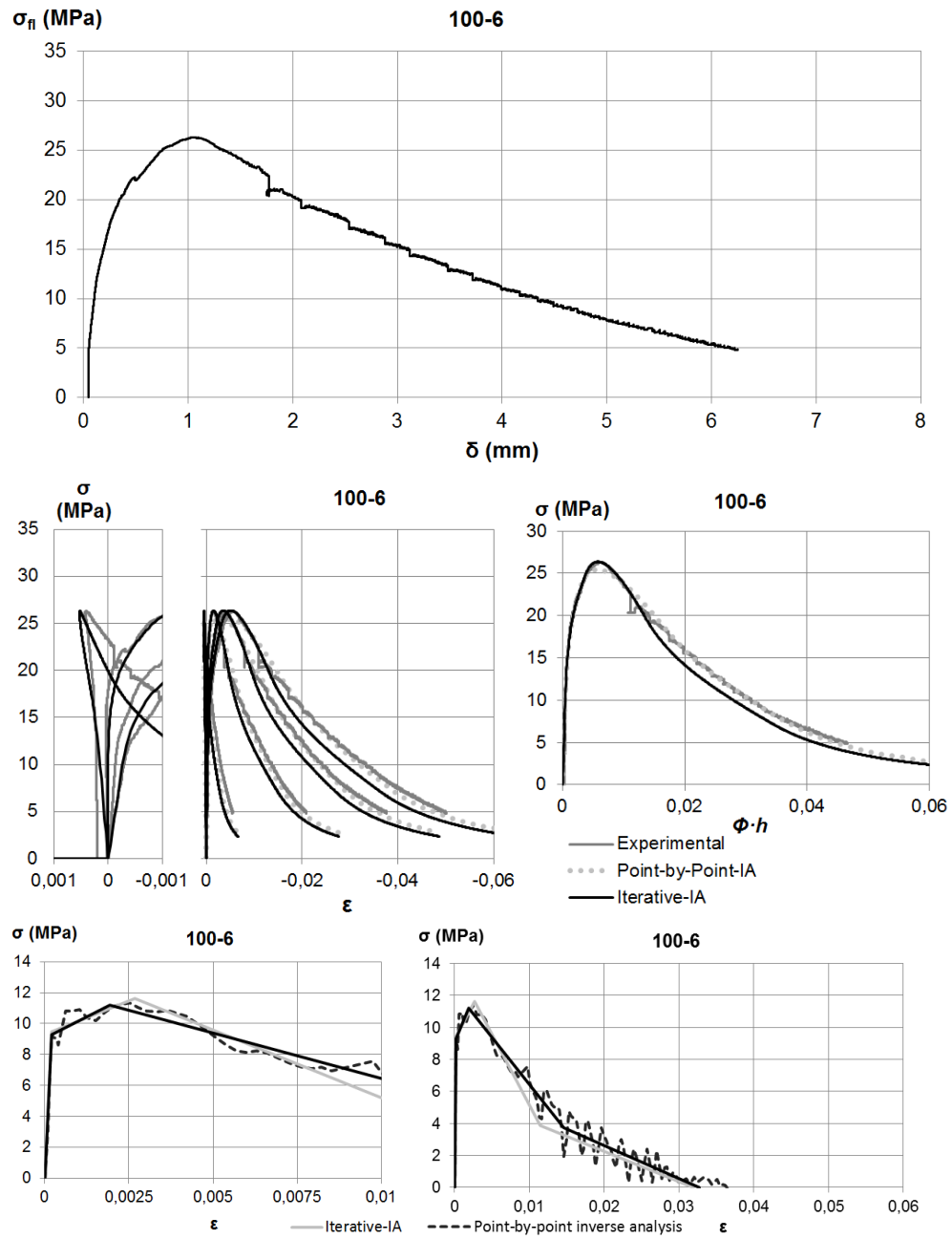
150-1
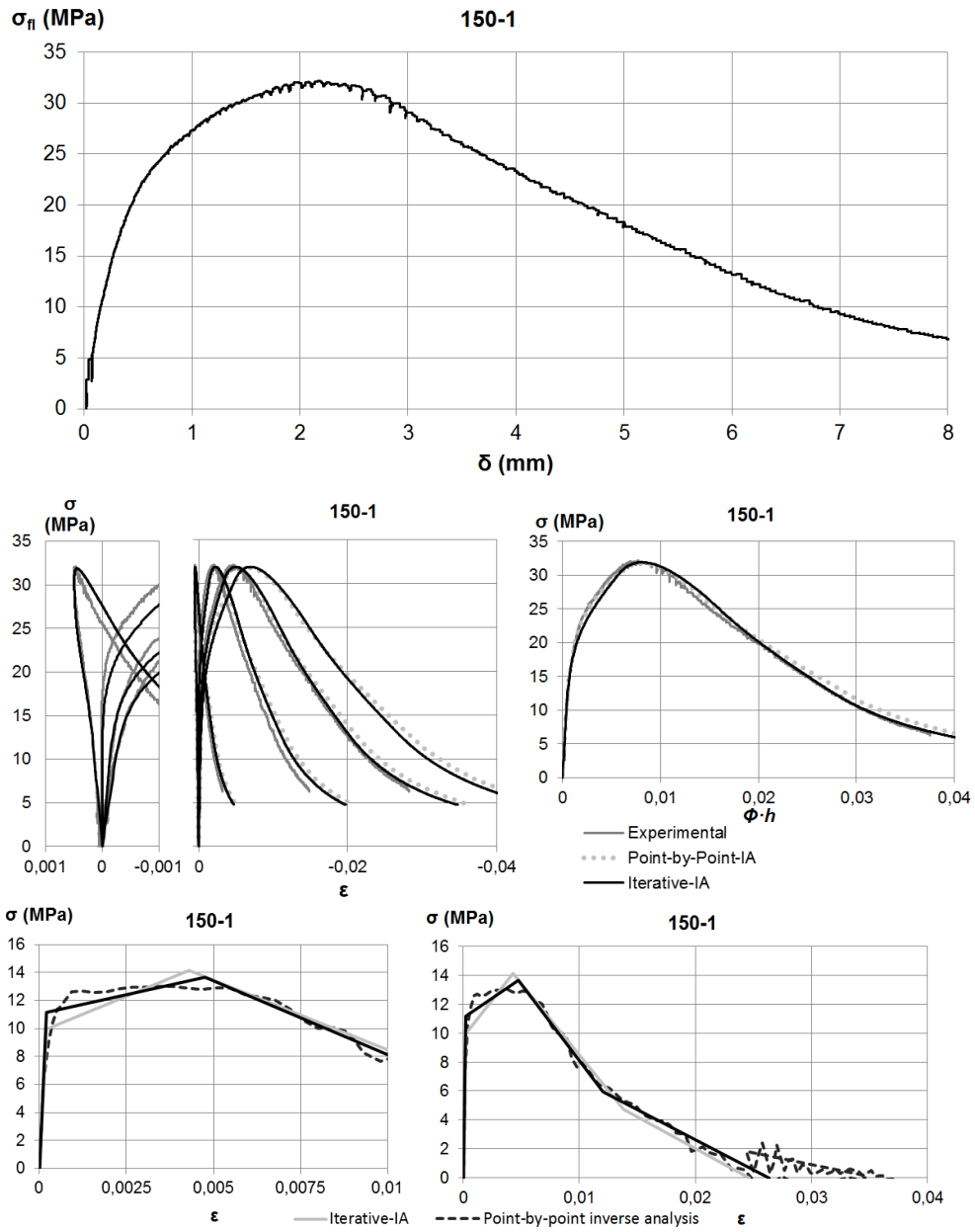
150-2

150-3
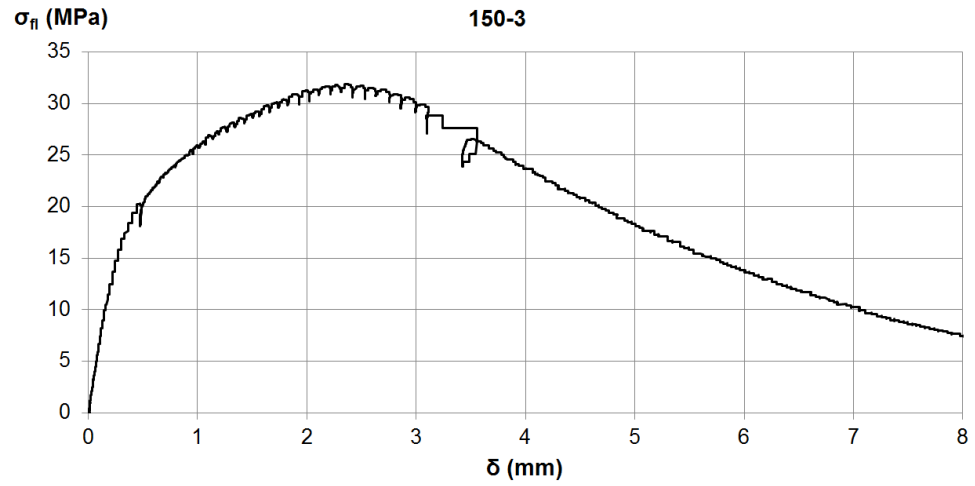
AP.I.2.1. Deviation from experimental results

$$s_d \ (MPa) = \sqrt{\frac{\sum_{i=1}^{n}\left(\sigma_{fl_{exp,i}} - \sigma_{fl_{IA,i}}\right)^2}{n-1}}$$

Table AP.I.3 Curvature deviation values between experimental results and those derived from the inverse analysis used

Specimen height	50 mm						100 mm						150 mm		
Specimen number	1	2	3	4	5	6	1	2	3	4	5	6	1	2	3
s_d 5P-IA (MPa)	-	1.0	2.6	-	1.2	1.9	0.5	0.6	-	1.1	0.5	1.0	0.5	0.6	0.4
s_d PBP-IA (MPa)	-	2.8	1.2	-	1.5	0.9	0.4	0.6	-	0.4	0.6	0.5	0.4	0.5	0.3

Table AP.I.4 Average strain at hinge length deviation values between experimental results and those derived from the inverse analysis used.

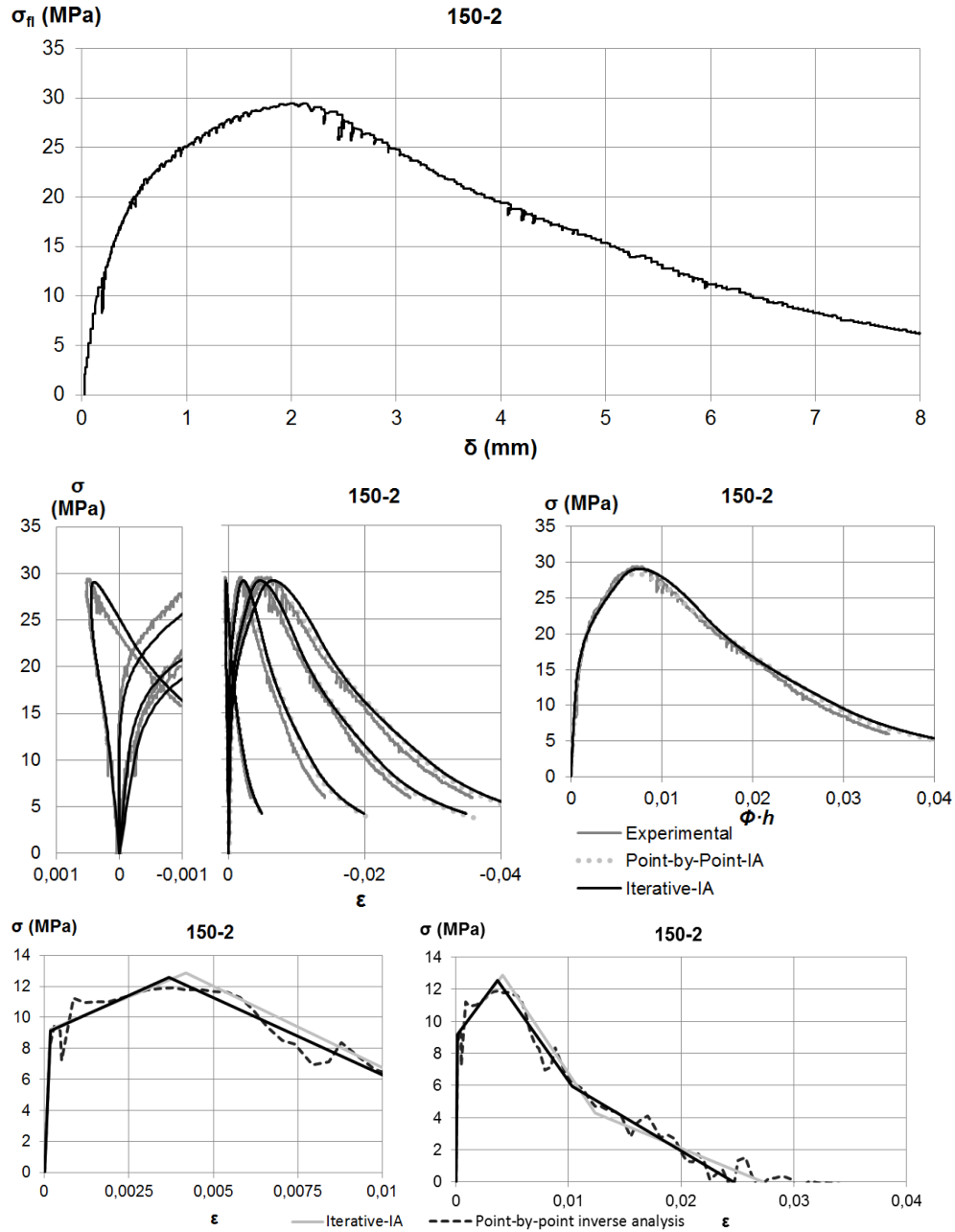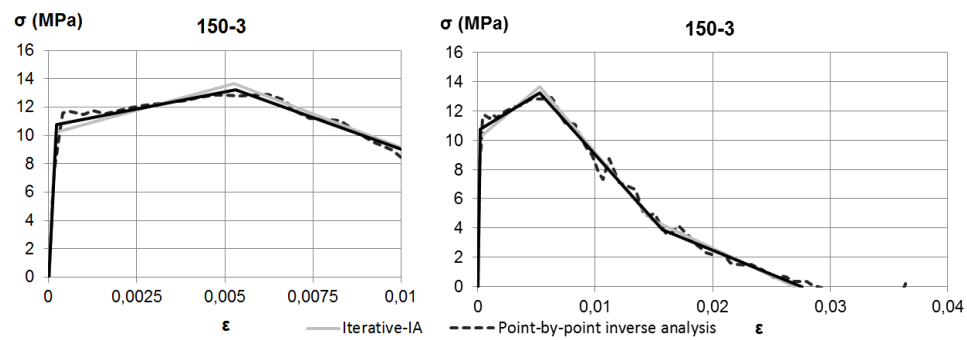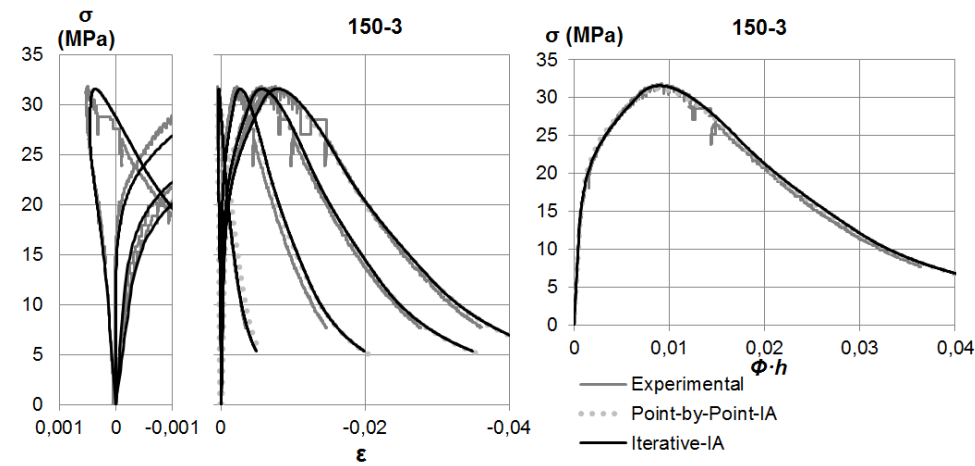|	s_d (MPa)							
	Iterative Inverse Analysis				Point-by-Point inverse analysis			
	ε_c	ε_m	ε_t	ε_{cl}	ε_c	ε_m	ε_t	ε_{cl}
50.1	-		-		-		-	
50.2	1,24		0,65		0,47		1,85	
50.3	1,77		2,90		0,89		1,25	
50.4	2,61		-		1,42		-	
50.5	0,98		1,24		1,29		1,66	
50.6	1,18		1,37		1,47		0,67	
100.1	0,21	0,38	0,45	-	0,19	0,21	0,34	-
100.2	0,27	0,75	0,50	1,16	0,29	0,79	0,62	1,30
100.3	-	0,97	1,12	-	-	0,93	1,50	-
100.4	1,78	1,53	1,72	2,06	1,53	0,92	0,90	1,10
100.5	0,38	0,41	0,53	1,71	0,41	0,48	0,59	1,78
100.6	1,00	0,85	1,01	1,27	0,71	0,42	0,40	0,60
150.1	0,39	0,84	0,52	-	0,49	0,98	0,67	-
150.2	0,27	0,96	0,63	0,90	0,25	0,86	0,51	0,77
150.3	0,19	0,91	0,45	0,64	0,16	0,80	0,38	0,58

AP.I.2.2. Constitutive relationships obtained from PBP-IA

Specimen			E (GPa)	$f_t(MPa)$	$f_t(MPa)$	$\varepsilon_{t,u}$‰	$f_{t,d}(MPa)$	$\varepsilon_{t,d}$‰	$\varepsilon_{t,c}$‰	$w_d(mm)$	$w_c\,(mm)$
Point-by-Point Inverse Analysis	50-mm	1	46	10.63	10.63	1.7	4.34	19.1	88.3	1.37	6.59
		2	47	8.85	10.58	1.8	2.97	22.0	68.5	1.58	5.09
		3	48	11.06	13.23	2.2	6.93	12.2	84.8	0.83	6.31
		4	49	13.19	13.50	2.4	5.80	18.6	82.3	1.29	6.11
		5	48	13.34	13.48	5.8	4.49	11.5	66.2	0.37	4.51
		6	46	9.76	13.30	1.9	3.28	28.3	101.6	2.05	7.59
	100-mm	1	49	10.48	12.77	5.5	5.80	7.2	32.1	0.41	4.21
		2	54	10.69	12.09	3.8	5.32	11.9	37.6	1.36	5.27
		3	54	10.78	11.63	6.1	3.83	17.3	36.1	1.81	4.70
		4	48	10.50	12.15	3.0	4.99	11.6	30.2	1.41	4.27
		5	48	11.59	16.09	5.2	6.71	10.5	30.9	0.97	4.12
		6	47	9.30	11.19	1.9	3.74	14.6	32.8	2.03	4.81
	150-mm	1	49	11.18	13.67	4.8	5.96	12.1	26.3	1.87	5.20
		2	49	9.16	12.56	3.7	5.93	10.4	24.6	1.71	5.03
		3	49	10.77	13.25	5.3	3.91	15.7	27.6	2.57	5.35

Point-by-Point IA results
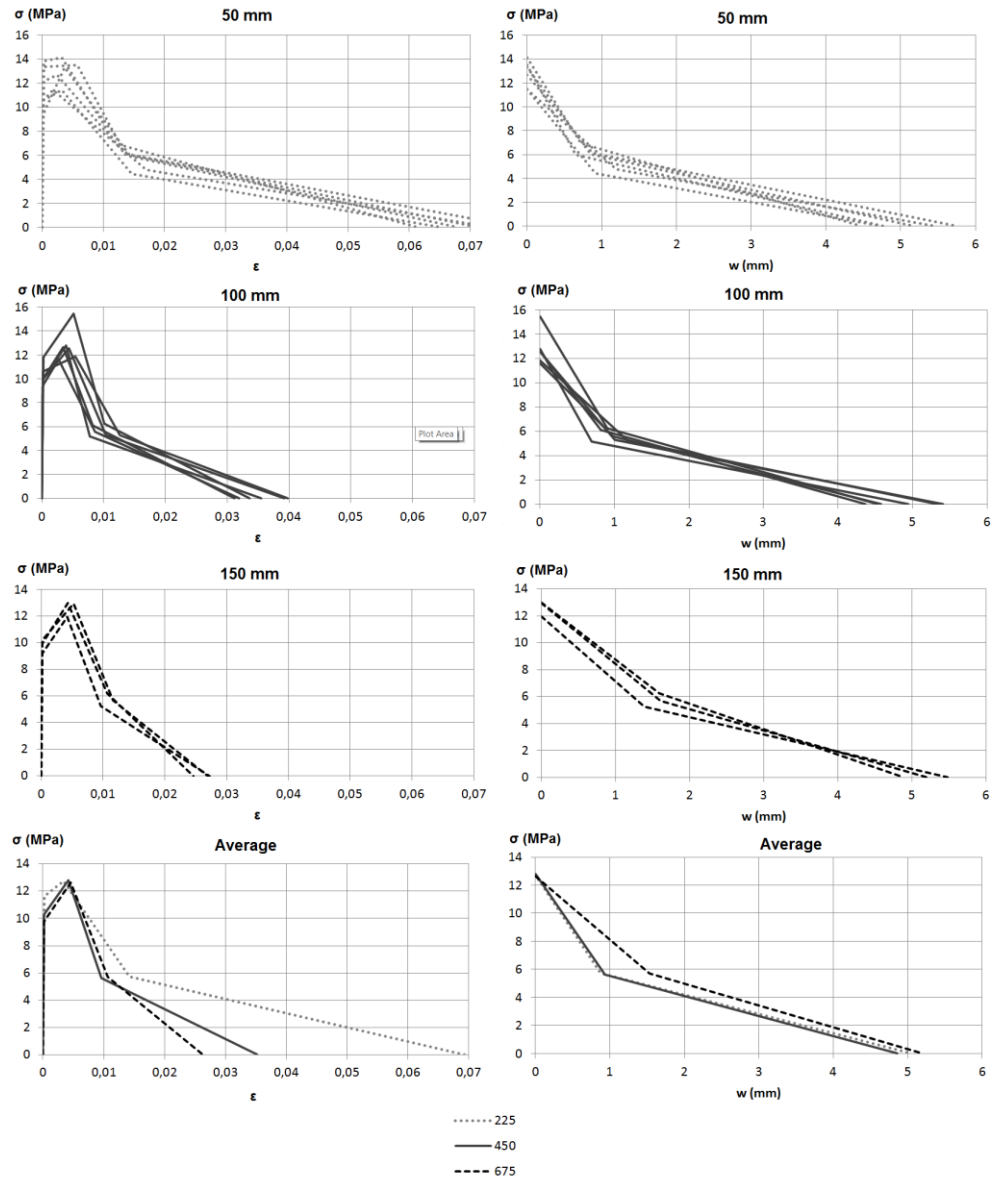
AP.I.2.3. Constitutive relationships obtained from I-IA

Specimen			E (GPa)	$f_t(MPa)$	$f_t(MPa)$	$\varepsilon_{t,u}\text{‰}$	$f_{t,d}(MPa)$	$\varepsilon_{t,d}\text{‰}$	$\varepsilon_{t,c}\text{‰}$	$w_d(mm)$	w_c (mm)
Iterative Inverse Analysis	50-mm	1	46	10.58	11.44	1.8	3.81	13.5	83.4	0.94	6.21
		2	47	10.55	11.45	3.2	3.82	20.4	75.0	1.35	5.48
		3	48	12.13	12.68	2.5	4.23	19.0	106.9	1.31	7.93
		4	49	13.84	14.15	3.2	4.72	16.5	75.7	1.07	5.55
		5	48	13.34	13.48	5.8	4.49	17.7	81.5	0.97	5.79
		6	46	9.39	13.33	3.7	4.44	19.6	85.7	1.26	6.26
	100-mm	1	49	9.96	12.80	3.9	4.27	9.7	35.5	1.00	4.95
		2	54	9.96	12.54	4.4	4.18	13.4	39.2	1.49	5.44
		3	54	10.61	11.86	5.5	3.95	16.2	39.8	1.75	5.35
		4	48	9,96	12.62	3.4	4.21	10.6	31.1	1.21	4.37
		5	48	11.81	15.47	5.1	5.16	12.6	33.6	1.30	4.53
		6	47	9.47	11.62	2.7	3.87	11.5	31.9	1.45	4.58
	150-mm	1	49	9.96	14.13	4.3	4.71	13.8	24.6	2.37	4.93
		2	49	9.22	12.85	4.2	4.28	12.4	27.3	2.06	5.51
		3	49	10.20	13.67	5.3	4.56	14.8	27.0	2.38	5.23

Iterative IA results
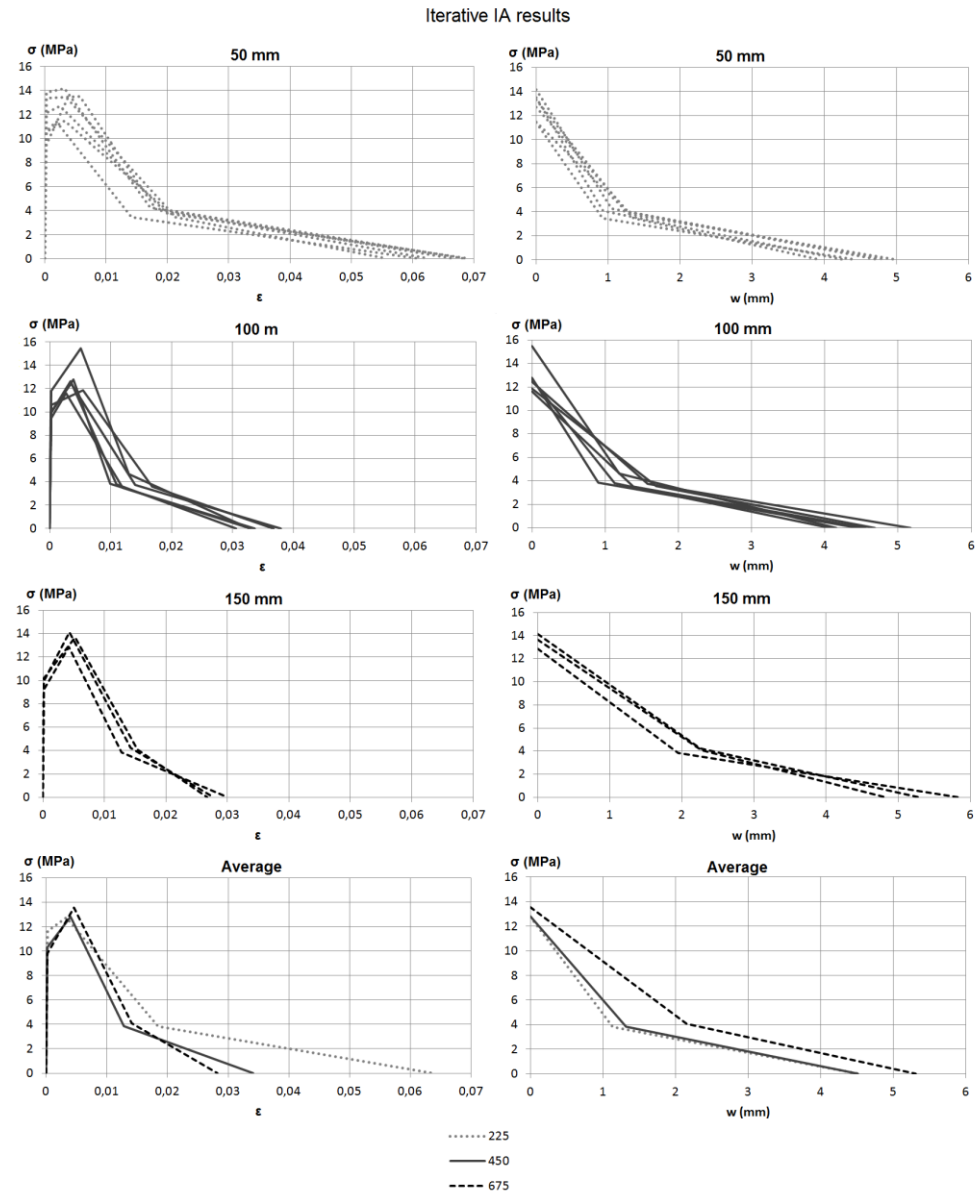
Appendix II:
Experimental Programme II

AP.II.1 Experimental programme

The UHPFRC used had an average compressive strength of 169.89 MPa, obtained from a total of 61 cubes of 100 mm length with a coefficient of variation of 4.78%. A fibre amount of 2% of 13/0.2 steel fibres in volume was used.. Test setup configuration is shown in Figure AP.II.1.

A total of sixteen TPBTs on 100-mm square cross-section specimens were tested. Half of them were tested with a slenderness ratio of 3 while the other half was tested with a slenderness ratio of 4.5. The only experimental measurements taken were the displacement at mid span and its associated load. Specimens were cast in eight different batches, casting two specimens each batch. One specimen from each batch was tested with a slenderness ratio of 3, while the other one was tested with a slenderness ratio of 4.5. Naming used is "D$i\lambda$j", where i is the batch number and j is the slenderness ratio. Specimens were turned 90° degrees from their casting position for testing.

From TBPTs the equivalent strength versus displacement at mid span curves were directly obtained. Measurement of parameter d (crack position) according to Figure 3.28 is shown in Table AP.II.1 for each specimen tested.

Table AP.II.1 Measurement of the parameter d

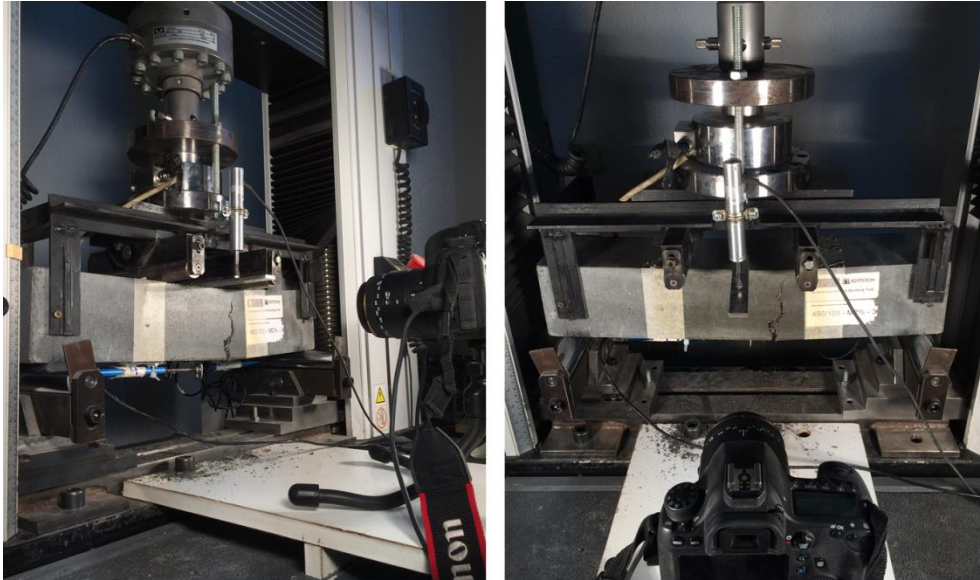| d (mm)	D1	D2	D3	D4	D5	D6	D7	D8
$\lambda3$	30	50	5	35	0	25	5	0
$\lambda4.5$	75	20	15	75	70	35	75	50

Figure AP.II.1 Experimental test setup for a TPBT of a 100-mm square cross-section specimenwith a slenderness ratio of 4.5.

The main objectives of this experimental programme are: (i) validation of the 5P-IA by its comparison to PBP-IA results; (ii) evaluation of the influence on the consideration of the crack's position; (iii) evaluation of the influence of the slenderness ratio on the material behaviour of UHPFRC; (iv) determination of the coefficient of variation for each parameter. Result analysis is made in subsequent subsections.

AP.II.2 Summary of results

For each specimen tested following results are included:

- Experimental load – deflection curve
- Experimental load – deflection curve after crack location correction
- Load – curvature curves for different hinge lengths assumptions according to non-linear hinge model described in Chapter 3
- Stress-strain and stress-crack opening constitutive behaviour obtained from 5P-IA and PBP-IA

In addition, average constitutive behaviour for each hinge length considered and for both inverse analysis procedures is included. Finally, average constitutive behaviour for each hinge length considered and for both inverse analysis procedures is shown. Deviation between these two methods is also presented.

D1λ3
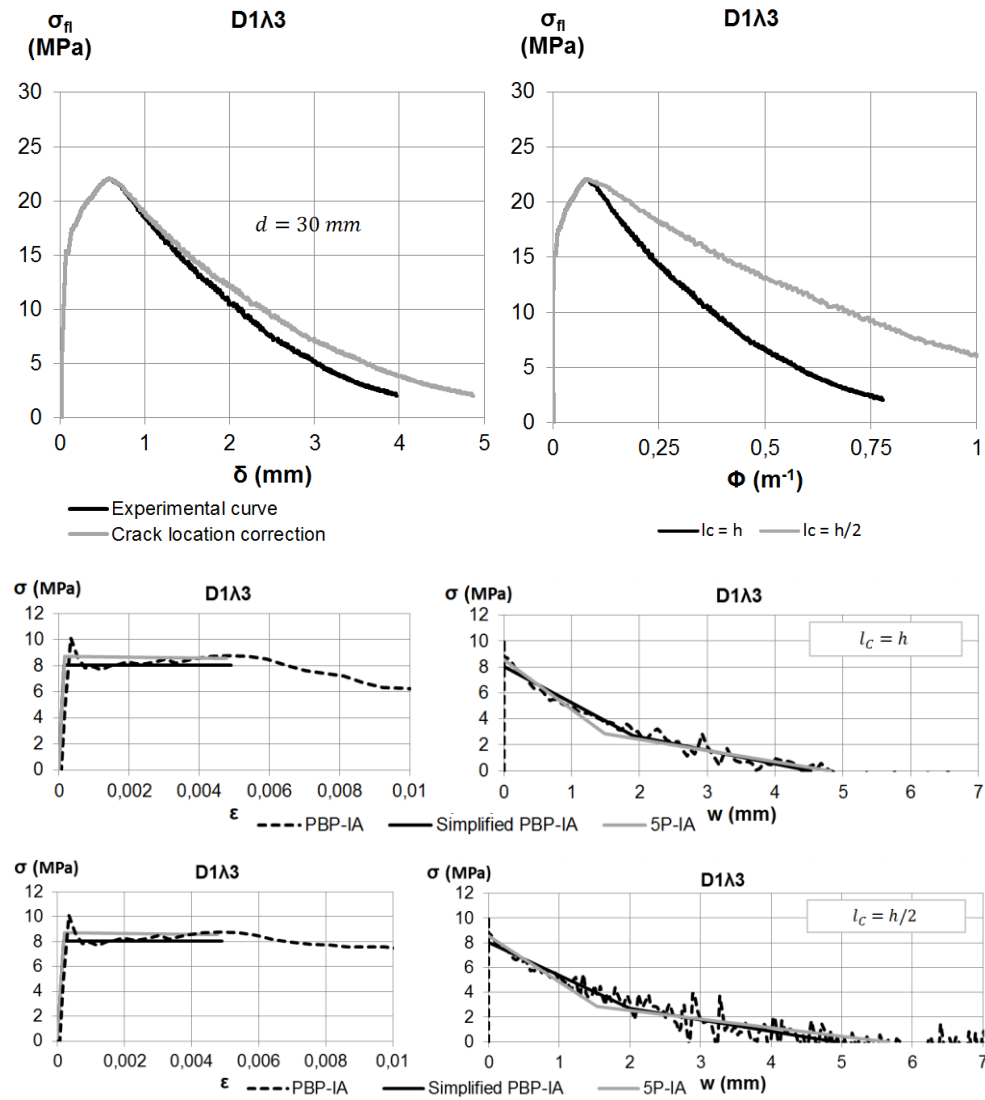
D2λ3
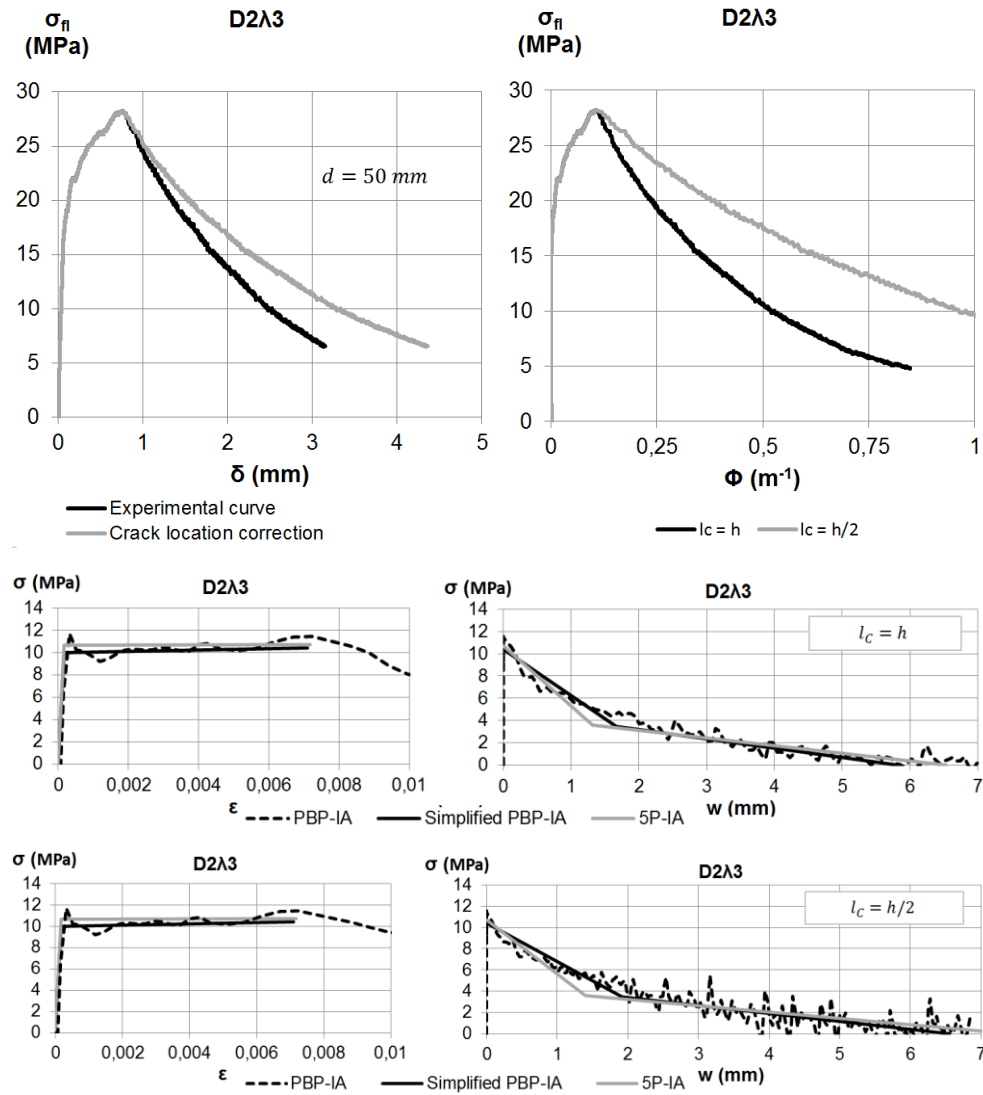
D3λ3
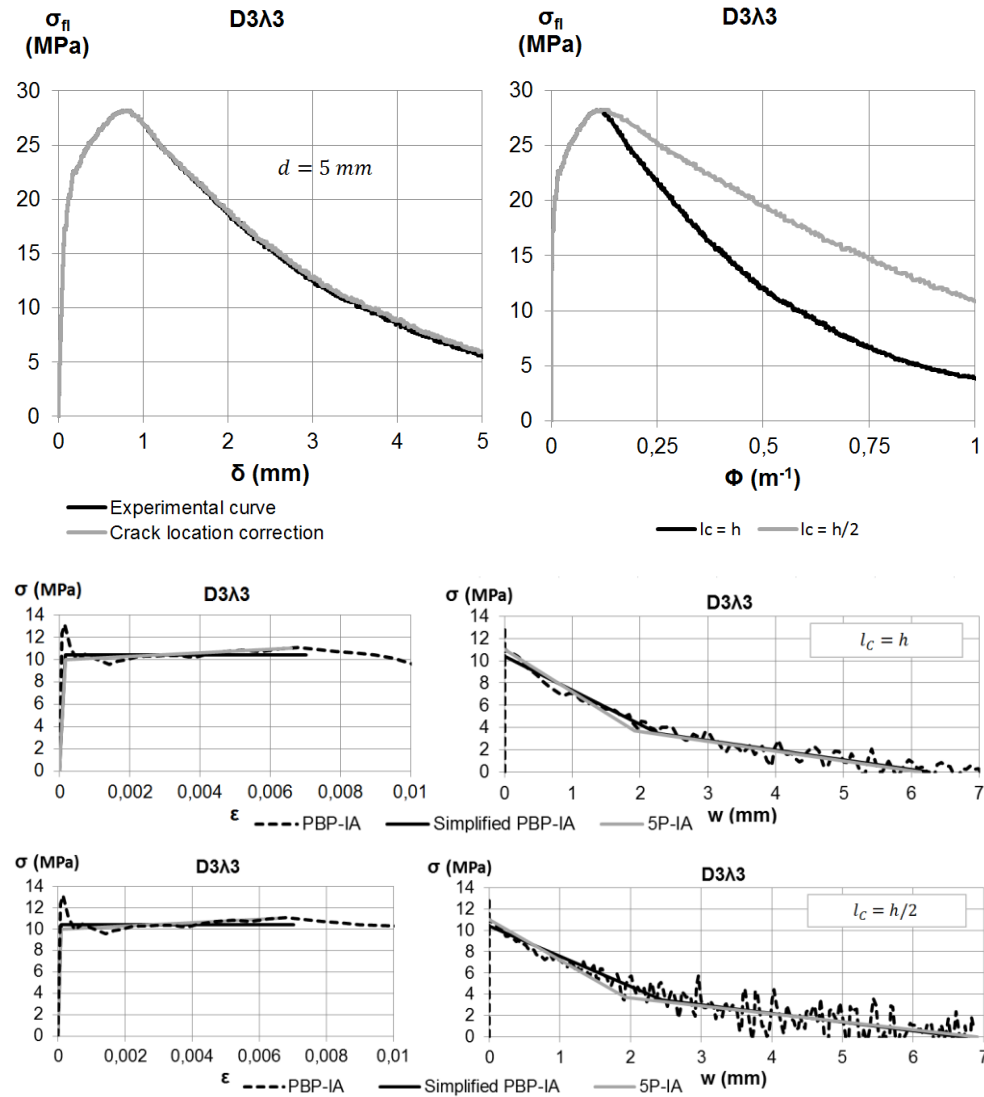
D4λ3
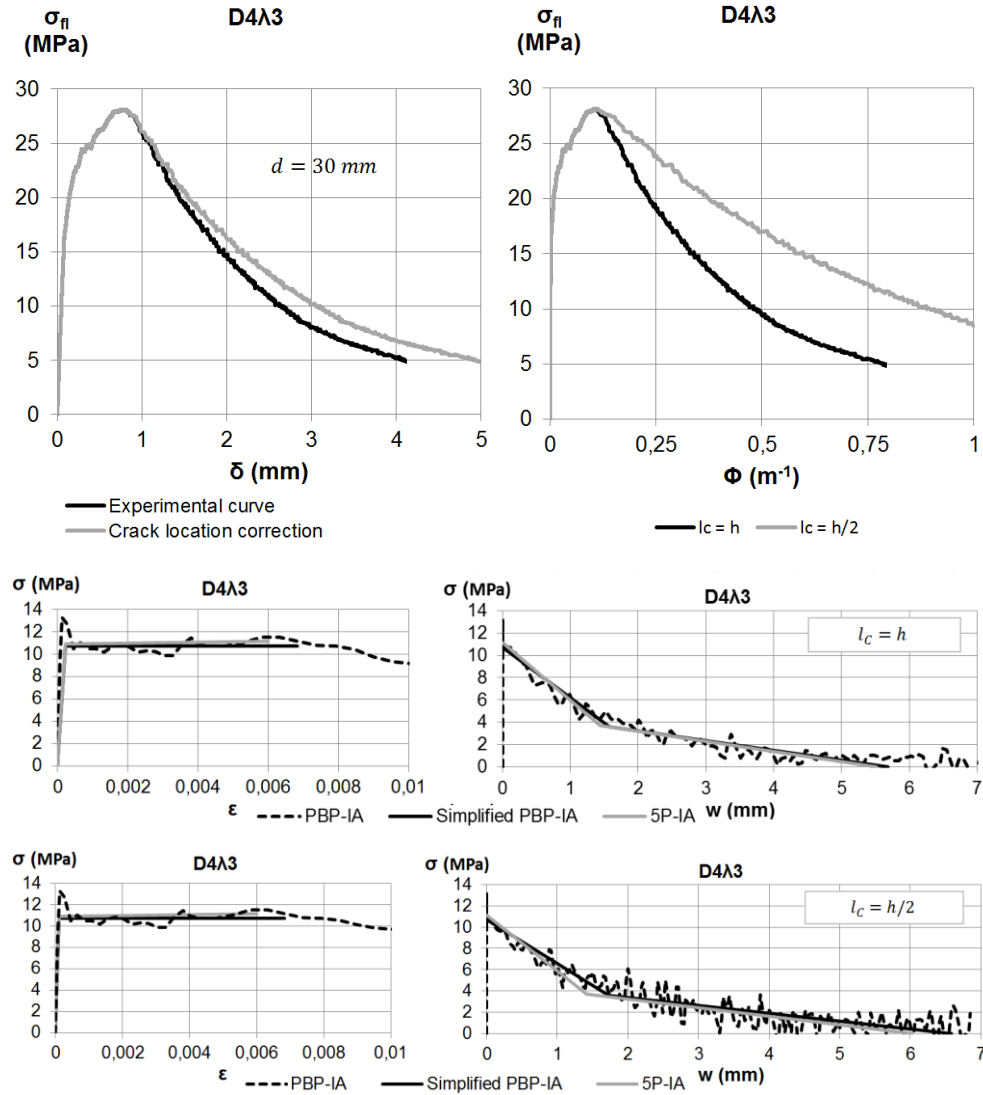
D5λ3
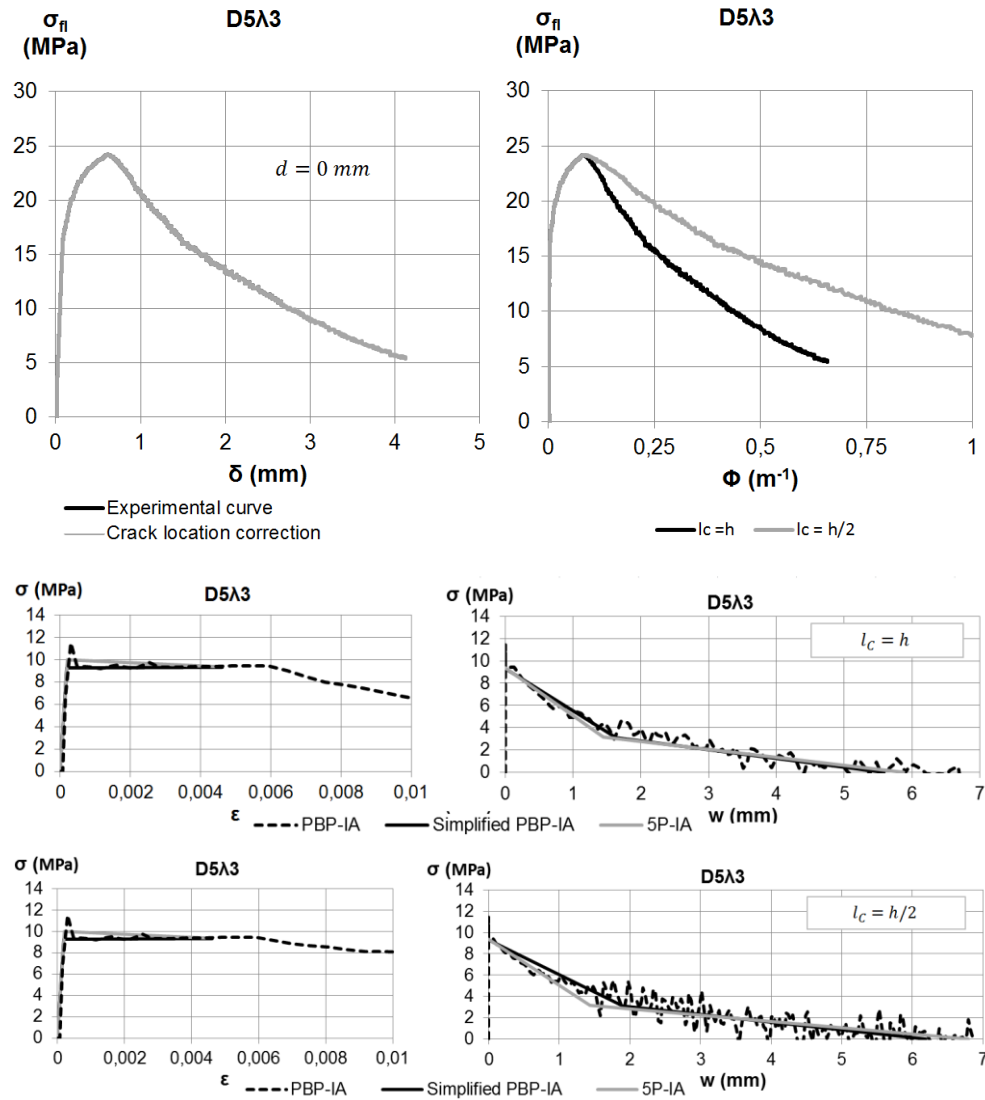
D6λ3
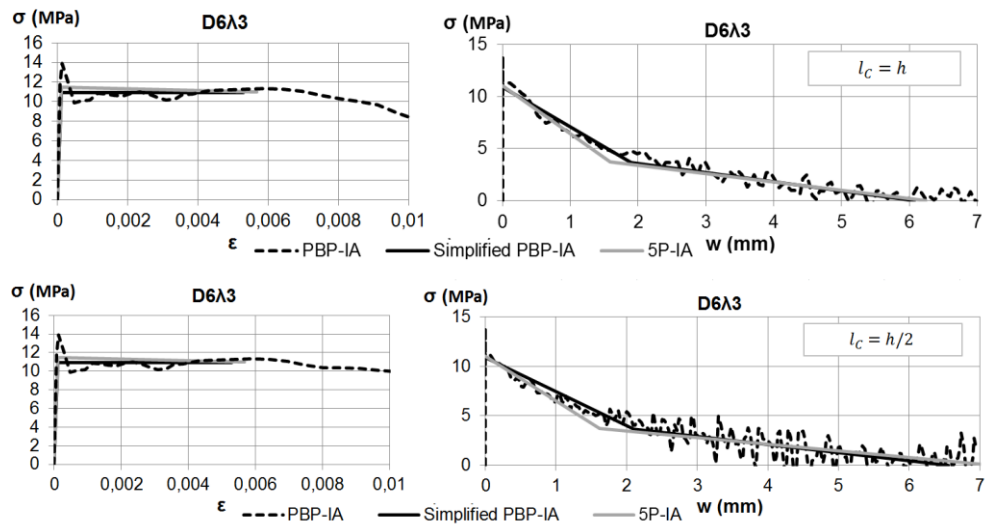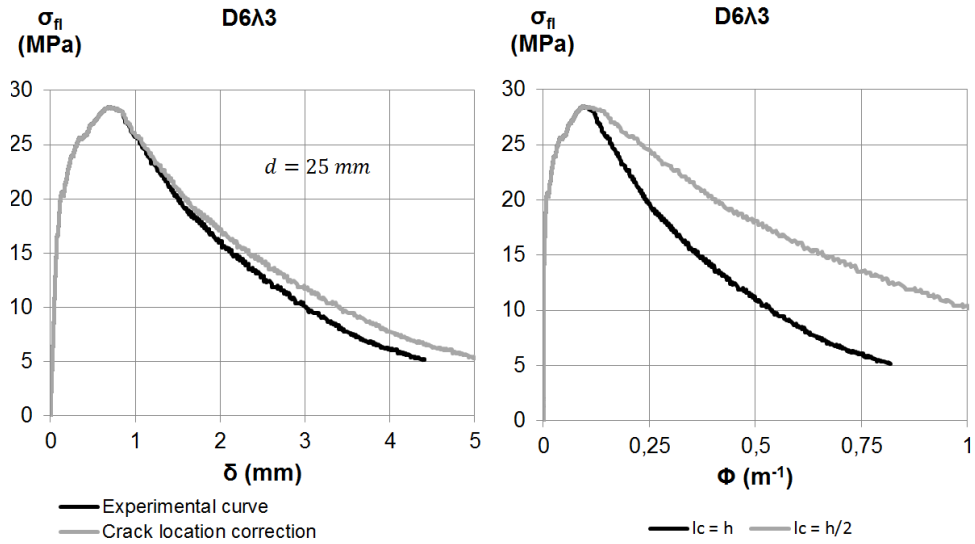
D7λ3
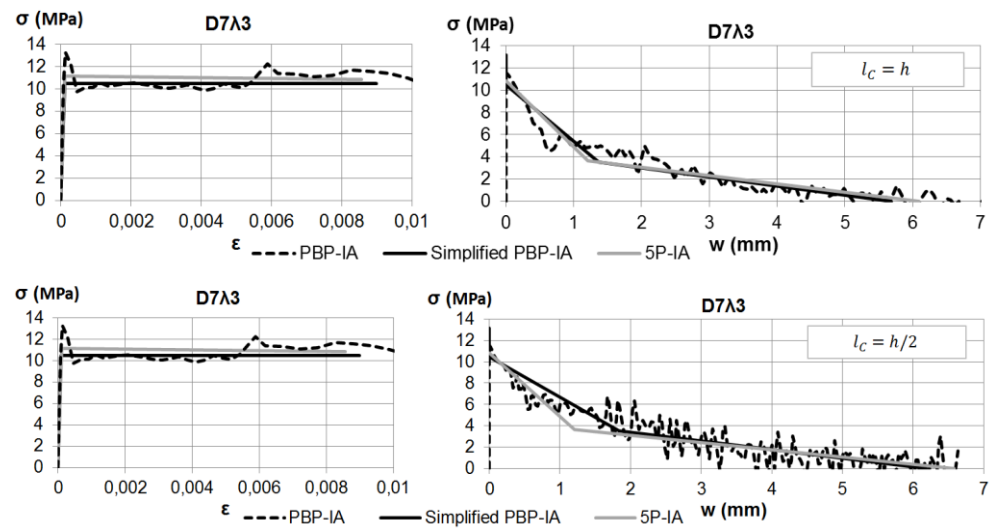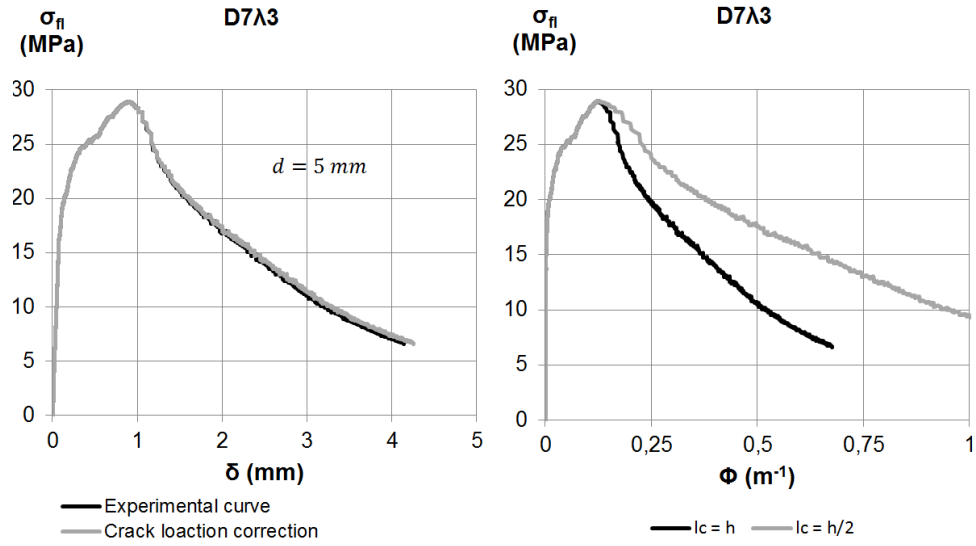
D8λ3
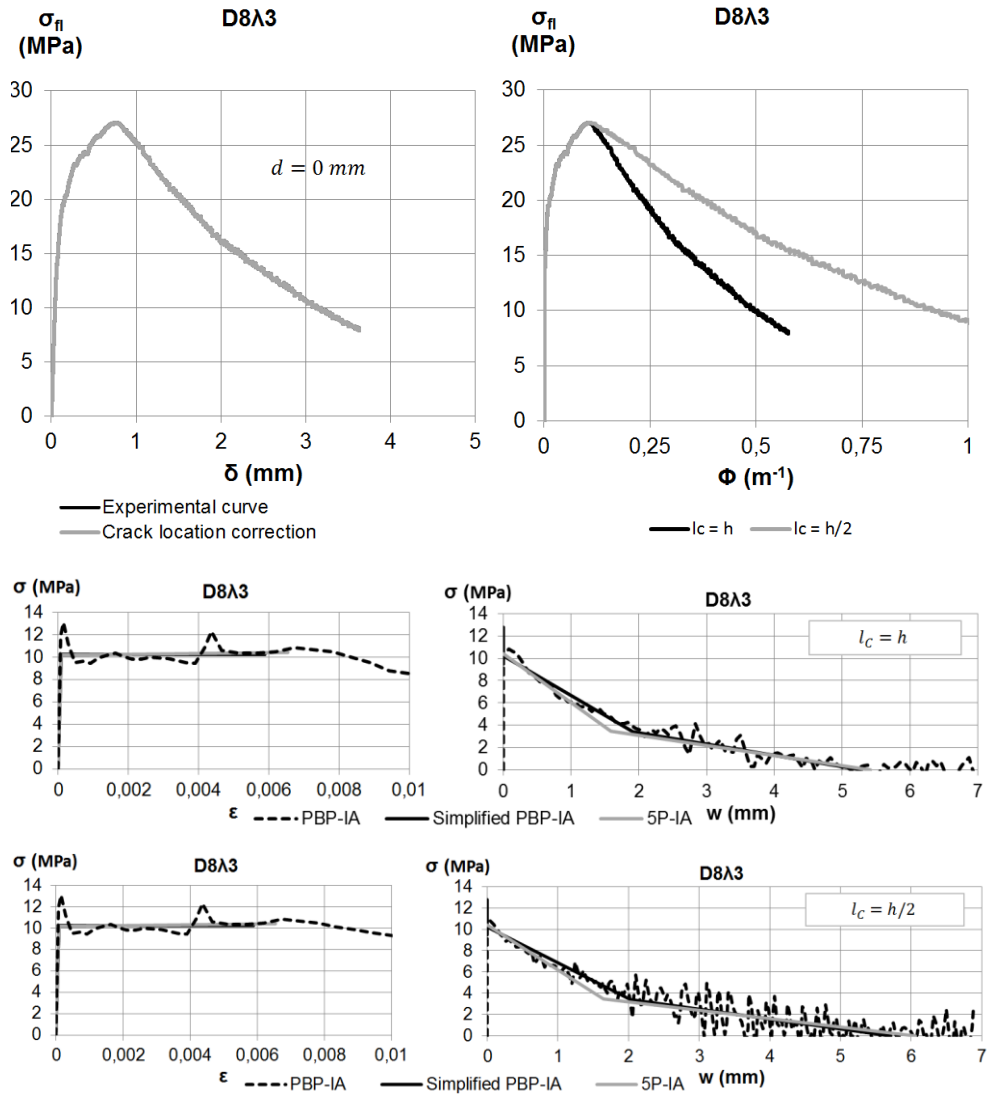
D1λ4.5
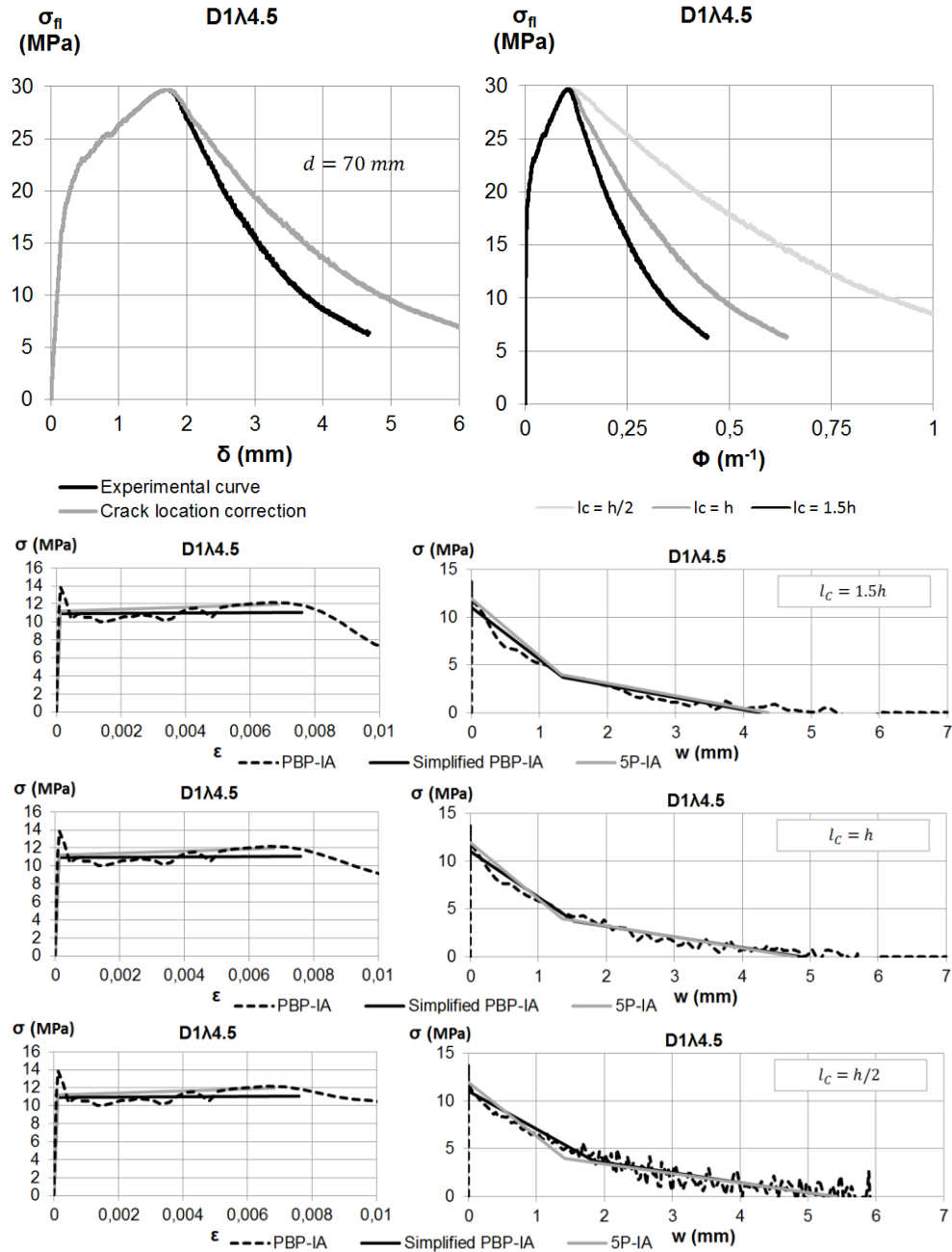
D2λ4.5
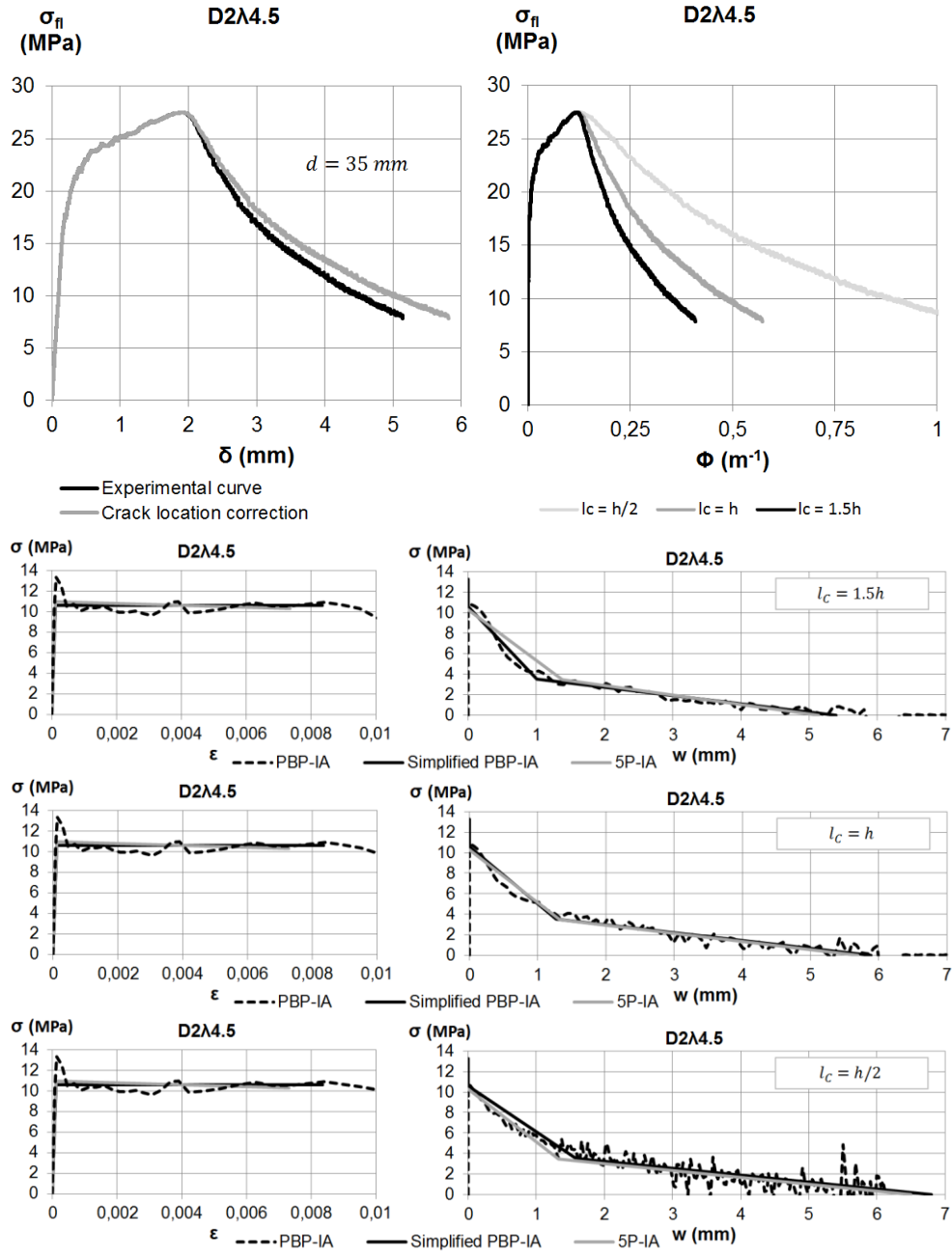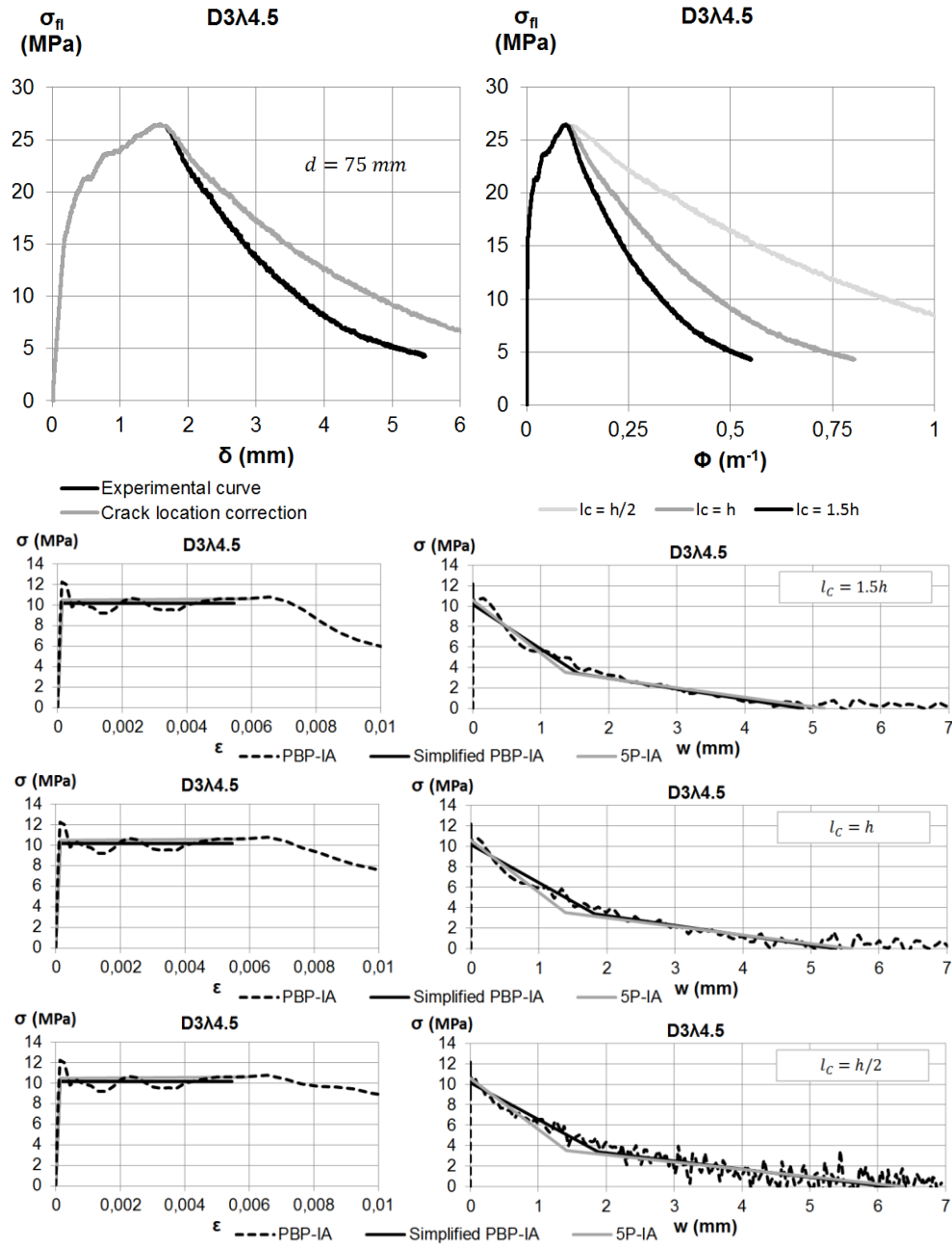
D3λ4.5
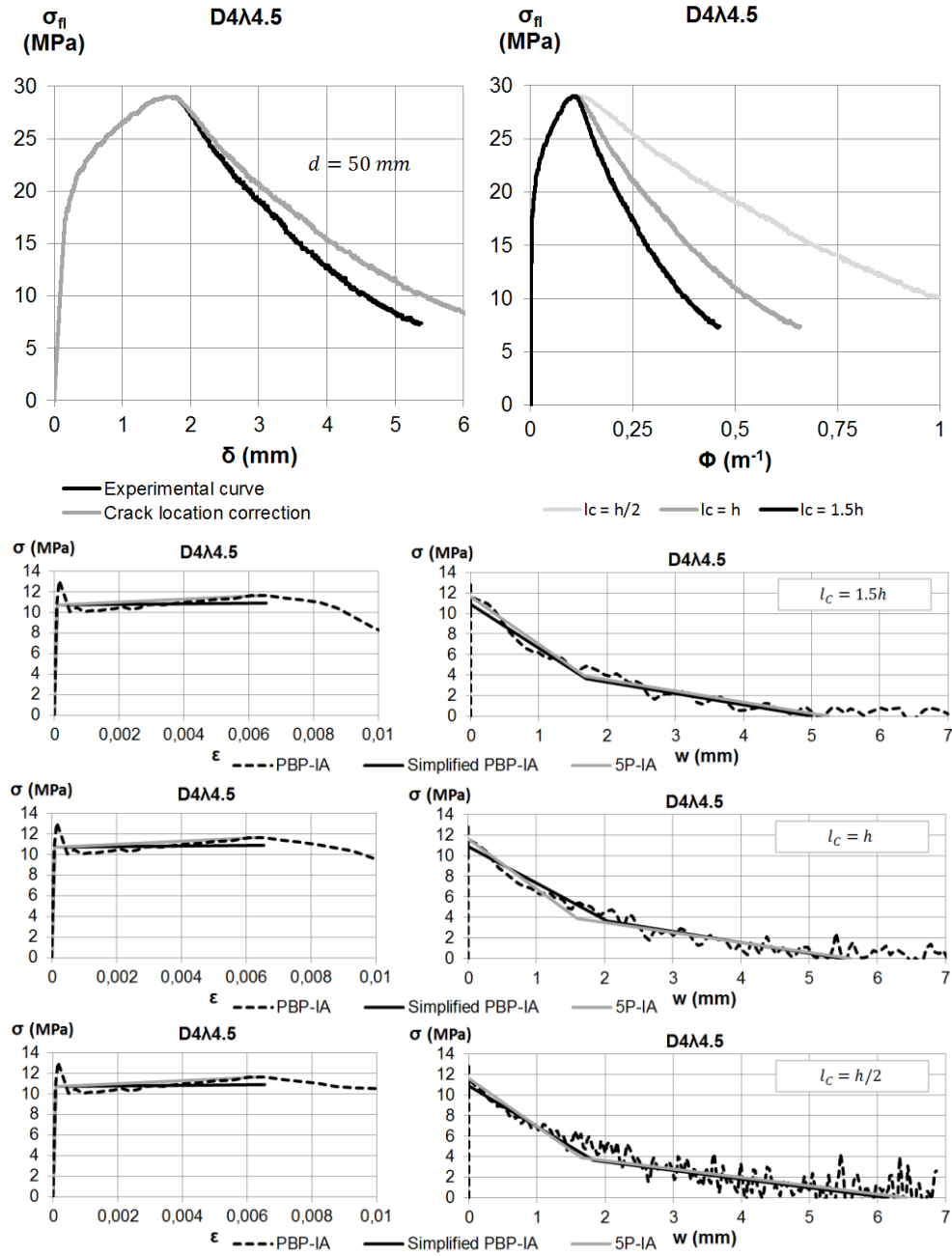
D5λ4.5
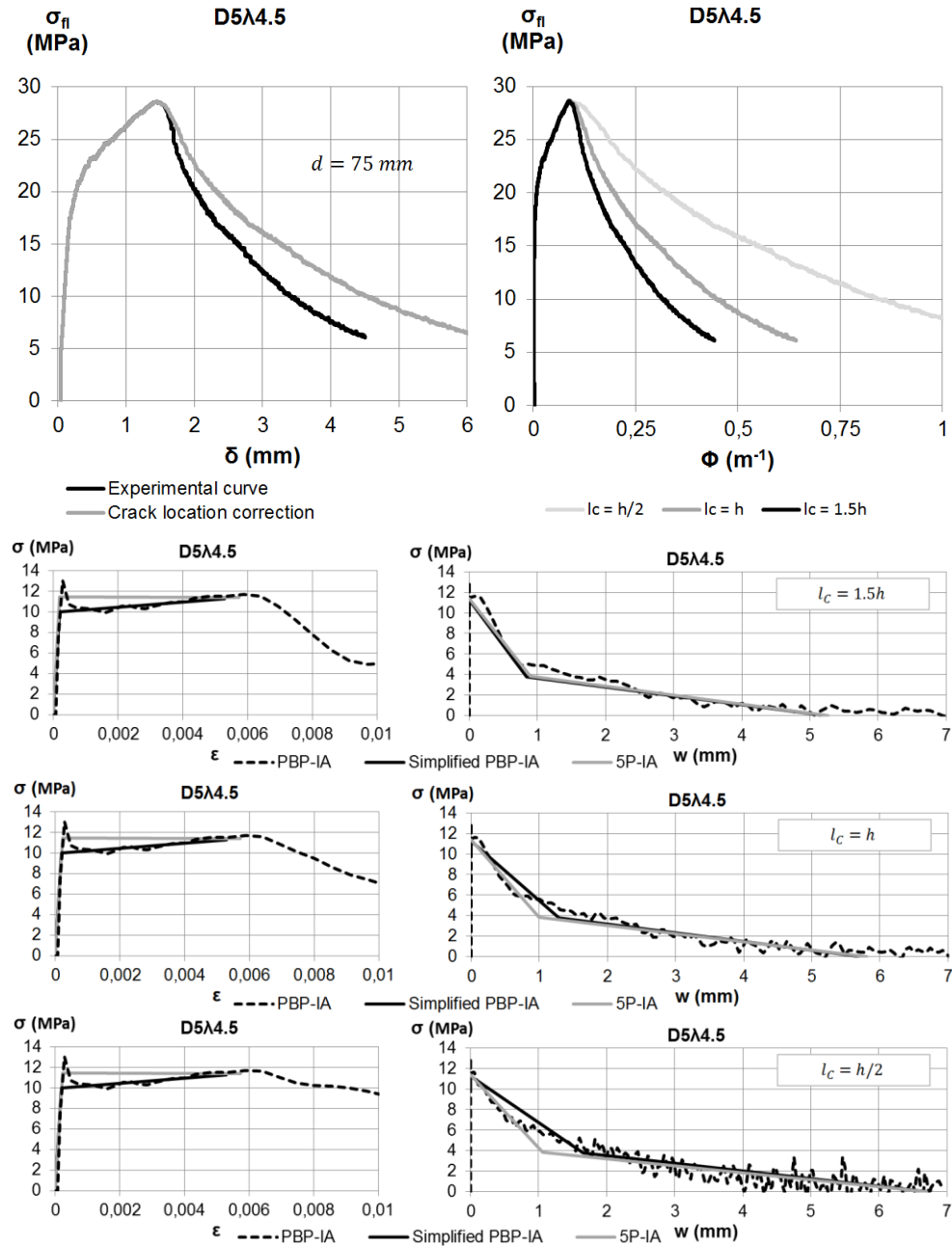
D6λ4.5
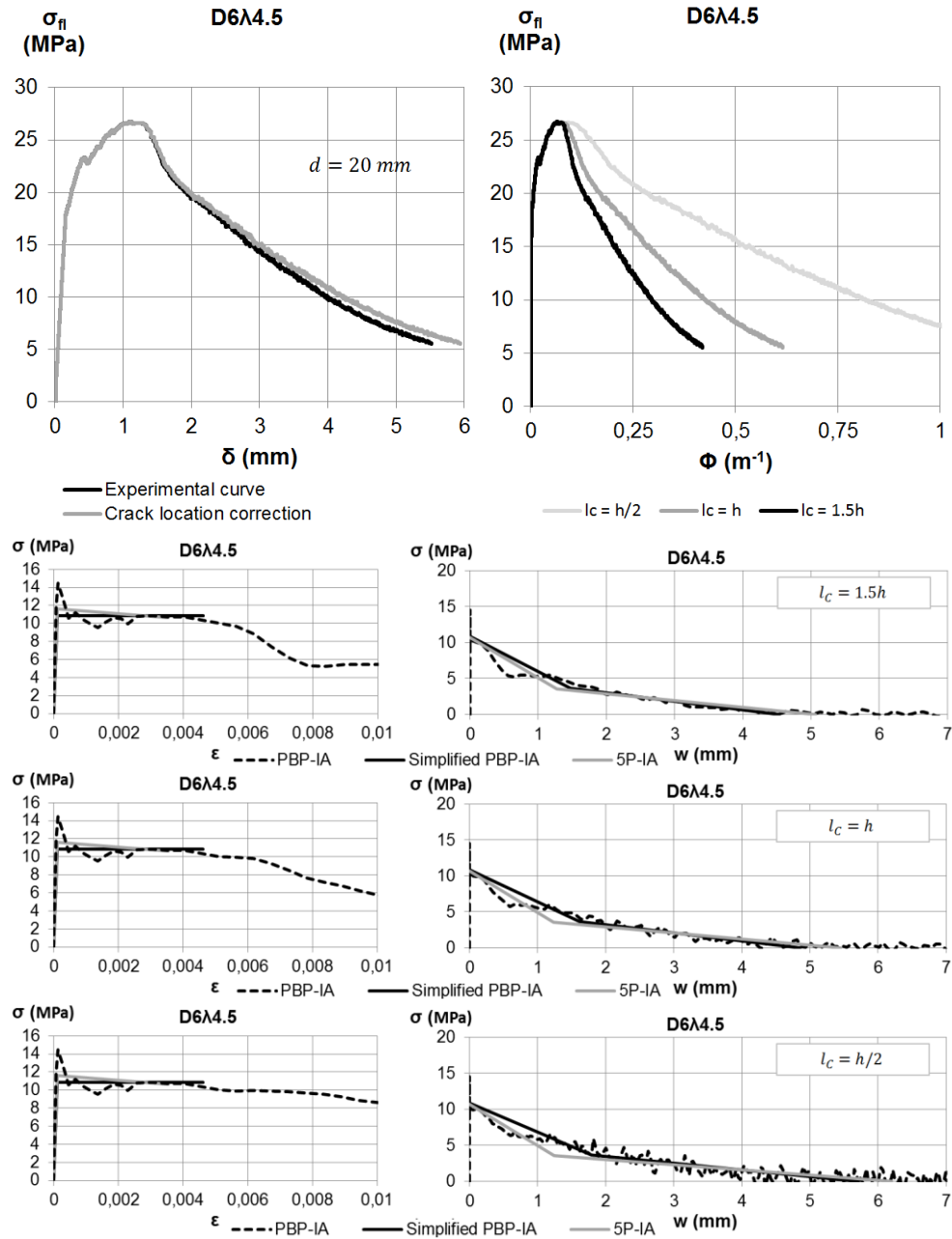
D7λ4.5

D8λ4.5
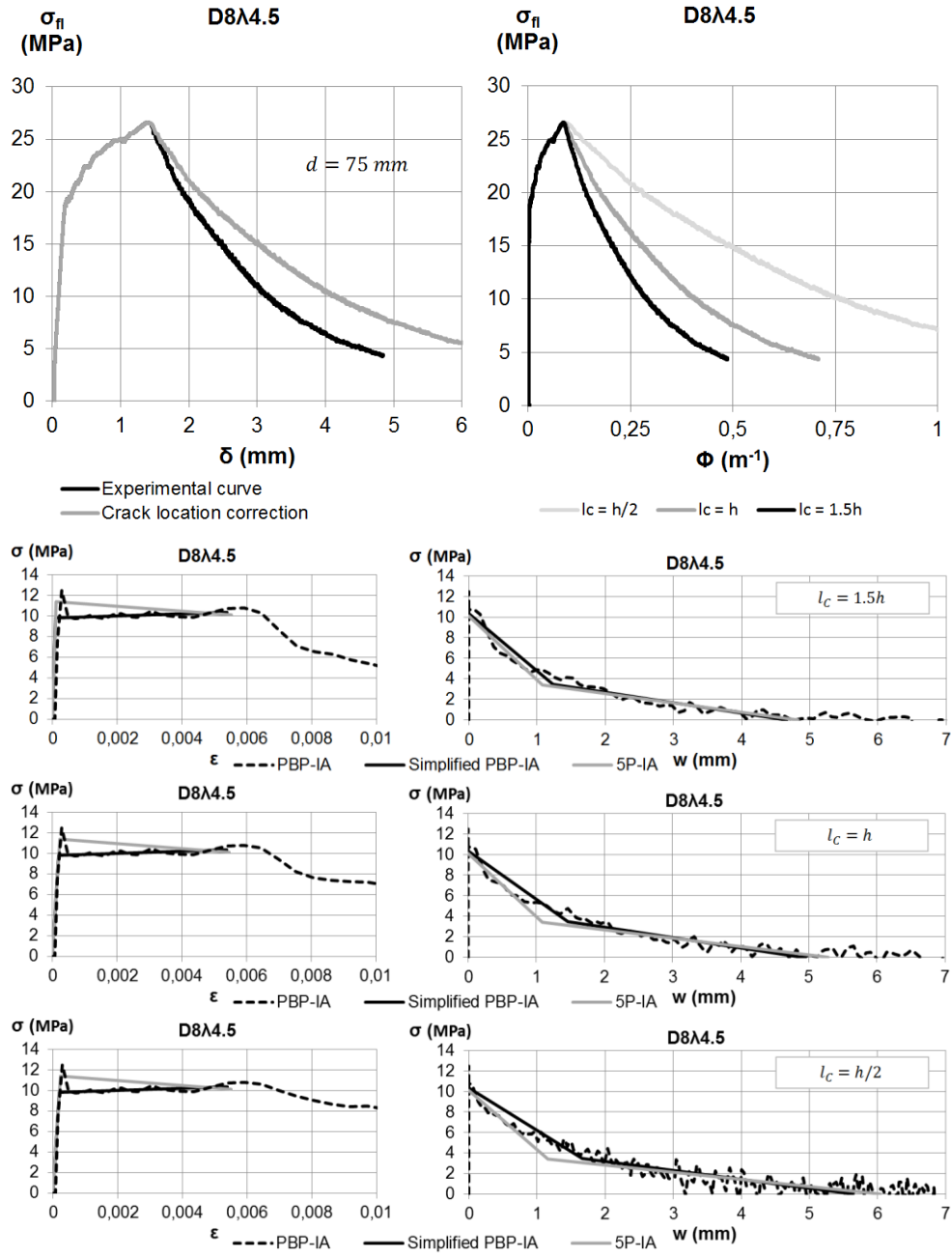
AP.II.2.1. Average constitutive curves
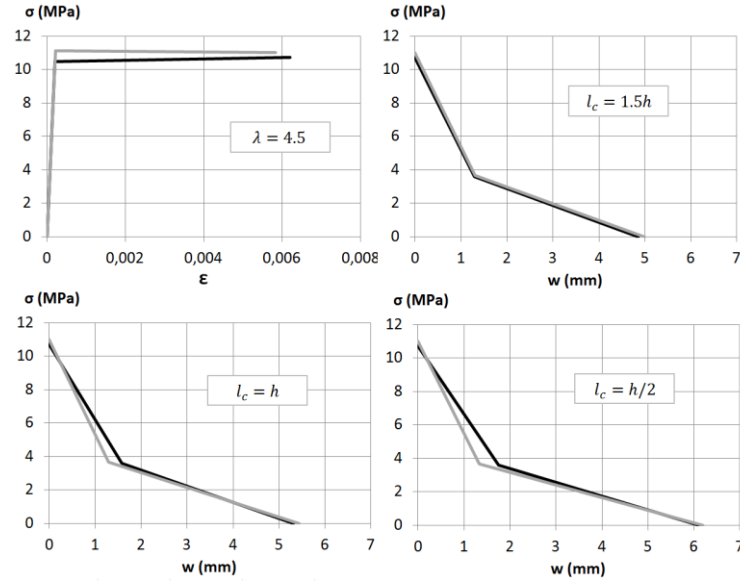
Figure AP.II. 2 Average inverse analysis results for specimens tested with a slenderness ratio of 4.5 from PBP-IA (black line) and 5P-IA (grey line).
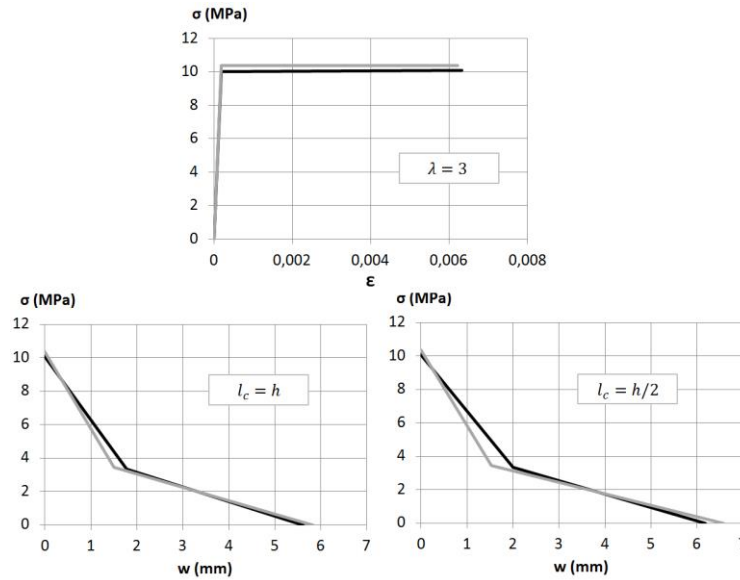
Figure AP.II. 3 Average inverse analysis results for specimens tested with a slenderness ratio of 3 from PBP-IA (black line) and 5P-IA (grey line).

AP.II.2.2. Stress-strain constitutive results summarise

Table AP.II.2 Stress-strain results from 5P-IA in MPa

5P-IA									
L/h = 3					**L/h = 4,5**				
	f_t	f_{tu}	ε_{tu}	E		f_t	f_{tu}	ε_{tu}	E
D1λ3	8,7	8,5	0,0048	53600	**D1λ4.5**	11,2	11,9	0,0068	49900
D2λ3	10,7	10,7	0,0072	62500	**D2λ4.5**	11,0	10,3	0,0073	49800
D3λ3	10,0	11,0	0,0066	61100	**D3λ4.5**	10,5	10,6	0,0059	42500
D4λ3	10,9	11,1	0,0060	46700	**D4λ4.5**	10,7	11,6	0,0063	55300
D5λ3	10,0	9,4	0,0044	48700	**D5λ4.5**	11,4	11,4	0,0057	52300
D6λ3	11,4	11,0	0,0057	53800	**D6λ4.5**	11,6	10,7	0,0035	53700
D7λ3	11,1	10,8	0,0086	50700	**D7λ4.5**	11,2	11,5	0,0058	49600
D8λ3	10,2	10,4	0,0065	52800	**D8λ4.5**	11,3	10,1	0,0055	52100
AVERAGE	**10,4**	**10,4**	**0,0062**	**53738**	**AVERAGE**	**11,1**	**11,0**	**0,0058**	**50650**
DESV	0,8	0,9	0,0012	5196	**DESV**	0,4	0,6	0,0010	3615
COV %	7,8	8,4	20,0	9,7	**COV %**	3,2	5,8	17,7	7,1

Table AP.II.3 Stress-strain results from PBP-IA in MPa

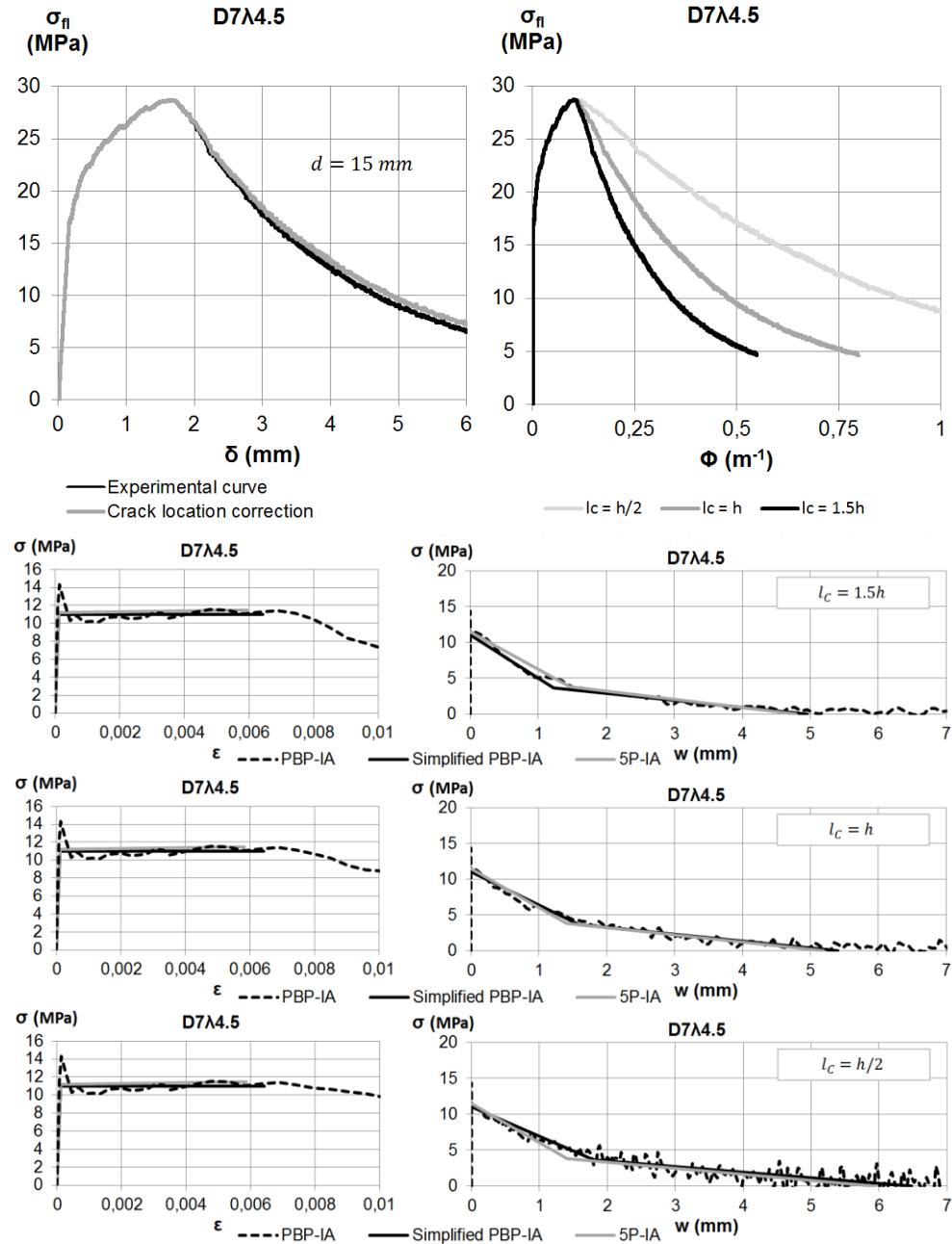| PBP-IA									
L/h = 3					**L/h = 4,5**				
	f_t	f_{tu}	ε_{tu}	E		f_t	f_{tu}	ε_{tu}	E
D1λ3	8,0	8,0	0,0049	53600	**D1λ4.5**	10,9	11,0	0,0076	49900
D2λ3	10,0	10,4	0,0071	62500	**D2λ4.5**	10,6	10,6	0,0084	49800
D3λ3	10,4	10,4	0,0070	61100	**D3λ4.5**	10,1	10,1	0,0055	42500
D4λ3	10,7	10,7	0,0068	46700	**D4λ4.5**	10,7	10,9	0,0065	55300
D5λ3	9,3	9,3	0,0046	48700	**D5λ4.5**	10,0	11,2	0,0053	52300
D6λ3	10,9	10,9	0,0053	53800	**D6λ4.5**	10,8	10,8	0,0046	53700
D7λ3	10,5	10,5	0,0090	50700	**D7λ4.5**	11,0	11,0	0,0064	49600
D8λ3	10,2	10,2	0,0059	52800	**D8λ4.5**	9,8	10,3	0,0054	52100
AVERAGE	**10,0**	**10,1**	**0,0063**	**53738**	**AVERAGE**	**10,5**	**10,7**	**0,0062**	**50650**
DESV	0,9	0,9	0,0014	5196	**DESV**	0,4	0,4	0,0012	3615
COV %	8,8	8,7	21,3	9,7	**COV %**	4,1	3,3	19,1	7,1

Table AP.II.4 Deviation in % of the results obtained from the 5P-IA in comparison to those obtained by PBP-IA

DEVIATION							
L/h = 3				**L/h = 4.5**			
	f_t	f_{tu}	ε_{tu}		f_t	f_{tu}	ε_{tu}
D1λ4.5	-7,9%	-6,2%	2,6%	**D1λ4.5**	-2,4%	-8,4%	10,9%
D2λ4.5	-6,7%	-2,6%	-0,9%	**D2λ4.5**	-3,6%	2,7%	13,0%
D3λ4.5	4,0%	-6,2%	6,1%	**D3λ4.5**	-3,2%	-4,7%	-7,1%
D4λ4.5	-1,4%	-3,8%	12,0%	**D4λ4.5**	-0,2%	-7,0%	4,0%
D5λ4.5	-7,9%	-0,4%	4,5%	**D5λ4.5**	-14,3%	-1,1%	-8,1%
D6λ4.5	-5,0%	-1,1%	-7,4%	**D6λ4.5**	-7,4%	1,4%	23,4%
D7λ4.5	-6,1%	-3,5%	4,6%	**D7λ4.5**	-1,7%	-4,4%	9,3%
D8λ4.5	0,5%	-2,0%	-11,0%	**D8λ4.5**	-16,2%	2,0%	-1,2%
AVERAGE	**-3,6%**	**-3,2%**	**1,8%**	**AVERAGE**	**-5,9%**	**-2,5%**	**6,0%**

AP.II.2.3. Stress-crack opening constitutive results summarise

Table AP.II.5 Stress-crack opening results for $\lambda=3$ from 5P-IA

5P-IA L/h=3					
Lc = h			**Lc = h/2**		
	w_d	w_c		w_d	w_c
D1λ3	1,49	4,82	**D1λ3**	1,54	5,66
D2λ3	1,32	6,53	**D2λ3**	1,40	7,43
D3λ3	1,92	6,13	**D3λ3**	1,93	6,91
D4λ3	1,44	5,52	**D4λ3**	1,42	6,02
D5λ3	1,45	5,87	**D5λ3**	1,44	6,80
D6λ3	1,59	6,24	**D6λ3**	1,62	7,19
D7λ3	1,20	6,10	**D7λ3**	1,21	6,58
D8λ3	1,59	5,42	**D8λ3**	1,65	6,06
AVERAGE	**1,50**	**5,83**	**AVERAGE**	**1,52**	**6,58**
DESV	0,20	0,51	**DESV**	0,20	0,58
CV %	13,4	8,8	**CV %**	13,2	8,8

Table AP.II.6 Stress-crack opening results for $\lambda=3$ from PBP-IA

PBP-IA L/h=3					
Lc = h			Lc = h/2		
	w_d	w_c		w_d	w_c
D1λ3	1,91	4,53	D1λ3	2,00	4,93
D2λ3	1,66	5,82	D2λ3	1,92	6,56
D3λ3	2,27	6,26	D3λ3	2,45	6,72
D4λ3	1,57	5,68	D4λ3	1,73	6,58
D5λ3	1,64	5,58	D5λ3	1,90	6,19
D6λ3	1,90	6,08	D6λ3	2,10	6,56
D7λ3	1,37	5,68	D7λ3	1,83	6,18
D8λ3	1,91	5,29	D8λ3	2,02	5,71
AVERAGE	**1,78**	**5,62**	AVERAGE	**2,00**	**6,18**
DESV	0,26	0,50	DESV	0,20	0,56
CV %	14,5	8,8	CV %	10,1	9,1

Table AP.II.7 Deviation in % of the results obtained from the 5P-IA in comparison to those obtained by PBP-IA for $\lambda=3$

DEVIATION L/h=3					
Lc = h			Lc = h/2		
	w_d	w_c		w_d	w_c
D1λ4.5	21,9%	-6,5%	D1λ4.5	23,1%	-14,8%
D2λ4.5	20,9%	-12,4%	D2λ4.5	27,4%	-13,3%
D3λ4.5	15,2%	2,0%	D3λ4.5	21,0%	-2,8%
D4λ4.5	8,5%	2,8%	D4λ4.5	17,8%	8,5%
D5λ4.5	11,5%	-5,2%	D5λ4.5	24,5%	-9,8%
D6λ4.5	16,3%	-2,6%	D6λ4.5	23,0%	-9,6%
D7λ4.5	12,1%	-7,3%	D7λ4.5	34,1%	-6,4%
D8λ4.5	17,0%	-2,4%	D8λ4.5	18,6%	-6,1%
AVERAGE	**15,7%**	**-3,8%**	AVERAGE	**23,6%**	**-6,5%**

Table AP.II.8 Stress-crack opening results for λ=4.5 from 5P-IA

5P-IA L/h=4.5								
Lc = 1,5h			Lc = h			Lc = h/2		
	w_d	w_c		w_d	w_c		w_d	w_c
D1λ4.5	1,33	4,37	D1λ4.5	1,35	4,79	D1λ4.5	1,41	5,42
D2λ4.5	1,38	5,14	D2λ4.5	1,32	5,70	D2λ4.5	1,33	6,50
D3λ4.5	1,36	5,18	D3λ4.5	1,39	5,60	D3λ4.5	1,42	6,38
D4λ4.5	1,68	5,25	D4λ4.5	1,60	5,62	D4λ4.5	1,65	6,43
D5λ4.5	0,90	5,27	D5λ4.5	1,00	5,80	D5λ4.5	1,06	6,70
D6λ4.5	1,27	5,06	D6λ4.5	1,23	5,45	D6λ4.5	1,24	6,20
D7λ4.5	1,46	4,79	D7λ4.5	1,41	5,20	D7λ4.5	1,41	5,94
D8λ4.5	1,08	4,83	D8λ4.5	1,09	5,29	D8λ4.5	1,16	6,04
AVERAGE	**1,31**	**4,99**	AVERAGE	**1,30**	**5,43**	AVERAGE	**1,33**	**6,20**
DESV	0,22	0,29	DESV	0,18	0,31	DESV	0,17	0,38
CV %	16,8	5,8	CV %	13,7	5,6	CV %	12,9	6,1

Table AP.II.9 Stress-crack opening results for λ=4.5 from PBP-IA

PBP-IA L/h=4.5								
Lc = 1,5h			Lc = h			Lc = h/2		
	w_d	w_c		w_d	w_c		w_d	w_c
D1λ4.5	1,35	4,25	D1λ4.5	1,52	4,87	D1λ4.5	1,85	5,38
D2λ4.5	1,01	5,39	D2λ4.5	1,27	5,89	D2λ4.5	1,58	6,80
D3λ4.5	1,55	4,85	D3λ4.5	1,82	5,37	D3λ4.5	1,88	6,14
D4λ4.5	1,69	5,00	D4λ4.5	2,04	5,49	D4λ4.5	1,83	6,15
D5λ4.5	0,84	5,24	D5λ4.5	1,28	5,74	D5λ4.5	1,65	6,70
D6λ4.5	1,47	4,53	D6λ4.5	1,61	4,85	D6λ4.5	1,79	5,69
D7λ4.5	1,22	4,95	D7λ4.5	1,59	5,40	D7λ4.5	1,80	6,48
D8λ4.5	1,23	4,66	D8λ4.5	1,47	4,90	D8λ4.5	1,67	5,64
AVERAGE	**1,30**	**4,86**	AVERAGE	**1,58**	**5,31**	AVERAGE	**1,76**	**6,12**
DESV	0,26	0,35	DESV	0,24	0,38	DESV	0,10	0,49
CV %	20,4	7,2	CV %	15,3	7,1	CV %	5,8	8,0

Table AP.II. 10 Deviation in % of the results obtained from the 5P-IA in comparison to those obtained by PBP-IA for λ=4.5

DEVIATION L/h=4.5								
Lc = 1,5h			Lc = h			Lc = h/2		
	w_d	w_c		w_d	w_c		w_d	w_c
D1λ4.5	1,5%	-2,7%	D1λ4.5	11,3%	1,6%	D1λ4.5	23,5%	-0,8%
D2λ4.5	-37,1%	4,7%	D2λ4.5	-3,9%	3,2%	D2λ4.5	15,9%	4,4%
D3λ4.5	12,0%	-6,8%	D3λ4.5	23,6%	-4,3%	D3λ4.5	24,6%	-3,9%
D4λ4.5	1,0%	-4,9%	D4λ4.5	21,6%	-2,3%	D4λ4.5	9,7%	-4,5%
D5λ4.5	-7,1%	-0,6%	D5λ4.5	22,3%	-1,1%	D5λ4.5	36,1%	0,0%
D6λ4.5	13,4%	-11,6%	D6λ4.5	23,5%	-12,3%	D6λ4.5	30,7%	-8,9%
D7λ4.5	-19,4%	3,3%	D7λ4.5	11,4%	3,9%	D7λ4.5	21,4%	8,4%
D8λ4.5	12,1%	-3,6%	D8λ4.5	25,7%	-7,9%	D8λ4.5	30,6%	-7,1%
AVERAGE	-1,0%	-2,6%	AVERAGE	17,6%	-2,2%	AVERAGE	24,0%	-1,3%